ADDIS ABABA UNIVERSITY
COLLEGE OF NATURAL AND COMPUTATIONAL SCIENCES
SCHOOL OF EARTHSCIENCES

Mapping Geological Structures Using Integrated Geophysical Methods and Their Possible Implications, a Case Study of the Ziway-Shala Lakes Basin, Central Main Ethiopian Rift

by

Hailemichael Kebede

A Thesis Submitted in Partial Fulfillment of the Requirements for the Degree of Doctor of Philosophy

in

Geophysics (Applied Geophysics)

Addis Ababa University

Addis Ababa

Ethiopia

October, 2020

ADDIS ABABA UNIVERSITY

COLLEGE OF NATURAL AND COMPUTATIONAL SCIENCES

SCHOOL OF EARTHSCIENCES

This is to certify that the thesis prepared by Hailemichael Kebede, entitled: "Mapping geological structures using integrated geophysical methods and their possible implications, a case study of the Ziway-Shala Lakes Basin, central Main Ethiopian Rift" and submitted in partial fulfillment of the requirements for the degree of Doctor of philosophy in Applied Geophysics complies with the regulations of the university and meets the accepted standards with respect to originality and quality.

Signed by the examining committee:

	Signatures	Date
Examiner Prof. Kevin Mickus (External examiner)	_____	_____
Examiner Prof. Bekele Abebe (Internal examiner)	_____	_____
Advisor Dr. Abera Alemu (Principal advisor)	_____	_____
Advisor Dr. Desie Nedaw (Co- advisor)	_____	_____
Advisor Dr Shimeles Fisseha (Co- advisor)	_____	_____

_____

Chair of department or Graduate program coordinator

Abstract

Mapping Geological Structures Using Integrated Geophysical Methods and Their Possible Implications, a case Study of The Ziway-Shala Lakes Basin, Central Main Ethiopian Rift

Hailemichael Kebede

Addis Ababa University, 2020

The Ziway-Shala Lakes Basin in the Central sector of the Main Ethiopian Rift ($38^0$00' E - $39^0$30' E and $7^0$00' N -$8^0$30' N), has been affected by active Cenozoic tectonic, volcanic and sedimentation processes. These processes are mainly responsible for the current geological and structural setting of the basin. Even though there exists numerous works on the surface and deep structure of the region, the shallow to intermediate depth litho-structural set up of the Ziway-Shala Lakes Basin is least studied. For its implications on hydrology, geothermal and hydrocarbon resources, this PhD research focuses on delineating the shallow to intermediate depth litho-structural features of the basin using gravity, magnetic and seismic noise data with application of various mathematical enhancements and numerical algorithms. These mathematical techniques include derivatives filters, upward continuation, Line module algorithm, Source Parameter Imaging, Power Spectral Analysis, 2D Werner De-convolution, joint 2D forward modeling and 3D structural inversion. The orientations of subsurface lineaments obtained from gravity and magnetic data analysis are dominantly oriented in NNW-SSE to NW-SE and E-W directions. These results appear to differ from the general orientation of surface geologic structures (NNE-SSW to NE-SW) in the Central Main Ethiopian Rift which is the major tectonics of the Cenozoic rift. The shallow to intermediate depth structural trends revealed in this study seem to reflect the influence of the pre-existing Mesozoic Ogaden rift. Gravity and magnetic depth estimation along the rift axis shows the northward thickening of the

low-velocity volcano-sedimentary layer. Furthermore, about 561 m thick horizon, possibly of Mesozoic sediments, has been identified between the Tertiary ignimbrite layer and the crystalline basement for the first time. The information obtained with regard to water balance of the basin, salinity level of the lakes and the conceptual hydrological flow model adopted appear to reveal that the groundwater flow in the study region is controlled by subsurface structures (lineaments and the mapped interface topographies). Interpretation of the compiled magnetic anomaly maps reveal the existence of a structural path, between 1.5 km and 3 km of depth, along a traverse running from the Aluto-Langano geothermal field to the Silti Debre Zeyte Fault zone. The structural path is thought to serve as a conduit connecting the Aluto-Langano geothermal field and the likely heat source located around the locality of the Silti Debre Zeyte Fault Zone. The study also identified magnetic lineaments most of which are oriented in the direction of pre-existing Mesozoic structures and in the direction of thermally altered structures. Mesozoic sediment delineated under a thick volcanic cover (2.5 km) could be taken as a favorable geologic setting for accumulation of hydrocarbon and CO2 degassing in the region. Generally, the identified geological structures of shallow to intermediate depth are useful in understanding the groundwater dynamics, geothermal heat sources and hydrocarbon accumulations associated with the regions.

Acknowledgements

Above all, I am indeed grateful to my heavenly father, Jesus Christ for the sustenance and strength to the successful completion of my PhD program. Secondly, my deep gratitude goes to my Advisors Dr Abera Alemu, Dr Desie Nedaw and Dr Shimeles Fisseha for taking the position of an advisor in this research. They give me proper direction and support all the way through my research. I especially appreciate Dr. Abera Alemu for his patience and willingness to devote much of his time and energy at all stages of my work. The status of his health has not hindered him from giving critical comments and suggestion. His fatherly approach and unconditional effort have given me the opportunity to explore more in my future research work.

I appreciate the Institute of Geological Survey of Ethiopia and US Geological Survey for gravity data and Tromino seismometer respectively. Furthermore, my special thanks goes to Dr. Abera Alemu for the raw secondary gravity and magnetic data

My special thanks go to the Ambo University for sponsoring my stay at the Addis Ababa University and some funding supplementing my research work. Secondly, my thanks goes to the Addis Ababa University for financial and logistic support during geophysical data collection. I don't want to jump from recognizing my brother Dr. Seifu Kebede for his moral, academic support and financial assistance whenever gaps existed. Really, I want to acknowledge his wife Rahel and daughter Ella for their encouragement and support.

My particular thanks goes to my considerate wife Birhane Zewude, my daughter, Melala and son Beka for their endurance and understanding while I was engaged with the Dissertation. Furthermore, I would like to extend my sincere thanks to my brothers Dr. Ing. Tesfaye Kebede and Sintayehu Kebede for their moral support and encouragement. I would like to thank my lovely mother Dengie, father Col. Kebede, sisters Woinshet and her family, Bizu and her family, Zewiditu and her family, Marta and her family and Selamwit Kebede for their patience support, appreciation and pray during my PhD study at AAU.

Last but not least, my thanks goes to all the staff and colleagues of the School of Earth Sciences who directly or indirectly contributed to my PhD research work. Particularly, I am grateful to Prof. Bekele Abebe, Prof. Tilahun Mamo, Prof. Tigistu Haile and Dr. Ameha Atnafu for their support in the accomplishment of this Dissertation.

Table of Contents

Contents

List of Figures

List of Tables

List of Abbreviations

1D, 2D and 3D- One, Two and Three Dimension

EARS- East African Rift System

MER- Main Ethiopian Rift

ZSLB- Ziway-Shala Lakes Basin

IGRF- International Geomagnetic Reference Field

RMS- Root Mean Square

RTP - Reduction to Pole

DRTP- Differential Reduction to Pole

UTM- Universal Transverse Mercator

SDFZ- Silti Debrezyte Fault Zone

WFB- Wonji Fault Belt

YTVL- Yerer Tulu Welel Volcanic Lineament

WGS- World Geodetic System

DEM: Digital Elevation Model

IGSN71: International Gravity Standardization Network 1971

ASTER: Advanced Space-borne Thermal Emission and Reflection Radiometer

VDR, **FVDR, SVDR** and **TDR**: Vertical derivative, First Vertical Derivative, second Vertical Derivative and tilt derivative

PCA: Principal Component Analysis

ArcGIS: Aeronautical Reconnaissance Coverage Geographic Information System

QGIS software: Quantum Geographic Information System software

ENVI 5.1: Environment for Visualizing Images

PCI Geomatica: Remote sensing desktop software package for processing earth observation data

HVSR: Horizontal to Vertical Spectral Ratio

IAGA: International Association for Geomagnetism and Aeronomy

IGRF: International Geomagnetic Reference Field

Chapter 1: General Introduction

1.1 Background

The principles and laws of physics are used to investigate the Earth's internal structures and processes (Reynolds, 1997). Geophysical methods using gravity, magnetic and seismic noise data are integrated to map and characterize the subsurface geology and geological structures of the Ziway-Shala Lakes Basin (Central Main Ethiopian rift (CMER)) bounded by 38^{0}00' E - 39^{0}30' E and 7^{0}00 N'-8^{0}30' N. Understanding of these structures is important as they have subsurface resources (groundwater, geothermal energy and petroleum) implications. The region is known by tectonic, volcanic and sedimentation processes which are responsible for the current geological and structural setting of the area (Le Turdu et al., 1999). These geological processes in the study region resulted in geological structures like folds, faults (Woldegabriel et al., 2000), contacts, fractures and lithological geometric variations. Previously extracted geological structures in the East Africa Rift documented by various researchers mainly target on extracting the surface structures of the shallow earth origin (Molin and Corti, 2015; Agostini et al., 2011). Furthermore, the subsurface structures of deep origin in the same region were extracted from potential field data, most of which focus on mapping crustal structures thickness and Moho depths undulations (Mickus, 2007; Tiberi et al., 2005; Tessema and Antoine, 2004; Mahatsente et al., 1999). However, there is less known about shallow to intermediate depth geological structures to different depth levels in the Ziway-Shala Lakes Basin, Central Main Ethiopian Rift. These features were extracted from gravity and magnetic anomalies with analysis made with some available mathematical and computer algorithms. The other geophysical method employed in the area was the passive seismic survey. This method measures seismic noise of its analysis gives the shallowest impedance contract (bed rock topography) of the region. Validation

of the mapped subsurface structures is determined using previously mapped geology and geologic structural maps of the area. Furthermore, in this study a Digital Elevation Model data (DEM) was used to trace surface lineaments (structures) which could help to validate the subsurface structures mapped in the region considered. The mapped geological structures of intermediate depth are deemed to be useful in understanding/characterizing the groundwater dynamics, sources of geothermal and hydrocarbon resources.

1.2 Rationale and Objectives of the study

1.2.1 Overview of Previous Studies

A well-known previous geophysical study conducted in study region along the rift axis includes the controlled-source seismic survey conducted by Ethiopia Afar Geo-scientific Lithospheric Experiment (EAGLE) project (Maguire et al., 2006). It includes a 400 km profile subsurface velocity image along the axis of the Main Ethiopian rift (MER). The main findings of this study includes crustal and sub-Moho P-wave velocity model (Maguire et al., 2006). Compared to the depth of investigation (> 50 km), the shallow subsurface structures were mapped with low resolution of data (Maguire et al., 2006). In conjunction to refraction/wide-angle seismic reflection survey, 2.5 D gravity model were generated to map a preliminary crustal structure (Mickus et al., 2007). The maximum depth of investigation obtained based on this model is about 120 km (Mickus et al., 2007). We thus consider that, these models have mapped the shallow/intermediate structures of the MER with a low resolution.

Though the depth extent was not mentioned, Korme et al. (2004) identified a pre-existing NW-SE Ogaden Mesozoic rift fault from gravity data. These structures cross the main Ethiopian rift orthogonally (Korme et al., 2004). On the other hand there are no studies that have targeted the

shallow/intermediate depth geological structures to different depth levels in the Ziway-Shala lakes basin.

The gravity and magnetic data were processed, analyzed and modeled to extract the subsurface structures of shallow to intermediate depths. Validations of the extracted structures are made based on previous geological and geophysical studies in the region under study. In this study surface structures are traced using 30 m resolution of DEM data to confirm the mapped subsurface structures.

1.2.2 General Objective

To map subsurface geological structures using integrated geophysical, mainly gravity and magnetic methods and determine their possible significance.

1.2.3 Specific Objective

The specific objectives of this study are:

1. To map the regional and residual potential field anomalies which could respectively related to deep and shallow subsurface geology and geologic structures, respectively.
2. To map the subsurface geologic lineaments at multiple depths using gravity data and validate it with surface lineaments traced from Digital Elevation Model (DEM) data and previously mapped structures
3. To map magnetic anomaly patterns and volcano-tectonic features associated with geothermal energy sources
4. To determine the gravity and magnetic source depths which could tell the subsurface structures (lithological geometries) in the region considered
5. To model the subsurface layers topography (undulations) using constrained 3D gravity Interface Inversion

6. To map the shallowest bedrock topography in between water divide using HVSR of passive seismic data
7. To determine the possible implications of the mapped structures to groundwater dynamics, geothermal heat sources and hydrocarbon accumulations.

1.3 Significance of the study

The comprehensive study of the shallow/intermediate depth geological structures in the Ziway-Shala Lakes Basin, Central Main Ethiopian rift, are made using analysis of potential field and seismic noise geophysical data. These mapped geological structures in the region under consideration are useful implication in mapping/characterizing the subsurface resources.

1.4 Thesis structure

The thesis work consists of ten chapters where four have been either published or submitted manuscript in refereed scientific journals (Appendix 1.1 to 1.4). Two of them are ready to be submitted to peer-reviewed journals. The title and abstract of each manuscript including where they were published and where they are submitted are described in Appendices (Appendix 1.1 to 1.4). It should be noted that each chapter have independent findings which supplements each other. However, each paper/chapter may contain unavoidable duplication in background information. The brief description of the organization of the thesis is described as follows

Chapter 1 states the general introduction describing the background of the study. In this section, after setting up and documenting the foundation of the studies through reviewing the previous studies in the area, the main and specific objectives of the study are described. Finally, the thesis structures and flow chart describing the overall activities of the thesis work are documented.

Chapter 2 presents the general overview of the study area starting with defining location and physiography of the study area, secondly geologic and structural settings in the region under

consideration are described and finally climate, hydrology and hydrogeology of the study region is illustrated.

Chapter 3 begins with describing the overall description of the theoretical foundations of gravity and magnetic methods. The governing equations (mathematical formulation) of gravity and magnetic methods are accompanied by their detail gravity and magnetic data reductions are introduced. Finally, the point gravity and magnetic data distributions including anomaly maps are shown for the study area.

Chapter 4 firstly presents gravity and magnetic data acquisition and secondly describes the detail descriptions of gravity field data decomposition methods in which the observed gravity field is separated into its regional and residual components which respectively show deep and shallow geologic sources. As there is no single chosen method, the varied separations methods are described and documented. The frequently used upward continuation and trend surface methods are picked out for inter-comparison in relation to better regional field estimations. Vertical derivative, power spectral analysis, well log data and surface geology of the area are used to validate the finally chosen upward continuation method as gravity data separation techniques. The chapter describes the first main result of the thesis work targeted to show the state of the art on choosing the appropriate gravity field decomposition methods.

Chapter 5 documented geological structures (lineaments) extracted from gravity and DEM. It begins with an introduction describing location of the study area, geology, geologic structures and objective of the study and secondly, the data and the different filtering methodologies used to map geologic structures (lineaments) are documented. Thirdly, subsurface lineaments extracted from gravity data at different depth levels are made and validated against surface

geologic structures extracted previously by different researchers and topographic lineaments traced in this study from DEM data. Hydro-geological significance of the mapped lineaments is also documented in this section. This chapter describes the second main result of the thesis work that targets on mapping gravity lineaments (structures) extracted at different depth levels and possible hydro-geological significance of these structures.

Chapters 6 maps the magnetic anomaly patterns and volcano-tectonic features associated with geothermal heat sources in the study area. It begins with introduction which could incorporate the basic background that leads to define the gaps (problems) in the study area, secondly location of the study area and geologic/structural settings of the area. Thirdly, the mathematical filtering methods used to extract the subsurface structures are described. Fourthly, magnetic and well-log data sets used in the study area clearly described. The collected magnetic data anomaly shows high and low value signals which may not occur over the sources generating them as the survey area is located at low magnetic latitude. The chapter documented how these problems are tackled with the reduction to pole procedures which is chosen differently by different researchers. The chapter fully describes the different pole reduction procedures in low latitude area and chooses the appropriate reduction method. The pole reduced total magnetic field need to be separated into regional and residual components which respectively indicate the deep and shallow subsurface geology. This chapter is taken as the third main finding of the thesis work that target on mapping geothermal related structural features and subsurface magnetic lineaments in the region considered.

Chapter 7 focuses on estimating potential field source depths using the varied inversion methods including power spectral analysis, 2D Werner Deconvolution, Source Parameter Imaging (SPI), 2D joint forward modeling and 3D layer based gravity inversion. The chapter begins with

introduction, location, geology/geologic structures and objective of the chapter. Secondly, the data sets and the inversion methodology are clearly documented. Causative source depth locations and interfaces undulation along the rift axis and rift floor are getting interpreted in result section of the chapter. Groundwater resource implication of these structures is also documented in discussion section. This chapter documented the fourth main findings of the thesis work.

Chapter 8 target on mapping the subsurface interface topography and layers thickness using inverse modeling of residual gravity data. It describes layers based gravity inversion under chapter title entitled "Application of constrained 3D gravity interface Inversion techniques to map shallow Earth layer structures". It begins with introduction describing the study location, previously extracted geological structures, problem definition (gaps) and objective of the study. Parker-Oldenburg structural inversion algorithms and constraining parameters are documented in detail. Layers undulation (geometries) of the bottom most crystalline basement, Mesozoic layer and tertiary ignimbrite layer are documented and validated in results and discussion part of this chapter. This study for the first time identified a new Mesozoic horizon in between Tertiary ignimbrite layer and crystalline basement layer at a depth in between -2499 m and -3060 m having maximum thickness of 561 m. The analyses of this layer in relation to hydrocarbon potential are discussed. Finally, summary and recommendation of the chapter are made under conclusion section. This chapter is the fifth main finding of the thesis work.

Chapter 9 finally presents geologic structures of the shallowest earth origin in between the Ziway-Shala Lakes Basin and Awash basin. This chapter is compiled to supplement and validate potential field geophysical results documented in previous chapters. The study aims at characterizing subsurface structures of very shallow level. Passive seismic survey is carried out

to record a three component measurements of ambient seismic noise data. This data are processed and analyzed using average horizontal to vertical spectral ratio to determine resonance frequencies of the region. The depth to shallowest layer is determined for each sites and this depth value is gridded and mapped to show subsurface topography of the highest frequencies.

Chapter 10 finally put the general conclusions and future directions of the thesis work starting with summery of the research work. Though each chapter winded up with concluding remarks, this chapter independently made to document the general conclusions of the overall dissertation work. The synthesis of the contribution of the research work are made particularly on extracting information about structural control of groundwater dynamics, geothermal heat sources and hydrocarbon accumulation of the mapped geologic structures. Limitation of the thesis work, future direction and recommendation in the area is finally documented.

Having defining the objectives of the study, the next chapter describes the general overview of the Study Area.

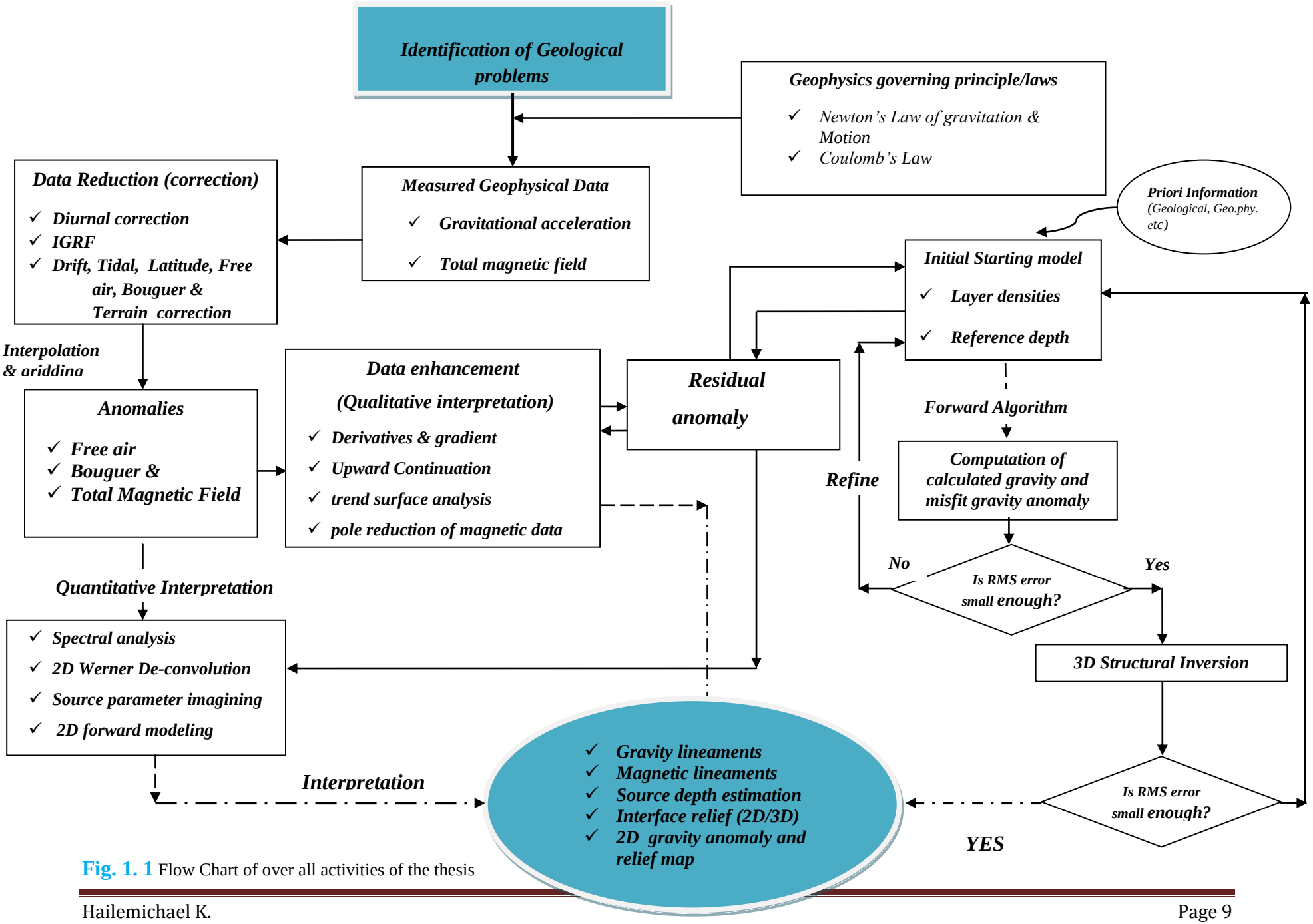

Fig. 1. 1 Flow Chart of over all activities of the thesis

Chapter 2: General Overview of the Study Area

2.1 Location and Physiography

The Ziway-Shala Lakes Basin (Central Main Ethiopian rift) is part of Main Ethiopian rift bounded between $38^{0}00$'E-$39^{0}30$' E and $7^{0}00$'N - $8^{0}30$' N (Fig. 2.1). It is located some 180 km south of the capital city, Addis Ababa.

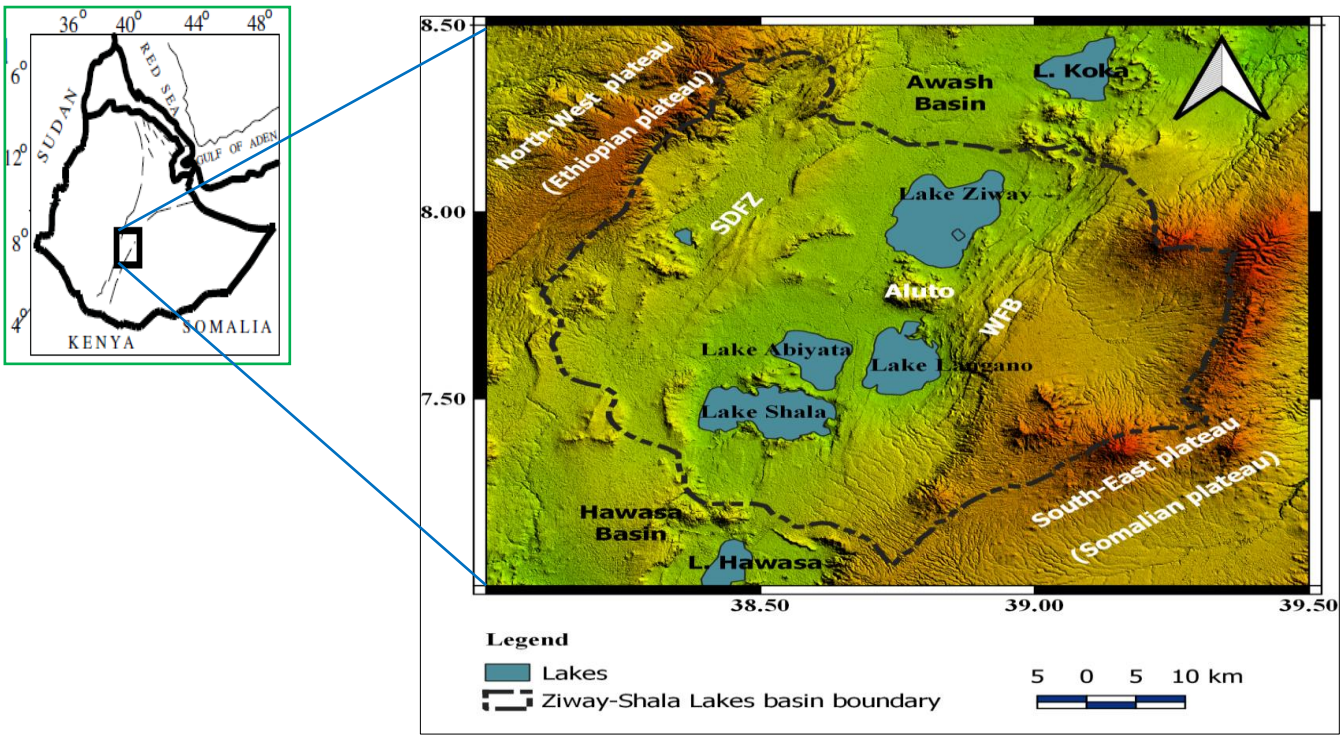

Fig. 2. 1. Location and elevation (physiographic) map of the Ziway-Shala Lakes Basin and surroundings, Central Main Ethiopian Rift.

The rift floor, the east and west fault escarpments and the NW and SE highlands characterize the physiographic features of the area (Fig. 2.2). The elevation varies from shallowest 1342 m a. s. l

to highest 4168 m a. s. l as read from DEM of 30 m resolution. The low elevations corresponds to rift floor and while the high corresponds to mountains of the plateau (Fig. 2.2).

Ziway-Shala Lakes Basin (ZSLB) is bounded in the north and north-east by its adjacent Awash River basin, in the south and south-west by Hawasa basin, in NW by Ethiopian plateau and in SE by Somalian plateau.

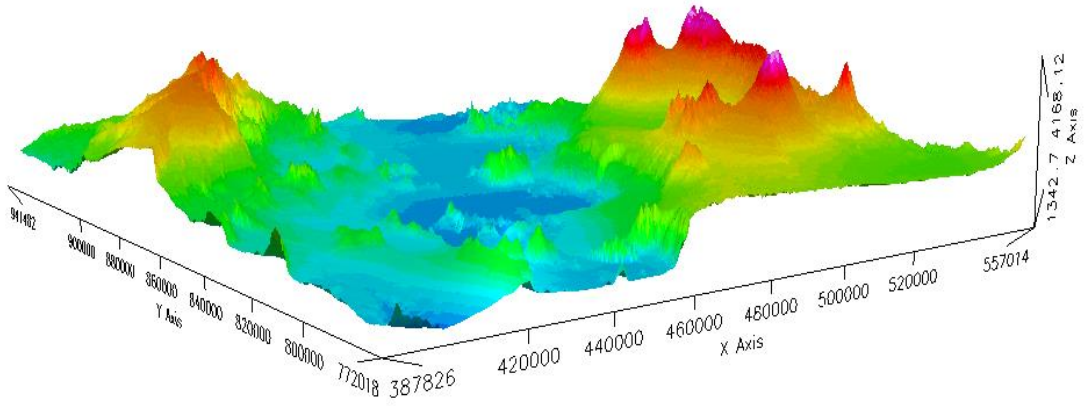

Fig. 2. 2 Elevation map of the Ziway-Shala Lakes Basin (CMER).

2.2 Geologic and Structural Settings

The Main Ethiopian Rift (MER) where the study lies was developed over a span from the Oligocene to the Quaternary (Le Turdu et al., 1999; Woldegabriel et al., 2000). The current geologic and geomorphic features are due to geological processes including tectonic, volcanic and sedimentation processes. The surface structures mainly named Wonji Fault Belt (WFB) (Mohor, 1962), Silti Debrezit Fault Zone (SDFZ) and their associated boundary faults (Boccaletti et al., 1998). They mainly trend N-S to NNE-SSW, NE-SW, E-W and NW-SE (Korme et al., 2004) orientation. These youngest and active faults crosscut the pre-existing NW-SE Ogaden fault (Korme et al., 2004) (Fig. 2.3(b)).

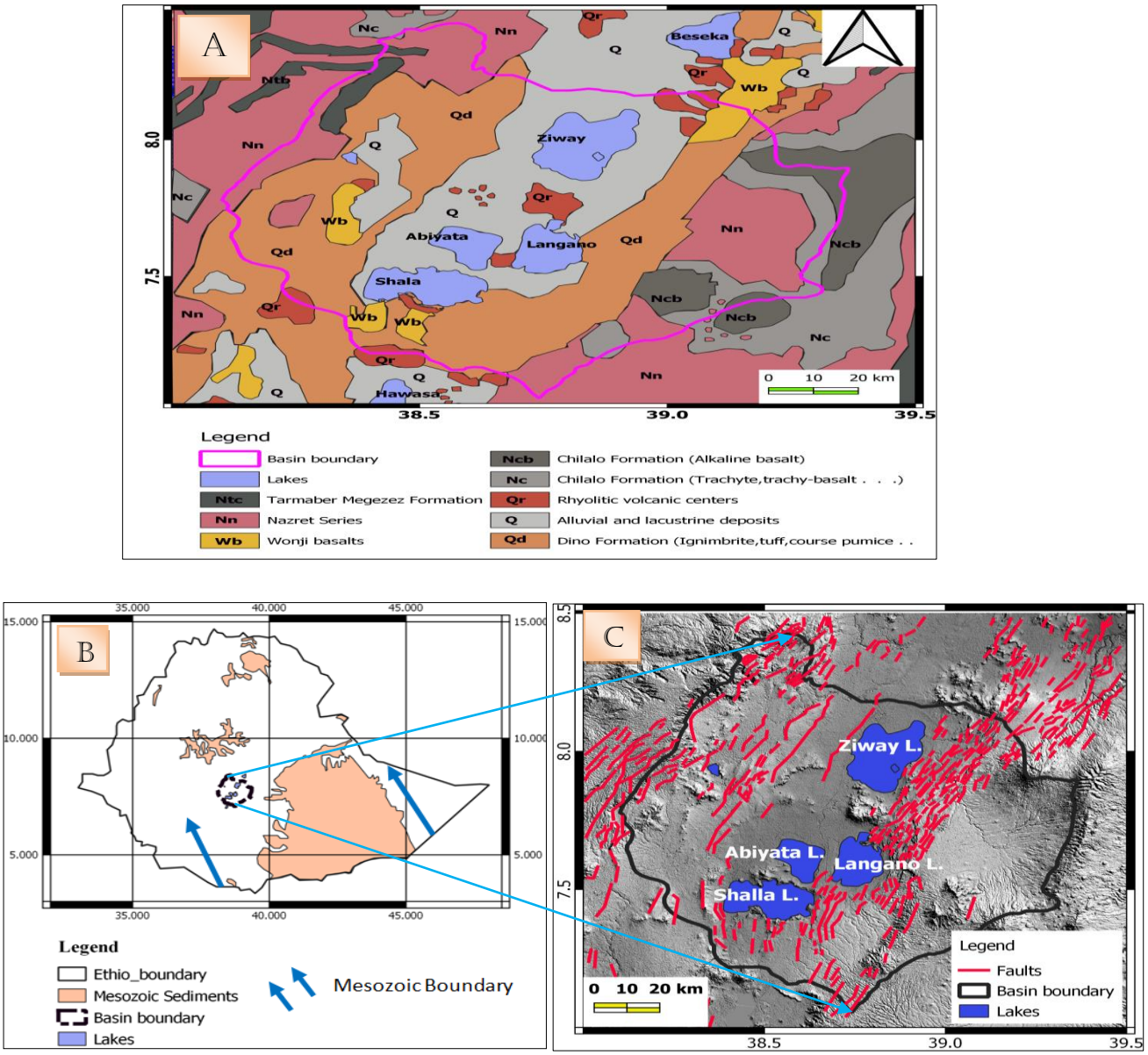

Fig. 2. 3 Geology of the Ziway-Shala lakes Basin, Central Main Ethiopian rift modified from Tefera et al.(1996) and Molin and Corti (2015) (a) **M**esozoic sediment surface outcrop, distribution and orientation of the outcrop surrounding the Ziway-Shala Lakes Basin (study area) (b) Cenozoic fault map in the Ziway-Shala lakes basin located in Main Ethiopian Rift modified from Agostini et al.(2011**)** and Molin and Corti, (2015**)** (c).

Geologic section within the CMER are poorly exposed (Woldegabriel et al., 2000). Woldegabriel et al. (2000), however, identified localized crystalline basement, Mesozoic sedimentary rocks, and Miocene and Pliocene mafic and silicic lavas and tephra are exposed in the western rift

margin in this area. Woldegabriel et al (2000) further identified crystalline basement, Mesozoic sandstone, limestone and mudstone at north-east of CMER (along the southern Afar margin). These rocks contributed much in accumulation of sedimentary succession in the rift floor. Mesozoic succession is present in the Blue Nile Basin which is formed as a NW-trending rift (Gani et al., 2008), in the eastern margin of the Ethiopian Rift with the adjacent Ogaden Basin, southern border of the Ethiopian Rift around Dire Dawa town (Bosellini et al., 2001) and at Kella along the western margin of the Central Main Ethiopian Rift (MER) (Abebe et al., 2010). Though the observed Mesozoic outcrops are found far away from the study area, it could be concluded that the outcrops are shown to surround the study region of the Ziway-Shala Lakes Basin (or CMER) (Fig. 2.3(b)).

2.3 Climate, Hydrology and Hydrogeology

Two climate variables such as rainfall and temperature were investigated (Le Turdu et al. 1999) (Ayenew, 2002) and analyzed in the ZSLB. According to Le Turdu et al. (1999) and Ayenew, (2002), the mean annual rainfall estimates ranges from 1150 mm in the eastern and western highlands to around 650 mm in the rift floor. Similarly, the annually weighted actual evapo-transpiration values of the rift, the escarpments and the highlands are 656, 892 and 917 mm respectively with averaged value of 821 mm/year. The annual evaporation values from Abiyata, Langano, Shala and Ziway Lakes are estimated to be 2060, 2010, 2112 and 2022 mm, respectively, with an average value of 2051mm. These annual evaporation and evapotranspiration estimates are deemed to help calculation of the water balance of the basin.

The main lakes within the rift floor of the Ziway-Shala Lakes Basin from north to south listed as Ziway, Abiyata, Langano and Shala (Fig. 2.4). These lakes are remnants of a large fresh-water lake that existed during the Early-Mid Holocene and the Late Pleistocene (Legesse et al., 2004).

Except the Shala Lake and its catchments the remaining three lakes are connected by a surface water network (Fig. 2.4). Ketar River from eastern escarpments and Meki River from western escarpments are the two major rivers that discharge water to Lake Ziway (Fig. 2.4). Lake Ziway delivers a majority of its surface water to Lake Abiyata through the Bulbula River (Fig. 2.4). Five major rivers (Fig. 2.4) supply their water to Lake Langano and significantly less water is discharged from this lake to Lake Abiyata. Lake Abiyata is the terminal lake (Ayenew, 2005) and has been undergoing significant lake level changes (Ayenew, 2002). Lake Shala gets its surface inflow from two main sources that enter from the southeastern and western rift escarpments (Le Turdu et al., 1999).

The total area of the Ziway–Shala Lakes basin is about 14,640 km^2 and hydrologically closed (Le Turdu et al., 1999) (Chernet et al., 2001). There is no evidence of significant groundwater outflow (Legesse et al., 2004) from this basin. Using isotopic evidences (Darling et al., 1996) and groundwater flow modeling results the groundwater flow direction is determined to be from Lake Awassa basin (southern basin) towards the low-lying and deep Ziway-Shala lakes basin (Ayenew, 2001). This groundwater flow direction is thought to increase both the groundwater and surface water resource in the basin.

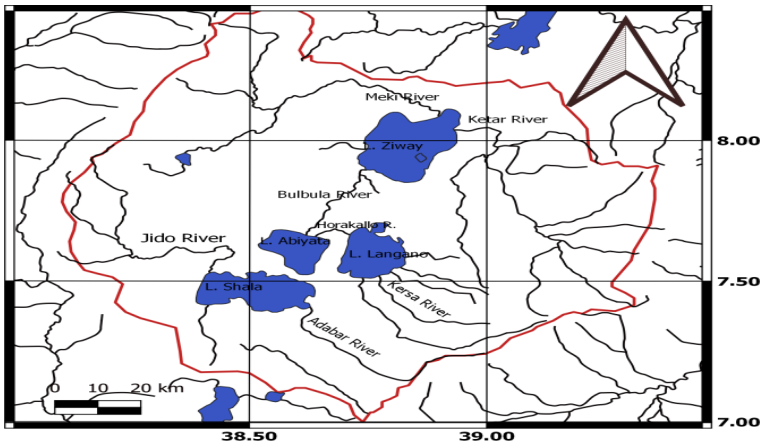

Fig. 2. 4 Hydrological network of the Ziway-Shala Lakes bain.

Total dissolved solids (TDS) of the Lakes in the MER depends on inflow and outflow conditions (Gizaw, 1996). Table 2.1 shows the TDS estimates determined for the six Lakes that reside in the MER including Afar (Gizaw, 1996; Ayenew, 2005).

S.N	Lakes Name	TDS(mg/l)	Source
1	Abiyata	13,480	(Ayenew, 2005)
2	Langano	3,175	(Gizaw, 1996)
3	Shala	7,262	(Gizaw, 1996)
4	Ziway	579	(Gizaw, 1996)
5	Afdera	145,129	(Ayenew, 2005)
6	Lakes in Dallol	274,467	(Gizaw, 1996)

Table 2. 1 TDS estimates of six Lakes in the MER and Afar

It is confirmed that, salinity increases from catchment divides to the valley floors and in the direction of groundwater flow (Salama et al., 1999). The observed salinity levels of the Lakes or basin is thought to be governed by groundwater dynamics which intern governed by subsurface geologic structures.

Chapter 3: Potential Field Theory

3.1 Introduction

Geophysics is the application of the principle and laws of physics (Reynolds, 1997) in the study of earth to discover or explore what lies beneath the earth. These can be Earth's dynamic processes and subsurface structures. Geophysical methods are based on the study of different physical fields being propagated through the earth's interior. The most important geophysical fields are gravity, magnetic, electrical, electromagnetic, and seismic wave fields. The observed values of these fields depend on the physical properties of underlying rocks. The source data for studies of geologic structures (lineaments and layers topography) in this study include gravity, magnetic and seismic noise data.

3.2 Gravity Methods

3.2.1 Introduction

Gravity method is one of a geophysical technique that measures differences in the earth's gravitational field (Telford et al., 1990). Information about the subsurface lithologies and structures are extracted through analysis of gravity data.

3.2.2 Governing equations

The basis on which the gravity method depends is encapsulated in two laws derived by Newton's second law of motion (Telford et al., 1990)

$$\vec{F} = m_o \vec{g} \qquad 3.1$$

and Newton's Universal Law of gravitation (Telford et al., 1990)

$$\vec{F} = -\frac{G \times m_o \times m}{r^2} \hat{e_r} \qquad 3.2$$

In Cartesian coordinates, F describes the mutual force between two point masses, m at $Q = (x', y', z')$ and m_0 at $P = (x, y, z)$

Equating equations (3.1) and (3.2), we have (Eq. 3.3)

$$\vec{g} = -\frac{G\,x\,m}{r^2}\hat{e_r} \qquad 3.3$$

This is a gravitational attraction produced by one mass, where

- ✓ G is the universal gravitational constant, $(G) = 6.67x10^{-11}Nm^2kg^{-2}$
- ✓ $r = \sqrt{(x - x')^2 + (y - y')^2 + (z - z')^2}$ is the distance between the two masses and
- ✓ $\hat{e_r} = \frac{1}{r}[(x - x')i + (y - y')j + (z - z')k]$ is the unit vector in Cartesian coordinates directed from the mass $\boldsymbol{m}$ to the location $\boldsymbol{P}$.

The minus sign in equation 3.3 appears due to the convention that $\hat{e_r}$ points away from the source toward the observation point.

The gravitational field (Eq. 3.3) is a conservative field and thus expressed by a scalar function called scalar potential $\emptyset(P)$ which varies with distance or position relative to the mass, m. It is given mathematically as

$$\emptyset(P) = -\int_{\infty}^{r} g.\,dr = -Gm\int_{\infty}^{r}\frac{\hat{e_r}.dr}{r^2} = -Gm\int_{\infty}^{r}\frac{dr}{r^2} = \frac{Gm}{r} \qquad 3.4$$

The gravity field $\vec{g}$ with respect to gravitational potential is then given by

$$\vec{g}(P) = (g_x, g_y, g_z) = -\frac{G\,m}{r^2}\hat{e_r} = \frac{\partial}{\partial r}\left(\frac{Gm}{r}\right) = \frac{\partial}{\partial r}\emptyset(P) = \nabla\emptyset(P) = -\left(\frac{\partial\emptyset}{\partial x}, \frac{\partial\emptyset}{\partial y}, \frac{\partial\emptyset}{\partial z}\right) \qquad 3.5$$

We expressed $\vec{g}$ in terms of a scalar three dimensional potential function $\emptyset(P)$ (Eq. 3.5) which is the case that we call it a potential field technique in exploration geophysics.

The vertical component of equation 3.5 is given in equation 3.6 and is the quantity which mostly measured by gravimeter in gravity surveying.

$$g_z = \frac{\partial \emptyset}{\partial z} \tag{3.6}$$

The gravitational potential of a continuous distribution of matter, which is described as a collection of very small mass, $dm = \rho(x, y, z)dv$, where $\rho(x, y, z)$ is the density distribution can be calculated as

$$\emptyset(\mathrm{P}) = \mathrm{G}\int_{\mathrm{V}} \frac{dm}{\mathrm{r}} = \mathrm{G}\int_{\mathrm{V}} \frac{\rho(Q)}{\mathrm{r}}\mathrm{dv} \tag{3.7}$$

Where, P is the point of observation, Q is the point of integration within the mass, and r is the distance between P and Q. Integration is over the volume of the entire mass, V.

Taking Laplacian of both sides of equation 3.7, we get Poisson's equation (Eq. 3.8) for gravitational potential as

$$\nabla^2\emptyset(\mathrm{P}) = -4\pi G\rho(P) \tag{3.8}$$

The gravitational attraction g at a point $P = (x, y, z)$ due to a volume V can be expressed in an integral form by

$$g(P) = -G\int_V \rho\frac{\hat{e}}{r^2}dv \tag{3.9}$$

where ρ is density as a function of space, r is the distance from the observation point P to an element of the body dv, $\hat{e}$ is a unit vector pointing from an element of the mass to P, and G is the universal gravitational constant

From Eq. 3.9, we extract the vertical gravitational attraction of a mass distribution with density ρ (x_0, y_0, z_0) observed at point (x, y, z) is then given as

$$g_z = -G\int_{z'}\int_{y'}\int_{x'} \rho(x', y', z')\frac{(z-z')}{r^3}dx'dy'dz' \tag{3.10}$$

The governing equation can be solved analytically (directly) by integrating (Eq. 3.10). This volume integral however, suffer from singularities and is computationally inefficient, particularly

when using large data sets associated with complex density distributions. Due to this limitation the numerical solution of Poisson's equation in equation 3.8 are solved using finite difference, finite-element and finite-volume approach. These methods generally discretize the domain using a rectangular grid and then gravitational potential within each cell is approximated. Back substituting the solution to the equation 3.6 gives an approximation to the vertical component of gravity field. The third approach is the direct solution of gravitational field

$$\nabla^2 g_z = -4\pi G \frac{\partial \rho}{\partial z} \qquad 3.11$$

Obtained from substituting equation 3.6 into equation 3.8

g_z is solved numerically using finite difference and finite-volume formulations, given a density distribution ρ (note that ρ= 0 outside the source volume). This solution inherently avoids the types of singularities that arise in the direct solution of the integral. The finite-difference and finite-volume formulations of this method result in a linear system of equation (Eq. 3.12).

$$g_z = d_i = \sum_{j=1}^{M} \boldsymbol{\rho_j} \left\{ \boldsymbol{G} \int_{\Delta V_j} \frac{\boldsymbol{z - z_0}}{|\vec{\boldsymbol{r}} - \vec{\boldsymbol{r}}_{oi}|^3} \boldsymbol{dv} \right\}$$

$$d_i = \sum_{j=1}^{M} \boldsymbol{\rho_j G_{ij}} \qquad \textbf{3.12}$$

$\boldsymbol{\rho_j}$ is the density

$\Delta \mathbf{V_j}$ is the volume of $\mathbf{j}^{\mathbf{th}}$ cell

$\mathbf{d_i}$ is introduced as a generic symbol for the i'th datum,

Expressed in matrix notation, the gravity data consisting of N observations are given by

$$G\,\vec{\rho} = \vec{d} \qquad 3.13$$

Where,

$d = (d1; \ldots; dN)^T$ is the data vector (gravitational acceleration)

$\boldsymbol{\rho} = (1; \ldots; M)^T$ is the vector containing the density values of the M cells.

G is a sparse banded matrix that connects elements of the system with one another

Based on these governing principles, the ground-based gravity survey can be conducted using an instrument, Worden gravimeter, Scintrex gravimeter and the Lacoste and Romberg model gravity meter.

3.2.3 Gravity Data Reductions

After gravity field data have been collected all the necessary reduction are applied to remove known variations unrelated to the geology. These corrections include

a) Drift Correction (Instrumental Drift)

Gravimeters exhibit time-variant changes in their dial reading (gravimeter reading). The continual variation in the instrument reading observed over a defined time interval is caused mainly by the slow and continual creep (temperature effects) of the gravimeter springs as they are not perfectly elastic bodies. Instrumental drift is calculated based on the error between the first and last base reading given by

$$d = \frac{(r_{B_2} - r_{B_1}) - (g_{B_2} - g_{B_1})}{t_{B_2} - t_{B_1}}$$

Where,

d is Drift reading in milligals/hour

r_{B_1} is base 1 reading

r_{B_2} is base 1 reading

g_{B_1} is base 1 absolute G in milliGals

g_{B_2} is base 2 absolute G in milligals

t_{B_1} is base 1 time

t_{B_2} is base 2 time

d is intended to remove the changes caused by the instrument itself. It is a scale factor that corrects a reading to a relative milliGal value. The corrected reading in milliGals is thus defined as

$$r_c = r.d$$

Where,

r is Instrument reading in dial units

d is scale factor (milligal/dial units)

r_c is gravity reading in milligal

b) Tidal correction

The sun and moon have gravitational effect called tidal effect which is a time-variant gravity changes that also affect the gravimeter. Tidal variations are slow and can be considered as a part of the drift of the instrument and remove it via a drift correction. Otherwise the combined time variant changes over a certain time interval are normally displayed in the form of a graph. The correction is then made using the analysis of this graph.

c) Elevation Reduction

Each reading is corrected for the height of the instrument above the station

$$0.3086\ h_i$$

Where, h_i is an instrument height in meter

d) Free Air Correction

The elevation reduction to the geoid is calculated as

$$\delta g_f = \frac{2g_0}{R} h = 0.3086\, h \text{ mGal}$$

Where, h is height above sea level in meters

This correction neglects the matter contained between the geoid and the Earth's surface

e) Bouguer Reduction

It corrects for the effect of masses of rock that exists between the station elevation (observation point) and the geoid. This is the gravitational attraction of an infinite horizontal slab (Bouguer slab) of rock material of thickness equal to h and density ρ

$$\delta g_B = 2\pi g \rho h = 0.0419 * \rho\, h \text{ mGal}$$

Where, ρ Bouguer density of rock in g/cc

h is station elevation in meters

f) Latitude Correction

The latitude correction requires the theoretical gravity at the station location on the Earth's spheroid. There are three formulas for the theoretical gravity of 1930, 1967 and 1980 of which the 1967 is given by

$$\gamma_\emptyset = 978031.846[1 + 0.005278895\, sin^2\emptyset + 0.000023462\, sin^4\emptyset]$$

Where, $\gamma_\emptyset$ is theoretical gravity in milligal

$\emptyset$ is geodetic latitude of the station

g) Free Air Anomaly

The free air anomaly is calculated by subtracting the latitude correction (theoretical gravity) from the absolute gravity and adding a correction for the station elevation

$$\Delta g_f = g_a + 0.3086\,.h - \gamma_\emptyset$$

Where, Δg_f is free air anomaly in milligals

g_a is absolute gravity

$\gamma_\emptyset$ is latitude correction

h) Simple Bouguer gravity anomaly

$$\Delta g_{ba} = g_a + 0.3086.h - 0.0419 * \rho\, h - \gamma_\emptyset$$

Where,

Δg_{ba} is Bouguer gravity anomalyin milligals

ρ is Bouguer density of rock in g/cc

h is station elevation in meters

i) Terrain Correction (δg_T)

The Bouguer correction assumed the slab to be infinite in the horizontal direction. This is not true, due to topography and Earth's curvature. The correction for the Earth curvature is used in a large scale surveys and we will leave it out now. The hill above the Bouguer slab with its own gravity force pulls in the opposite direction than the Earth, therefore decreasing the measured acceleration. In a similar way, the valley also decreases the value, because when computing the Bouguer correction we have already subtracted the Bouguer slab (with a flat surface) and did not account for the missing masses of the valley. Hence the terrain correction is always added. The terrain corrections are calculated using the DEM (DEM) GTOPO30

j) Complete Bouguer gravity anomaly anomaly

The Complete Bouguer gravity anomalycorrects the Bouguer gravity anomalyfor irregularities of the earth due to terrain in the vicinity of the observation point

$$\Delta g_{cba} = g_a + 0.3086.h - 0.0419 * \rho\, h - \gamma_\emptyset + \delta g_T$$

Where,

Δg_{cba} is complete Bouguer gravity anomalyin milligals

δg_T is terrain correction in milligals

3.3 Magnetic method

3.3.1 Introduction

Magnetic method is a another potential field method and is more complex and localized field (Kearey et al., 2002; Telford et al., 1990). This is due to dipolar and varied direction of magnetic field. Variations in susceptibility of rocks perturb this field. The aim of a magnetic survey is to investigate subsurface geology on the basis of anomalies in the Earth's magnetic field resulting from the magnetic properties of the underlying rocks (Kearey et al., 2002).

3.3.2 Governing equation

The geomagnetic method measures variations in the Earth's magnetic field which either a total intensity or the intensity of one or more individual components. The mathematical formulation for the total field start with defining the magnetic force F (Kearey et al., 2002) through an inverse square law of Coulomb's given as Eq. 3.14

$$\vec{F} = \frac{p_1 p_2}{4\pi\mu r^2}\vec{e} = k\frac{p_1 p_2}{r^2}\vec{e} \qquad 3.14$$

Magnetic field is the force exerted by a pole of strength p_2 on a unit pole at distance, r.

From Eq. 3.14, we get Eq. 3.15

$$B(r) = \frac{F}{p_2} = \frac{\mu_0}{4\pi\mu_r}\frac{p_1}{r^2} = k\frac{p_1}{r^2} \qquad 3.15$$

Where,

p_1 and p_2 magnetic pole strengths

$\vec{e}$ is unit vector from p_1 to p_2

r is separation distance between p_1 and p_2

p_1 and p_2 are pole strength

$\mu = \mu_r\mu_0$ is magnetic permeability

μ_r is relative permeability

μ_0= permeability of free space (4π x10^{-7} H/m)

Setting, $k = 1$, the unit of the magnetic **B**-field has dimensions $dyne^{1/2}\ cm^{-1}$ in c.g.s. units and is called a gauss. Geophysicists employ a smaller unit, the gamma ,γ, to describe the geomagnetic field and to chart magnetic anomalies (1 γ =10^{-5} gauss).

The proportionality constant k = $\frac{\mu_0}{4\pi}$ is not dimensionless, it takes the dimension of μ_0 and μ_0 is called the permeability constant and is equal to $4\pi \text{ x} 10^{-7}\ Hm^{-1}$ $(Henry/meter)$ which is equivalent to NA^{-2}).

Magnetic potential at a distance r is given by Eq. 3.16

$$W = -\int_r^{\infty} B\ dr = \frac{\mu_0 p}{4\pi r} \qquad 3.16$$

To define the potential of a pair of magnetic poles, let two equal and opposite poles, $p\ and\ -\ p$, be located a distance d apart. The potential W at a distance r from the midpoint of the pair of poles (Fig. 3.1), in a direction that makes an angle θ to the axis, is the sum of the potentials of the positive and negative poles.

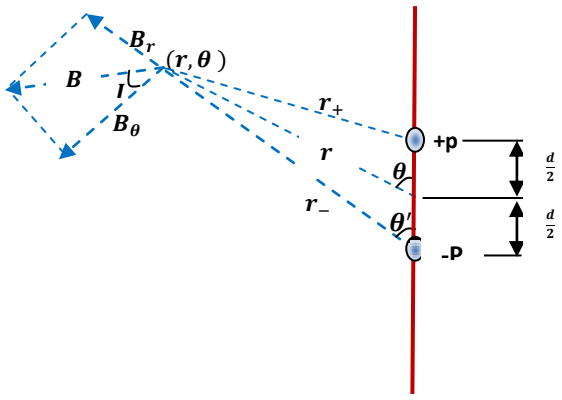

Fig. 3. 1 Geometry for the calculation of the potential of a pair of magnetic poles.

The line joining the positive and negative poles defines an axis, about which the field has rotational symmetry.

At the point (r,θ), at a distances r_+ and r_- respectively from positive and negative poles we get a magnetic potential (Eq. 3.17) of the pair

$$W = \frac{\mu_0 p}{4\pi}\left(\frac{1}{r_+} - \frac{1}{r_-}\right) = \frac{\mu_0 p}{4\pi}\left(\frac{r_- - r_+}{r_+\, r_-}\right) \qquad 3.17$$

The pair of opposite poles is considered to form a dipole when their separation becomes infinitesimally small compared to the distance to the point of observation $(i.e.\, \boldsymbol{d} << r)$.

For,$d << r$, we have $r_+ \approx r - \frac{d}{2}\cos\theta$ and $r_- \approx r + \frac{d}{2}\cos\theta'$

When, $d \ll r$, we can write $\theta \approx \theta'$ and terms of order $(\frac{d}{2})^2$ and higher can be neglected. This leads to the further simplifications Eq. 3.18

$$\left.\begin{aligned} r_- - r_+ &\approx \frac{d}{2}(\cos\theta' + \cos\theta) \approx d\cos\theta \\ r_+ r_- &\approx r^2 - \frac{d^2}{4}\cos^2\theta \approx r^2 \end{aligned}\right\} \qquad 3.18$$

Substituting Eq. (3.18) in Eq. (3.17) gives the dipole potential (Eq. 3.19) at the point(r, θ)

$$W = \frac{\mu_0\ (dp)cos\theta}{4\pi\ r^2} = \frac{\mu_0}{4\pi}\frac{m\ cos\theta}{r^2} \qquad 3.19$$

The quantity $m = dp$ is called the magnetic moment of the dipole

Similar to the gravity field, the earth's magnetic field (B) is a conservative field and is given by taking gradient of the earth's magnetic potential W given as in Eq. 3.20

$$\vec{B} = -\nabla W = \frac{\partial W}{\partial r} e_r + \theta \frac{1}{r} \frac{\partial W}{\partial \theta} e_\theta + \frac{1}{r sin\theta} \frac{\partial W}{\partial \emptyset}\, e_\emptyset \qquad 3.20$$

In other words the radial, tangential and longitudinal components at any point $P(r, \theta, \emptyset)$ and in their respective direction $(r, \theta, \emptyset)$ are given by Eq. 3.21

$$\left.\begin{aligned} \mathrm{B_r} &= -\frac{\partial}{\partial \mathrm{r}}\left(\frac{\mu_0}{4\pi}\frac{\mathrm{m\,cos\theta}}{\mathrm{r^2}}\right) = -2\frac{\mu_0}{4\pi}\frac{\mathrm{m\,cos\theta}}{\mathrm{r^3}} \\ \mathrm{B_\theta} &= -\frac{1}{\mathrm{r}}\frac{\partial}{\partial \theta}\left(\frac{\mu_0}{4\pi}\frac{\mathrm{m\,cos\theta}}{\mathrm{r^2}}\right) = -\frac{\mu_0}{4\pi}\frac{\mathrm{m}}{\mathrm{r^3}}\mathrm{sin\theta} \\ \mathrm{B_\emptyset} &= -\frac{1}{\mathrm{rsin\theta}}\frac{\partial}{\partial \emptyset}\left(\frac{\mu_0}{4\pi}\frac{\mathrm{m\,cos\theta}}{\mathrm{r^2}}\right) = -\frac{1}{\mathrm{rsin\theta}}\frac{\partial}{\partial \emptyset}\left(\frac{\mu_0}{4\pi}\frac{\mathrm{m}}{\mathrm{r^2}}\mathrm{cos\theta}\right) = 0 \end{aligned}\right\} \qquad 3.21$$

$\mathrm{B_\emptyset} = 0$, Implies that W doesn't vary with longitude $\emptyset$

The total magnetic field strength B denoted by $B(\mathrm{r}, \theta, \emptyset)$ at any point $p(\mathrm{r}, \theta, \emptyset)$ is given by Eq. 3.22

$$B = \sqrt{{B_r}^2 + {B_\theta}^2 + {B_\emptyset}^2} = \frac{\mu_0}{4\pi}\frac{m}{r^3}\sqrt{1 + 3cos^2\theta} \qquad 3.22$$

The **torque (τ)** can be calculated by considering the forces exerted by a uniform magnetic field ***B*** on a pair of magnetic poles of strength ***p*** separated by a distance ***d*** (Fig. 3.2).

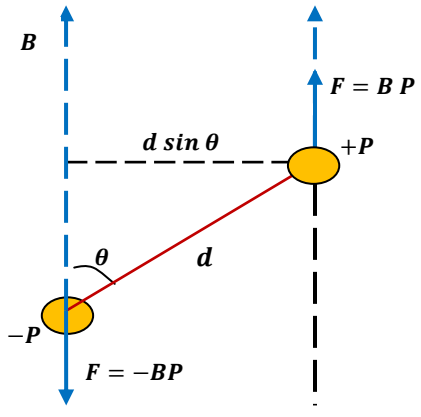

Fig. 3. 2 Definition of the magnetic moment , *m*, of a pair of magnetic poles.

A force equal to (BP) acts on the positive pole and an equal and opposite force (BP) acts on the negative pole. If the magnetic axis is oriented at angle θ to the field, the perpendicular distance between the lines of action of the forces is, **d sin θ** .

The torque **τ** felt by the magnet (Eq. 3.23) is thus

$$\tau = F\ d\ sin\theta = \ BP\ d\ sin\theta = m\ x\ B \qquad 3.23$$

The torque exerted by a magnetic field (Eq. 3.23) turns the magnet parallel to the field direction (B) and is proportional to magnetic moment(**m**). Thus, the net magnetic moment of a volume V of the material depends on the degree of alignment of the individual atomic magnetic moments. It is the vector sum of all the atomic magnetic moments in the material.

Magnetization (M) (Eq. 3.24) is defined as the ratio of magnetic moment per unit volume of the material

$$M = \sum \frac{m_i}{V} \qquad 3.24$$

The dimension and SI unit of Magnetization is $[\mathrm{M}] = \frac{[\mathrm{m_i}]}{[\mathrm{V}]} = \frac{\mathrm{Am^2}}{\mathrm{m^3}} = \mathrm{Am^{-1}}$ and $\frac{[\mathrm{B}]}{[\mu_0]} = \frac{\mathrm{NA^{-1}m^{-1}}}{\mathrm{NA^{-2}}} = \mathrm{Am^{-1}}$

In general, the magnetization M inside a magnetic material will not be exactly equal to, $\frac{\mathrm{B}}{\mu_0}$; let the difference be H (Eq. 3.25), so that

$$H = \frac{B}{\mu_0} - M \qquad 3.25$$

H is a magnetizing field which is a readily computed quantity that is useful in determining the value of the true magnetic field B in a medium.

Inside a magnetizable material the magnetic B-field has two sources. One is the external system of real currents that produce the magnetizing field H; the other is the set of internal atomic currents that cause the atomic magnetic moments whose net alignment is expressed as the magnetization M.

In general, in anisotropic magnetic material B, M and H are not parallel. However, many magnetic materials are not strongly anisotropic and the elementary atomic magnetic moments align in a statistical fashion with the magnetizing field. In this case M and H are parallel and proportional to each other (Eq. 3.26)

$$M = kH \tag{3.26}$$

The constant of proportionality $\boldsymbol{k}$ is a physical property of the material and is called magnetic susceptibility. This equation implies that a magnetic body placed in a magnetic field becomes magnetized by induction. This is a measure of the degree to which a material gets magnetized. The magnetization (M) is proportional to the inducing external magnetizing field (H). The larger the susceptibility the greater the intensity of induced magnetization M and hence the bigger will be the anomaly produced relative to the earth's field(B). The susceptibility of rocks is almost entirely controlled by the amount of ferromagnetic minerals, their grain size, and mode of distribution and hence is highly variable.

The fact that, M *and* H have the same units (A m^{-1}) and k is a dimensionless quantity Equation 3.25 can be rewritten as Eq. 3.27

$$B_T = \mu_o (H + M) \tag{3.27}$$

The components of B is then given by

$$\left.\begin{aligned} B_x &= \mu_o (H_x + M_x) \\ B_y &= \mu_o (H_y + M_y) \\ B_z &= \mu_o (H_z + M_z) \end{aligned}\right\}$$

The Earth's total magnetic field B_T (Eq. 3.27) is classified as main (Dipole), external and anomalous (rock magnetism) magnetic field. This is the parameter that is measured during magnetic survey.

The Earth's main field *(H)* represents the main components of the geomagnetic field and is believed to be originated in the Earth's outer core as a result of convective changes in the core. This field varies relatively slowly and its magnitude on the earth's surface is given in terms of geomagnetic field elements (Fig. 3.3). It is described by a vertical component Z and a horizontal component H in the direction of magnetic north. The dip of B_D is the inclination I of the field and the horizontal angle between geographic and magnetic north is the declination,D.

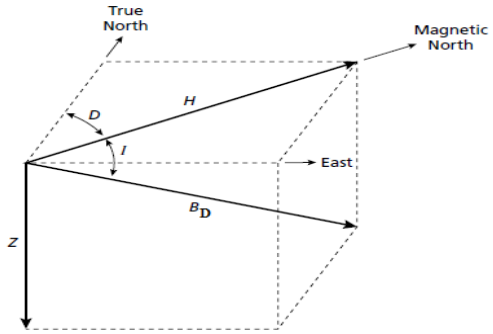

Fig. 3. 3 The geomagnetic elements.

B_D is the total dipole magnetic field vector

H is the horizontal component of the total dipole field vector

Z is vertical component of the field vector

D is the declination

I is the inclination and where

$$\left.\begin{array}{c} B_D = \sqrt{\mathrm{H}^2 + \mathrm{Z}^2} \\ \mathrm{I} = \tan^{-1}(Z/H) \\ \mathrm{D} = \tan^{-1}(H_E/H) \end{array}\right\} \quad 3.28$$

H_E is the east component of the horizontal component of the total dipole field

It is customary to express the internal component of geomagnetic field ***(H)*** as the gradient of a scalar potential, $\boldsymbol{V}$. The function V is usually expressed as an orthogonal expansion in spherical harmonics. In the spherical coordinate system, $(\mathrm{r}, \theta, \emptyset)$, the expansion of V can be written as (Eq.3.29)

$$V(r, \theta, \emptyset) = R_E \sum_{n=1}^{\infty} \sum_{m=0}^{n} \left(\frac{R_E}{r}\right)^{n+1} (g_n^m \cos m\emptyset + h_n^m \sin m\emptyset) p_n^m (\cos\theta) \quad 3.29$$

Where, $\mathrm{R_E}$ is the mean radius of the Earth (6371.2 km), and $\mathrm{p_n^m}(\cos\theta)$ are the quasi Schmidt-normalized associated Legendre functions.

This expansion is an infinite series, but in practice it is usually limited to n = 10 or n = 12. The coefficients g_n^m and h_n^m are determined experimentally by combining Earth-based and satellite measurements of the geomagnetic field, and are time-dependent. The International Association for Geomagnetism and Aeronomy (IAGA) defined and periodically updates the International Geomagnetic Reference Field (IGRF). The IGRF consists of a series of sets for the coefficients in the expansion given above, corresponding to different epochs, in units of nT.

The external magnetic field is small portion of the geomagnetic field that appears to be associated with electric currents in the ionized layers of the atmosphere (external activities) (Telford et al., 1990). The time variations of this field portion are much more rapid than for the main field.

Crustal (anomalous) magnetic field is a Local change in the main field result from variations in the magnetic mineral content of near surface rocks. The sources of local magnetic anomalies

cannot be very deep because of the Curie temperature. Thus local anomalies must be associated with features in the upper crust (Telford et al., 1990).

Generally the total magnetic field can be expressed by (Eq. 3.30)

$$B_T = B_{ext} + B_{int} = B_{ext} + B_D + B_{rm} \quad 3.30$$

Where, B_T is the total magnetic field

B_{ext} is external magnetic field,

B_D is dipole field, which is mainly generated by the fluid outer core and

B_{rm} is the field of rock magnetism

3.3.3 Magnetic data Reduction

The observed total field B_T has to be corrected for the effect of diurnal variation and the effects of spatial variations of the dipole field.

Diurnal variation (δB_D): Magnetic effects of external origin cause the geomagnetic field to vary on a daily basis to produce diurnal variations. It is the correction applied to the observed total field B_T to remove the time varying external component B_{ext}. Magnetic readings taken at a fixed Base station periodically over the period of a survey help the compilation of the diurnal correction.

Geomagnetic (IGRF) corrections (B_D): corrections for spatial variations (secular variations) in the strength of the dipole field. It is a theoretical field value ($B_{th} = B_D$) obtained from the International Geomagnetic Reference Field (in accordance with Eq. 3.28) which will be employed to remove main field. It is a mathematical model which is a function of location; time and elevation (Eq. 3.29) that help to compute the dipole field B_D. This correction might be conducted by using IGRF maps published every five years or by using different computer

programs that are available to compute the values of the geomagnetic correction (B_D). They are monitored by measuring changes in I, D and B_D at observatories. Because this variation occurs slowly with respect to the time of completion of a typical exploration magnetic survey, these variations will not complicate data reduction efforts.

In addition to correction for diurnal and spatial variation due attention should be given to magnetic storms. This is an occasionally occurring magnetic activity in the ionosphere. The occurrence of such storms correlates with enhanced sunspot activity. The magnetic field observed during such times is highly irregular and unpredictable which complicate the reliability of magnetic data. Therefore, magnetic survey should not be conducted during such a time. This is because the variations in the field that they can produce are large, rapid, and spatially varying. Therefore, it is difficult to correct for them in acquired data.

The part of the magnetic field that remains after subtracting the diurnal correction(δB_D) and the geomagnetic correction (B_D) is known as the anomalous magnetic field (ΔB) and is given by (Eq. 3.31)

$$\Delta \mathbf{B} = \mathbf{B_T} - (\boldsymbol{\delta} \mathbf{B_D} + \mathbf{B_D}) \qquad \mathbf{3.31}$$

It is possible to correct for latitude and elevation but these corrections are generally smaller than typical magnetic field anomalies. They are only important if the survey has a large spatial extent.

This chapter generally describes the theories behind gravity and magnetic methods and in the next chapter after documenting and showing how to acquire potential field data, the chapter is devoted to show the procedures on how to estimate the regional gravity anomaly which can be subtracted from Bouguer gravity anomalyto give residual anomaly of the study area.

Chapter 4: Potential field data acquisition and gravity data separation related to deep and shallow subsurface geology

4.1 Potential field Data Acquisition

4.1.1 Gravity Data Acquisition

A total of 3013 ground based gravity data obtained from PhD thesis work (Alemu, 1992) and from the Ethiopia Geological Survey (EGS) are considered in this research work. The station spacing is variable with an average spacing between 2 km to 10 km. The data distributions are shown in Fig. 4.1. These data are collected along gravel and asphalt roads, seasonal roads and off road transect (Alemu, 1992).

The compiled data set is reprocessed and homogenized with reference to the International Gravity Standardization Network 1971 (IGSN71). The 1967 international gravity formula, a reduction density of 2.67 g/cm^3 and sea level as a datum are used. The data limits (minimum and maximum) is shown in (Fig. 4.2(a)).The computed complete Bouguer gravity anomalydata are gridded and mapped (Fig. 4. 2(b)) using the Geosoft Oasis montaj version 7.1.

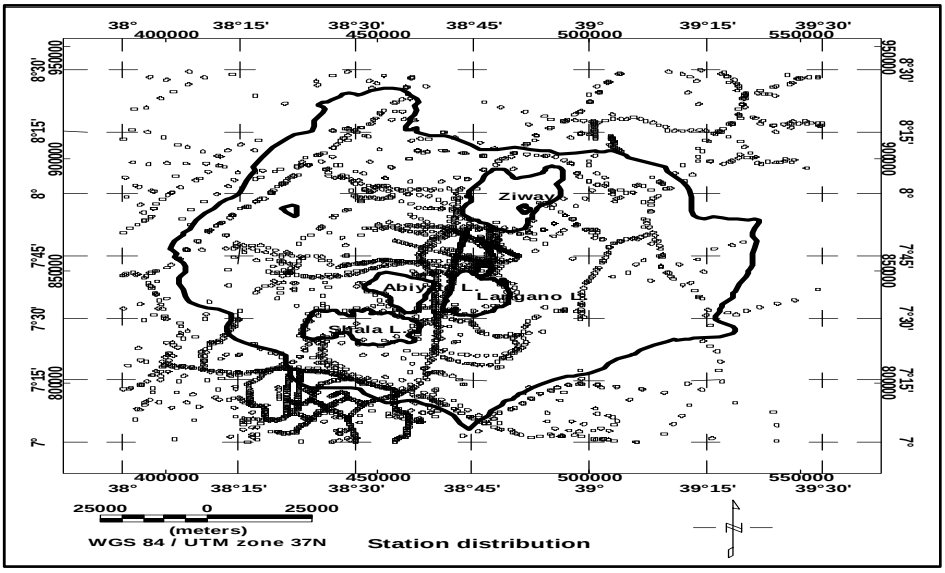

Fig. 4. 1 Gravity data station distribution in the Ziway-Shala Lakes Basin, Central Main Ethiopian Rift.

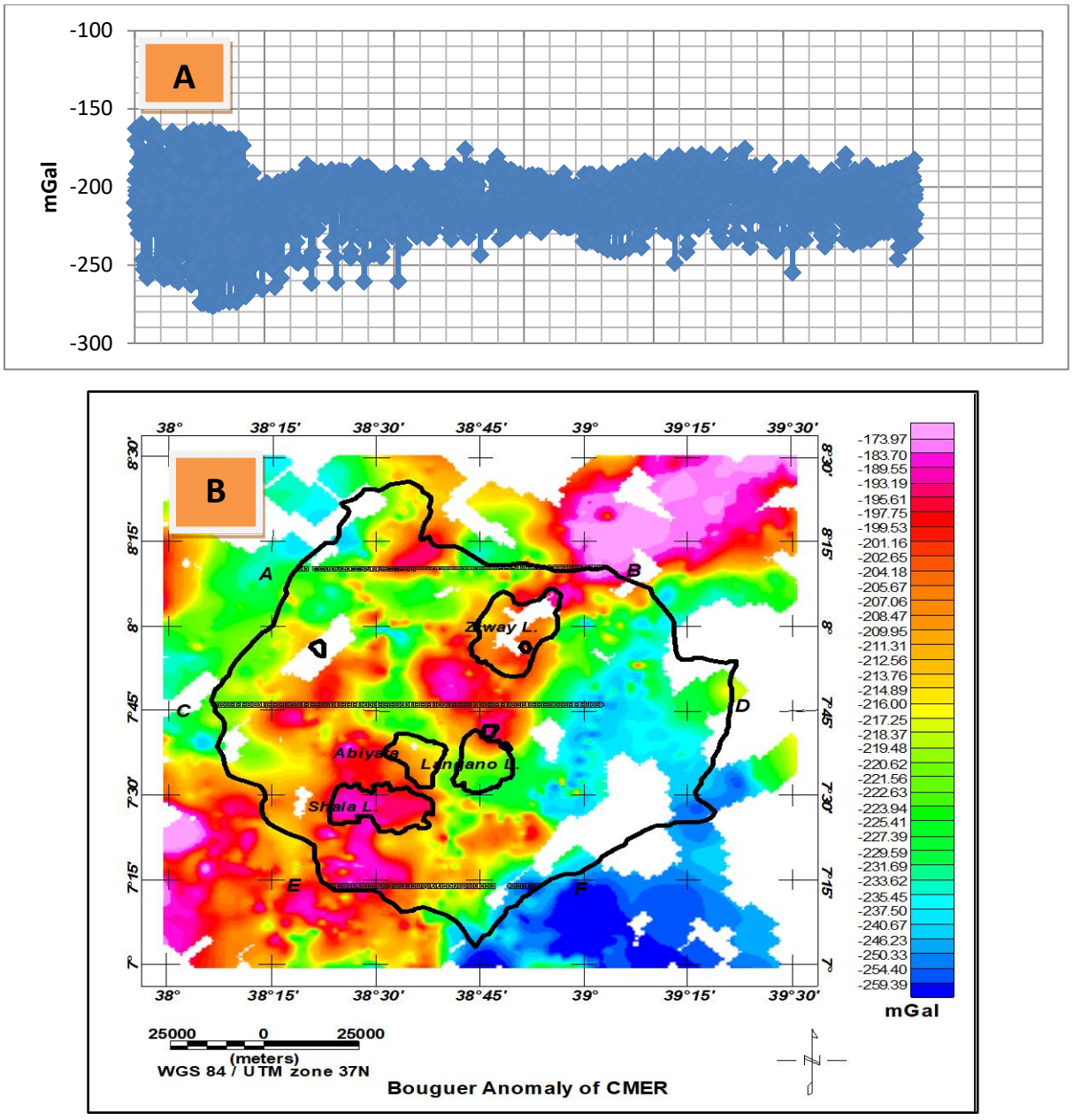

Fig. 4. 2 (a) The final reprocessed gravity data limits **(b)** Bouguer gravity anomaly map over and surrounding the Ziway-Shala Lakes Basin also shown are the location of three west-east extending profiles the will be used as an input to power spectral analysis operator.

4.1.2 Magnetic Data Acquisition

About 263 primary total intensity magnetic field measurements were collected by the author in the Ziway-Shala Lakes Basin, Central Main Ethiopian Rift using Proton Magentometer. This data are merged with 592 secondary total intensity magnetic field data collected from 2014 to 2016 by individual researchers (Kelemework, 2016; Berhane, 2015; Berhane, 2015) adding up to 855. The geographic distributions of these data are shown in Fig. 4.3 and corresponding maximum/minimum value of the intensity is shown in Fig. 4.4 (a). The data set is gridded using minimum curvature technique (Fig. 4.4(b)).

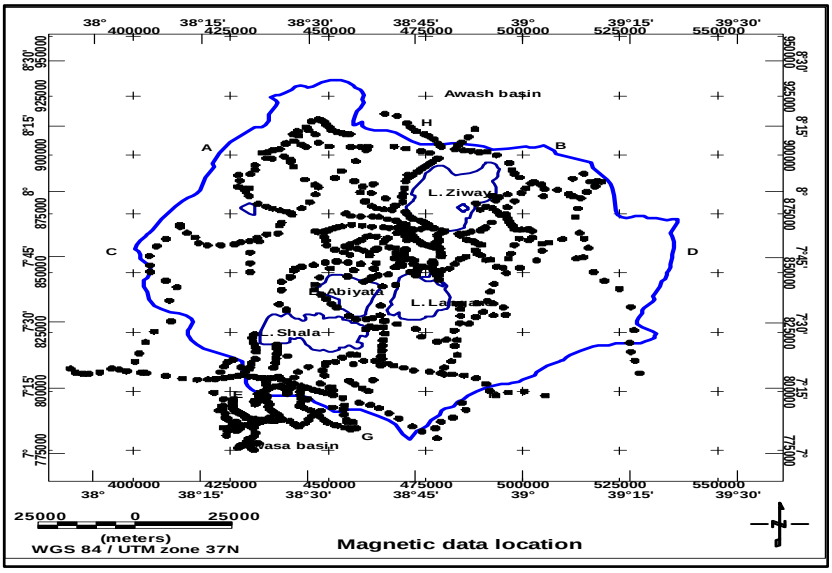

Fig. 4. 3 Total magnetic field intensity data locations distribution in Ziway-Shala lakes basin, central Main Ethiopian Rift.

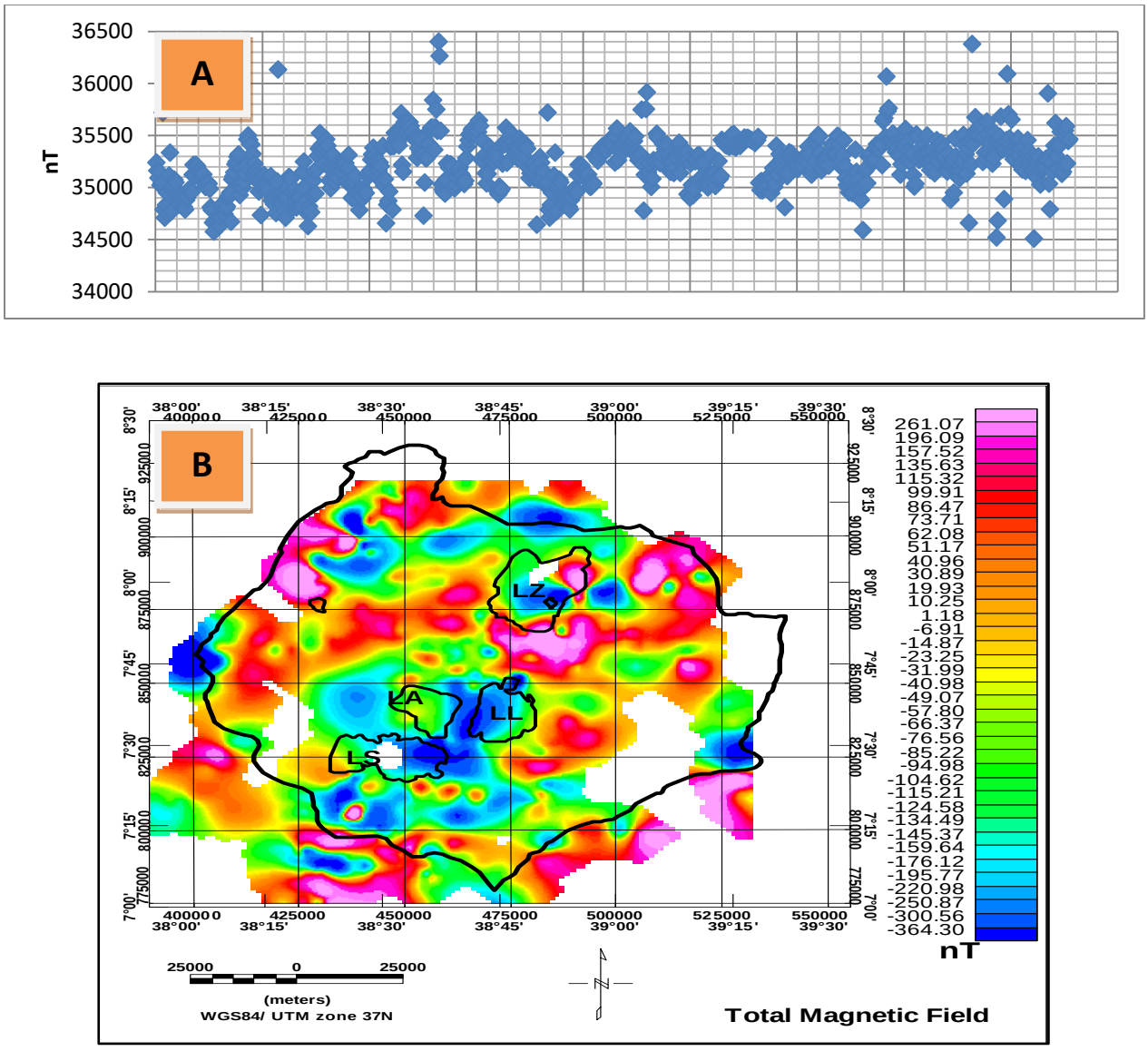

Fig. 4. 4 Total magnetic field intensity data values (minimum and maximum) in Ziway-Shala lakes basin, Central Main Ethiopian rift (a) Total magnetic field anomaly map of the study area (b).

4.2 Gravity anomaly separation

4.2.1 Introduction

The computed complete Bouguer gravity anomaly is a superposition of the effect of shallow and deep anomaly signatures which need to be separated in to their respective components before scheduling quantitative interpretation of the data.

The upward continuation technique (Mammo, 2010) , polynomial surface fitting (Okiwelu et al., 2010), Wavelet Transform (Xu et al., 2009), spectral analysis (Saibi et al., 2012), graphical methods (V. K. Gupta & Ramani, 1980), Preferential filtering (Guo et al., 2013), non-linear filter (Keating et al., 2011) were applied to gravity data to approximate the regional anomaly in their respective study area. These show that no single best chosen method is a reliable to decompose the observed anomaly into its regional and residual components. Each of the methods has a merit and demerit which could be considered depending on the problem and appropriateness. In this research, the most frequently used method such as upward continuation and polynomial trend surface analysis have been applied and compared and the best approach is forwarded for Ziway-Shala lakes basin, Central Main Ethiopian Rift.

4.2.2 Methods

Among the filtering techniques mentioned in section 4.2.1, the upward continuation and the trend surface fitting methods were chosen and their detailed mathematical formulation are given as follow

4.2.2.1 The Upward continuation

Upward continuation can be used to separate the anomaly of the deeper geology from shallower geology (Jacobsen, 1987). It is a transformation of gravity anomaly computed at a point, $Q(x_0, y_0, z_0 = 0)$, on the mean sea level to a point $p(x_0, y_0, z_0 = -h)$, on some higher flat surface upward continued to, $z = -h < 0$ (Fig. 4.5).

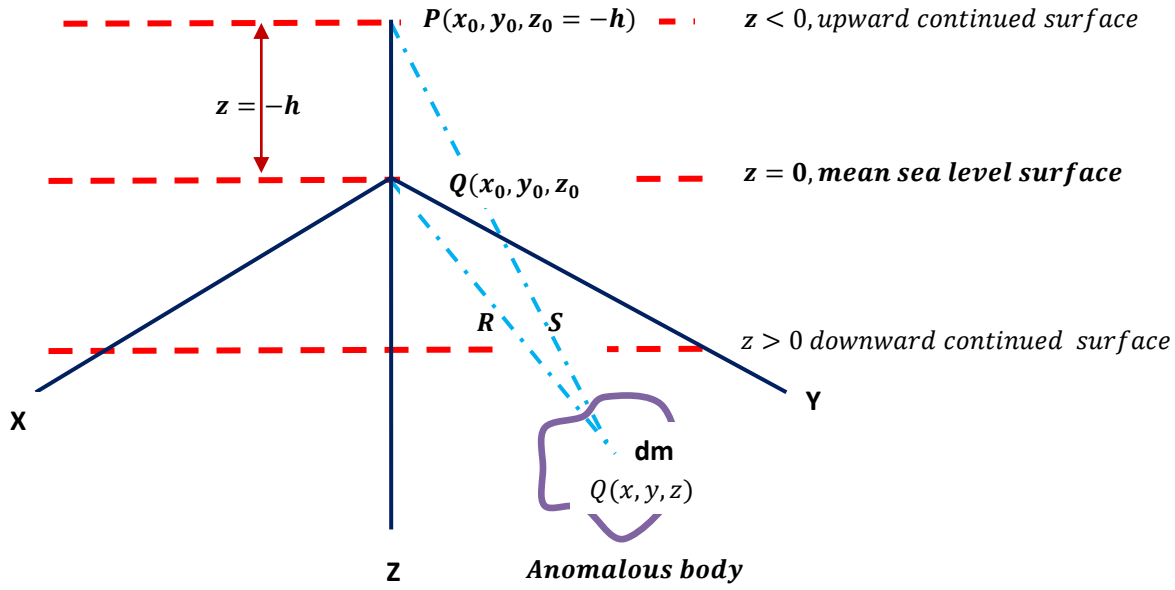

Fig. 4. 5 Pictorial representation of upward continuation technique in Cartesian coordinate system

The gravitational attraction per unit mass of an anomalous source body of mass, ***dm***, at mean see level, $O(x_0, y_0, z_0 = 0)$, at distance R from the source location point $Q(x, y, z)$, is computed by

$$dg = \frac{Gdm}{R^2} = \frac{Gdm}{(x - x_0)^2 + (y - y_0)^2 + (z - z_0)^2} \qquad 4.1$$

The vertical component, dg_z, gives the gravity anomaly, Δg_0, of the source at the mean sea level surface point as

$$dg_z = \Delta g_0 = \frac{Gdm}{R^2}\frac{z}{R} = Gdm\frac{z}{R^3} = Gdm\frac{z}{[(x - x_0)^2 + (y - y_0)^2 + (z)^2]^{3/2}} \qquad 4.2$$

Thus the gravity anomaly, Δg_p, of the anomalous source at the upward continued surface point P is

$$\Delta g_p = \frac{Gdm}{S^2}\frac{z+h}{S} = Gdm\frac{z+h}{S^3} = Gdm\frac{z+h}{[(x-x_0)^2+(y-y_0)^2+(z+h)^2]^{3/2}} \quad 4.3$$

Equation 4.3 represents the gravitational attraction of dm at a height, ′h′ , above mean sea level surface. This filter attenuates the short wavelength anomaly components while enhancing the long wavelength ones. This equation therefore represents an algorithm for developing an upward continuation filter.

4.2.2.2 Trend surface fitting

Trend surface fittings is a mathematical methods (Menke, 1989) used to approximate the regional component of the gravity field. It is obtained by fitting a low order polynomial surface to the gravity data using least square techniques. Thus, the multiple regression equation involving two independent variables which define the form of the first degree surface fit is given by

$$T(x_i, y_i) = \boldsymbol{b_0} + \boldsymbol{b_1}x_i + \boldsymbol{b_2}y_i + \varepsilon \quad 4.4$$

Where

$T(x_i, y_i) -$ *is estimated value of the dependent variable*

$\boldsymbol{b_0} -$ *is point of intercept on the* $y -$ *axis* $T(x_i, y_i)$

$\boldsymbol{x}$ ***and*** $\boldsymbol{y}$ *are the two independent variables being considered*

$\boldsymbol{b_1} -$ *is corrosponding change in* $T(x_i, y_i)$ *for each unit change in* x, *while* y *held constant*

$\boldsymbol{b_2} -$ *is corrosponding change in* $T(x_i, y_i)$ *for each unit change in* y, *while* x *held constant*

$\boldsymbol{Here}, \boldsymbol{b_0}, \boldsymbol{b_1}$ *and* $\boldsymbol{b_2}$ *are known as coefficients of regression*

This implies that the regression of the dependent variable on the particular independent variable is measured while holding the value(s) of other variable(s) constant.

From equation (4.4) the error ε is expressed as

$$\epsilon = \sum (T(x_i, y_i) - (b_0 + b_1 x_i + b_2 y_i))^2 \ \textit{which is to be minimized}$$

From concepts of calculus, we have

$$\left.\begin{aligned} \frac{\partial \varepsilon}{\partial b_0} &= -2 \sum \ (T(x_i, y_i) - (b_0 + b_1 x_i + b_2 y_i) = 0 \\ \frac{\partial \varepsilon}{\partial b_1} &= -2 \sum (T(x_i, y_i) - (b_0 + b_1 x_i + b_2 y_i) x_i = 0 \\ \frac{\partial E}{\partial b_2} &= -2 \sum (T(x_i, y_i) - (b_0 + b_1 x_i + b_2 y_i) y_i = 0 \end{aligned}\right\} \quad 4.5$$

Re-arranging and writing equation (4.5) in matrix form, $\boldsymbol{Am = d}$, we have after some manipulation

$$\begin{pmatrix} \boldsymbol{n} & \sum x_i & \sum y \\ \sum x_i & \sum {x_i}^2 & \sum x_i y \\ \sum y & \sum x_i y & \sum y^2 \end{pmatrix} \begin{bmatrix} b_0 \\ b_1 \\ b_2 \end{bmatrix} = \begin{pmatrix} \sum T(x_i, y_i) \\ \sum T(x_i, y_i) x_i \\ \sum T(x_i, y_i) y \end{pmatrix} \quad 4.6$$

This is a system of equation with three unknowns and three equations that can be solved as a least square over determined problems given by

$$\boldsymbol{m^{est}} = \begin{bmatrix} \boldsymbol{b_0} \\ \boldsymbol{b_1} \\ \boldsymbol{b_2} \end{bmatrix} = [\boldsymbol{A^T A}]^{-1} \boldsymbol{A^T d} \quad \textbf{4.7}$$

Equation 4.7 is a two-dimensional first degree polynomial surface parameters solution of equation 4.4 or 4.6. Similar approach can be followed to get solutions for the second, third and any higher order.

4.2.2.3 Vertical Derivative

The vertical derivative is one of the filtering techniques used for the enhancement of the shallow source features in the data. This transformation magnifies the short wavelength features (Mammo, 2012) which could reflect the residual anomalies. The gridded gravity anomaly data in Fig. 4.2(b) can be expressed as a function in Cartesian co-ordinate system, i.e $F = f(x, y, z)$. The vertical derivative which shows the change of field with depth (z) is expressed as;

$$FVD = -\frac{\partial f}{\partial z} \tag{4.8}$$

The residual anomalies obtained through subtraction of upward continued 6 km and trend surface of order one from Bouguer gravity anomalyare compared against vertical derivative anomaly map to see whether the shallow earth anomalies are satisfactorily picked or not.

4.2.2.4 Spectral analysis

The profile data extracted from the observed gravity field anomaly (Fig. 4.2 (b)) can further be analyzed by transforming the data from space domain to frequency domain. The discrete Fourier transform in one dimension (1D) is given by

$$F(k) = \sum_{k=0}^{N-1} f(n)\, e^{-i\frac{2\pi kn}{N}} \tag{4.9}$$

$F(k)$, is the discrete amplitude spectrum which could be respectively written as a sum and product of real and imaginary

$$F(k) = a(k) + ib(k)$$

Or

$$F(k) = |F(k)|e^{i\varphi(k)} \tag{4.10}$$

where

$|F(k)| = \sqrt{a^2(k) + b^2(k)}$, is an amplitude spectrum and

$k = 2\pi f$ is the wave number

Spectral analysis thus describes the variation of the energy (amplitude) as a function of frequency (wavelength). The filter estimate subsurface density contrast depth given by Spector and Grant (1970) as

$$h = -\frac{1}{4\pi}\left(\frac{logE_1 - logE_2}{K_1 - K_2}\right) \quad 4.11$$

Where E_1 and E_2 are power spectra of the gravity field,

$\log E_1$ and $\log E_2$ are logarithms of the power spectra

k_1 and K_2 are wave numbers

h is depth to interfaces (layer boundaries)

Equation (4.11) gives the average depth, h, which is obtained from difference of the power spectrum curve slopes divided by -4π. This filter designed to determine the top of density contrasts causing gravity anomalies.

4.2.3 Results and Analysis

The Bouguer gravity anomaly field (Fig. 4.2(b)) is the cumulative sum of the sources at different depth levels which are broadly classified as sources at shallower and deeper levels. These source anomalies need to be decomposed for better investigation of the subsurface. In this work, the upward continuation and trend surfaces approximation methods are applied to accomplish this task. The two methods were choosen because they are used frequently by different researchers and because of their simplicity in understanding how they work. However, one method shouldn't be simply picked and applied on approximation of low frequency signature. That is, one needs to work on whether the chosen regional approximation method best represent the deep geology

which in turn should result in shallow earth (residual anomaly) of the area than the other methods. This paper is devoted to select a single appropriate method for Bouguer gravity anomaly separation.

4.2.3.1 Upward continuation

To estimate the appropriate upward continuation height the Bouguer gravity anomaly(Fig. 4.2 (b)) are upward continued to a height of 250 m, 500 m, 1.0 km, 2 km, 3 km, 4 km, 5 km and 6 km. As the continuation height increases the effect of shallower features disappears (Fig. 4.6(b-i)). Particularly, at a continuation height of 6000 m (Fig. 4.6(i)) most of the shorter wavelengths are removed. This is evidently justified by the west-east extending Bouguer gravity anomaly profile (Fig. 4.7) subjected to upward continuations. The anomaly profile curve gets smoother as continuation heights increased from 500m to 1000m, from 1000m to 5000m and from 5000m to 6000m. Thus, the continuation height chosen characterizes the regional anomaly field in the region under study.

According to Jacobsen (1987) when the gravity field is upward continued to a height z, it maps the sources found at and below the depth, $z/2$. Thus, the upward continuation of Bouguer gravity anomaly(Fig. 4.6 (a)) to height of 250m (Fig. 4. 6 (b)) to height of 500m (Fig. 4. 6 (c)) to height of 1.0 km (Fig. 4. 6 (d)) to height of 2.0 km (Fig. 4. 6 (e)) to height of 3.0 km(Fig. 4. 6 (f)) to height of 4.0 km (Fig. 4. 6 (g)) to height of 5.0 km (Fig. 4. 6 (h)) and to height of 6km (Fig. 4. 6 (i)) are used to image sources buried at and below the depths 125m (b), 250m(c), 500m(d), 1km(e), 1.5km(f), 2km(g), 2.5km(h) and 3 km(i) respectively.

The residual anomaly obtained after subtracting the regional field estimated through upward continuation to a height of 6000m is shown in Fig. 4.8.

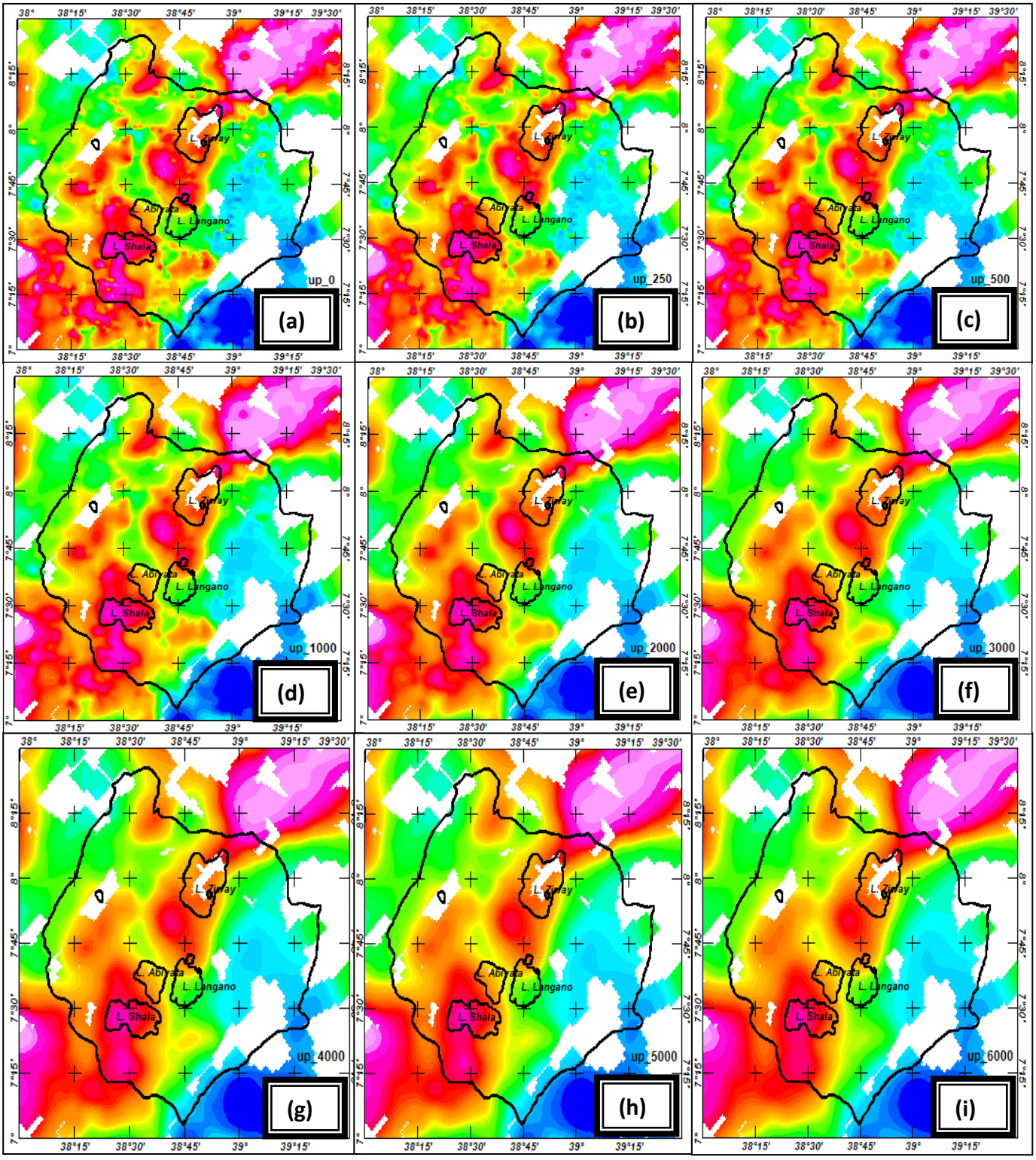

Fig. 4. 6 Bouguer gravity anomaly (a) upward continued to height of 250m (b) to height of 500m (c) to height of 1.0 km (d) to height of 2km (e) to height of 3km (f) to height of 4km (g) to height of 5km (h) and to height of 6km (i) to image sources buried at and below the depths

125m (b) 250m (c) 500m (d) 1.0 km (e) 1.5 km (f) 2.0 km (g) 2.5 km (h) and 3.0 km (i) respectively.

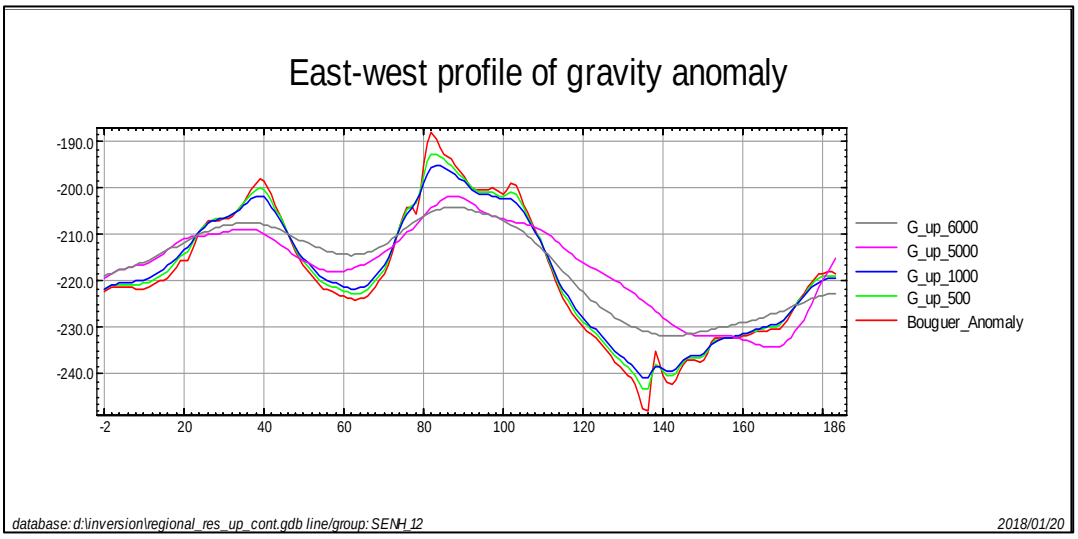

Fig. 4. 7 Regional gravity anomaly profiles estimated using upward continuation to heights of 500 m, 1km, 5km and 6km across west-east at $7^0$45'N latitude. The gray color profile anomaly map (upward continued to 6km) is smoother than others anomaly maps.

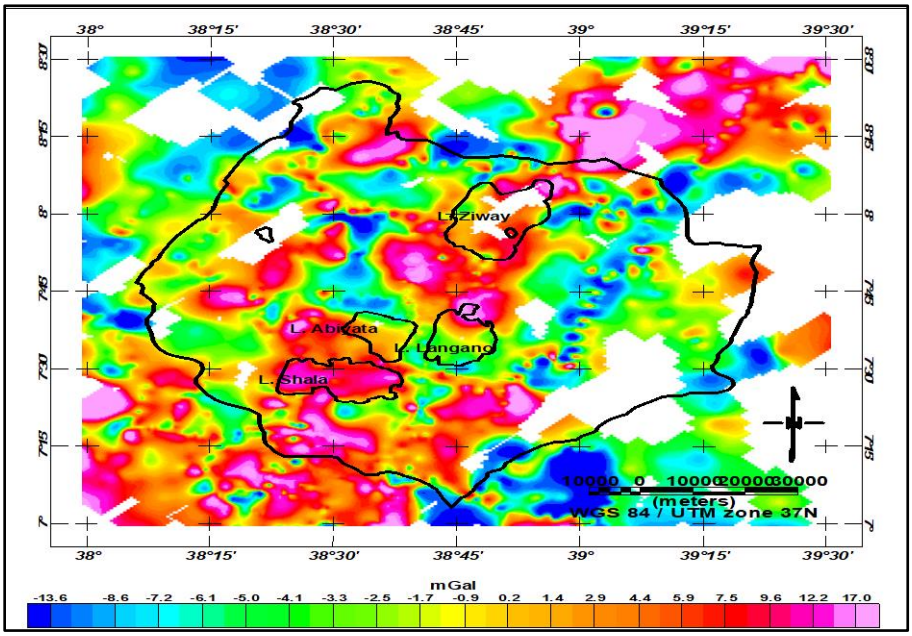

Fig. 4. 8 Residual gravity anomaly map of the Ziway-Shala lakes basin after the anomaly sources deeper than 3km (upward continued 6km) are removed which is characterized by negative and positive gravity values.

4.2.3.2 Trend surface analysis

The residual anomalies obtained through approximation of regional field with trend surface of first, second and third orders respectively are shown in the Fig. 4.9 (a, b and c). These anomalies do not show the varied residual anomalies of the area as that of the upward continuation method.

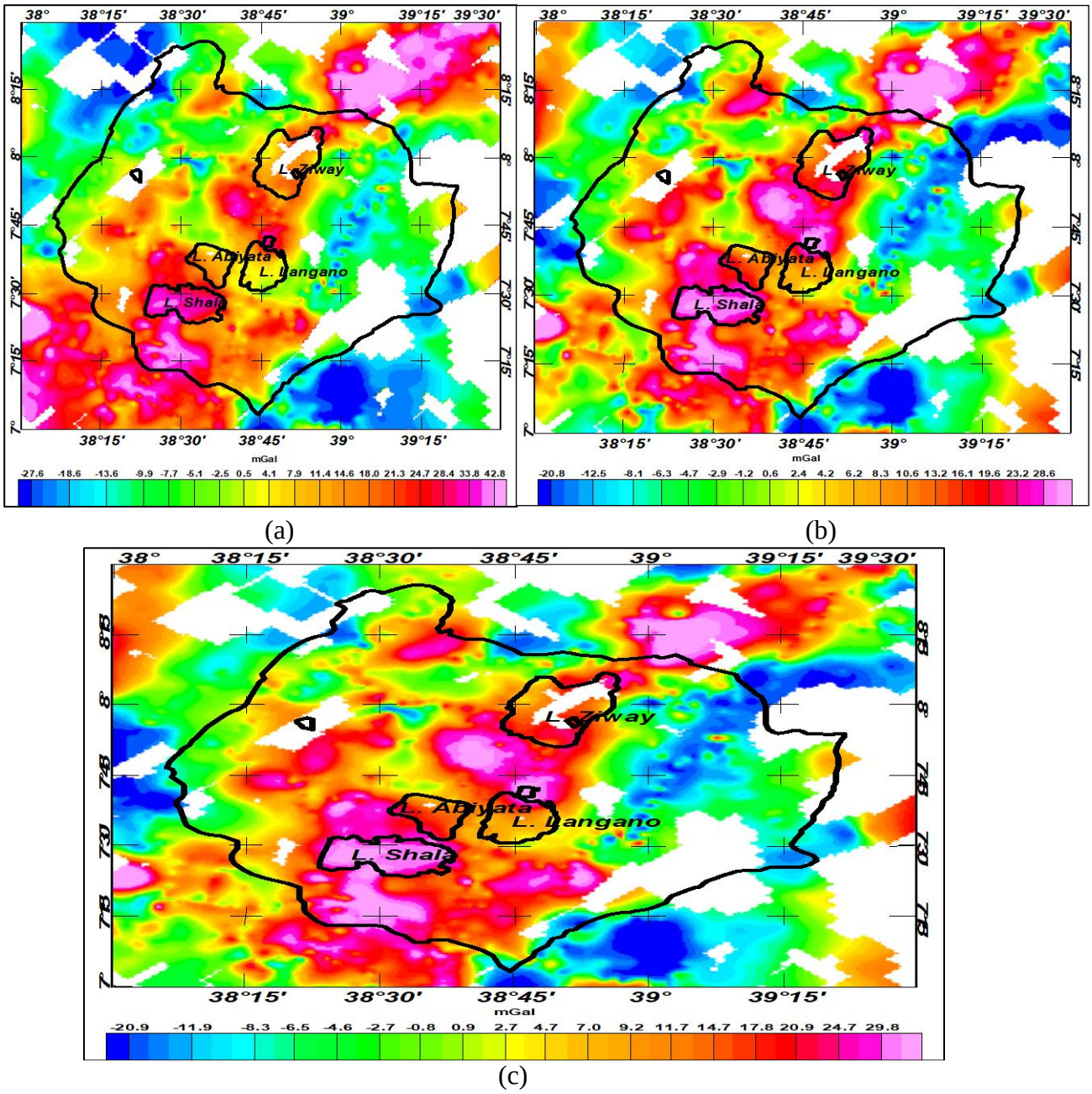

(a) (b)

(c)

Fig. 4. 9 Linear first, second and third order polynomial trend surface removed from Bouguer gravity anomaly generates the residual anomalies (a), (b) and (c) respectively**.**

The correlation coefficient between the west-east (along **$7^0$45'N** latitude) oriented residual anomaly profiles obtained using upward continuation to height of 6km with those of first, second and third order trend surface polynomial are calculated to be 0.91, 0.87 and 0.86 respectively. Fig. 4.10 supports consistency of the computed correlation coefficients for the upward continuation and trend surface methods. Moreover, the correlation coefficients 0.91 corresponding to the first order polynomial trend surface best elucidate the shallow geologic features of the area than those of the second and third order surface trend polynomials.

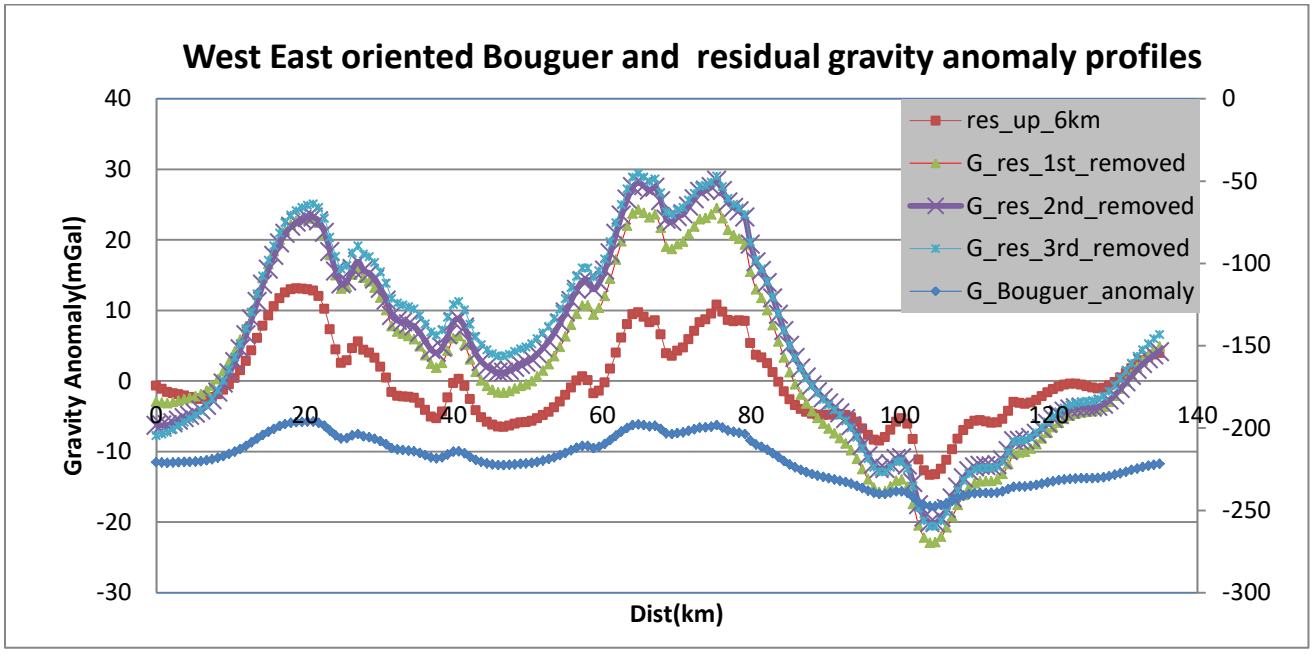

Fig. 4. 10 Relationship between Bouguer gravity anomaly and residua gravity anomalies generated by subtraction of regional gravity anomalies estimated through upward continuation and trend surface fits of first, second and third order polynomials.

4.2.3.3 Vertical derivative

To validate the residual gravity field results obtained from upward continuation to a height of 6km, the first vertical derivative of the Bouguer gravity anomalyis generated (Fig. 4.11). The results appear to better match the residual anomalies generated using upward continuation technique than the one generated through first order trend polynomial fit. The comparison is based on residual (or local) anomaly signatures resulting from shallow origin subsurface masses. Shallower source signatures are better observed using the residual gravity anomalies obtained through upward continuation than the residuals using trend surface analysis.

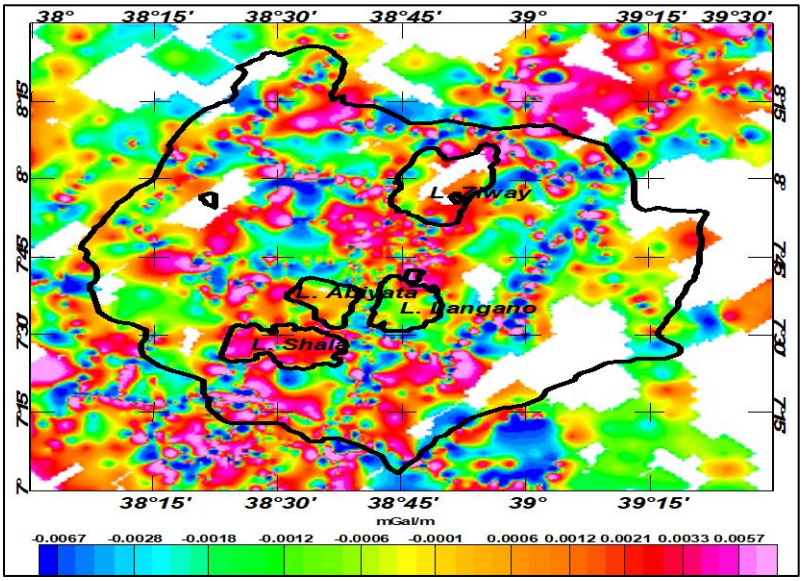

Fig. 4. 11 First vertical derivative of Bouguer gravity anomaly.

4.2.3.4 Spectral analysis

Spectral analysis is one of the quantitative depth estimation methods for gravity anomaly source bodies. The upward continuation method is another filtering technique which is used to determine anomaly sources occurring at variable depths. These two techniques can be jointly applied to estimate source depths and make a comparison of the results obtained from the two methods.

In this study, profiles AB, CD and EF are extracted from Bouguer gravity anomalymap (Fig. 4.2(b)) and a first order polynomial is removed to generate the residual anomalies (Fig. 4.12 (a), (b) and (c)). The residual anomaly field is analyzed by transforming the data from space domain to discrete frequency domain (Equation 2.9). The one dimensional Fourier series expansion of these profiles data are subjected to spectral analysis to decompose anomaly signals based on wavelength. The average depth to the anomaly sources contrast can be estimated based on the slope of power spectral magnitude versus wave number. Fig. 4.13 (a), (b) and (c) shows the three logarithmic amplitude spectrums of profile AB , CD and EF with their corresponding lowest wave number anomalous signal (Fig. 4.14 (a), (b) and (c)).

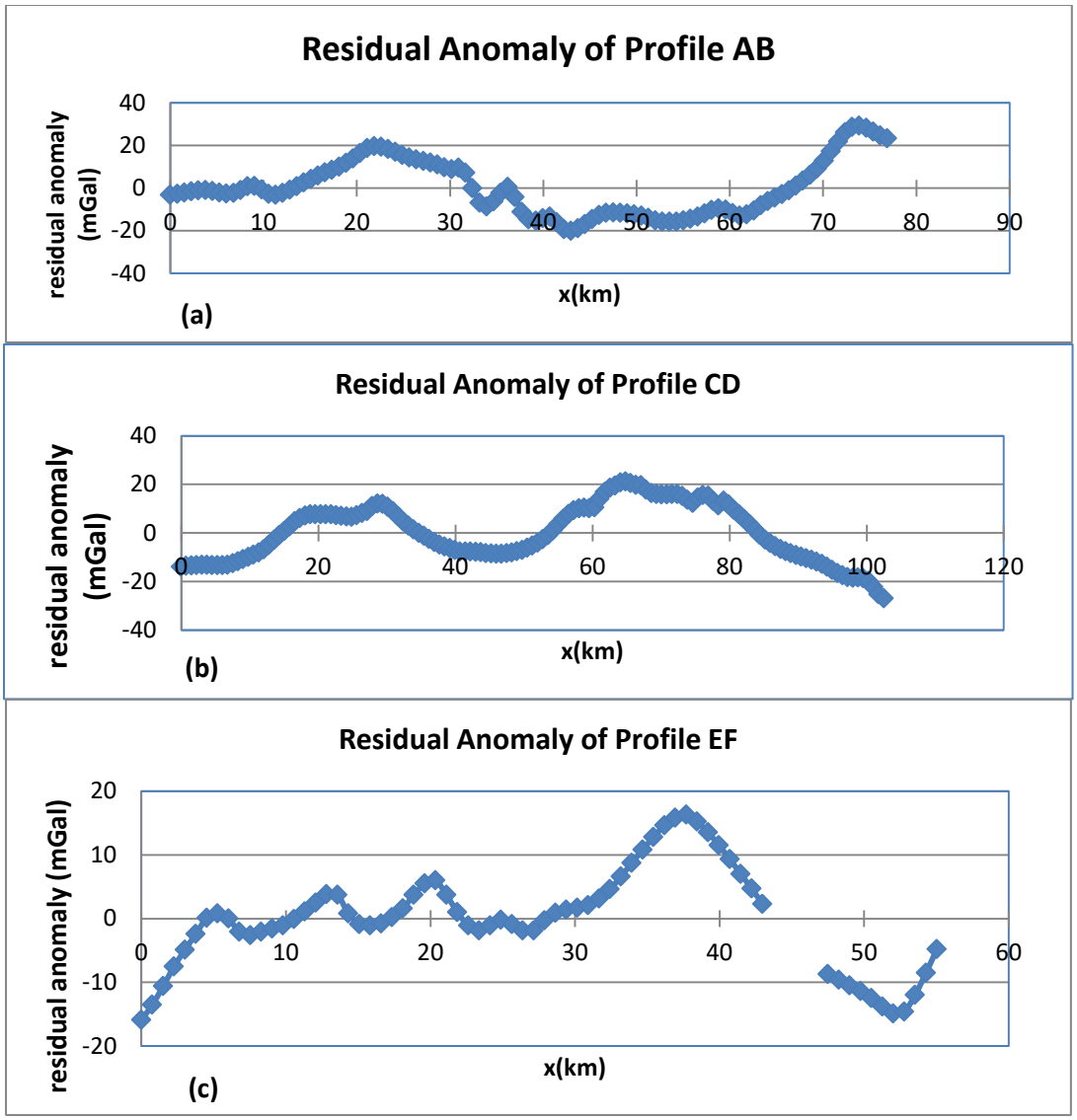

Fig. 4. 12 Residual gravity anomaly maps along profile AB (a), along profile CD (b) and along profile EF (c).

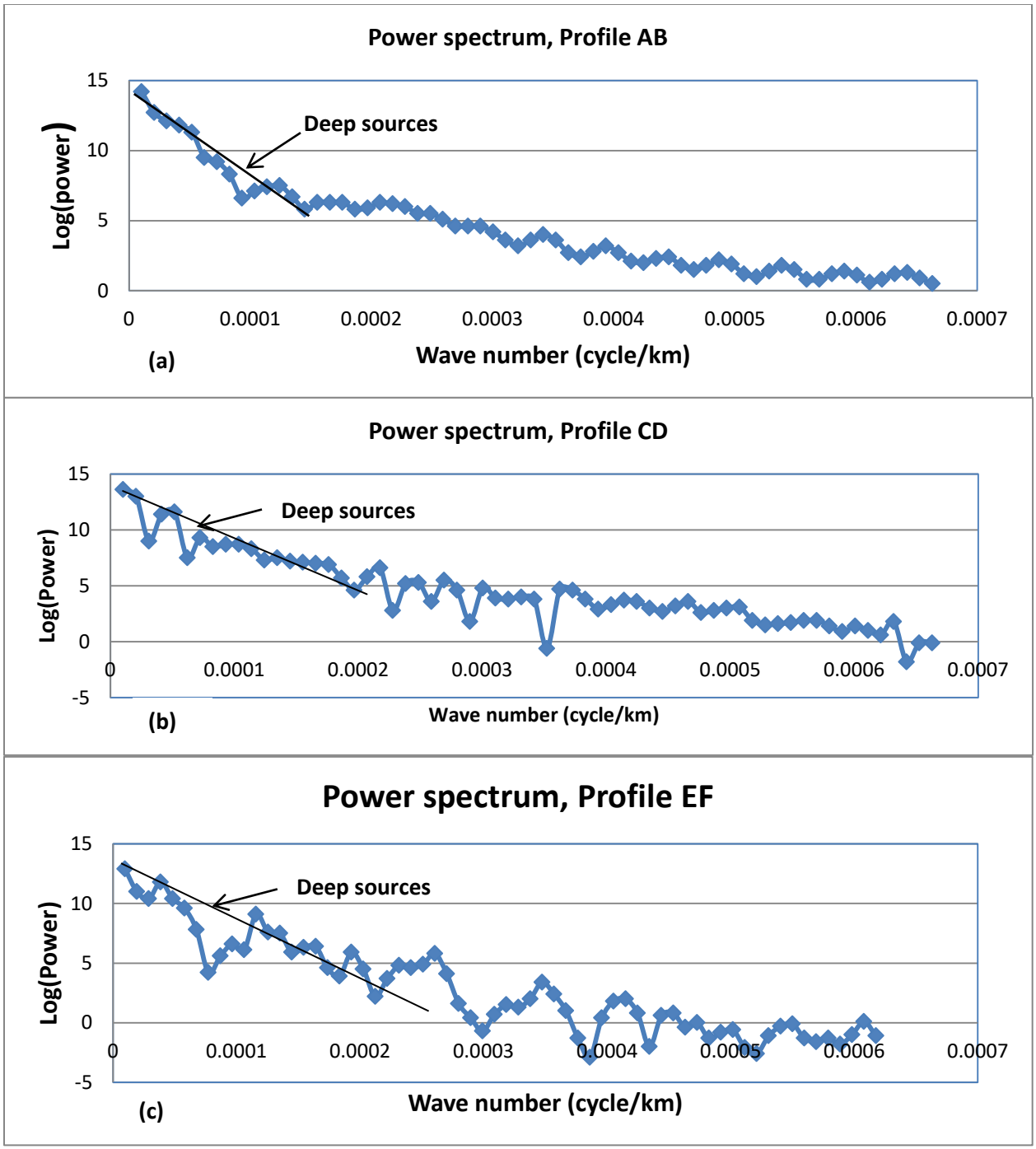

Fig. 4. 13 Logarithmic power spectrums of profiles AB (a), CD (b) and EF (c)

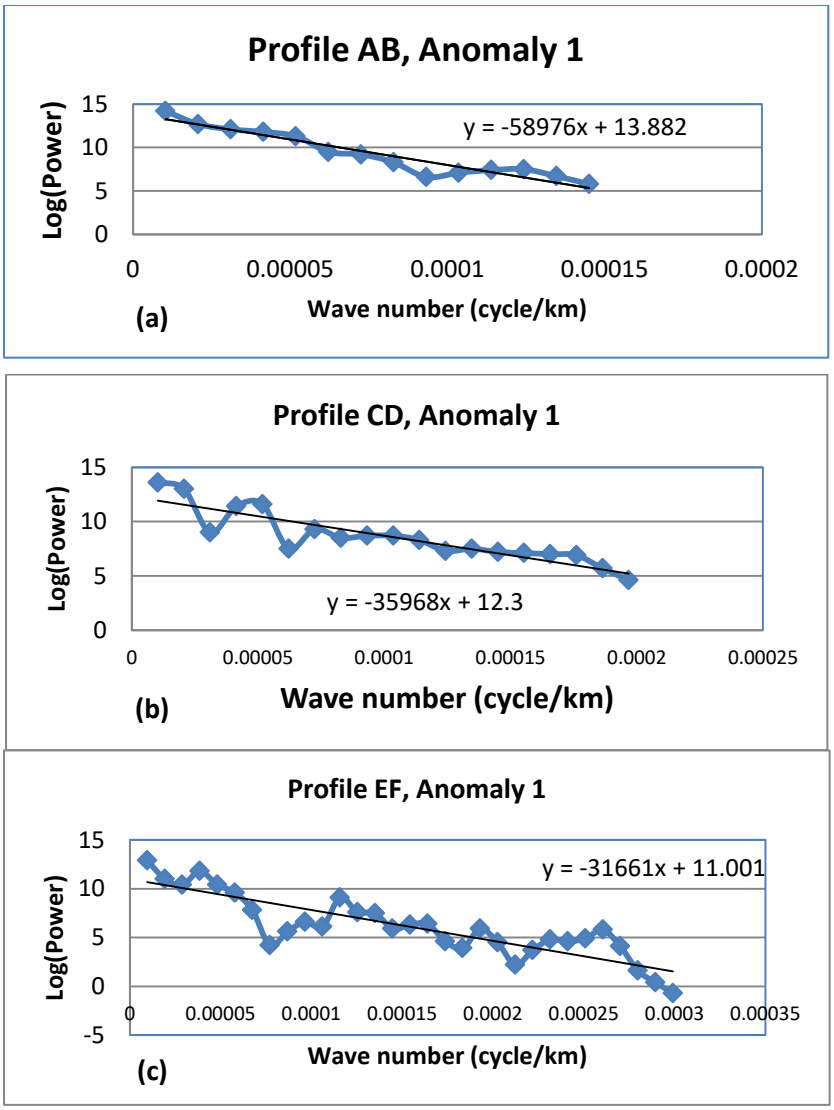

Fig. 4. 14 Lowest wave number anomalies signal of profile AB (a), CD (b) and EF(c) with their trend polynomial line fit which could help to read the gradient estimates.

Though we were able to extract the deep, the intermediate and shallow depth density contrast locations from logarithmic power spectrum profile maps (Fig. 4.13); we are interested in the lowest frequency signal signature (Fig. 4.14). This lowest frequency signal corresponds to the deep source density contrast depth.

Table 4. 1 The regional gravity anomaly source fields and approximated depth of the three profiles AB, CD and EF.

Profile Name	Gradients	Depth(m)	Source Location	**Average(m)**
(Profile AB)	58976.00	4695.54	Deep	3284.423
(Profile CD)	35968.00	2636.95	Deep	
(profile EF)	31661.00	2520.78	Deep	

The mean depth values corresponding to the deeper density contrast for the three selected profiles AB (north), CD (central) and EF (south) approximated using spectral method are 4695.54 m, 2636.95 m and 2520.78 m respectively. The average value of the estimated depths amounts to 3.284 km (Table 4.1). This mean depth possibly approximates the deeper source (crystalline basement) in the region considered.

The mean depth (3.284km) estimated using spectral analysis fairly agrees with the top of density contrast causing the regional gravity anomalies estimated using upward continuation filter (3km).

4.2.3.5 Comparison with well log data and surface geology

The analysis made in sections 4.1 to 4.3 would help to conclude that the upward continuation at 6.0 km height better approximates the regional field anomaly of the area than the other continuation heights. This is supported by the well-log data geologic model of the Aluto-Langano Geothermal field (Hutchison et al., 2016; Wilks et al., 2017; Cherkose & Mizunaga, 2018). The model shows the depth to crystalline basement rock is found at depth below 2.5 km. This basement rock is the source of the regional gravity anomaly deduced by the upward continuation height of 6 km. According to Jacobsen (1987) when the gravity field is upward continued to a height 6 km, it maps the sources found at and below the depth 3 km.

The residual gravity anomaly map (Fig. 4.15) with color contrast designated by “H” for high and “L” for low gravity anomaly values are compared with surface geology of the area constructed by (Tefera et al., 1996; Molin and Corti, 2015). The contrasting gravity anomalies and there corresponding geologic sources are summarized in Table 4.2. The comparison made is consistent.

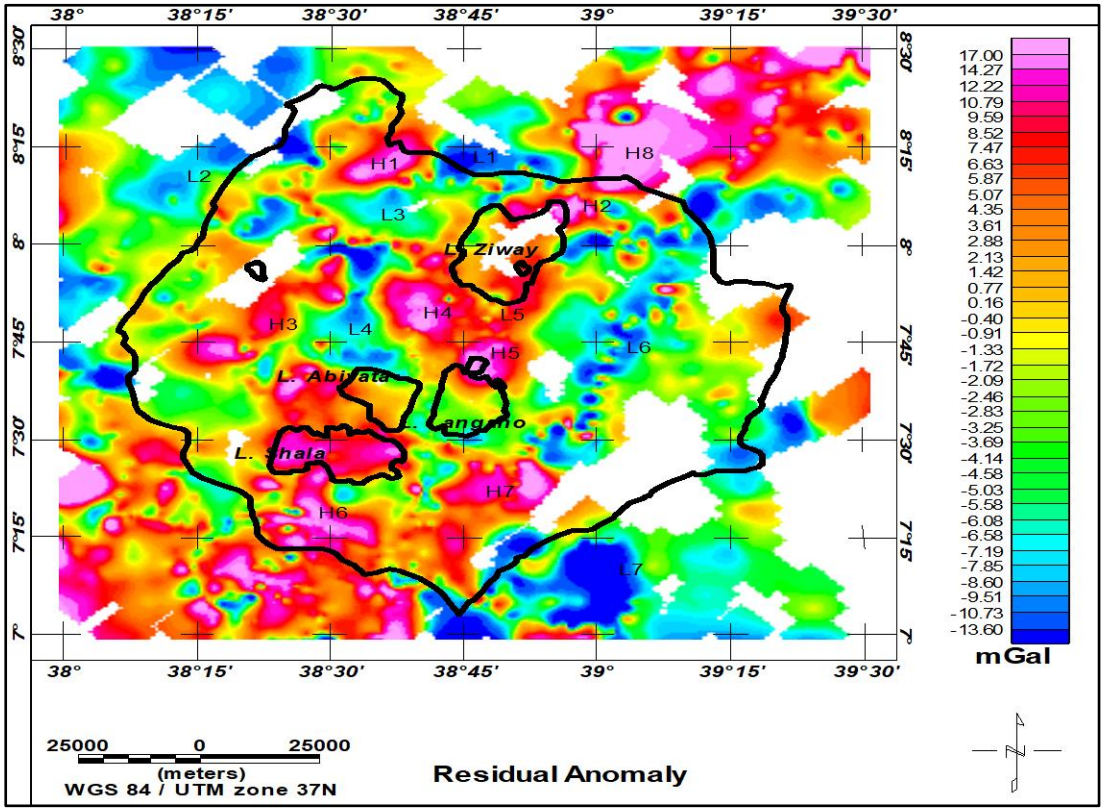

Fig. 4. 15 Residual gravity anomaly of the region categorized as high (H) and low (L) anomalies

Table 4. 2 Relationships of the anomalous gravity source with surface Geology of the area.

S.N	Signal Strength	Correlation with existing geological map	Sources
1	**H1**	Nazret pyroclastic rocks: Rhyolitic ignimbrite lava flows and domes (Late Miocene – Pliocene) embedded in Chefe Donsa Pyroclastic deposits (Rhyolitic ash flows and fall deposits) Dino formation: Ignimbrite, tuff, course pumice, water lain pyroclastic rocks with rare intercalations of lacustrine sediments	(Molin & Corti, 2015) (Tefera et al., 1996)
2	**H2**	Southern extension of Bora-Bericha rhyolites: Rhyolitic and trachytic lava flows and domes, pyroclastic deposites(Pleistocene-Holocene) Rhyolitic volcanic centers, Obsidian pitchstone, pumice, ignimbrite, tuff, subordinate trachytic flows (predominantly per alkaline in composition)	(Molin & Corti, 2015) (Tefera et al., 1996)
3	**H3**	Wonji basalts: Basaltic lava flows, scoria and phreatomagmatic deposit(Pleistocene-Holocene) overexposed on Chefe Donsa Pyroclastic deposits (Rhyolitic ash flows and fall deposits)	(Molin & Corti, 2015)
4	**H4, H5 and H8**	Bora-Bericha rhyolites: Rhyolitic and trachytic lava flows and domes, pyroclastic deposites(Pleistocene-Holocene) Rhyolitic volcanic centers, Obsidian pitchstone, pumice, ignimbrite, tuff, subordinate trachytic flows (predominantly per alkaline in composition)	(Tefera et al., 1996) (Molin & Corti, 2015)
6	**H6**	Wonji basalts: Basaltic lava flows, scoria and phreatomagmatic deposit(Pleistocene-Holocene)	(Molin & Corti, 2015)
7	**H7**	Chilalo volcanics(formation): Trachytic lava flows(alkaline basalt) and pyroclastic deposits (Pliocence-Pleistocence)	(Molin & Corti, 2015) (Tefera et al., 1996)
9	**L1**	Alluvial and Lacustrine sediments: sand, silt, clay, diatomite lime stone and beach sand (Pleistocence-Holocene)	(Tefera et al., 1996) (Molin & Corti, 2015)
10	**L2**	Nazret pyroclastic rocks: Rhyolitic ignimbrite lava flows and domes (Late Miocene – Pliocene) embedded in Chefe Donsa Pyroclastic deposits (Rhyolitic ash flows and fall deposits)	Molin and Corti, 2015
12	**L3**	Chefe Donsa Pyroclastic deposits (Rhyolitic ash flows and fall deposits) Alluvial and Lacustrine sediments: sand, silt, clay, diatomite lime stone and beach sand (Pleistocence-Holocene)	(Tefera et al., 1996) (Molin & Corti, 2015)
13	**L4**	Chefe Donsa Pyroclastic deposits (Rhyolitic ash flows and fall deposits) Alluvial and Lacustrine sediments: sand, silt, clay, diatomite lime stone and beach sand (Pleistocence-Holocene)	(Tefera et al., 1996) (Molin & Corti, 2015)
14	**L5**	Accumulated sediments	(Searle & Gouin, 1972)
15	**L6**	Nazret pyroclastic rocks: Rhyolitic ignimbrite lava flows and domes (Late Miocene – Pliocene)	(Molin & Corti, 2015)
16	**L7**	Chefe Donsa Pyroclastic deposits (Rhyolitic ash flows and fall deposits)	(Molin & Corti, 2015)

4.2.4 Conclusion

The Bouguer gravity anomalies need to be decomposed into its regional and residual component sources before making any interpretation. Though, numerous decomposition techniques are available in literature for approximating the low frequency signals, no specific information is available for the choice of a particular representative method. Furthermore, the method of separation is non-unique and thus no single technique exists. For example, the use of spectral analysis and upward continuation require the wise choice of slope change locations and continuation heights respectively. This requires to work on more than one method and select the best for a given study area. In this research, upward continuation and trend surface analysis methods are compared to map shallow surface geologic and tectonic features of the study area. Accordingly, the upward continuation technique is chosen to be the more reliable approach as it mapped the shallow earth gravity sources better than the trend surface analysis. This is confirmed by comparison of the obtained anomaly with the anomaly generated through analysis of first vertical derivative, power spectral analysis, well-log data and surface geology of the area. The subjectivity and non-uniqueness of the existing separation techniques thus requires comparison of the various decomposition techniques in order to choose the best method for the approximation of the regional and the residual fields of a given area.

This chapter is a published manuscript in Heliyon Journal, Elsevier, and has been reproduced here with the permission of the copyright holder. Having the required anomalies, the next chapter devoted to extract gravity lineaments which could show the subsurface structures of the area.

Chapter 5: Mapping Geologic Structures from Gravity and Digital Elevation Models

5.1 Introduction

The Main Ethiopian Rift (MER) encompassing three segments, southern, central and northern MER (Woldegabriel et al., 1990) (Bonini et al., 2005) and is part of a bigger East African Rift system (EARS) that links the Afar triple junction and the Kenya Rift regions. The study area, Ziway-Shala Lakes Basin, is located in the central part of the Main Ethiopian rift (Ayenew, 2001) and is bounded within the limits of $38^0$00'-$39^0$30'E and $7^0$00'-$8^0$30'N. The region is characterized by volcano-tectonic depressions having three physiographic features, the rift floor and the flanking escarpments and plateaus. The mean elevation varies from 1632 masl to 3448 masl (Fig. 5.1).

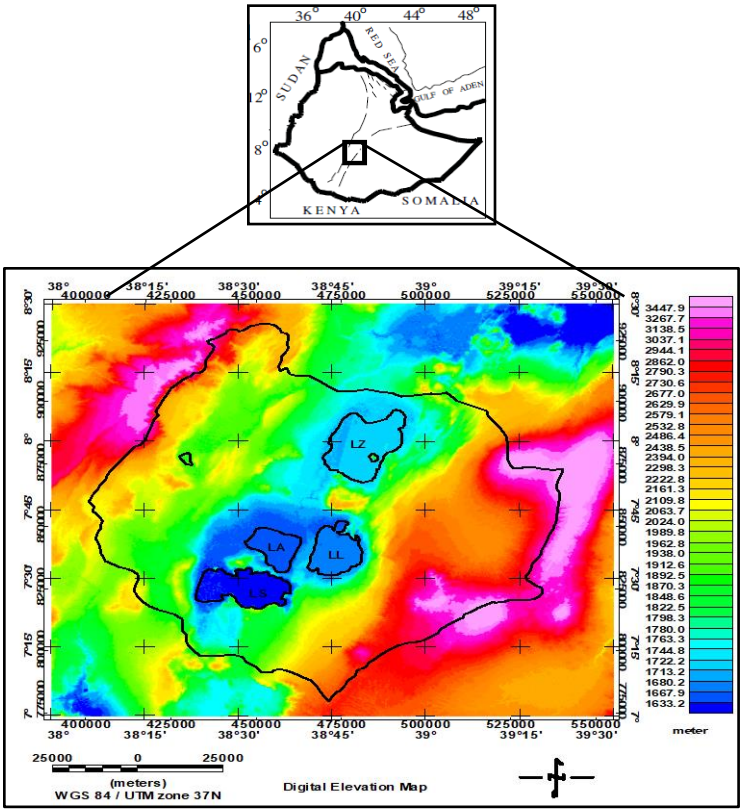

Fig. 5. 1 Location and topographic map of the Ziway-Shala Lakes Basin and its surroundings with the main physiographic elements.

5.1.1 Geologic and structural settings

The geology and geologic structures observed in the region are due to active Cenozoic volcanic, tectonic and sedimentation processes (Abebe et al., 2007; Woldegabriel et al., 2000; Le Turdu et al., 1999). The observed structures are faults, joints and fractures which have surface expression as shown in the geologic map (Fig. 5.2) and the structural map (Fig. 5.3(b)) of the area and are generally have N-S to NNE-SSW and NE-SW to N-S orientation (Korme et al., 2004). These structures are collectively called Wonji Fault Belt (WFB) (Mohor, 1962) and accompanied boundary faults (Boccaletti et al., 1998). The WFB is the youngest and most active fault system cross-cut by the pre-existing NW-SE Mesozoic Ogaden rift fault (Korme et al., 2004) (Fig. 3(a)). These pre-existing structures have been proven to exert a significant control on the accommodation of deformation and on the distribution of strong volcanic activity (Corti et al., 2013; Abebe et al., 2007) in the region.

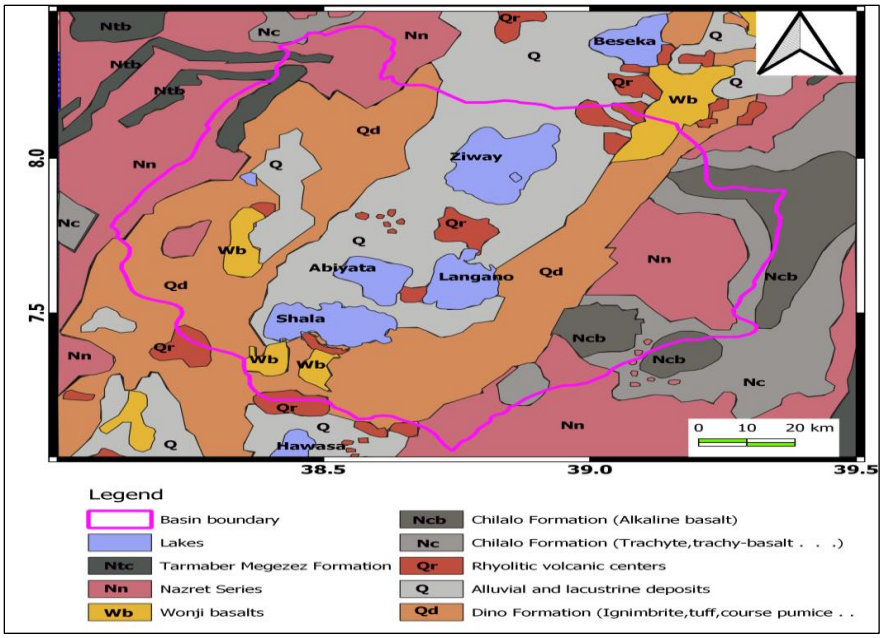

Fig. 5. 2 Geology of the Ziway-Shala Lakes basin, central Main Ethiopian rift modified from Tefera et al. (1996).

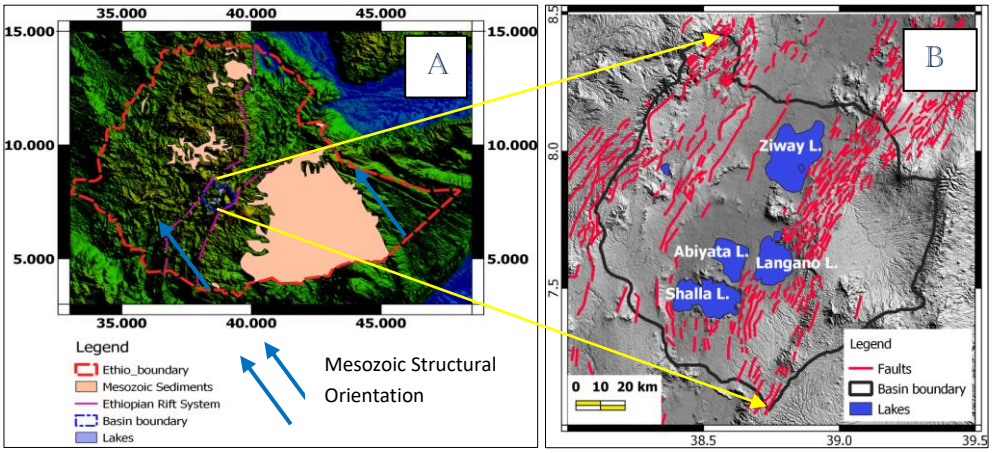

Fig. 5. 3 Outcropped Mezozoic structural orientation which is called pre-existing Mesozoic structures (a) Surface structural map of the study area modified from Agostini et al.(2011) and Molin and Corti (2015) (b).

5.1.2 Rationale and objective of the study

The geological structures in the EAS documented in different literatures mainly target on extracting the surface structures of shallow Earth origin (Molin and Corti, 2015; Agostini et al., 2011). The data used to trace these surface structures were DEM images. The surface structures in the Ziway-Shala Lakes basin mapped using DEM data and actual field observations (Agostini et al., 2011) is shown in Figure 5.3(b). The subsurface structures of deeper origin for the same region are inferred by geophysical data (mainly gravity and seismic), most of which focus on mapping crustal structures thicknesses and Moho depth undulations. Based on gravity data, various studies have shown that the crust thins northward along the rift (Mickus et al., 2007; Tiberi et al., 2005; Tessema and Antoine, 2004; Mahatsente et al., 1999). Refraction/wide-angle seismic reflection survey conducted along the rift (Maguire et al., 2006) support the results from gravity data. Though, its depth extent is not mentioned Korme et al. (2004) identified a pre-existing NW-SE extending Mesozoic Ogaden rift fault from gravity data. These structures cross

the main Ethiopian rift in an approximately orthogonal fashion (Korme et al., 2004). In this respect, there is lack of studies that have targeted on delineating the intermediate depth (between shallower and deeper earth) geological structures at different depth levels in the Ziway-Shala Lakes basin.

By taking into consideration all the points mentioned, the objectives of this study are thus defined:

- ✓ To map the subsurface geologic structures/lineaments to a depth of the crystalline basement (3km) using gravity data
- ✓ To map surface structures (topographic lineaments) from DEM data and use this information to validate (constrain) the subsurface structures mapped using the gravity data.
- ✓ To investigate the influence of subsurface lineaments (structures) on groundwater flow and salinity control

5.2 Data

Gravity and DEM data sets are examined for subsurface and surface structures beneath the Ziway-Shala Lakes Basin, Central Main Ethiopian Rift. The data acquisition and processing are documented as follows

5.2.1 Gravity Data

Ground based gravity data were obtained from Geological Survey of Ethiopia and PhD thesis work (Alemu, 1992). This data were reprocessed and homogenized to the International Gravity Standardization Network 1971 (IGSN71). The 1967 international gravity formula, a reduction density of 2.67 g/cm^3 and sea level as a datum are used. The computed complete Bouguer gravity anomaly values are gridded to generate the complete Bouguer gravity anomaly map (Fig.

5.4(b)) of the study area. The regional gravity anomaly is estimated using upward continuation filter with an upward continuation height of 6 km (H. Kebede et al., 2020) (Fig. 5.4(c)). The residual gravity anomaly map (Fig. 5.4(d)) of the region is then compiled by subtracting the estimated regional from the observed complete Bouguer gravity anomaly.

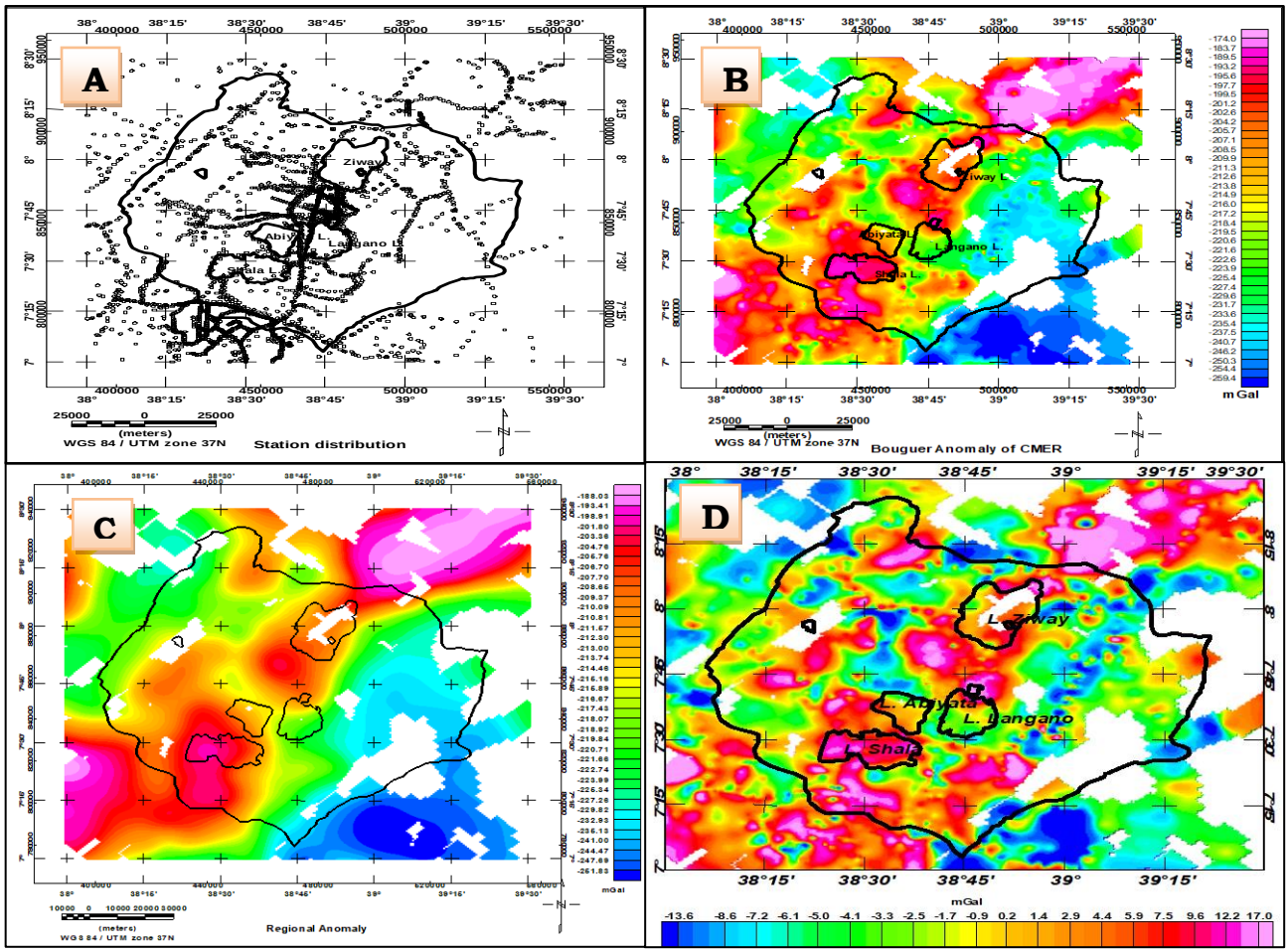

Fig. 5. 4 Gravity stations distribution map (a) Bouguer gravity anomaly map (b) regional gravity anomaly map (c) and residual gravity anomaly map (d).

5.2.2 Digital Elevation Model (DEM)

A DEM is an Advanced Space-borne Thermal Emission and Reflection Radiometer (ASTER) gridded imagery data used to represent elevation information of the study area from which surface geologic structures are mapped from. The DEM data employed here have a 30 m spatial resolution (Fig. 5.5).

According to Wladis (1999) since DEM data are a gridded data, grid-based interpretation methods used in analysis of potential field data can be used to extract surface lineaments for a region of interest.

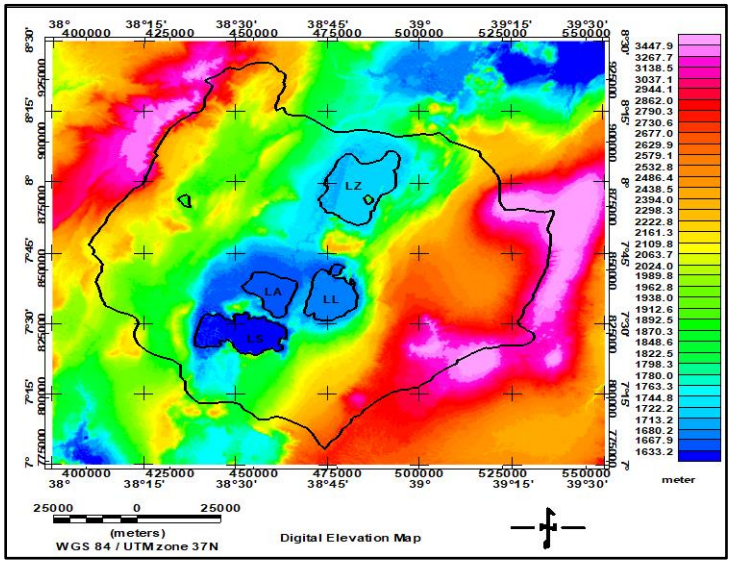

Fig. 5. 5 DEM of the Ziway-Shala lakes basin and its surroundings.

5.3. Methodology

Mapping surface and subsurface structures based on DEM and potential field data are a well practiced and established procedure. Contacts between rocks that have different physical properties usually occur along lineaments which may consist of faults, fractures and etc. Such lineaments which could show major subsurface structures are extracted using image filtering algorithms applied on gravity anomaly data (Aydogan, 2011; Saibi et al., 2008). Topographic

lineaments (Kassou et al., 2012; Abdullah et al., 2010; Jordan et al., 2005; Wladis, 1999) are traced from DEM data using the same filtering techniques used in the analysis of gravity data.

In this research the filter types used include first vertical derivative, second vertical derivative, tilt derivative, upward continuation and line module algorithm of PCI Geomatica. The application of these filters on gridded image map help to extract information on surface and subsurface structures of the area. The governing mathematical equations for the filter types considered are described below

5.3.1 First and second vertical derivative

Gridded gravity and DEM anomaly data input to VDR filters can be expressed as a function in Cartesian co-ordinate system denoted by $F = f(x, y, z)$.

The vertical derivatives of this function which shows the change of field/elevation with respect to depth (z) is expressed as first vertical derivative $(FVDR)$ (Eq. 5.1):

$$FVDR = -\frac{\partial f}{\partial z} \tag{5.1}$$

and second vertical derivative $(SVDR)$ (Eq. 5.2):

$$SVDR = -\frac{\partial^2 f}{\partial z^2} \tag{5.2}$$

The Oasis montaj Geosoft standard software is used to generate the first and second order derivatives of the gridded DEM image. The procedures have effects of enhancing localized shallow (near surface) sources and generate lineaments.

5.3.2 Tilt derivative

The tilt derivative (θ) of gravity anomaly, **F**, is expressed as a ratio of its first vertical derivative to total horizontal derivative (Verduzco et al., 2004) (Eq. 5.3):

$$\theta = TDR = tan^{-1}\frac{\frac{\partial F}{\partial z}}{\sqrt{\left(\frac{\partial F}{\partial x}\right)^2+\left(\frac{\partial F}{\partial y}\right)^2}} \tag{5.3}$$

Where, $\frac{\partial F}{\partial x}, \frac{\partial F}{\partial y}$ and $\frac{\partial F}{\partial z}$ are the derivatives of the gravity anomaly, **F,** with respect to $x, y\ and\ z$ directions.

θ lies between $-\frac{\pi}{2}$ and $-\frac{\pi}{2}$ or between-90^0 and 90^0.

The filter enhances and sharpens the anomalies with zero value contours (zero crossing) which indicate lithological /structural contacts.

5.3.3 Upward continuation

Vertical derivative and tilt derivative filters generally enhance effect of the shallower earth but not necessarily effect of the deeper earth. The regional anomaly resulting from the deeper earth is approximated using the upward continuation filter which is mathematically expressed by Gupta and Ramani (1980) and Jacobsen (1987) (Eq. 5.4) as:

$$H_{reg}(k) = S_0(k)\, e^{-2\pi k z_0} \tag{5.4}$$

Where $S_0(k)$ is Bouguer gravity anomaly anomaly, k is the wave number and $\boldsymbol{z_0}$ is the continuation height

The deeper gravity source signatures are isolated by upward continuing the observed Bouguer anomalies to a higher elevation. According to Jacobsen (1987), if a potential field is upward continued to a certain height, Z, then it will map sources situated at and below the depth $Z/2$. The residual anomaly is then obtained through subtraction of this regional anomaly from the observed Bouguer anomalies.

Jacobsen (1987) also showed that the field generated by a slab located at depths in between Z_1 and Z_2 is simply the difference between the fields resulting from upward continued heights of $2Z_1$ *and* $2Z_2$ (Fig. 6).

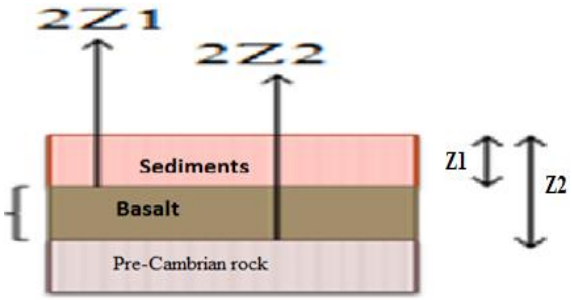

Fig. 5. 6 Schematic representation of three earth layers for extraction of the gravity field anomaly response of a slab (eg. basaltic rock formation) located between depths Z_1 and Z_2 by upward continuation to heights of $2Z_1$ *and* $2Z_2$

The following procedures are followed for the extraction of lineaments emanating from a sandwiched (sliced) gravity source distribution (Fig. 5.6).

- ✓ upward continuation of the observed Bouguer gravity anomaly to a heights of 0.5, 1, 2, 3, 4, 5 and 6 kms
- ✓ Obtaining differences of consequently upward continued anomalies to generate anomalies originating from slabs (slices) located at consecutive depths between 0.25 & 0.5, 0.5 and 1, 1 and 1.5, 1.5 and 2, 2 and 2.5, 2.5 and 3.0, 1.5 and 3km.
- ✓ For anomalies resulting from each slice, line module algorithm of PCI Geomatica and tilt derivative filters are applied to extract lineaments resulting from each slice.

The Bouguer gravity anomalymap (Fig. 5.4(a)) is upward continued to heights of 0.5, 1, 2, 3, 4, 5 and 6 km in order to image sources buried at depths of 0.25, 0.5, 1, 1.5,2, 2.5 and 3.0 km respectively. This upward continuation filter (low-pass filter) generates regional anomalies subtracted from each other giving rise to regional anomalies generated by slabs (sliced slabs)

located at depths between 0.25 & 0.5, 0.5 & 1, 1 & 1.5, 1.5 & 2, 2 & 2.5 , 2.5 & 3.0 and 1.5 & 3 km. As an illustration, the anomalies generated by sliced slabs between the depths 0.25 & 0.5 km, 1.5 & 2 and 2.5 and 3 km are depicted in Figure 5.7(a), Figure 5.7(b) and Figure 5.7(c).

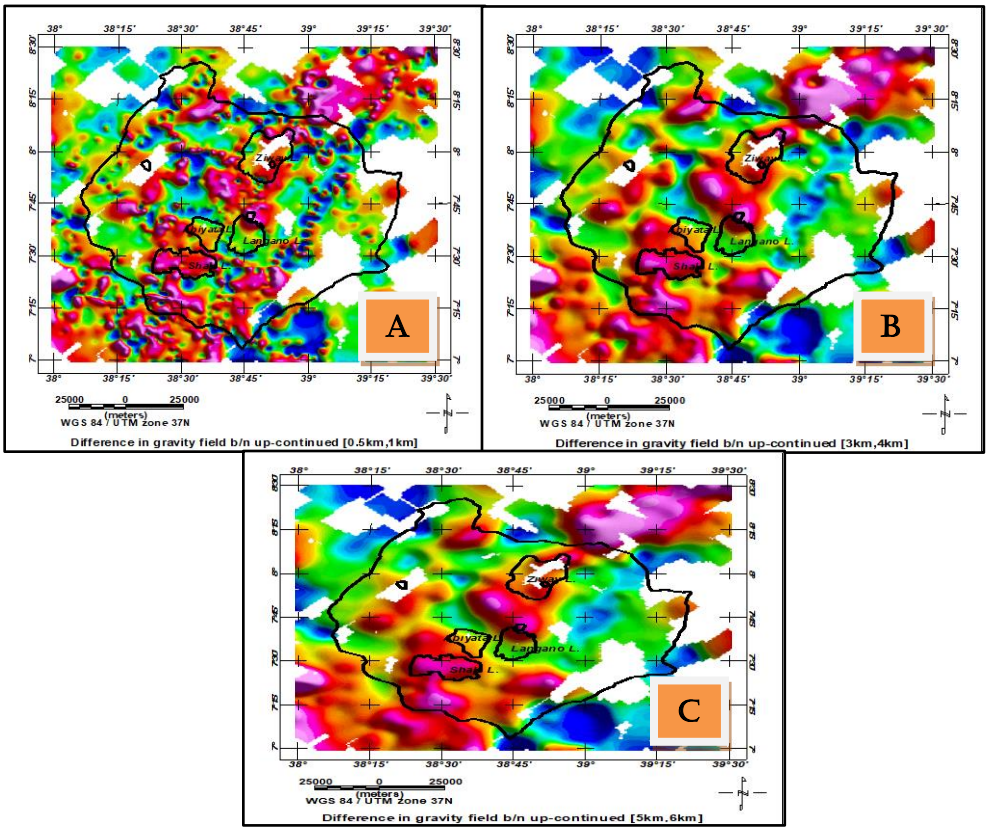

Fig. 5. 7 The gravity anomaly maps of sources (sliced slabs) compiled by taking the differences in up-continued gravity field between 0.5km and 1km (a) 3 km and 4km (b) 5 km and 6 km (c)

The regional gravity anomalies generated by sliced slabs located at the depths considered are used to extract the geologic lineaments occurring in the area to a depth of 3 km (≈ mean crystalline basement depth). The differenced regional anomalies (anomalies of the slabs) are exported as shaded-relief Geotiff 256 Grey (8 bit) images to be used as an input to the Line module algorithm of PCI Geomatica V10. The exported images emphasize gradients in anomaly grids and are useful for displaying strong linear features observed in the images. The methods automatically identify

lineation in three steps including edge detection, thresholding and curve extraction (details given in section 5.3.4).

5.3.4 Line module Algorithm

The LINE option of PCI Geomatica software extracts lineaments automatically from images and records the polylines in a vector segment (Abdullah et al., 2010). This algorithm is designed to extract linear and curvi-linear features from radar images or from optical images.

For mapping reasonably acceptable lineaments, the images should be enhanced with different filtering techniques which may include shaded-relief methods performed using ArcGIS 10.3 software or principal component analysis (PCA) method performed using Image processing software such as ENVI 5.1. The PCA is a statistical technique which removes data redundancy and isolates noises by enhancing images which could finally be used as an input to the filters for extracting geological lineaments (Adiri et al., 2016).

The other image enhancement method is the shaded-relief image techniques which generate a pan sharpened 8 bit gray scale reflected bands to be used as input to Line module of PCI Geomatica V10 software to automatically extract geological lineaments. This algorithm detects the lineation in three steps which include edge detection step, thresholding step and curve extraction step. The input output parameters pertaining to this algorithm including their relationship can be found in the website http://www.pcigeomatics.com/geomatica-help/references/pciFunction_r/python/P_line.html.

The optimal choice of the input/output parameters is chosen by a trial and error process with the shape and density of the generated lineaments taken in to consideration. The default input parameters used by PCI Geomatica algorithm including the selections made in this research are listed in Table 5.1.

No	Parameters	Parameters value option	Default (Choice 0)	Choice 1	Choice 2	Choice 3
1	Radius of filter in pixels (RADI)	5,10,20,50,100	10	10	5	5
2	Threshold for edge gradient(GTHR)	5,10,20,50,100,200,255	100	20	20	30
3	Threshold for curve length(LTHR)	5,10,20,50,100	30	30	20	10
4	Threshold for line fitting error(FTHR)	1,3,5,7,9,10,20,50,100	3	3	3	3
5	Threshold for angular difference(ATHR)	0,15,30,45,60,75,90	30	30	15	15
6	Threshold for linking distance(DTHR)	5,10,20,50,100	20	20	10	10

Table 5. 1 The different parameters input to line module PCI Geomatica software to automatically extract lineaments in Ziway-Shala Lakes Basin

Mapping geological structures (lineaments) of intermediate depth in the region considered are performed using different software such as Geosoft, ENVI 5.1, PCI Geomatica V10, ArcGIS 10.3 and QGIS.

5.4 Results and Discussion

Geologic structures which could be faults, fractures and joints can be extracted from analysis of gravity and DEM data. The application of different filtering algorithms on these anomalies/images generates gravity and topographic lineaments outlined here below.

5.4.1 Subsurface lineaments extracted from gravity slice anomalies

Figure 5.8 reveals gravity lineaments extracted in the study area based on the methodologies mentioned in sections 5.3.2, 5.3.3 and 5.3.4. These includes lineaments extracted based on Line module algorithm (Fig. 5.8 (a, c and e)), tilt derivative techniques (Fig. 5.8 (b, d and f)) and rose

diagram plot showing the overall subsurface lineaments orientation constructed based on line direction histogram module of QGIS (Fig. 5.8(g))

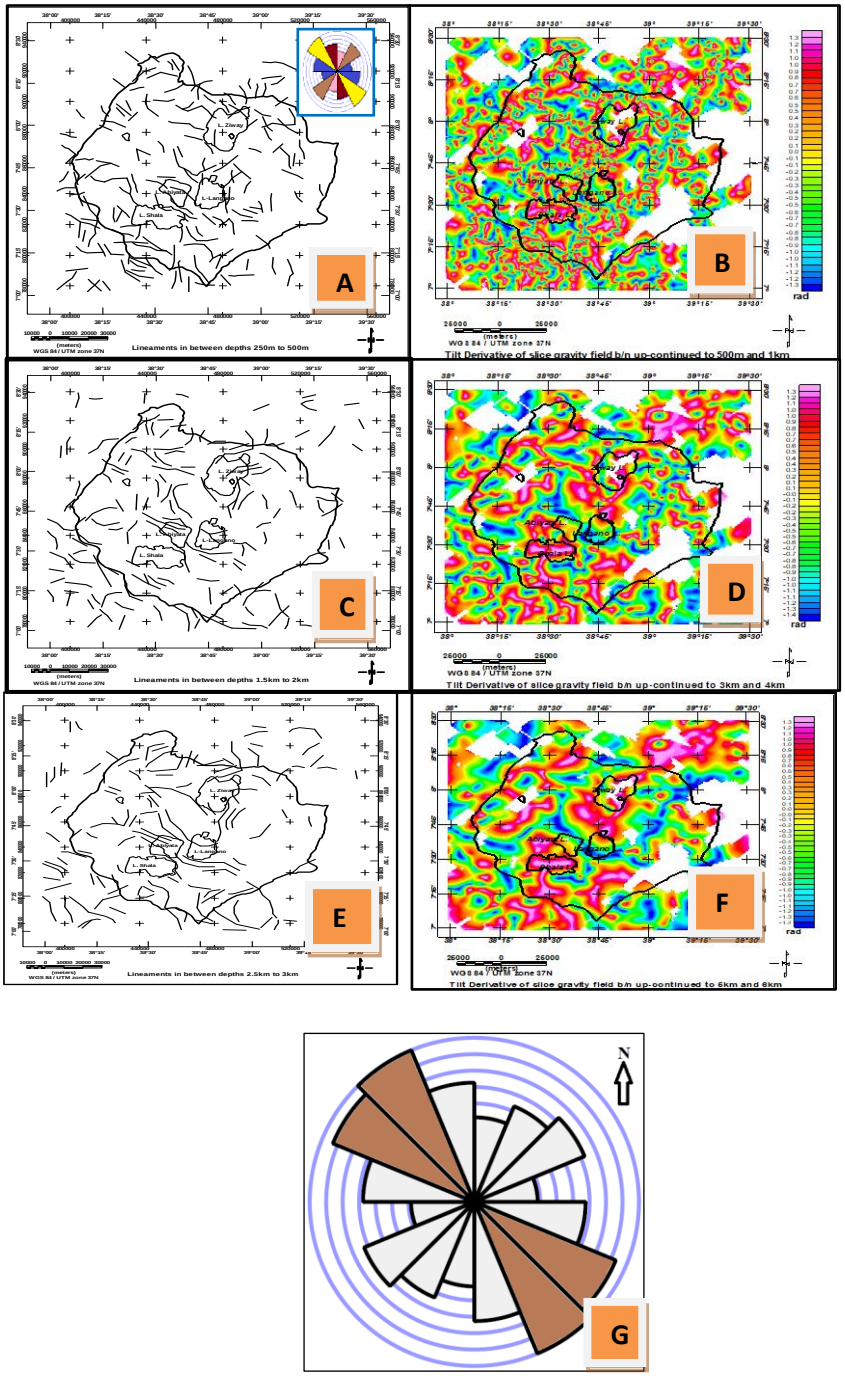

Fig. 5. 8 Lineament maps (a), (c) and (e) for depths between 250m and 500m, 1.5 and 2.0; 1.5 and 2.5 and 3km respectively compared with lineament maps generated using tilt derivative (b), (d) and (f) and rose diagram plot (g) showing orientations of the subsurface lineaments (g)

The major geological structures (lineaments) (Fig. 5.8) were determined through our gravity data. The line module algorithm of PCI Geomatica is used to extract these lineaments (Fig. 5.8 (a), (c) and (e)). These lineaments are compared with lineaments mapped using the tilt derivative method (Fig. 5.8 (b), (d) and (f)). Their comparison shows that both methods give similar results in identifying the location, orientation and density of gravity lineaments in the study area. The extracted lineaments are dominantly oriented NNW-SSE to NW-SE and E-W (Fig. 5.8(g)) which thought to coincide with the direction of pre-existing Mesozoic structures previously identified in the area (Korme et al., 2004). The result also shows lineaments trending NE-SW (Fig. 5.8(g)) that coincides with the orientation of the quaternary faults of the Main Ethiopian Rift system that comprises the study area.

The subsurface lineaments can also be extracted from residual gravity anomalies at different depth levels. The estimated regional anomalies generated using upward continuation to heights of 0.5, 1, 2, 3, 4, 5 and 6 km are subtracted from observed Bouguer gravity anomalyto extract residual anomalies caused by sources extending to depths of 0.25 km, 0.5 km, 1.0 km, 1.5 km, 2.5 km and 3.0 km respectively. These residual anomalies are then converted to 8 bit shaded relief images to be used as an input to line module algorithm which help to extract subsurface lineaments at different depth levels. The identified lineaments (Fig. 5.9 (a), (b), (c), (d), (e) and (f)) are dominantly oriented in a NW-SE direction as also revealed by the rose diagram plot (Fig. 5.9(g)). These linear features (lineaments) are in agreement with respect to their location, orientation and density with those lineaments extracted based on the regional gravity anomalies caused by sliced slabs (Fig. 5.8).

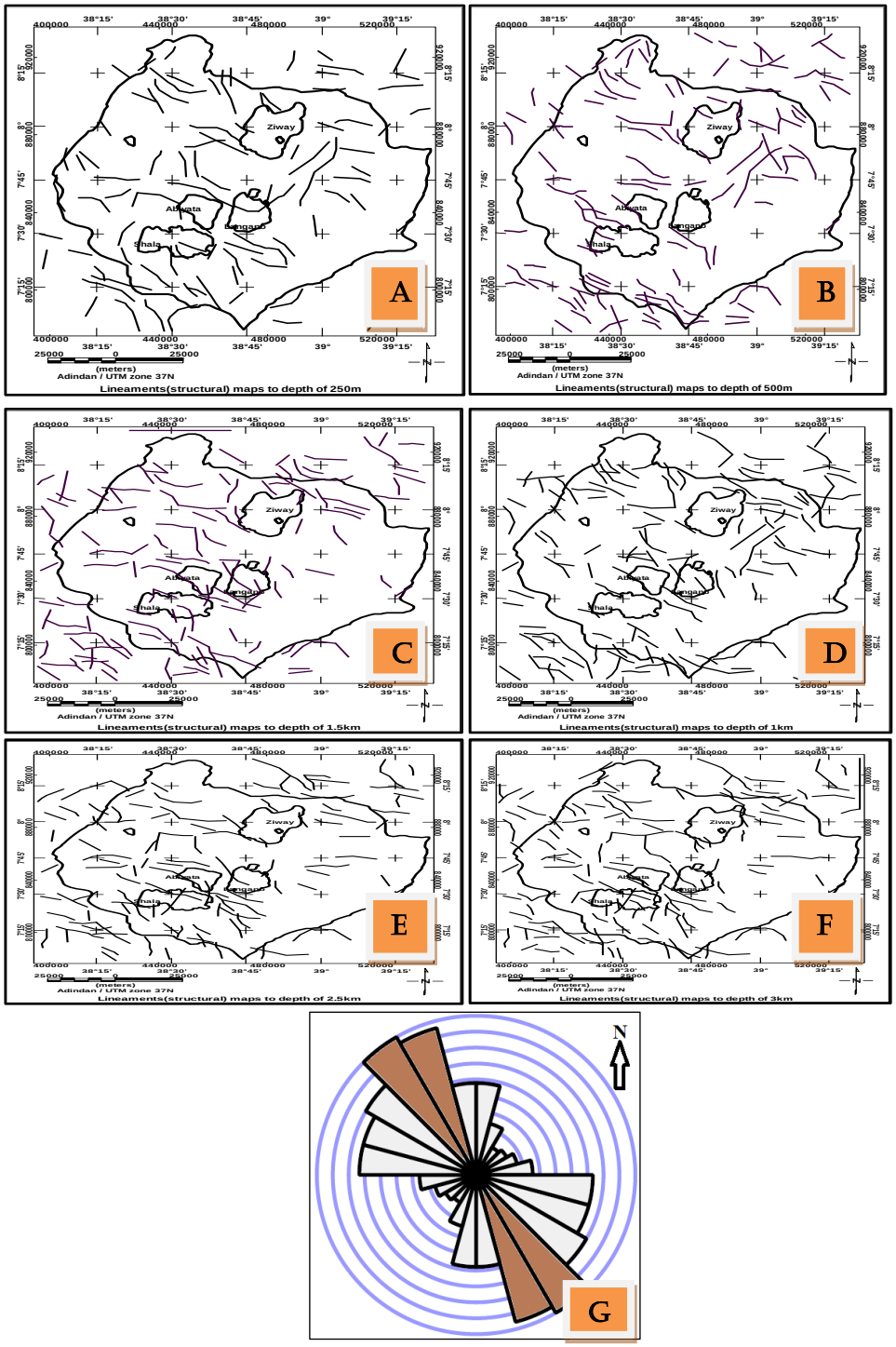

Fig. 5. 9 Lineaments maps extracted from the residual gravity anomaly map to depths of 0.25km (a), depth of 0.50 km(b), to depth of 1.0 km (c), to depth of 1.5 km (d), to depth of 2.5 km (e) and to depth of 3.0 km (f) rose diagram plot showing orientations of the subsurface lineaments (g)

5.4.2 Surface Lineaments extracted from DEM

The topographic lineaments considered in this section are traced using the procedure and methods outlined in sections 5.3.1 and 5.3. 4.

5.4.2.1 Surface lineaments extracted using first and second vertical derivative

The application of first vertical derivative filter on DEM image map generates slope image map shown in Fig. 5.10 (a). This map reveals surface structures coinciding with the existing Cenozoic fault patterns observed in the study area (Agostini et al., 2011). The second order derivative filter was used for detection of lineaments (Wladis, 1999). This method has the effect of enhancing anomalies over anomalous sources. The topographic lineaments (Fig. 5.10(b)) mapped using this method also shows the dip directions of the structure towards blue color contrast.

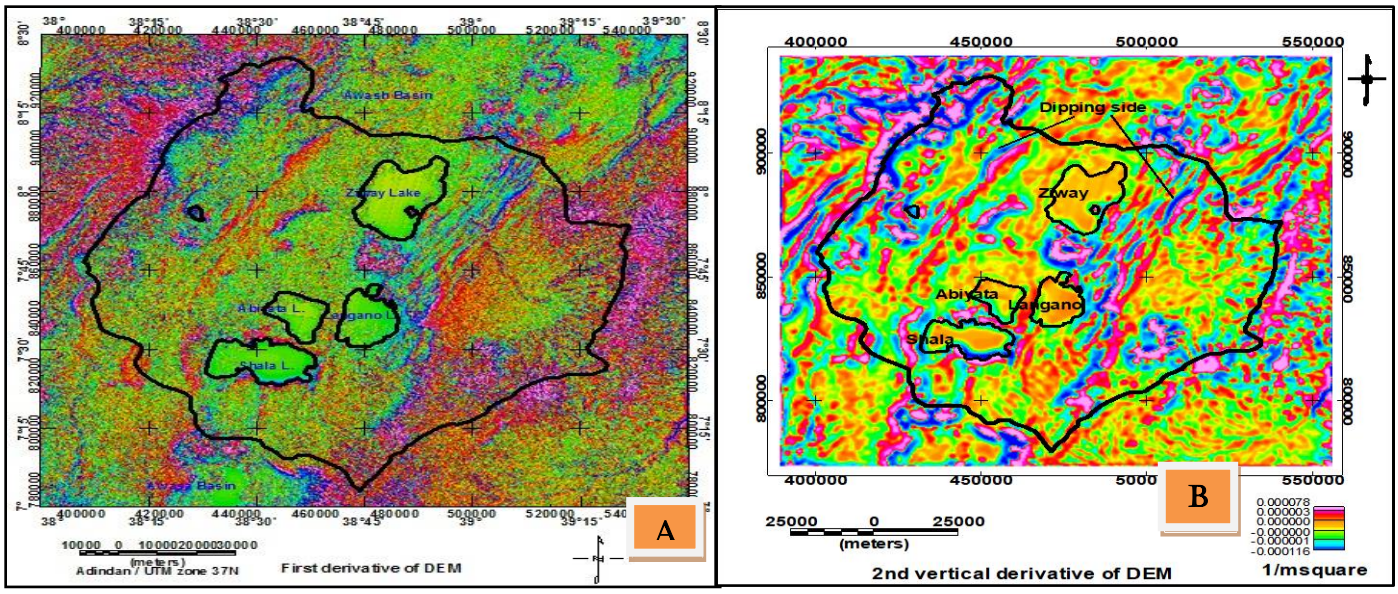

Fig. 5. 10 First vertical derivatives of topographic (DEM) data (a) Lineaments extracted from DEM using second order derivative with dip directions towards blue color contrast (b)

The lineaments extracted using derivative filters (Fig. 5.10) from DEM give clearer picture of shallow source anomalies with the linear features indicating geologic structures observed in the area. Furthermore, the linear topographic lows may be thought to indicate depressions.

5.4.2.2 Surface lineaments

Lineaments are automatically extracted using the Line module algorithm with enhanced slope image of DEM and the input parameters options as choice 1 and choice 2 indicated in Table 5.1 resulting in Figure 5.11(a) and Figure 5.11 (b). A lineament density map (Figure 5.11 (c)) is derived from the slope image lineament map (Figure 5.11 (a)) fed as an input to ArcGIS software.

With the default parameters (choice 0) (Table 5.1) in PCI Geomatica software few lineaments (faults) were mapped in the area. However, with a change of threshold edge gradient from 100 to 20 (choice 1) and all the others parameters kept constant, the algorithm generates the lineaments shown in Figure 5.11 (b).

Similarly, the result based on input parameters given in choice 2 produces lineaments shown in the Figure 5.11 (a). These structures are all similar in orientation and location to that of lineaments traced based on choice 1. However, they are more linear in shape and shorter in size. In this case all the curved structures are wiped-out with their linearity preserved. Generally, the two parameter options chosen mostly generate lineaments of the study area. However, there is a need to experiment on the selection of the input parameters for better extraction of lineaments in the study area. The lineation density map (Figure 5.11 (c)) and (Figure 5.12 (c)) shows more lineaments on the Eastern escarpment where the WFB is located as compared to those on the Western escarpment where Silti Debre Zeyete Fault Zone (SDFZ) is located including their

accompanying border faults. The extracted geological structure (lineaments) statistically analyzed (trend analyzed) and plotted in the form of rose diagrams (Figure 5.11(d)).

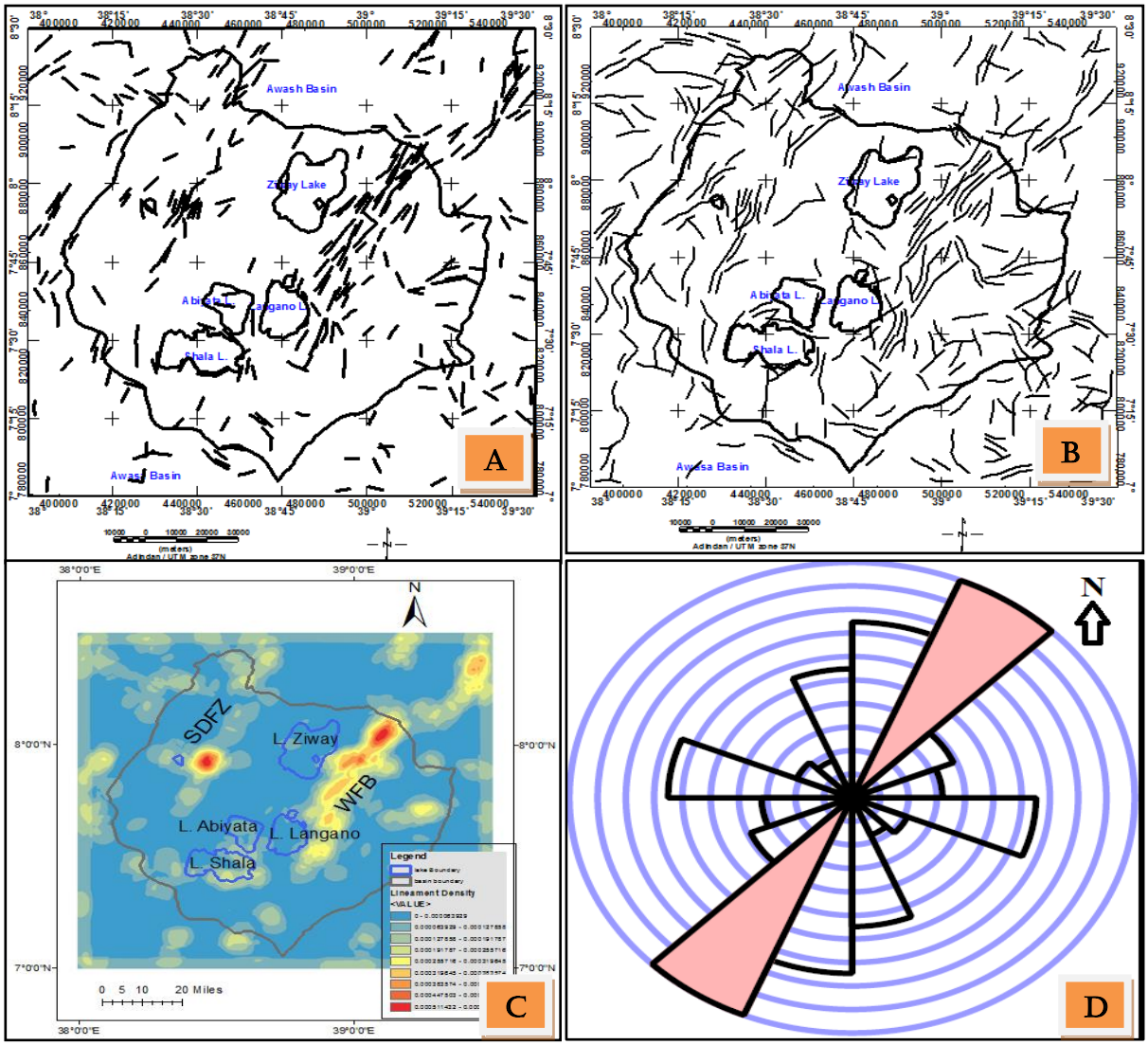

Fig. 5. 11 Automatically extracted lineaments with DEM slope gradient as an input to PCI Geomatica with parameters taken from choice 1 of Table 5.1 (a); choice 2 of Table 5.1 (b) and lineament density map of the study area (c) using lineaments shape file from lineaments in (a) as an input. Rose diagram showing the overall orientation (directional trend) of surface lineaments extracted from DEM (d)

The lineaments generated using a PCA enhanced DEM image (Figure 5.12(a)) input to the line module of Geomatica software is shown in Figure 5.12(b). The result shows that, the mapped structures agree with previously identified fault maps in location, orientation and density. However, in this work more lineaments were mapped. Higher densities of lineaments are observed at WFB and SDFZ and lower density of lineaments corresponding to the sedimentary units of the rift floor Figure 5.12(b).

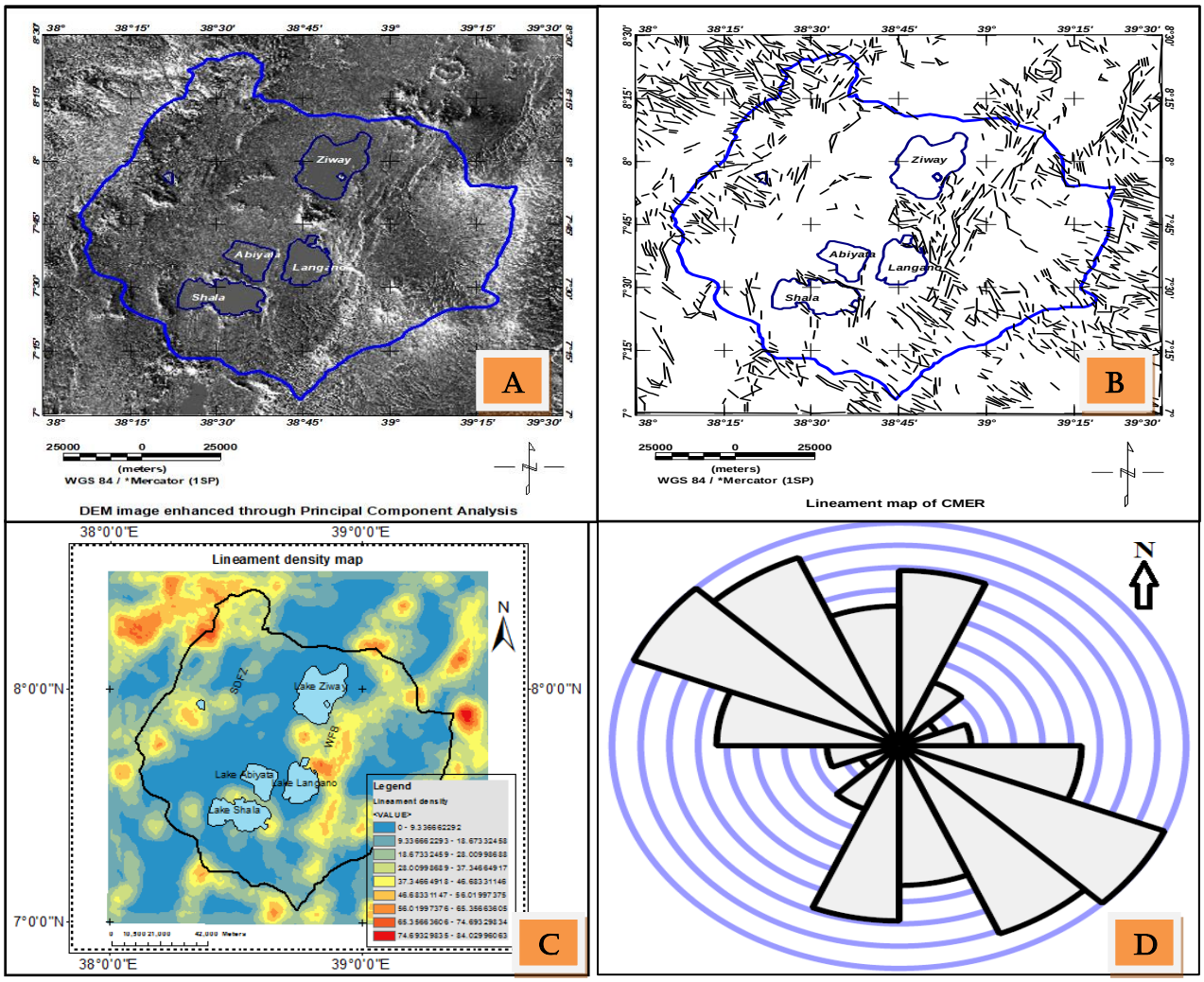

Fig. 5. 12 Enhanced DEM map using PCA (a) automatically extracted lineaments from PCA enhanced DEM (b) density map of the mapped lineaments (c) rose diagram showing dominant NW-SE trending lineaments (d)

In summary, the lineaments extracted with first derivative of DEM as an input to Line module PCI Geomatica (Figure 5.11(a)) mostly agree with fault map (Figure 5.3(b)) previously mapped in the area. Most of these lineaments oriented NNE-SSW as the summery made by line density rose diagram shows (Figure 5.11(d)). PCA enhanced DEM input to Line module algorithm of

PCI Geomatica (Figure 5.12(b)) equivalently map the structure with more new lineaments. In both lineament extraction procedures it is observe that too many lineaments than the true faults or tectonic features of the study area.

Most of the deep seated lineaments extracted from the gravity data oriented NNW-SSE to NW-SE (Figure 5.8 (g) and Figure 5.9(g)). Few of these lineaments traced using these data trends N-S and NE-SW. Majority of the traced lineaments from DEM image trends NNE-SSW to NE-SW and N-S (Figure 5.11(d)) direction which agree with few gravity lineaments in the study area (Figure 5.8 (g) and Figure 5.9(g)). This shows few surface lineaments continued down depth. Minor surface lineaments trending along NW-SE coincide with the orientation of most subsurface lineaments extracted using gravity data.

Most surface and subsurface lineaments out of the Cenozoic rifting in an Ethiopian plateau oriented in the direction of pre existing structural orientation (NW-SE) (Figure 5.12 (d)). This was also reveled by different researchers that the crust outside the rift axis in Ethiopian Plateau has not been modified significantly by Cenozoic rifting and magmatism (Dugda et al., 2005) (Gani et al., 2008).

5.4.3 Hydro-geological significance of the mapped lineaments

The Ziway–Shala lakes Basin is hydrologically closed (Le Turdu et al., 1999) (Chernet et al., 2001). Observation shows that there is no evidence of significant groundwater outflow from this basin (Legesse et al., 2004). Isotopic studies (Darling et al., 1996) and groundwater flow modeling (Ayenew, 2001) showed the ground water flow from southern Awassa basin towards the low-lying and deep Ziway-Shala lakes basin. These should increase the water resource in the basin. However, the water in the basin is declining from time to time.

Using hydrological data taken from (Ayenew, 2002), the computation of the water balance of Ziway-Shala lakes basin was conducted and showed positive value. These lead the conclusion

that there should be a structural unit that conducts groundwater outflow from this basin and among the inter-basins in the region. Therefore, the subsurface structures mapped at different depth levels in this study and those lineaments crossing the water divide believed to govern the groundwater outflow from Ziway-Shala lakes basin.

The other variable that describes the hydro-geology of the Ziway-Shala lakes basin is total dissolved solute (TDS) of the Lakes in MER which depends on inflow and outflow conditions (Gizaw, 1996). The TDS of different lakes in the rift valley compiled form (Ayenew, 2005) (Gizaw, 1996) is shows in Table 5.2.

S.N	Lakes Name	TDS(mg/l)	Source
1	Abiyata	13,480	(Ayenew, 2005)
2	Langano	3,175	(Gizaw, 1996)
3	Shala	7,262	(Gizaw, 1996)
4	Ziway	579	(Gizaw, 1996)
5	Afdera	145,129	(Ayenew, 2005)
6	Lakes in Dallol	274,467	(Gizaw, 1996)

Table 5. 2 TDS of some lakes in Ethiopian rift valley

The salinity level of lakes in Ziway-Shala lakes basin such as Abiyata , Langano, Shala and Ziway shown in Table 2 remains relatively low and stable as compared to others closed rift valley lakes such as Lake Afdera and Lakes in Dallol (Table 5.2). The low salinity observed among lakes in the basin indicates the existence of groundwater dynamics within and among the inter-basin which thought to be controlled by the mapped lineaments.

5.5 Conclusion

One way of studying the geological structure of an area is through studying linear features (lineaments) which could be extracted from gridded data anomalies. In this paper gravity and DEM anomaly data are used to map the corresponding gravity and topographic lineaments of the study area. The first and second vertical derivatives; tilt derivative, upward continuation, line module algorithms are used to automatically extract lineaments in the study area. Most subsurface lineaments extracted from gravity data oriented NNW-SSE to NW-SE directions which are against most surface structural orientation (NNE-SSW to NE-SW) mapped earlier by different researchers and extracted automatically based on DEM data considered in this research. The subsurface lineaments orientation might be due to the pre-existing subsurface structures crossing the rift orthogonally while surface structures might be due to Cenozoic rifting activities. A higher surface lineament density is observed in the eastern parts of the study area than the western side. Outside of rift most of the surface lineaments are oriented NW-SE which coincides with gravity data extracted pre-existing structures that strike the MER orthogonally. It can be concluded from the result that the integration of extracted topographic lineaments (surface structures) with potential field lineaments (subsurface structures) will add some information on the enhancements of the previously extracted structural map of the area. Furthermore, the mapped lineaments believed to govern groundwater dynamics among the inter-basins in the region under study.

Having extracted gravity lineaments at different depth levels, the magnetic anomalies are analyzed in the next chapter to extract magnetic anomaly patterns and magnetic lineaments which believed to show the geology and geologic structures of the area.

Chapter 6 Magnetic anomaly patterns and volcano-tectonic features related to geothermal activities

6.1 Introduction

The reasons for the ever-growing need in consumption of energy worldwide are due to the increase in world population, industrialization and improvement in the standard of living (Gupta & Roy, 2007). Development strategy of countries worldwide are thus depends on the availability of the energy sources (Teklemariam & Kebede, 2010) which could include hydropower, geothermal, solar, wind, petroleum and coal energy. Ethiopia as a country has locational advantages where all these resources exist in plenty. These resources are either partly exploited or being under studies. Utilization of such natural resources generally requires understanding of the geology and geologic structures. Volcanisms, tectonism and sedimentation processes are responsible for such structures (Woldegabriel et al., 2000). Extensional tectonic activities in EARS divide the Horn region in to two (Paola, 1972) and the dividing region in Ethiopia is called the Main Ethiopian Rift (MER). Associated with this tectonics, the region is volcanically active and is characterized by a number of volcanoes which could be the main source of geothermal energy. For example, the Aluto-Langano geothermal field has been established by drilling an eight exploration wells having depths ranging from 1300 m to 2500 m (Cherkose & Mizunaga, 2018) and a temperature ranging from ∼100 ◦C to ∼350 ◦C. The heat sources used for the geothermal energy were investigated using local seismic study conducted at Aluto volcano and was found below 9 km deep (Wilks et al., 2017). However, using magetotelluric (MT) data Samrock et al., (2015) arrived at a conclusion that no indication of an active deep magmatic system under Aluto. Following, the conclusion reached by Samrock et al., (2015); Hübert et al. (2018) generate 2-D electrical resistivity model of the crust using profile magnetotelluric data. The model was constructed along a 110 km transect crossing the whole rift and passing over Aluto volcanic center. The model showed, the existence of conductor near the Silti Debre Zeyt Fault Zone (SDFZ) (Fig. 6.1) approximately 40 km to the northwest of Aluto volcanic center (Hübert et al., 2018). It can be deduced from these observations that, there should be geology and geologic structures that is suitable for heat conduction between the claimed source location found nearby SDFZ and Aluto-langano geothermal field.

Many rocks exhibit magnetic properties which are induced by the geomagnetic field or a remnant magnetization or a combination of both (Weiler, 2007). These rocks magnetic properties result in magnetic data collected on the surface to show diverse magnetic anomaly patterns. The anomalies could show varied anomaly signatures (low, intermediate or high) depending on underlying rocks type as sedimentary, igneous and metamorphic. However, at all study locations simple interpretation of magnetic anomalies may not reflect the causative sources beneath. For example, the Ziway-Shala Lakes Basin (Fig. 6.1) is found at geomagnetic equator where magnetic data interpretation and information extraction found to be difficult. At low geomagnetic latitude, the inducing field direction is horizontal and smaller in strength which complicates interpretation of the magnetic anomaly data (Hansen & Pawlowski, 1989). The magnetic data collected in this area doesn't reflect the causative source bodies beneath. One solution to these problem is to make use of mathematical filtering and pole reduction algorithms (Nabighian,1972; Hansen & Pawlowski, 1989; Li & Oldenburg, 2001; Cooper & Cowan, 2005; Arkani-hamed, 2007, Ellis et al., 2012; Aisengart, 2013) which will help to get rid of the problems encountered and make geophysical magnetic methods usable and interpretable in the area.

The environments in which the rocks are found also affect the magnetic anomalies signal intensity. For example, in a geothermal environment where temperatures is high, rocks-fluid interactions result in mineral transformations (alteration) (Tapia et al., 2016) and decreases rocks susceptibility values (Mariita, 2007). Analyses of magnetic data are therefore useful in mapping high-temperature hydrothermal/geothermal systems because hydrothermal processes can significantly alter and reduce the rock magnetic susceptibilities (Mariita, 2007) which intern signify low magnetic anomalies. The analyses include data processing, correction/reduction, gridding, pole reduction with low latitude problems into consideration (Cooper & Cowan, 2005) and the other filtering techniques (Werner, 1953; Spector & Grant, 1970;Verduzco et al., 2004; Mammo, 2012; H. Kebede et al., 2020).

The objective of this study is thus to map magnetic anomaly patterns and structural features related to geothermal activities in low latitude area of the Ziway-Shala Lakes Basin. This is performed through analysis and interpretation of differentially pole reduced total magnetic field anomaly map.

6.2 The Study Area Location, Geologic and Structural Settings

The Ziway-Shala Lakes Basin is found in Central Main Ethiopian Rift (CMER) Latitudes $7^0$00'N-$8^0$30'N and Longitudes $38^0$00'E-$39^0$30'E. It is surrounded by two adjacent basins and two adjacent plateaus (Fig. 1). Hawasa Basin is found south of the Ziway-Shala Lakes Basin, in Southern Main Ethiopian Rift (SMER) and Awash River basin is found north of the Ziway-Shala Lakes Basin, in Northern Main Ethiopian Rift (NMER). The two adjacent plateaus are called North-West and South-East plateaus (Fig. 6.1). The Ziway-Shala Lakes Basin is bounded by alternating boundary faults that give rise to major fault escarpments separating the rift floor from the Ethiopian (NW) and Somalian plateaus (SE) (Fig. 6.1).

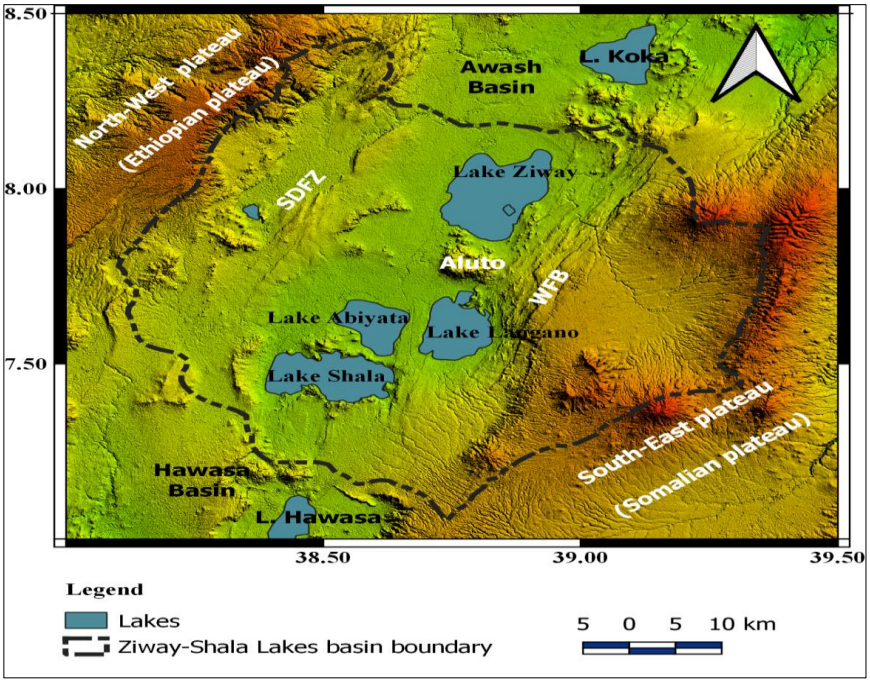

Fig. 6. 1 Location and Elevation (Physiographic) map of the Ziway-Shala Lakes basin and surroundings, CMER

The geological map (Fig. 6.2 (a)) constructed by EGS (Tefera et al., 1996) shows outcropped rock distributions which is considered surface geology of the region The region is known by active extensional tectonics and associated volcanic activities as well as sedimentation processes (Woldegabriel et al., 2000). The processes have generated complex geological structures (Fig. 6.2(a)), geology (Fig. 6.2(a)) and geomorphology (Fig. 6.1). A non-volcanic rocks (Lacustrine

sediments) (Paola, 1972), ignimbrites, basalt, tuff, pumice fall deposits, trachyitic and rhyolitic lava flows are the main rock types observed in the area (Fig. 6.2) (Tefera et al., 1996; Paola, 1972). The geological map is overlaid by structural (faults) map and is shown in (Fig. 6.2(a)). These Cenozoic surface structures are orientated NNE-SSW to NE -SW, N-S and NW-SE (Molin & Corti, 2015; Agostini et al., 2011) (Fig. 6.2 (a)).

The normal faults shown in Fig. 6.2(a) trends parallel to the rift axis and separates the NW and SE plateaus. These fault system are called Wonji Fault Belt (WFB) (Mohor, 1962) and Silti Debre Zyte Fault Zone (SDFZ) and their associated boarder faults (Fig. 2 (a)).

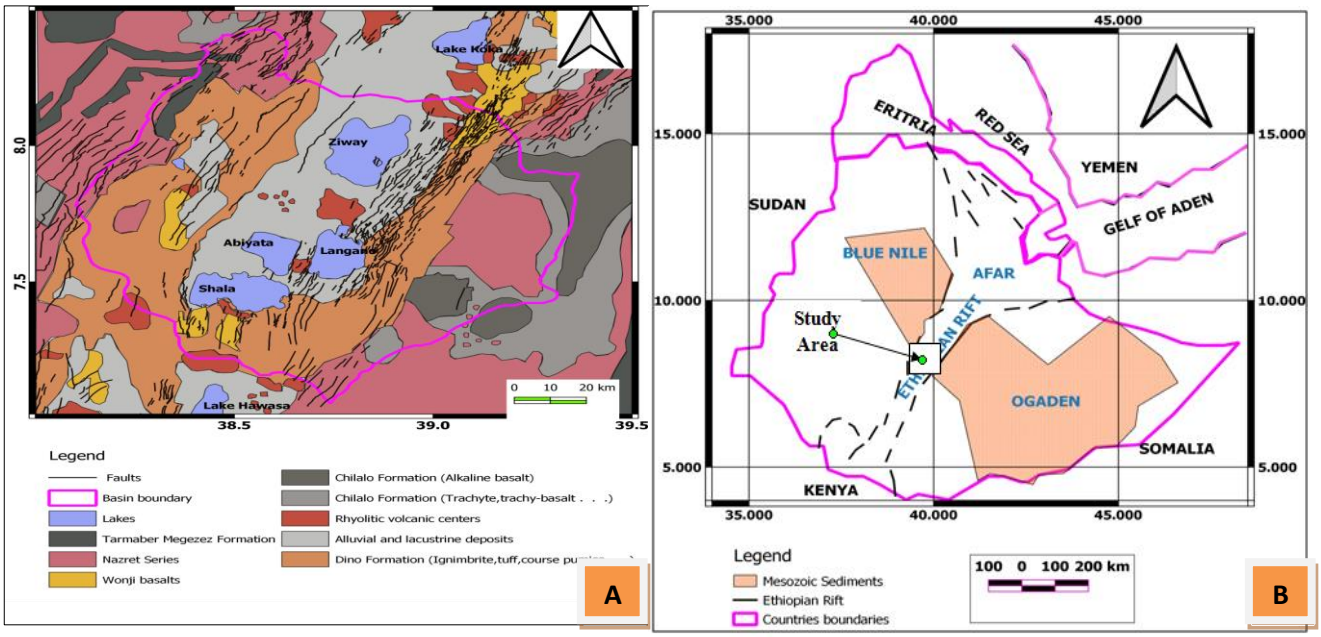

Fig. 6. 2 Geological map modified from Tefera et al.(1996) and structural map modified from Agostini et al. (2011) and Molin and Corti (2015) (a) Map showing the pre-existing Mesozoic structures crossing the Cenozoic Main Ethiopian rift perpendicularly (modified after Mammo, 2010) (b)

The previous studies (Korme et al., 2004) also show, the subsurface pre-existing Mesozoic structures which crosses the Cenozoic structures perpendicularly (Fig. 6.2b) and trends NNW – SSE to NW-SE (Fig. 6.2b) (B. Abebe et al., 2007; Korme et al., 2004). These subsurface structures were identified through an analysis of gravity data (Korme et al., 2004).

Voluminous mafic and silicic volcanisms characterize the Cenozoic geological history (Ayenew, 2001) in the area. Several shield volcanoes were developed on the plateaus (Woldegabriel et al.,

1990) and various volcanic episodes formed thick volcanic rock sequences (Ayenew, 2001). Though the MER is known by number of volcanoes, within the Ziway-Shala Lakes Basin depression only Aluto volcanic center is active and currently productive geothermal resources. Volcanisms, tectonism, sedimentation processes and reactivated pre-existing structures in the region formed the current complex geology and geological structures (Fig. 6.2(a)). These resulted in geophysical data collected in the region to show varied anomaly signatures (e.g. Fig. 6.6).

Seismic studies in Aluto-Langano geothermal indicated that the upper 2 km is interpreted in terms of hydrothermal system (Wilks et al., 2017). High seismicity and high b-values was observed which indicate a high fluid saturation and circulation. This fluid circulation is governed by subsurface geologic structures observed in an area (Saibi et al., 2012).

6.3 The Mathematical Filtering Methods used

6.3.1 Reduction to Pole

Reduction to pole (RTP) is a filter where gridded observed magnetic anomalies are input to the operator to change asymmetric anomalies to a symmetric form (Cooper & Cowan, 2005). The operator is expressed in frequency domain given as (Eq. 6.1)

$$\boldsymbol{A'}(u,v) = \frac{A(u,v)}{(\boldsymbol{sin\theta + i\ cos\ \theta\ sin}(\emptyset+\boldsymbol{\alpha}))^2.} \tag{6.1}$$

Where, $A(u,v)$ is the amplitude at frequencies(u,v), θ and $\emptyset$ are the geomagnetic inclination and declination respectively and α is $\tan^{-1}(v/u)$

This is the standard operation which transforms magnetic anomaly caused by an arbitrary source into the anomaly that the same source would produce if it is located at the pole and magnetized by induction only. However, at low geomagnetic latitudes (with small inclination) where magnetic source bodies possess remnant magnetization, the operator (Eq. 6.1) amplifies the noise present in the data and produces unacceptable result (Fig. 6.3).

A new algorithm suggested by Cooper & Cowan, (2005) is a Taylor series expansion in space domain (Eq. 6.2) and is called Differential Reduction to Pole (DRTP). This method solves the problems encountered in standard reduction to pole (RTP) **(Fig. 6.3).** The mathematical expression that solves the problem of standard reduction in low latitude area as the algorithm given by Cooper & Cowan, (2005) (Eq. 6.2)

$$RTP_{var} = RTP_{mean} + \Delta inc \frac{\partial RTP}{\partial inc} + 0.5\,\Delta inc^2 \frac{\partial^2 RTP}{\partial inc^2} + \Delta dec \frac{\partial RTP}{\partial dec} + 0.5\,\Delta dec^2 \frac{\partial^2 RTP}{\partial dec^2} + \ldots (6.2)$$

Where,

$\boldsymbol{RTP_{mean}}$ is the dataset reduced to pole using the average field inclination and declination of the area

$\Delta \boldsymbol{inc}$ is the difference between the inclination at a given point and the average inclination

$\Delta \boldsymbol{dec}$ is the difference between the declination at a given point and the average declination

The accuracy required by the space domain Taylor series expansion (Eq. 6.2) is guaranteed by analysis of remainder term of the Taylor series expansion of n terms given by (Eq. 6.3a) and Eq.6.3b)

$$R_n = \frac{(x-x_0)^{n+1} f^{n+1} x^*}{(n+1)!} \quad (6.3a)$$

where x^* lies between x and x_0. In terms of the pole reduction problem this becomes

$$R_n = \frac{\Delta inc^{n+1}}{(n+1)!} RTP_{MEAN}^{n+1} \quad inc^* + \frac{\Delta dec^{n+1}}{(n+1)!} RTP_{MEAN}^{n+1} \quad dec^* \quad (6.3b)$$

Where, inc^* lies between 0 and Δinc, and dec^* lies between 0 and Δdec.

This algorithm is computationally simple as the derivative in the series is approximated by differencing and that might be the reason for the name Differential Reduction to Pole (DRTP). In this study, the calculation of pole reduction using this algorithm is made using Oasis Montaj Geosoft software version 8.4.

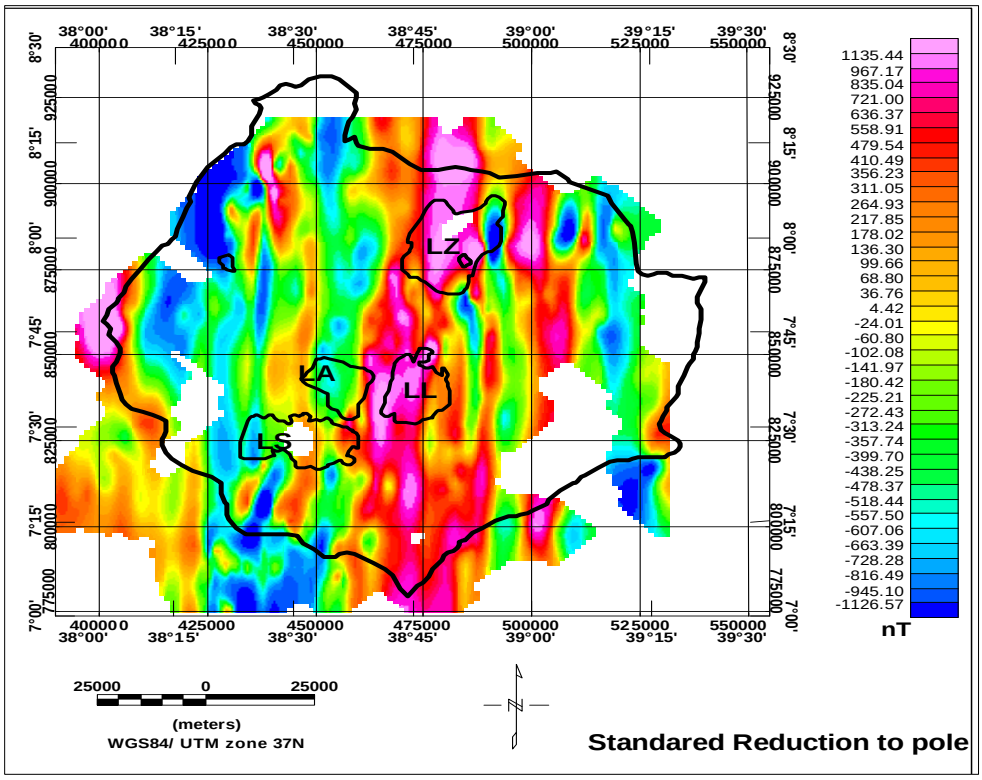

Fig. 6. 3 Reduced to pole magnetic map of the Ziway-Shala lakes basin. The lineation of the anomalies show the instability of the RTP operator at low magnetic latitudes

6.3.2 First vertical Derivative

The first vertical derivative of gridded total magnetic field anomaly ($F = f(x, y, z)$) is defined mathematically as (Eq. 6.4)

$$FVDR = -\frac{\partial f}{\partial z} \tag{6.4}$$

The filter helps to locate magnetic susceptibility boundaries (edges of anomalies) of shallow earth origin by accentuating high frequency signals and obscuring broader regional (low frequency). The derivative grid map is compared with differentially pole reduced residual anomalies of the area for shallow Earth interpretation.

6.3.3 Tilt Derivative

The tilt derivative (θ) of magnetic anomaly, **F**, is expressed as a ratio of its first vertical derivative to total horizontal derivative (Verduzco et al., 2004) (Eq. 6.5):

$$\theta = TDR = tan^{-1}\frac{\frac{\partial F}{\partial z}}{\sqrt{\left(\frac{\partial F}{\partial x}\right)^2+\left(\frac{\partial F}{\partial y}\right)^2}} \tag{6.5}$$

Where, $\frac{\partial F}{\partial x}, \frac{\partial F}{\partial y}$ and $\frac{\partial F}{\partial z}$ are the derivatives of the pole reduced magnetic anomaly, **F,** with respect to $x, y\ and\ z$ directions.

A mathematical property of arctan restricts the value of θ to lie between $-\frac{\pi}{2}$ and $-\frac{\pi}{2}$ or between-90^0 and 90^0.

This filter enhances and sharpens the anomalies with zero value contours (zero crossing) which indicate lithological /structural contacts. In this research, tilt derivative operator acted on differentially pole reduced residual magnetic anomaly grid to extract magnetic lineaments in the study region considered in this research work.

6.3.4. Upward Continuation

The derivative filters generally enhance effect of the shallower earth but not necessarily effect of the deeper earth. The regional anomaly resulting from the deeper earth is approximated using the upward continuation filter which is mathematically expressed by Gupta and Ramani (1980) and Jacobsen (1987) (Eq. 6.6) as:

$$H_{reg}(k) = S_0(k)\, e^{-2\pi k z_0} \tag{6.6}$$

Where $S_0(k)$ is Bouguer gravity anomaly anomaly, k is the wave number and $\boldsymbol{z_0}$ is the continuation height

The magnetic source signatures at different depth levels are isolated by upward continuing the observed differentially pole reduced magnetic field anomalies to a higher elevations. This is performed based on Jacobsen (1987) statement, stating when the potential field data are upward continued to a height $'z'$; it maps the sources found at and below the depth $'\frac{z}{2}'$.

6.4 Magnetic and Well-log Dataset

6.4.1 Magnetic Dataset

6.4.1.1 Total magnetic field Anomaly

A total of 855 ground based total magnetic field intensity data with their distribution shown in Fig. 4(a) were collected between the years 2014 and 2018 using Proton precession magnetometer. Out of 855 ground-based magnetic data collected 592 are secondary data (Kelemework, 2016; Berhane, 2015; B. Kebede, 2014) and 263 are primary data. These data sets were merged and a correction for main field was jointly made for the IGRF 2005 epoch. Finally, the reduced total magnetic field values are gridded to generate the total magnetic field anomaly map of the study area (Fig. 6.4 (b)). These anomalies reveal important information about crustal structures of a region (Gabriel et al., 2011).

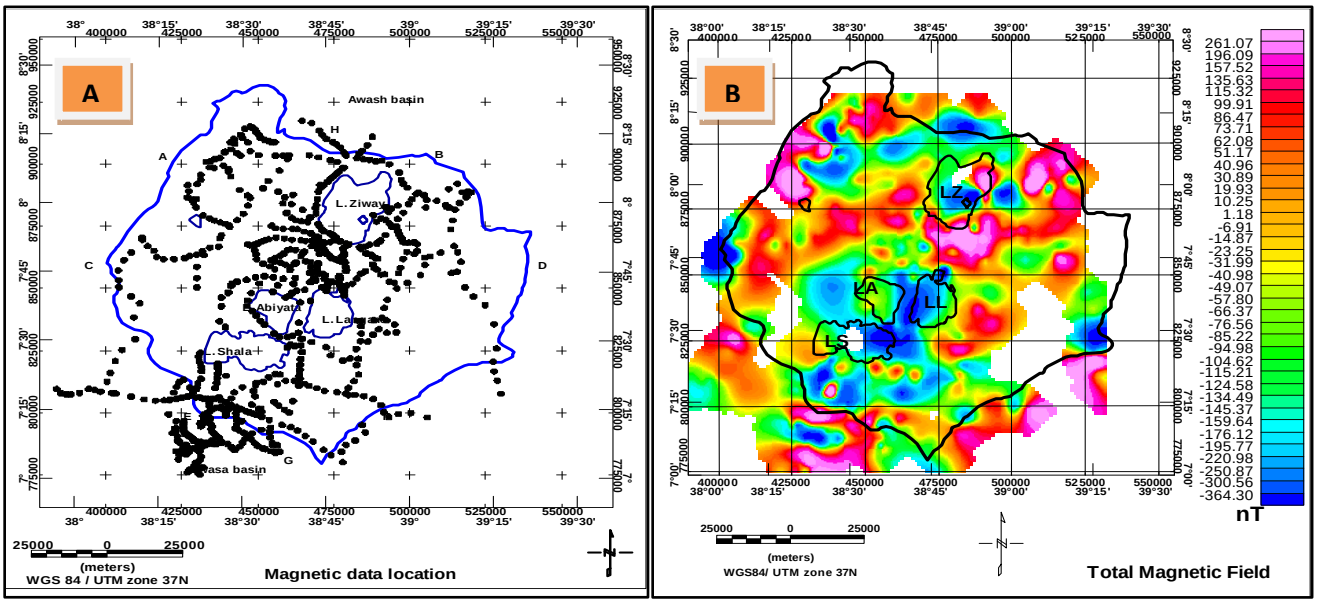

Fig. 6. 4 Magnetic data stations distribution map (a) Total field magnetic anomaly map of the Ziway-Shala Lakes basin (b)

6.4.1.2 Magnetic anomalies and Causative Geological Source Matching Through Reduction to Pole

The magnetic anomaly map (Fig. 6.4(b)) shows a color contrast reflecting the subsurface geology in the region considered. However, the highs and lows shown may not occur over the sources generating them. This could be due to the fact that the survey area is located at low magnetic latitude (Hansen & Pawlowski, 1989). These problems are solved through reduction to pole (RTP) filtering method. The standard RTP (SRTP) method can be used for latitudes 15-90 N and S. the region outside ±15° inclination. If used for regions lying within ± 15° latitudes (Silva, 1986), it would mislead the interpretation by amplifying the noise present in the data (Rajagopalan, 2003); (Cooper & Cowan, 2005). To solve the problem of low latitude effects several researchers used methods such as reduction to equator (RTE)(Yao et al., 2010), FFT filtering (Li & Oldenburg, 2001), Wiener filtering (Hansen & Pawlowski, 1989), analytic signal (Nabighian, 1972), differential reduction to pole (DRTP) (Arkani-hamed, 2007) and magnetic vector inversion (MVI) (Aisengart, 2013; Ellis et al., 2012) to substitute the standard RTP method. Though, each of the methods mentioned has a merit and demerit, each transformation technique has an advantage in magnetic data interpretation at low magnetic latitudes. For

example, RTE is a filter which helps to centre anomalous bodies over their exact positions (Fig. 6.5), where a positive magnetic susceptibility body will produce a negative magnetic anomaly (Fig. 6.5).

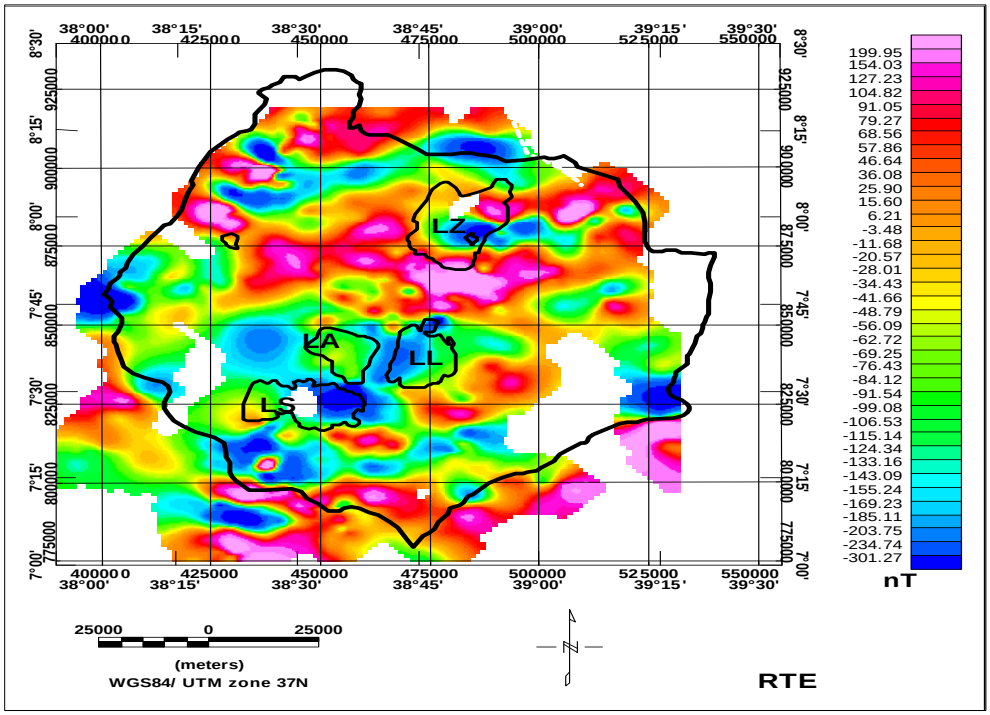

Fig. 6. 5 Reduction to equator as estimation to RTP

The action of standard RTP operator at this area produces noised anomalies (Fig. 6.3) and the result produced doesn't reflect underlying geology and is unacceptable. Therefore, in this paper differential reduction to pole (DRTP) operator is applied to the total magnetic field anomaly for generating anomalies which are related with the causative sources locations. In other words, DRTP method can be used to reliably relocate magnetic anomalies over their sources (Fig. 6.6).

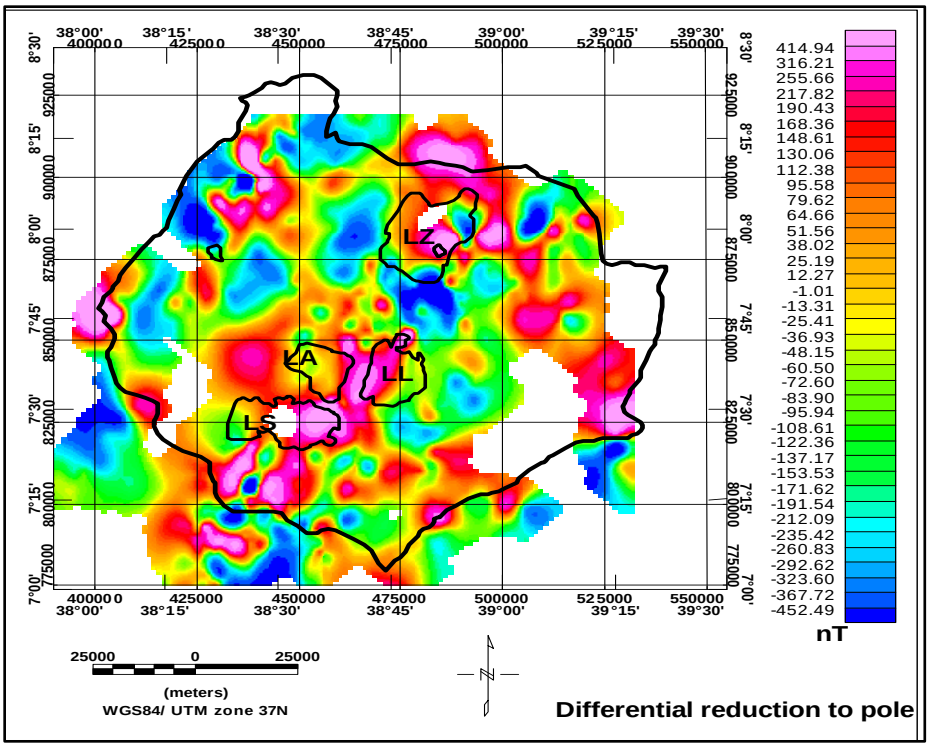

Fig. 6. 6 Total magnetic field anomaly reduced to magnetic pole using DRTP

6.4.1.3 Magnetic anomaly causative sources signifying deep and shallow subsurface geology

Differentially pole reduced total magnetic field (Fig. 6.6) anomalies can be separated in to regional (Fig. 9(a)) and residual (Fig. 9(b)) anomaly components to delineate the deep and shallow magnetic causative sources location respectively. The separation process is subjective and non-unique as there is no single best approach to approximate the low frequency signature (H. Kebede et al., 2020). Though there exist different methods (Keating et al., 2011;), (Mammo, 2010), (V. K. Gupta & Ramani, 1980)(Xu et al., 2009), the most frequently used upward continuation is used to estimate the regional anomaly of the region. Therefore, differentially pole reduced total magnetic anomaly is upward continued to different continuation heights of 250 m, 1000 m, 2000 m, 3000 m, 4000 m, 5000 m and 6000 m (Fig. 6.7) to filter out the regional magnetic field trend. As the continuation heights increases the shallow magnetic field signatures get attenuated and the regional magnetic field signatures get magnified. Visually it is observed that (Fig. 6.7) at upward continuation height of 6 km, most of the shallow signatures removed.

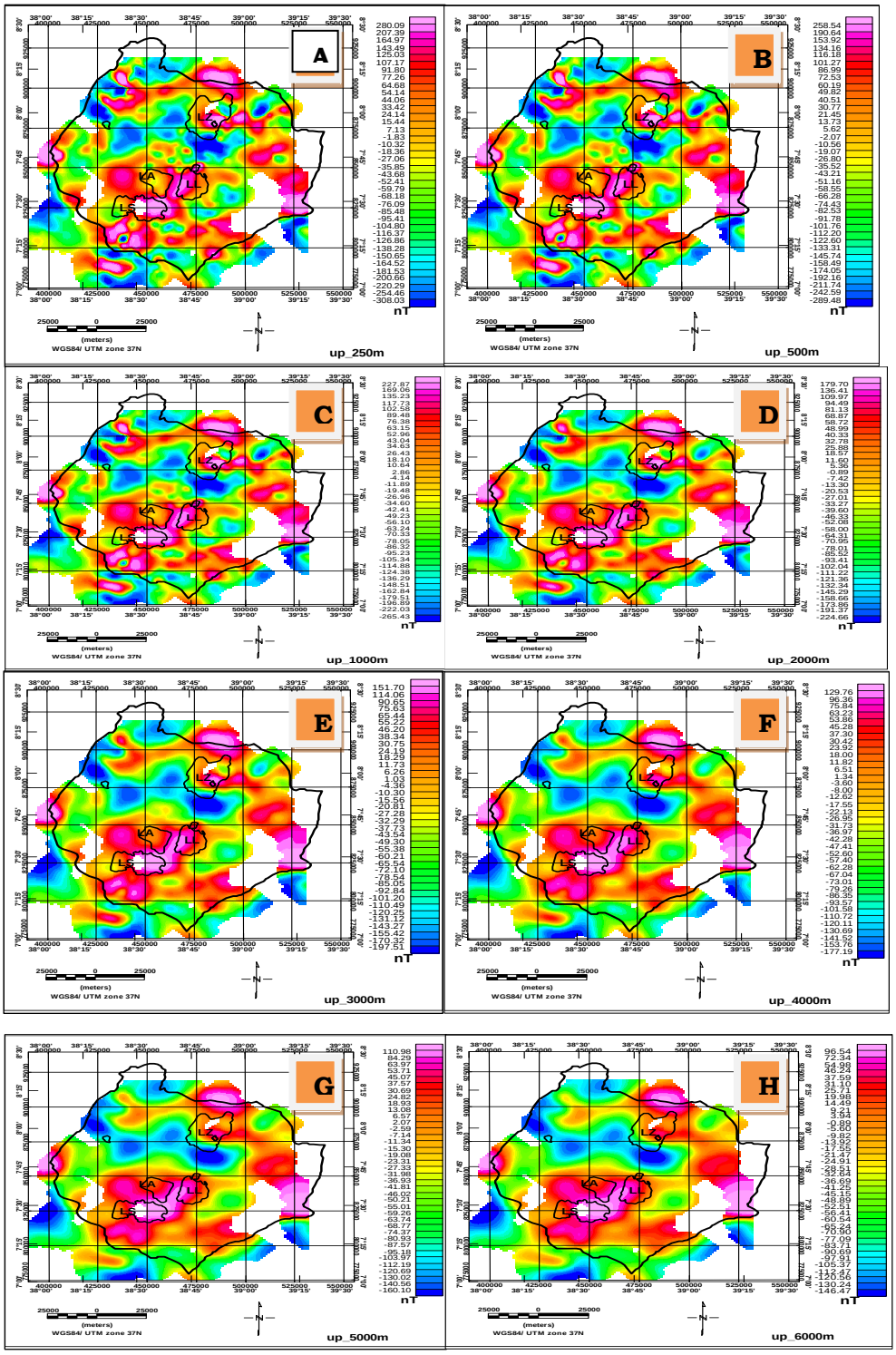

Fig. 6. 7 Differentially pole reduced total magnetic anomaly upward continued to height of 250 m (a) to height of 500 m (b) to height of 1.0 km (c) to height of 2 km (d) to height of 3 km (e) to height of 4 km (f) to height of 5 km (g) to height of 6 km (h)

This is also shown by extracted profile anomaly taken at $7^0$45’ (Fig. 6.8). As the continuation heights increases the estimated regional anomalies signatures get smoothened. Therefore, the continuation height of 6 km (Fig. 6.7 (h)) is chosen as an approximation to the regional magnetic anomaly of the region.

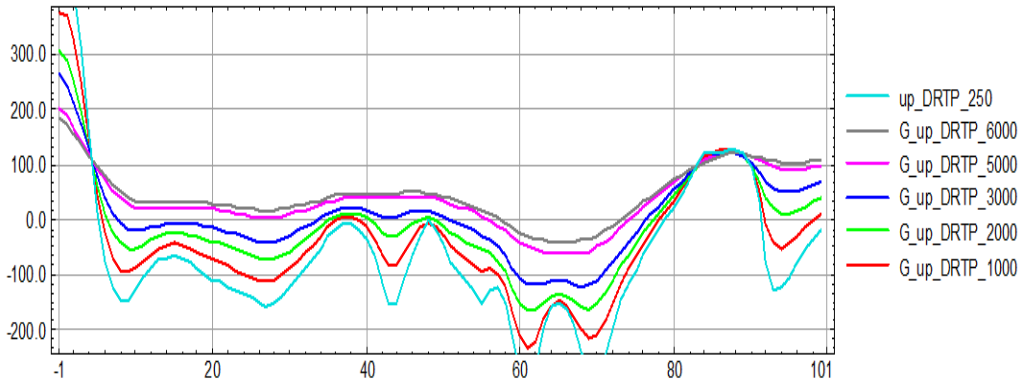

Fig. 6. 8 Profile magnetic anomaly at $7^0$45’ and at different upward continuation heights

It is observed that the continuation height (6 km) used in gravity data decomposition (Kebede et al., 2020) is adopted to equally apply here for estimation of the regional magnetic anomaly. The estimated regional magnetic anomaly is then subtracted from differentially pole reduced total magnetic anomaly to compile the residual magnetic anomaly map (Fig. 6.9(b)) of the study area.

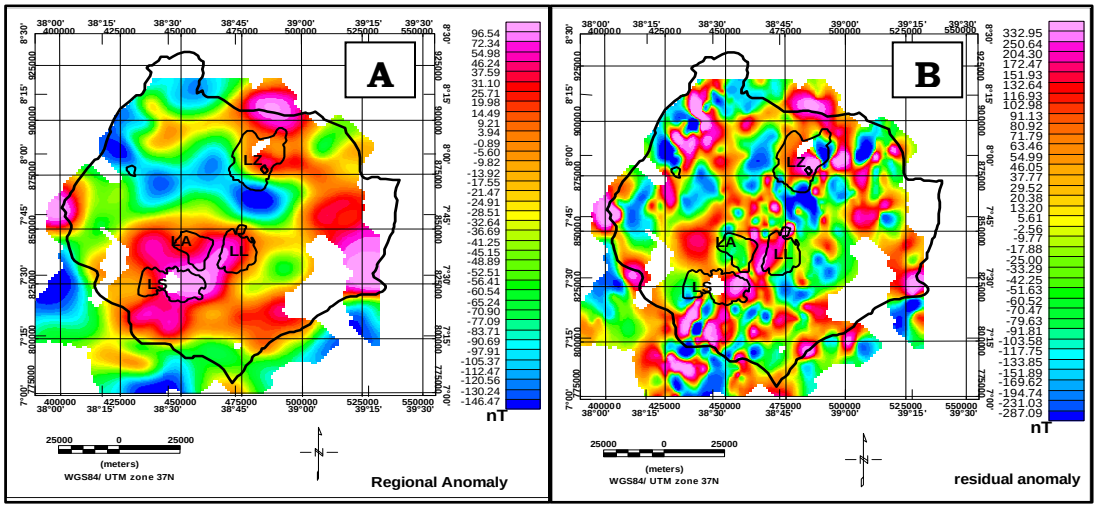

Fig. 6. 9 Regional magnetic anomaly map estimated using upward-continuation filter to height of 6 km (a) the residual magnetic anomaly map (b)

6.4.2 Geologic section constructed from well-log Data

The results obtained from magnetic data analysis and interpretations are validated by well-log data drilled in the Center of the Ziway-Shala Lakes Basin. The geologic section shown in Figure 6.10 was assembled from core-samples obtained from eight boreholes drilled for the purpose of studying the geothermal resources at Aluto-Langano geothermal field. This west-east extending section was constructed (Cherkose & Mizunaga, 2018; Wilks et al., 2017; Hutchison et al., 2016). The topmost layer is pyroclastic and lava flows, the second thin layer is lacustrine sediments which are used as clay cap over the hydrothermal system to seal the reservoir (Wilks et al., 2017), the third layer constituting Bofa basalt, tuff and berecia overlie the tertiary ignimbrite formation and the lowermost and oldest layer is Tertiary ignimbrite layer. This ignimbrite unit believed to hold geothermal reservoir (Wilks et al., 2017) in the area.

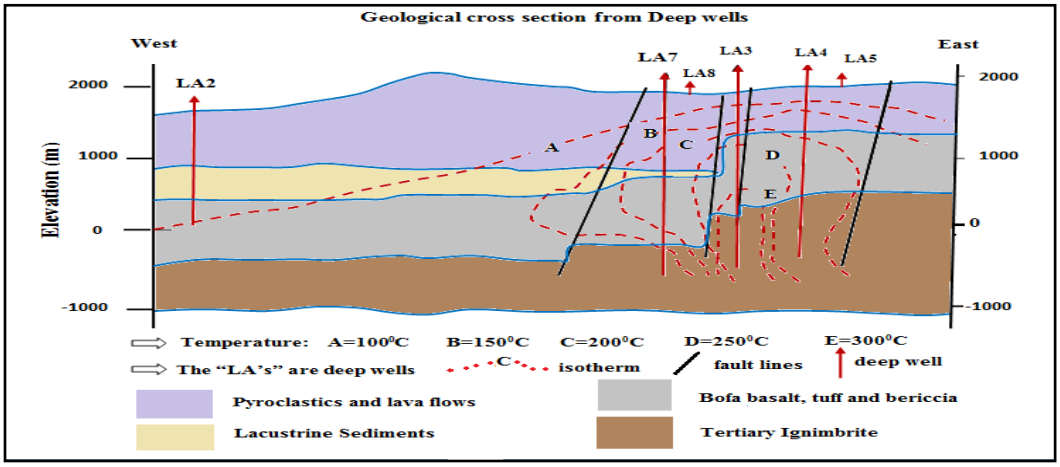

Fig. 6. 10 West-east geologic cross-section derived from core samples of the deep geothermal wells drilled in the Aluto-Langano geothermal field modified from Cherkose & Mizunaga, (2018)**.**

6.5 Results and Discussion

6.5.1 Geothermal Related Structural Features

The geology of the region is identified by a simple visual observation (or qualitative interpretation) of the magnetic anomaly maps (Figs. 6.9a, b). As the study area lies in a rift environment where tectonic, volcanic and sedimentation processes are active, the magnetic anomalies arising from these features are observed to show widely ranging anomaly patterns consisting of positive and negative anomaly signatures. These patterns can be observed on the differentially pole reduced total magnetic field map (Fig. 6.6), regional magnetic anomaly map (Fig. 6.9(a)) and residual magnetic anomaly map (Fig. 6.9b). Particularly, the residual magnetic anomaly map (Fig. 6.9b) shows that the WFB and SDFZ are marked by maximum magnetic anomalies ranging from 103 - 333 nT (Fig. 6.9b). On the other hand, the minimum residual magnetic anomalies mark silicic strata over which heat-flux in the form of surface hydrothermal activities are manifested. For example, the Aluto–Langano geothermal field is a well developed hydrothermal field associated with low magnetic anomaly patterns. The low magnetic anomaly observed on the total magnetic anomaly map over the Aluto geothermal field is seen to be extending down to a depth of 3 km. The magnetic anomaly lows beginning at Aluto and extending NW towards SDFZ and Western plateau border (Fig. 6.9a) is thought to link thermally altered geologic structures. The temperature at Aluto volcanic center is increasing downward (Fig. 6.10) to the bottom most ignimbrite layer suggesting that the source of the hot water is directly below the area being exploited. However, the existence of the source beneath Aluto was disproved by Samrock et al. (2015) and the source was identified some 40 km NW of Aluto near SDFZ (Hübert et al., 2018). According to Wilks et al., (2017) the bottom most ignimbrite layer is used as geothermal reservoir. This layer is one of the linking structures that connect the Aluto with SDFZ (where the source clamed to exist). This study estimated thermally altered structures at shallow depth of 1.5 km and extending down to depth of 3 km where the reservoirs believed to reside. The depths range are read from upward continuation of differentially pole reduced total magnetic anomalies to heights of 3km, 4km, 5km and 6km. Ignimbrite geologic unit constitutes one of the top layer reservoir identified in magnetic data analysis in this research. The low anomaly observed along the traverse from Aluto to SDFZ is thought to be the effect of a heat source tending to decrease the magnetic susceptibility (rock magnetization) of the rocks by

thermally altering susceptibility of magnetic minerals to have low values. A claimed heat source (magma) occurring near SDFZ was discovered by Hübert et al. (2018) using Magneto-telluric (MT) data. Our investigation result reveals the existence of a heat conduction path along the traverse from the Aluto-Langano geothermal field to the SDFZ which might prove the existence of the heat source discovered by Hübert et al. (2018).

6.5.2 Magnetic anomaly patterns reflecting shallow and deep sources

The study area is located in an equatorial region where the inducing magnetic field is low and direction of an inducing field is horizontal. These phenomenons make magnetic interpretation made in the region difficult. However, with mathematical filtering techniques mentioned in section 6.3.1, the low latitude problems get resolved with DRTP filter and the magnetic anomalies reflects the surface and subsurface geology of the region.

The rock magnetic properties of the shallow Earth, subsurface geologic structures and near-surface alteration in the study area cause the magnetic anomalies. Relationship between the near surface geology (Fig. 6.2(a)) and residual magnetic anomalies (Fig. 6.9 (b)) was made for better understanding of whether the anomalies pattern reflects the underlying surface geology or not. The first vertical derivative (Fig.6.11) filter of differentially pole reduced total magnetic anomalies is equally used to map the near surface geology (high frequency signature) of the area by suppressing the low frequency trend. Accordingly, the Silicic stratum at Aluto and Corbeti volcanic centers shows low magnetic anomalies signatures. The low magnetic anomalies are associated with heat effect in altering and reducing magnetic susceptibilities of rocks in the region considered. South of Shala Lake for example, magnetic minimum observed in between two maximum anomalies. The maximum are because of Wonji basaltic lava flows and the minimum is because of ignimbrite, tuff and course pumice rock origin. At plane of Butajira, the maximum are due to Wonji basaltic lava flows. Though the interpretation of the magnetic anomalies is made with respect to surface geology, the anomalies also reflect the subsurface geology of the area. For example, North of Ziway Lake shows maximum magnetic anomalies. The maximum are because of deep seated causative source (magnetic basement) than the shallow one. Similar interpretation is made for the remaining anomalies in the region considered.

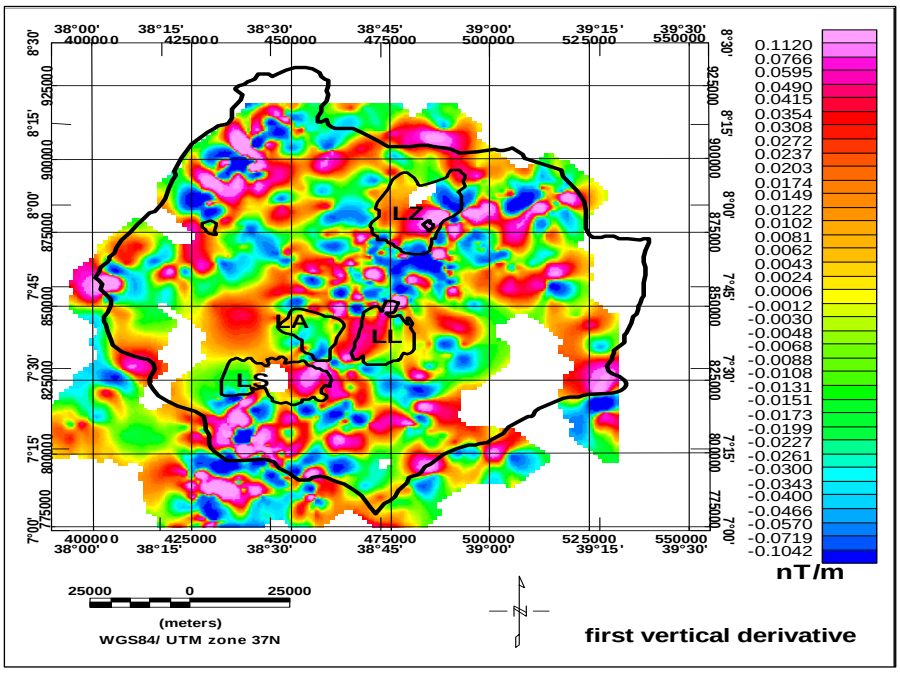

Fig. 6. 11 The first vertical derivative of the differentially pole reduced total magnetic anomaly showing the shallow magnetic sources

6.5.3 Magnetic Lineaments reflecting subsurface structures

Differentially pole reduced residual magnetic anomalies (Fig. 6.6) can be subjected to various filtering algorithms in order to extract the subsurface (magnetic) lineaments in the study area. The tilt derivative operator is applied to differentially pole reduced total magnetic anomaly to compile the tilt derivative magnetic map (Fig. 6.12(a)). The map shows a tilt derivative values ranging between -1.35 and +1.33 rad. The zero contours values of tilt derivative map indicate geologic structures (susceptibility contacts) that are seen as linear features commonly known as magnetic lineaments. The map shows subsurface structural features dominantly oriented NW-SE and NE-SW directions. Most of these linear features are not visible on the structural map of the area (Fig. 6.2(a)). Moreover, the lineaments reveled on the tilt derivative map (Fig. 6.12 (a) or Fig. 6.12 (b)) can be observed to generally coincide with structural orientation of the Mesozoic pre-existing Ogaden rift (Fig. 6.2b).

The tilt derivative filter applied to differentially pole reduced total magnetic anomaly (Fig. 6.12 (a)), magnetic lineaments extracted from differentially pole reduced total magnetic field (Fig. 6.12 (b)) and the structural trend analyses using line direction histogram show that the main subsurface structures oriented SSE-NNW to SE-NW direction (Fig. 6.12(c)). The structural orientation is nearly similar to that of thermal structural orientation which trends NW from Aluto volcanic center (Fig. 6.9 (a)).

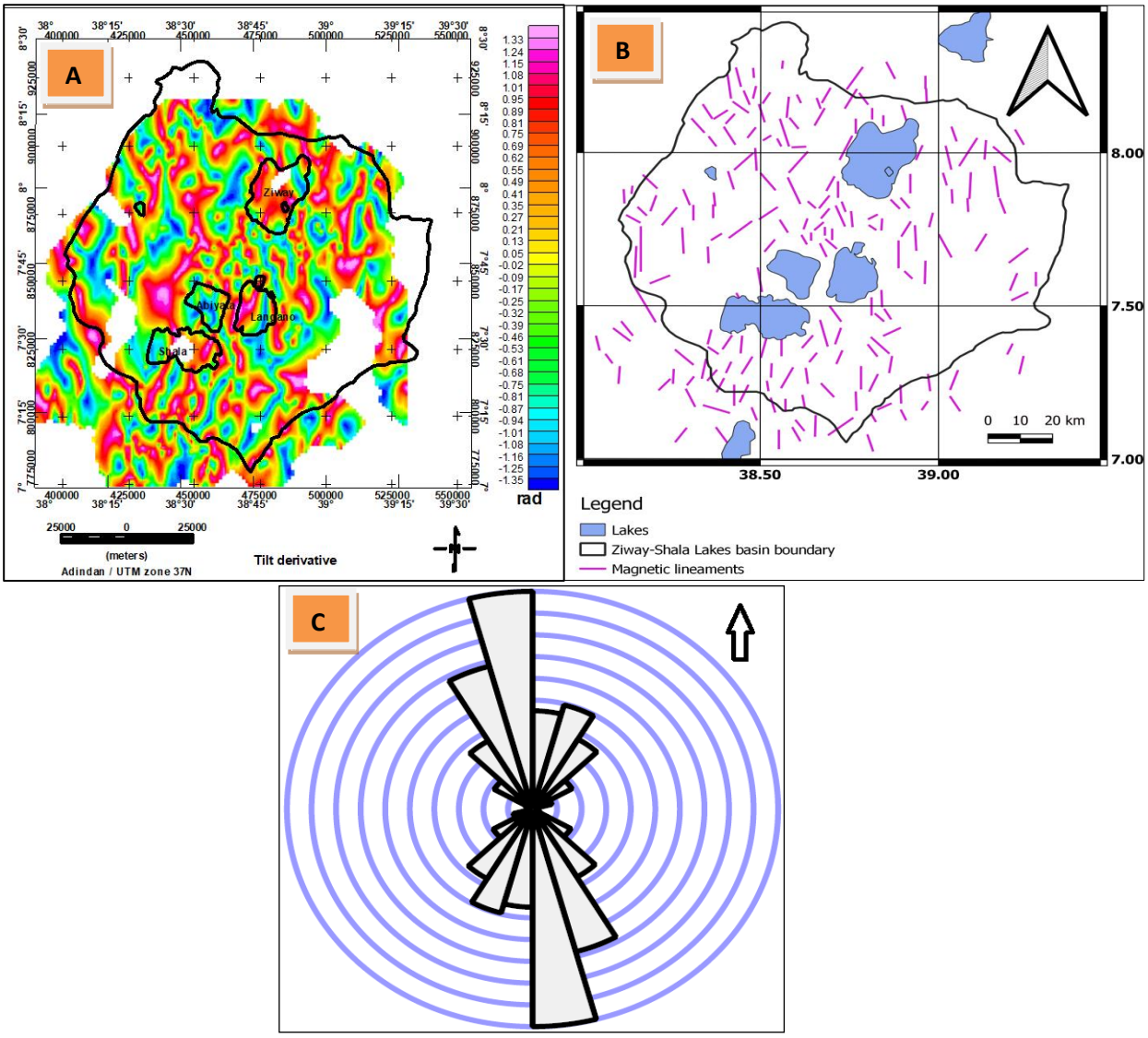

Fig. 6. 12 Tilt derivative map compiled from differentially pole reduced total magnetic anomaly (a) showing magnetic lineaments of the Ziway-Shala Lakes basin extracted with zero contour tilt derivatives (b) and rose diagram (c) constructed based on magnetic lineaments (b) as an input to Line direction histogram algorithm.

Generally, the rock units in Aluto-Langano geothermal system (Fig. 6.10) are important parameters in governing the resource exploration and exploitation activities in Aluto-Langano geothermal field. Equally, the identified structural lineaments (Fig. 6.12 (b)) are important factors in governing the resource exploration works in the area. The study then claim the geothermal reservoirs at Aluto-Langano geothermal field are closely associated with heat flow systems. The role such geological structure play in controlling fluid flow in geothermal systems is documented in different research work in different study area (Siler et al., 2019).

6.6 Conclusion and recommendation

In such areas where volcanic, tectonic and sedimentation processes are active the geology and geologic structures observed in the region is very complex and shows a varying magnetic anomalies. The pre-existing Mesozoic rift structures crossing the region perpendicularly also add further complexity. Such complexities result in different geophysical data to be analyzed differently. For example, the ambiguous results among researchers on the existence of heat sources beneath Aluto-Langano geothermal field. Though it contradicts with the previous research result, recent observations reveal the non existence of heat source (magma) beneath the Aluto-Langano geothermal field. Using MT data a heat source (magma) was identified in Western side of the rift near SDFZ. Our investigation reveals the existence of a heat conduction structural path that conduits heat sources along the traverse from the SDFZ to the Aluto-Langano geothermal field. The results might prove the most probable heat source location near SDFZ and which could be used as a heat source for Aluto-Langano geothermal field. This path is recognized by low magnetic anomalies resulted from temperature induced reduction in rock's magnetic mineral content (magnetic susceptibility). Finally, the conclusions made in this chapter are limited to the extent and distribution of magnetic data used. It is therefore, for better shallow Earth magnetic anomalies interpretation in the region it is recommended to consider a more refined and gridded magnetic data collection either airborne or ground based.

The gravity and magnetic lineaments mapped in the previous two chapters shows subsurface geologic contacts, fractures and faults. In the next chapter both gravity and magnetic anomalies are analyzed to map lithological geometries including undulations of crystalline basement along the rift axis.

Chapter 7: Depth estimates of anomalous subsurface sources using 2D/3D modeling of potential field data: Implications for groundwater dynamics

7.1 Introduction

The nature of heterogeneities of the solid Earth leads to uncertain location of its resources for exploration and exploitation activities to be performed. One way of studying these hidden resources is through charactering the geology and geologic structures of an area. Geophysical methods are determined to be the well-known and well-developed tools to study and delineate resources occurring beneath the Earth's surface. Geophysical methods further require the basic knowledge and skills of mathematics and computer algorithms which help to filter geophysical signals of shallow, intermediate and deep origin. Furthermore, extracting information about the subsurface requires an apriori independent knowledge about the geology and geological structures of an area. Potential field methods (gravity and magnetic) are important geophysical tools for mapping subsurface physical properties (density and magnetic susceptibility) distributions and geologic structures (Okiwelu et al., 2010; Grauch et al., 2006; Skilbrei, 1991). Subsurface deformational structures could be folds, faults, contacts, fractures, joints and subsurface relief. These structures could be mapped using gravity and magnetic anomalies through the application of different mathematical filtering techniques. The subsurface relief for example could be mapped by defining density/susceptibility interfaces (source-depths) using filters like upward continuation (Kebede et al., 2020), tilt depth (Chen et al., 2016; Salem et al., 2007), 3D Euler De-convolution (Mammo, 2010; P Keating & Pilkington, 2004) power spectral analysis (Mammo, 2012), 2D Werner deconvolution (Mammo, 2012), 2D forward modeling (Mickus et al., 2007), 3D structural inversion (Tiberi et al., 2005), genetic algorithm (Montesinos et al., 2016; Montesinos et al., 2005) and artificial neural network approach (Alimoradi et al., 2011). The above mentioned source depth estimations methods are some of the various methods and are chosen differently by different researchers implying that there is no single approach. It is therefore recommended to use more than one method for acceptable estimates of depths and density/susceptibility contrast interface geometries.

A prominent previous geophysical study conducted in study region along the rift axis includes the controlled-source seismic survey conducted by Ethiopia Afar Geo-scientific Lithospheric

Experiment (EAGLE) project (Maguire et al., 2006). It includes a 400 km long 2D velocity model along the axis of the Main Ethiopian rift (MER). The main findings of this study includes crustal and sub-Moho P-wave velocity model (Maguire et al., 2006). Though, the study focused on the deep structure, it also mapped the surface layer velocities along the rift axis with low resolution (Maguire et al., 2006). The low layer velocity recorded along this profile (Fig. 7.1a) approximately ranges from $2\,km/s$ to $5km/s$ (Fig. 7.1b). These low layer velocities as compared to layers below were interpreted by Maguire et al. (2006) as "sediment and volcanic".

From Fig. 7.1b), it appears that the low velocity (sediment–volcanic) layer (marked by dotted line) in the Ziway-Shala Lakes Basin tends to thicken northwards. However, compared to the depth of investigation ($>$ 50 km) and complexity of shallow subsurface structures (presence of several volcanic centers) the result is beyond the resolution of data (Maguire et al., 2006). In conjunction with the EAGLE seismic survey, 2.5 D gravity model were generated to map a preliminary crustal structure (Mickus et al., 2007). The maximum depth of investigation obtained based on these models is about 120 km (Mickus et al., 2007). We consider that these models have mapped the shallow structures of the MER with a low resolution.

This chapter is devoted to examine the shallow to intermediate litho-structural features of the study area using gravity and magnetic data through mapping source depth location and tracing the pattern of source depth undulations. To carry out this task, the standard quantitative techniques including power spectral analysis, 2D Werner deconvolution, source parameter imaging (SPI), joint 2D forward modeling and 3D gravity interface inversion were used.

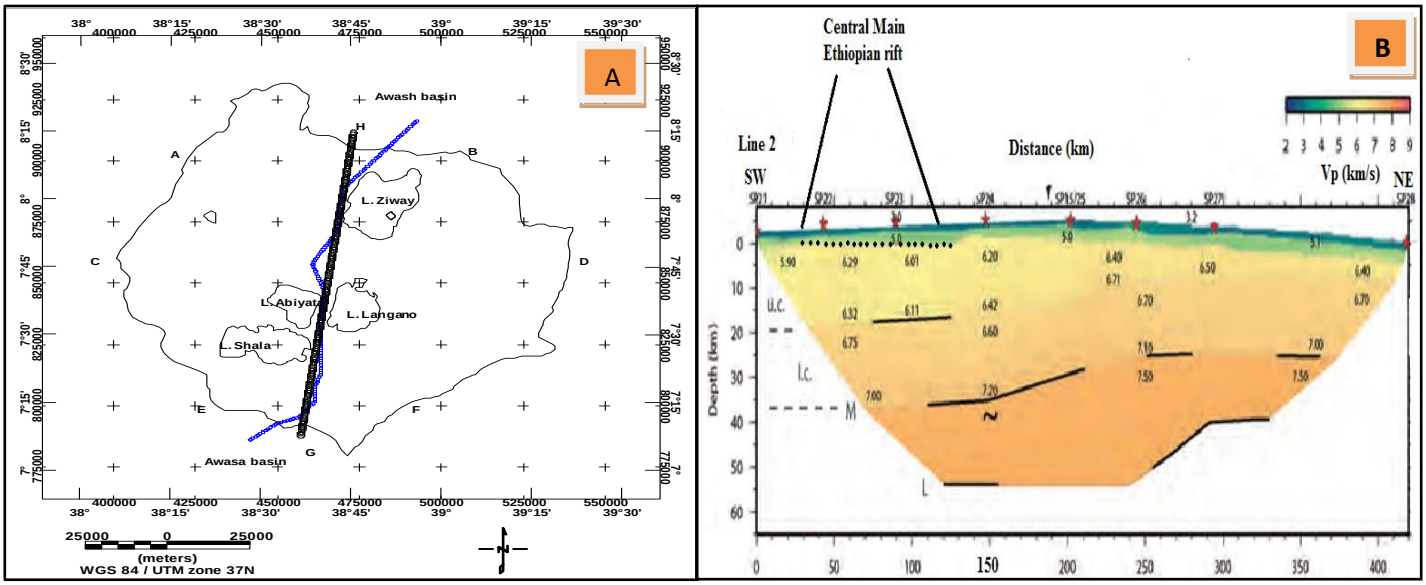

Fig.7. 1 Controlled-source survey line (blue color) conducted by Ethiopia Afar Geo-scientific Lithospheric Experiment (EAGLE) project (a) P-wave velocities in km/s along the rift axis (along the "blue color" profile line) adopted from Maguire et al.(2006) (b)

Summary of the overall activities performed in mapping the layers depths and density/susceptibility contrast interface undulations (topography) is described as a flowchart depicted in Figure 2. It starts by defining the geological problem to be solved; describes the physical principle/equations that govern the measurement of gravity and magnetic data; acquisition of gravity and magnetic data; acquired gravity and magnetic data reduction/correction procedures; gridding and interpolation of the corrected gravity/magnetic data; pole reduction of total magnetic field data with the consideration of low latitude problem; gravity/magnetic anomalies separation into regional and residual components; analyses of residual gravity/magnetic anomalies using automatic Inversion techniques, joint 2D gravity and magnetic modeling and 3D gravity structural inversions are made to estimate depth and geometries of the source interfaces.

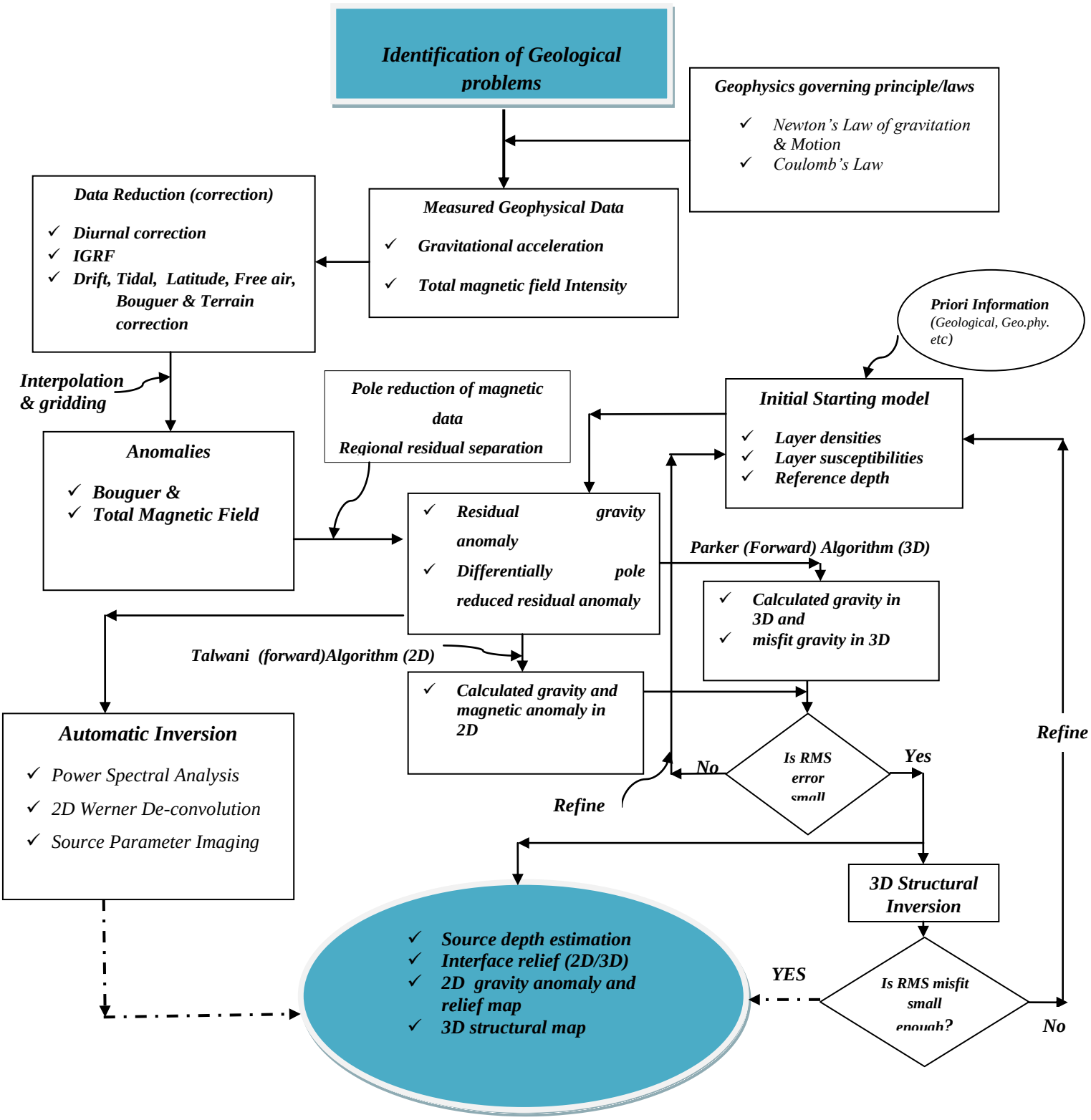

Fig.7. 2 Flow chart describing the overall modeling activities performed in determining depths and geometry of the density/susceptibility interfaces

7.1.1 Location of the Study Area

The Ziway-Shala Lakes Basin is found in the Main Ethiopian Rift (MER) being bounded by $38^0$00'E-$39^0$30'E and $7^0$00'N-$8^0$30'N (Fig. 7.3 (b)). The rift floor, the boarder faults escarpments and the uplifted plateaus characterize the physiographic features of the study area (Ayenew, 2005). The main lakes situating within the rift floor of the Ziway-Shala lakes basin are Ziway, Abiyata, Langano and Shala (Fig. 7.3(b)). These lakes are remnants of a large fresh-water lake that existed during the Early-Mid Holocene and the Late Pleistocene (Legesse et al., 2004). Except the Shala lake and its catchments the remaining three lakes are connected by a surface water network (Fig. 7.3(d)). Ketar River from eastern escarpments and Meki River from western escarpments are the two major rivers that discharge water to Lake Ziway (Fig. 7.3(d)). Lake Ziway delivers a majority of its surface water to Lake Abiyata through the Bulbula River (Fig. 7.3(d)). Five major rivers (Fig. 7.3(d)) supply their water to Lake Langano and significantly less water is discharged from this lake to Lake Abiyata. Lake Abiyata is the terminal lake (Ayenew, 2005) and has been undergoing significant lake level changes (Ayenew, 2002). Lake Shala gets its surface inflow from two main sources that enter from the southeastern and western rift escarpments (Le Turdu et al., 1999).

The Ziway-Shala Lakes Basin is bounded in the north and north-east by its adjacent Awash River basin, in the south and south-west by Hawasa basin, in NW by Ethiopian plateau and in SE by Somalian plateau. The total area of the basin is about 14,640 km^2 hydrologically closed (Le Turdu et al., 1999; Chernet et al., 2001) and the altitude varies from 1633 m to 3447 m above mean sea level as read from DEM map (Fig. 7.3(b)).

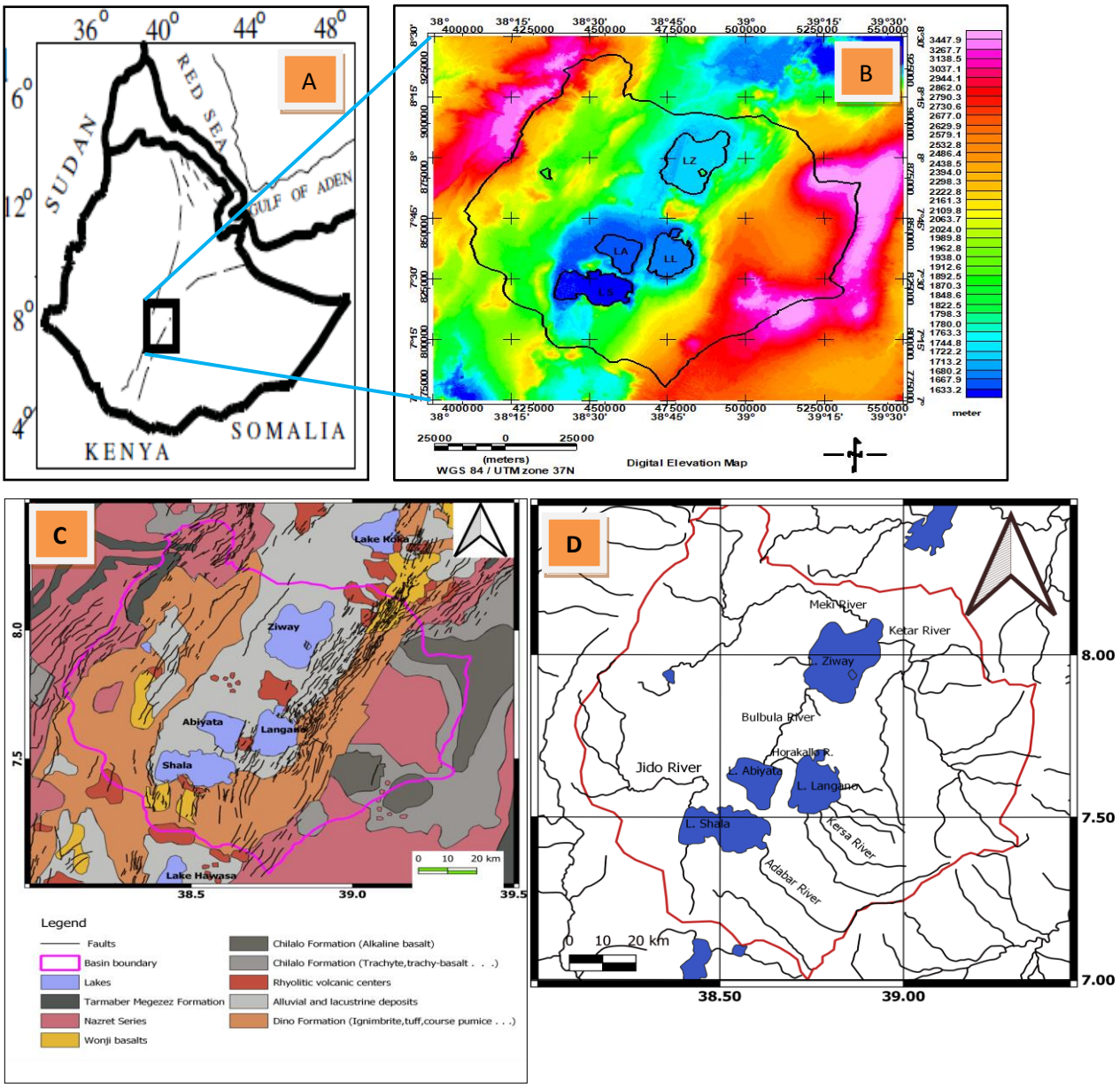

Fig.7. 3 Location of Ethiopia within the horn of Africa divided by the East African rift (adopted from Mammo, 2010) (a) Location and Elevation map of the Ziway-Shala lakes Basin and its surroundings (b) Geological map modified after Tefera et al.(1996) and structural map overlaid geological map modified after Agostini et al.(2011) and Molin and Corti (2015) (c) Hydrological network taken and modified from https://www.ethiogis-mapserver.org/ (d)

7.1.2 Geological and Structural settings

The geology and geologic structures (Fig. 7.3 (c)) underlying the basin have been determined to be due to volcanic, tectonic and sedimentation processes (Le Turdu et al., 1999). These processes are thought to result in structural depressions forming the Ziway-Shala Lakes Basin (bounded within pink color) (Fig. 7.3 (c)) which constitutes four major lakes, Ziway, Abiyata, Langano and Shalla lakes (Chernet et al., 2001; Le Turdu et al., 1999).

The surface structures generally have N-S to NNE-SSW, NE-SW, E-W and NW-SE (Korme et al., 2004) orientation and are collectively called Wonji Fault Belt (WFB) (Mohor, 1962), Silti Debre Zeyete Fault Zone (SDFZ) and corresponding boundary faults (Boccaletti et al., 1998). The WFB trending N-S to NNE-SSW is youngest and most active fault system cross-cut by the pre-existing NW-SE Mesozoic Ogaden rift fault (Korme et al., 2004).

7.2 Datasets and Methodology

7.2.1 Datasets

7. 2.1.1 Gravity Data

About 3013 ground based gravity data are obtained from the Geological Survey of Ethiopia and from PhD thesis work (Alemu, 1992). These data were reprocessed, homogenized to the IGSN71, reduced using the Geodetic Reference System 1967 (GRS67), corrected and gridded to generate the Bouguer gravity anomalymap of the study area (Fig. 7.4 (a)).

The Bouguer anomalies are the sum of the effect of shallow (high frequency) and deep (low frequency) causative sources which need to be separated into their respective components. The low frequency (regional) component is approximated by 6 km upward continuation of the Bouguer anomalies (Kebede et al., 2020) (Fig. 7.4 (b)) and the corresponding residual component (Fig. 7.4(c)) is calculated by subtracting the estimated regional (Fig. 7.4 (b)) from the gridded Bouguer anomalies map (Fig. 7.4(a)). The estimated residual anomalies are subjected to source depths estimation for the region under study.

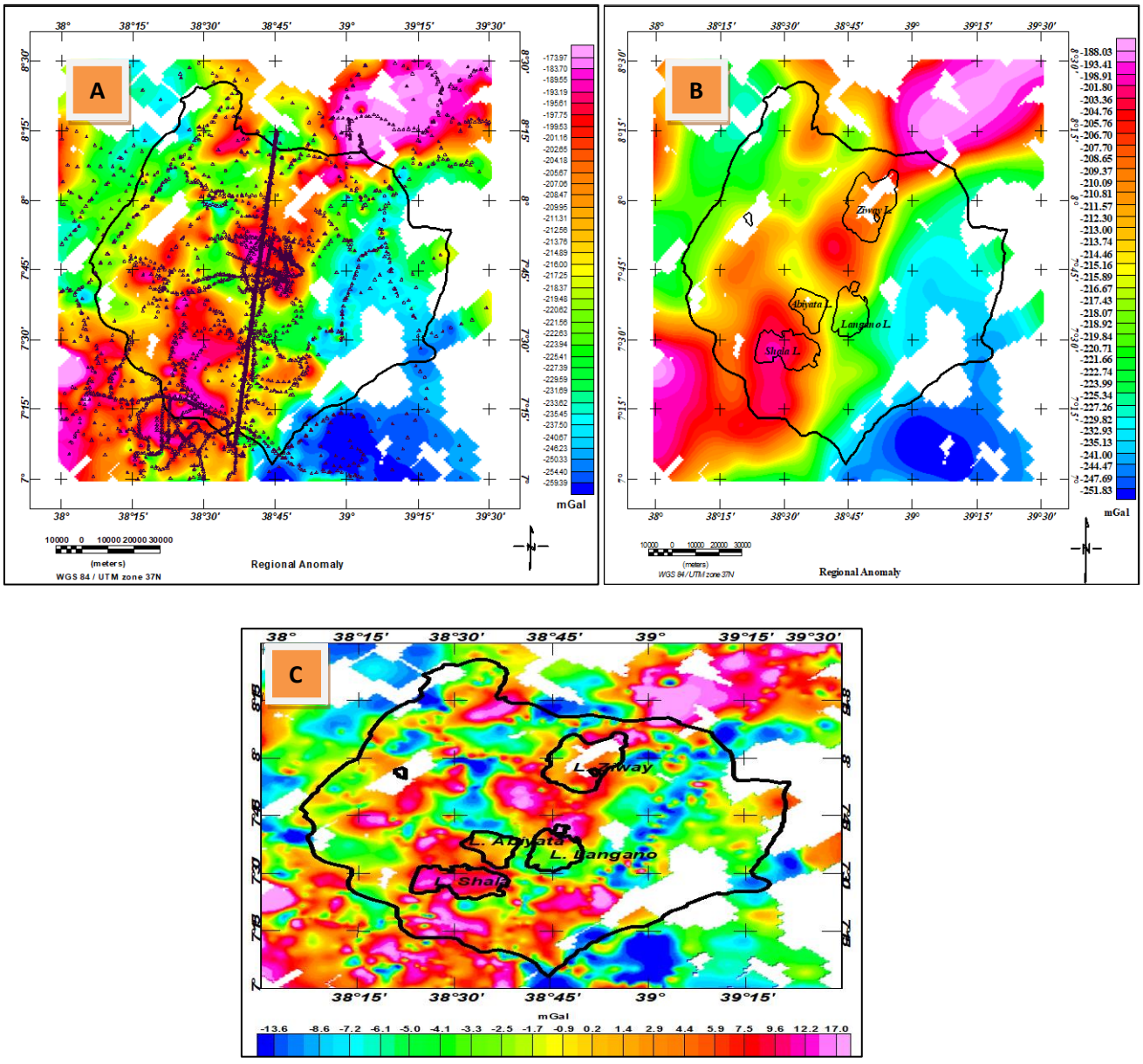

Fig.7. 4 Gravity station location distribution overlay Bouguer gravity anomaly of the central Main Ethiopian Rift and NNE-SSW extending profile line (a) 6km upward continued Bouguer gravity anomaly map which approximate the regional anomaly (b) and residual gravity anomaly map (c)

The residual anomalies map (Fig. 7.4 (c)) contains short, intermediate and long wavelength anomalies and it is this anomaly that is subjected to different filtering techniques and modeling.

7.2.1.2 Magnetic Data

About 263 total intensity primary magnetic field measurements are collected by the principal author using Proton Magentometer. These data are merged with about 592 secondary total intensity magnetic field data obtained from MSC thesis works of various researchers (Kelemework, 2016; Berhane, 2015; Kebede, 2014). The total of these (855) data are collected in years between 2014 and 2018 and the distribution of the data are shown in (Fig. 7.5(a)).

The standard magnetic data correction including correction for main field is made for the IGRF 2005 epoch. This data are gridded and mapped to generate total magnetic field anomaly map of the study area (Fig. 7.5 (b)).

The survey area is located at low magnetic latitude where the inducing field direction is horizontal and smaller in strength. These complicates interpretation of the magnetic anomaly data (Hansen & Pawlowski, 1989) and resulting in source and anomaly mismatched. This is solved using differential reduction to pole (DRTP) (V. K. Gupta & Ramani, 1980) operator acting on total magnetic anomaly. The differentially pole reduced total magnetic anomaly is shown in (Fig. 7.5 (c)).

The differentially pole reduced total magnetic anomaly need to be decomposed into regional and residual anomalies which are respectively related to deep and shallow subsurface geology. The regional anomaly is approximated using upward continuation of the pole reduced total magnetic anomaly to height 6 km (Fig. 7.5(d)). The final differentially pole reduced residual magnetic field is shown in Fig. 7.5(e).

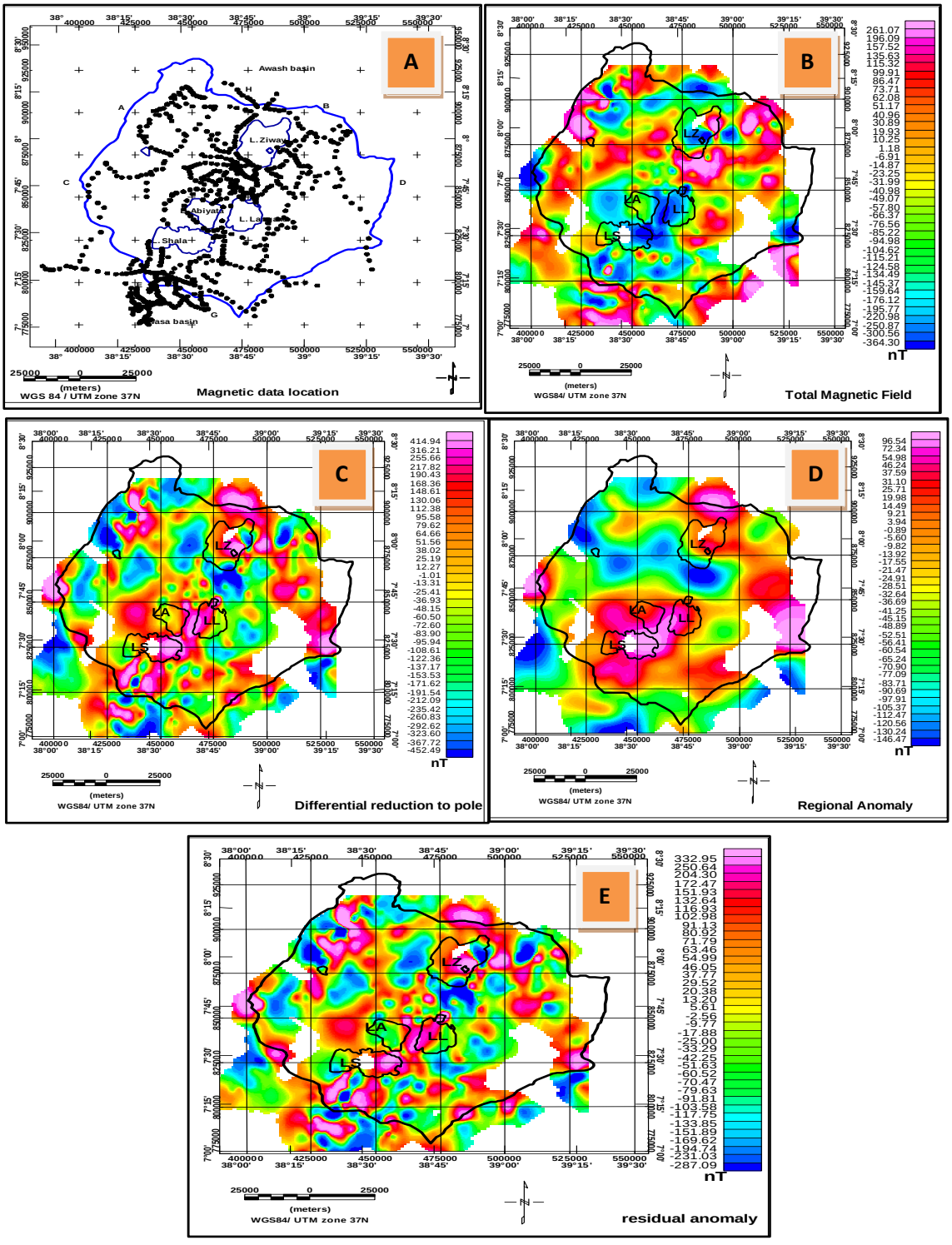

Fig.7. 5 Magnetic data stations distribution map (a) Total field magnetic anomaly map (b) Total magnetic field anomaly reduced to magnetic pole using DRTP (c) Regional magnetic anomaly estimated using upward-continuation filter to height of 6 km (d) the residual magnetic anomaly map (e) of the Ziway-Shala lakes basin, Central Main Ethiopian Rift

7.2.1.3 Well-log data

The well log dataset consists of core-samples obtained from eight boreholes drilled for the purpose of studying the geothermal resources of the Aluto-Langano geothermal field. These wells depth ranges from 1300 m to 2500 m below surface ground level. Based on these drilling data information the geologic section (Fig. 7.6) was constructed along west-east oriented profile by different researchers (Cherkose & Mizunaga, 2018; Wilks et al., 2017; Hutchison et al., 2016).

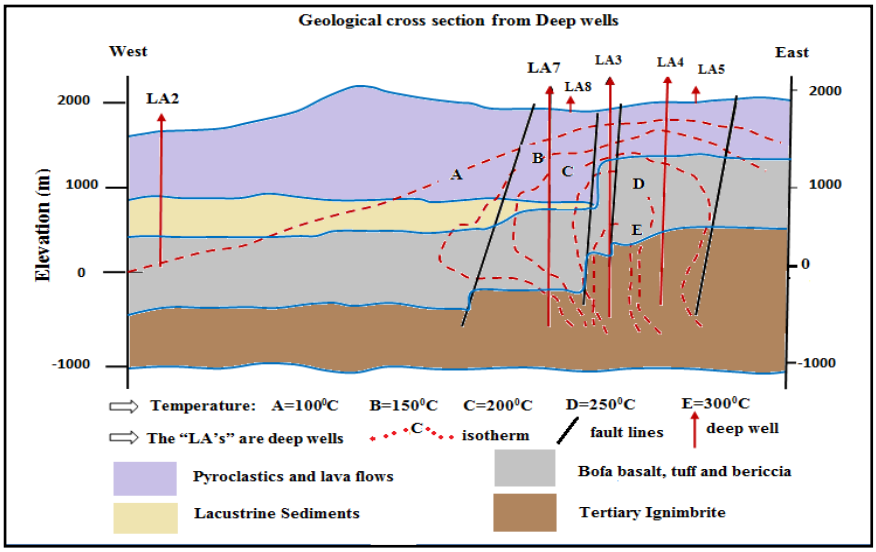

Fig.7. 6 West-east geologic cross-section derived from core samples of the deep geothermal wells drilled in the Aluto-Langano geothermal field modified from Cherkose & Mizunaga, 2018**.**

The geologic cross section (Fig. 7.6) information is used for constraining and cross-checking analysis of the gravity and magnetic data. Moreover, the geologic section is used to constrain the joint 2D forward gravity/magnetic model and 3D gravity interface based inversion.

7.2.2 Methodology

An inversion process generally includes an automatic (Werner, 1953), Fourier Transform method which includes spectral and 3D interface based inversion (Spector and Grant, 1970; Parker, 1972; Oldenburg, 1974) and optimization (voxel) methods (Li and Oldenburg, 1998; Williams, 2008). These inversion methods are used to invert potential field data into a 2D/3D densities/susceptibilities subsurface spatial distribution or subsurface topographic undulation that generate observed gravity/magnetic anomalies. Except for the voxel based inversion method, all the inversion methods mentioned above are employed in this research work. The governing equations for each method are described in sections 7.2.2.1 to 7.2.2.5 below.

7.2.2.1 Power Spectral Analysis

The application of power spectral analysis to potential field anomalies in one dimension can be performed by transforming the digitized gravity/magnetic data from space domain in to frequency domain. The transformation is used to compute the power or amplitude spectrum in accordance with equations (7.1) and (7.2) below

$$F_w = \sum_{k=0}^{N-1} f(k)\, e^{-i\frac{2\pi nk}{N}} \tag{7.1}$$

$F_{w,}$ is the discrete amplitude spectrum which could be respectively written as a sum of real and imaginary (Eq. 7.2)

$$F(\omega) = a(\omega) + ib(\omega) \tag{7.2}$$

Where

$|F(\omega)| = \sqrt{a^2(\omega) + b^2(\omega)}$, is an amplitude spectrum and

$\omega = 2\pi f$ is the angular frequency

Spectral analysis is thus describe the variation of the energy as a function of frequency (wave length) which help to estimate subsurface density contrast depth (Spector & Grant, 1970) given by (Eq. 7.3)

$$h = -\frac{1}{4\pi}\left(\frac{logE_1 - logE_2}{K_1 - K_2}\right) \tag{7.3}$$

Where E_1 and E_2 are power spectra of the gravity field,

$\log E_1$ and $\log E_2$ are logarithms of the power spectra

k_1 and K_2 are wave numbers

h is depth to interfaces (layer boundaries)

Equation (7.3) gives the depth, h, which are obtained from difference of the power spectrum curve slopes divided by -4π.

The method is a statistical estimation (Spector & Grant, 1970) based on low and high frequency anomalous bodies. These anomalies respectively categorized as sources of low, intermediate and high frequencies characteristics(H. Kebede et al., 2020).

In this study, the profile data along the rift axis (Fig. 7.1(a), black line) is extracted from the residual gravity anomaly and is inverted for sources depths at various density interfaces using power spectral analysis mentioned. The depths can be determined along the line in accordance with equations 7.1, 7.2 and 7.3. This method was used by various researchers to estimate depth to density interfaces (Mammo, 2012). The profile data and the result of the analysis (depths of density contrasts) using this depth estimation method are documented in result section of this manuscript.

7.2.2.2 Werner De-convolution

The mathematical formulation of 2D Werner deconvolution was developed by (Werner, 1953) and followed and extended by (Hartman et al., 1971). Accordingly, the governing equation of a total magnetic field for simple arbitrarily oriented thin sheets (dykes) or interfaces is given by (Eq. 7.4)

$$F(x) = \frac{Ah + B(x - x_0)}{(x - x_0)^2 + h^2} \tag{7.4}$$

Where,

$\boldsymbol{x}$ is the distance along a line perpendicular to the strike of the thin sheet, relative to an arbitrary origin;

$\boldsymbol{F(x)}$ is the total magnetic field intensity at $\boldsymbol{x}$;

$\boldsymbol{h}$ is the depth to the top of the thin sheet;

$\boldsymbol{x_0}$ is the position of the top, projected vertically to intersect the line;

$\boldsymbol{A\ and\ B}$ are parameters related to the magnetic properties and the thickness of the thin sheet as well as its orientation relative to the direction of the Earth's field.

For the more complex model, the anomalous magnetic field is considered to be the combination of the fields due to two thin sheets and a quadratic background magnetic interference which can be expressed as (Eq. 7.5)

$$F(x) = \frac{A_1 h_1 + B_1(x - x_1)}{(x - x_1)^2 + {h_1}^2} + \frac{A_2 h_2 + B_2(x - x_2)}{(x - x_2)^2 + {h_2}^2} + c_0 + c_1 x + c_2 x^2 \qquad (7.5)$$

Equation 7.5 has 11 unknowns,A_1, h_1, B_1 , x_1 , A_2 , B_2, h_2, x_2, c_0 , c_1 and c_2 of which the first eight variables are important to the interpretation and it is solved analytically. The equations defining the model are solved using observed data values which yield the position, depth, and magnetic/gravity contrast of buried interfaces. To solve for these unknowns at one point on the profile a 'window' of 11 equi-spaced observed data values are required. Solving these systems of equations, results in estimates of these coefficients. This intern allows one to estimate the position and depth of the thin-sheet bodies and geological interference.

This method is an automatic inversion method which does not require prior information. The method generates subsurface point source distribution in 2D.

In this study, profile residual gravity and magnetic anomalies along rift axis (in parallel to EAGLE seismic line) are first extracted respectively from gridded gravity and magnetic anomaly maps. Werner method is applied to these profile dataset to estimate corresponding depths to gravity and magnetic source interfaces. The method was used by different researchers in

different study area to estimate depths to gravity and magnetic sources(Mammo, 2012; Thakur et al., 2000).

7.2.2.3 Source Parameter Imaging (SPI)

The method is based on complex analytical signal (Eq. 7.6) which is defined as either in terms of total field or its Hilbert transform (Nabighian, 1972)

$$A(x,z) = \frac{\partial B(x,z)}{\partial x} - j\frac{\partial B(x,z)}{\partial z} \quad \text{or} \quad A(x,z) = |A|\exp(j\theta) \tag{7.6}$$

Where,

$|A| = \sqrt{\left(\frac{\partial B}{\partial x}\right)^2 + \left(\frac{\partial B}{\partial z}\right)^2}$ is analytical signal amplitude and

$\theta = tan^{-1}\left[\frac{\partial B}{\partial z} / \frac{\partial B}{\partial x}\right]$ is and the local phase.

-x and z are Cartesian coordinates for the vertical direction and the direction perpendicular to strike,

- $B(x,z)$ the magnitude of total magnetic field and

-j is the imaginary number

The method according to Thurston and Smith(1997) can also be expressed as the local frequency,f, given by (Eq. 7.7)

$$f = \frac{1}{2\pi}\frac{\partial}{\partial x} tan^{-1}\left[\frac{\partial B}{\partial z} / \frac{\partial B}{\partial x}\right] \tag{7.7}$$

In the analysis of potential fields, it is often more convenient to use local wave number, denoted by, k, rather than f which is given by (Eq. 7.8)

$$k = 2\pi f = \frac{1}{|A|^2}\left(\frac{\partial^2 B}{\partial x \partial z}\frac{\partial B}{\partial x} - \frac{\partial^2 B}{\partial x^2}\frac{\partial B}{\partial z}\right) \tag{7.8}$$

Thus, the peaks outline source edges (local depth) can finally derived at these location; $x = 0$, is (Eq. 7.9)

$$h = \frac{1}{k} \tag{7.9}$$

The depths to magnetic sources in the region under consideration are automatically estimated using Source Parameter Imaging (SPI) based on governing equations (Eq. 7.7, Eq. 7.8 and Eq. 7.9). Oasis Montaj Geosoft software version 7.1 SPI tool is used and the solutions are saved in a database. The work is started with calculating derivative grids $\left(\frac{\partial B}{\partial x}, \frac{\partial B}{\partial z} \; and \; \frac{\partial B}{\partial x}\right)$ of differentially pole reduced total magnetic field anomalies which are used as an input to SPI operator. The calculated SPI values are then gridded and mapped to show the magnetic source depths of the study area. This method has been used as magnetic source depths estimates by different researchers in different study locations (Tsepav, 2018; Salako, 2014).

7.2.2.4 Forward modeling

It describes the process of generating synthetic data (Menke, 1989) from a given Earth model with geometric elements and physical properties as an initial model.

The gravitational attraction g at a point $P = (x, y, z)$ due to a volume V can be expressed in line integral (Telford et al., 1990) as (Eq. 7.10)

$$g(P) = -G \int_V \rho \frac{\hat{e}}{r^2} dv \tag{7.10}$$

Where, ρ is density as a function of space

r is the distance from the observation point P to an element of the body dv,

$\hat{e}$ is a unit vector pointing from an element of the mass to P, and

G is the universal gravitational constant

The vertical component of the gravity anomaly simply expressed (Talwani et al., 1959) as (Eq. 7.11)

$$\Delta g_z = 2G\rho \sum_{i=1}^{n} z_i \tag{7.11}$$

Talwani et al. (1959) considered the case of an n-sided polygon and broke the line integral up into n-contributions, each associated with a side of the polygon. He derived expressions for z_i, that make extensive references to trigonometric functions which is clearly stated in his paper

Talwani et al. (1959). The model involves creating a hypothetical geologic model and calculating the gravity response to that earth model.

In this study, Oasis Montaj Geosoft modeling program called GM-SYS is used for intuitive, interactive and real time calculation of the profile residual gravity/magnetic response with change of density, susceptibilities and undulating geometries of layers. This modeling process is non-unique and thus need to be constrained with the present and earlier geological and geophysical knowledge. This method is an established procedures of estimating profile geometries of the interfaces since Talwani et al. (1959).

7.2.2.5 3D layered based inversion of gravity data

This is another spectral inversion method based on the spectral content of the data (Parker, 1972) (Oldenburg, 1974). It helps to map the depth to an interface separating two homogenous media using the sum of Fourier transform of gravity data and it differs from voxels (cube with 3D cells) on which 3D distribution of densities in each cell is estimated.

The gravity response (anomaly) caused by an uneven and non-uniform layer of material with constant density is calculated by Fourier transform of gravity data and the sum of the interface topography's Fourier transformation (Parker, 1972) (Eq. 7.12).

$$F(g(r)) = 2\pi G\Delta\rho e^{-|k|z_0} \sum_{n=1}^{\infty} \frac{k^{n-1}}{n!} F[h^n(\vec{r})] \qquad (7.12)$$

Oldenburg (1974) rearranged equation (7.12) to compute the depth to the undulating interface from the gravity anomaly by means of one dimensional Fourier transform in an iterative process (Eq. 7.13).

$$F[h(r)] = \frac{F[\Delta g(x)]e^{|k|z_0}}{2\pi G\Delta\rho} - \sum_{n=2}^{\infty} \frac{k^{n-1}}{n!} F[h^n(r)] \qquad (7.13)$$

Where:

$F[g(r)]$ is the Fourier transform of the gravity anomaly,

G is Newton's gravitational constant,

r is a horizontal plane

$\Delta\rho$ is the density contrast across the interface (two media),

k is the wave number,

n is an integer

$h(r)$ is the topography of the interface

z_0 is the mean (reference) depth of the horizontal interface.

$F[h^n(r)]$ is Fourier transform of the interface topography

Parker–Oldenburg iterative expression (Eq. 7.13) allows us to calculate the topography of the density interface (layer) iteratively using $\Delta\rho$ and z_0 as an input. The first term of equation (7.13) is computed by assigning, $h(r) = 0$. This value, $h(r)$, is then used in the equation to evaluate a new estimate of $h(r)$. This process is continued until a reasonable solution is achieved and the convergence criterion is guaranteed.

In this study the joint algorithm of Parker–Oldenburg inversion (Eq. 7.12 and Eq. 7.13) is applied on residual gravity anomaly grid (with constraining initial model compiled in section 7.2.2.6 and previous knowledge) in the region considered to map the geometries of the crystalline basement layer that is responsible for the observed residual gravity anomalies. The method has been used for crustal structures studies (Tiberi et al., 2005) and estimate of bedrock topographic undulations (Salimi & Motlagh, 2012).

7.2.2.6. Initial model

Both joint gravity/magnetic 2D forward modeling and 3D gravity structural inversions require a priori constraining information for a final model to be reasonable and acceptable with least tolerable error. The constraints were compiled from well-log data (Fig. 7.6), seismic velocity model (Fig. 7.1(b)) and depths determined from the spectral analysis, Werner Deconvolution and SPI (sections 7.2.2.1 to 7.2.2.3).

The parameters obtained from these data analysis are density, susceptibility, interfaces and corresponding causative source depths. In geological section described in section 7.2.3 (Fig. 7.6), there is no Mesozoic and crystalline basement surface till depth of 2.5 km (Fig. 7.6). The gravity data analysis in the study area show that the crystalline basement horizon is found at approximate mean depth of 3.0 km (H. Kebede et al., 2020) . In-between Tertiary ignimbrite and crystalline basement layers, however, there is Mesozoic layer (Woldegabriel et al., 2000). To determine the depth to the top of the Mesozoic layer, we performed a Multi-Layer 3D Gravity forward calculation with all the other interface depths set at predetermined location, varying the depth to the top of the Mesozoic layer (i.e., 2.6 km, 2.7 km, 2.8 km and 2.9 km) and recording how sensitive the misfit is as we vary the depth values considered. The final result which generates the least root mean square error (RMS) is taken as the feasible depth to top of Mesozoic layer. The depth to top of this layer is at 2.9 km as the RMS is smaller than others. The interfaces lithology, density and susceptibility value identified come from various sources. The summary of these parameters which are used as an initial model is described in Table 7.1. Graphical representation of this initial model is shown in Fig. 7.7.

Layer	**Layer Geology**	**Depth to top of the layer (m)**	**Density (gcm^{-3})**	**Susceptibility**	**References (Source for the parameters)**
1	Pyroclastic and Lava flows (Silicic products)	0	2.477	0.00113425	Well-log data, Seismic study, Spectral analysis, Werner De-convolution
2	Lacustrine sediments	1000	2.34	0.000505	Well-log data, Seismic study and Blaikie et al.(2014)
3	Bofa Basalt, tuff and breccias	1500	2.81	0.0019558	Well-log data, Seismic study, Spectral analysis, Werner De-convolution (Alemu, 1992)
4	Tertiary Ignimbrite	2500	2.58	0.0001825	Well-log data, Seismic study, Spectral analysis, Werner De-convolution (Alemu, 1992)
5	Mesozoic sediment	2900	2.5	0.016	(Mammo, 2010), Multi-Layer

					3D gravity forward modeling
6	Crystalline basement	3000	2.74	0.0033	Gravity analysis result (depth), seismic velocity-density conversion (Maguire et al., 2006)

Table 7. 1 Number of layers, depth to top of the layer and density value approximation for the six horizons

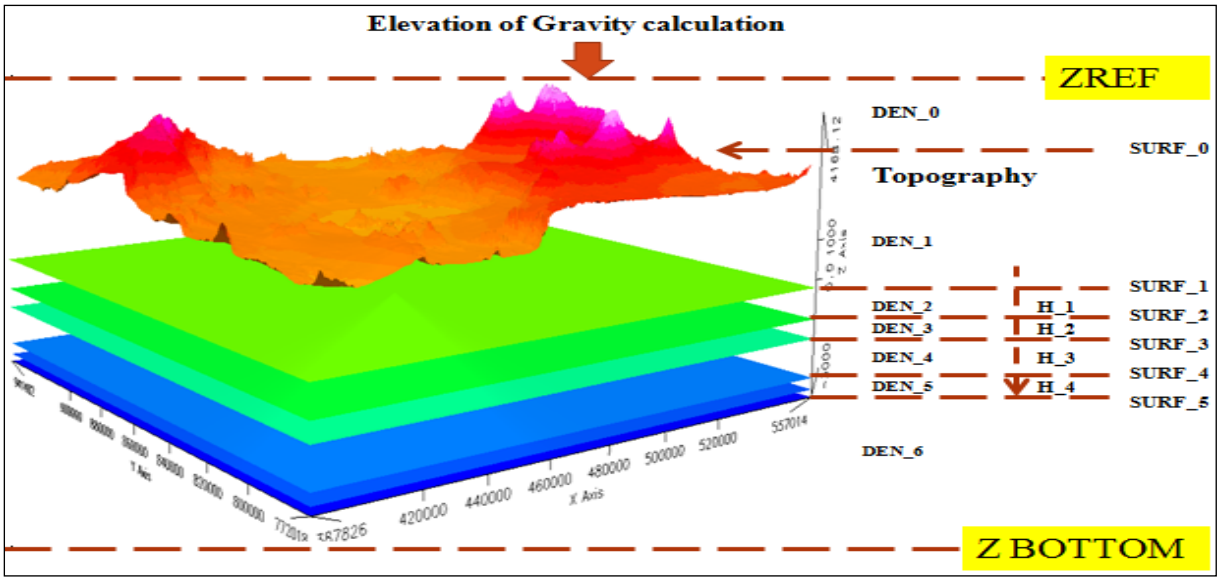

Fig.7. 7 Six geological horizons identified from the well-log data, previous geological and geophysical studies and current geophysical data analysis. The color of layers representing stacked horizons where density contrasts occurs. The top most layers represent elevation of the Central MER.

7.3 Results

The mathematical formulation of source depth estimation methods are described in the methodology sections. The first three methods are automatic methods that do not require aprior geological information as compared to the last two. The gravity and magnetic source depths estimated along the rift axis and rift floor. Fig. 7.8 shows a profile line (black color) where the residual gravity and magnetic anomalies are extracted and analyzed. The zigzag line (blue color) (Fig. 7.8) is a seismic line analyzed and interpreted by the EAGLE project for velocity statigraphic sections (Maguire et al., 2006) (Fig. 7.1(b)).

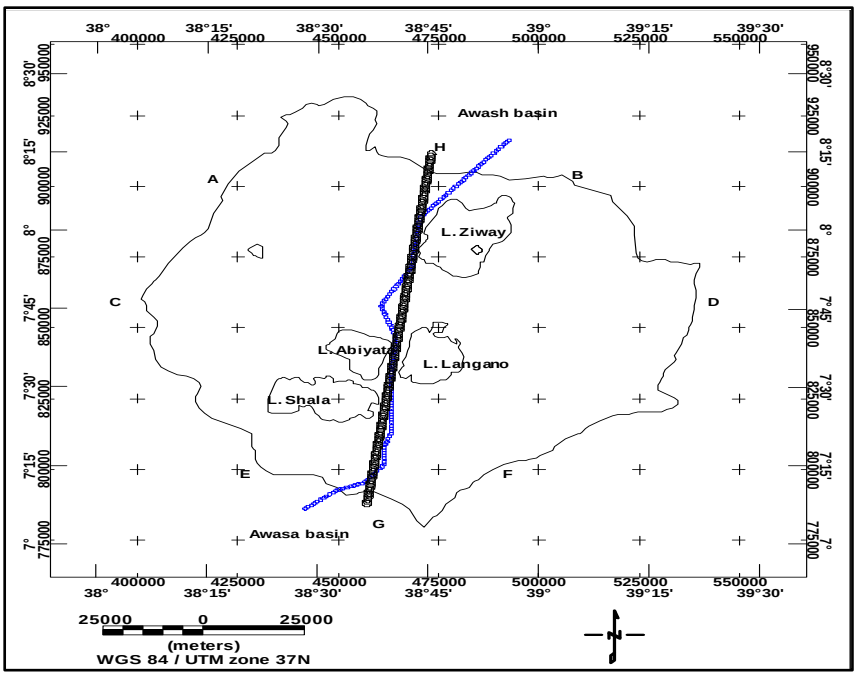

Fig.7. 8 EAGLE seismic line (blue) and gravity/magnetic profile line (black) for source depth estimation along the rift axis in the Ziway-Shala lakes basin

7.3.1 Spectral analysis

The profile residual gravity anomaly are extracted along the rift axis and rift floor (Fig. 7.7, black line) and is shown in (Fig. 7.9a). The one dimensional power spectrum technique is applied to residual gravity anomaly profile consisting of 166 data points (Fig. 7.9a). The calculated power spectrum curve is represented as log of spectral energy versus wave number (Fig. 7.9 (b)). The depth to top of the gravity source (density interfaces) is calculated from the slope (gradient) of power spectrum curve. The linear curves (from which slope values are read) are fitted to power spectral data based on a piece-wise least-squares linear curve-fitting approach (Fig. 7.9 (B1, B2 and B3)). The gradients (slopes) are read from the fitted lines which show weighted energy of the source origin from low, intermediate and high frequencies values. Much of this energy comes from the deep sources (low frequency) (Fig. 7.9 (B1).

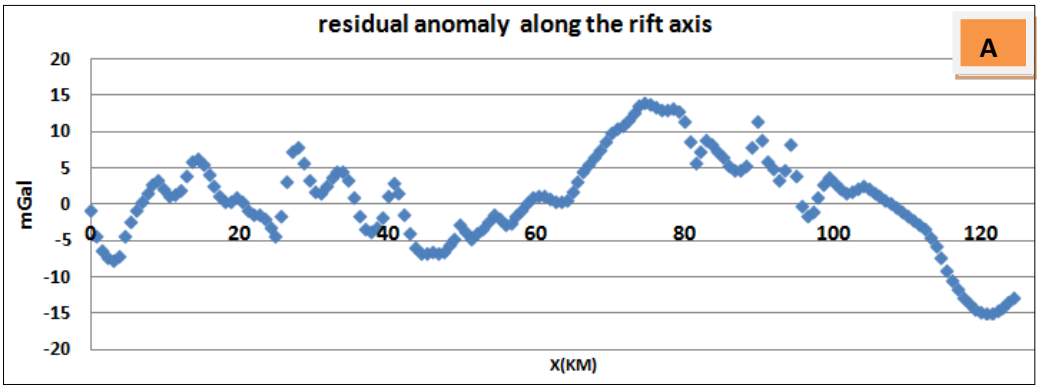
residual anomaly along the rift axis
A
mGal
X(KM)

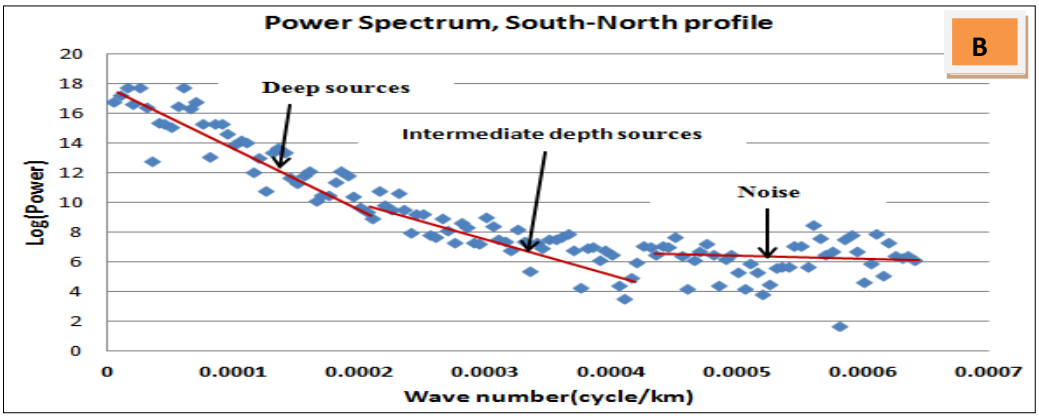
Power Spectrum, South-North profile
B
Deep sources
Intermediate depth sources
Noise
Log(Power)
Wave number(cycle/km)

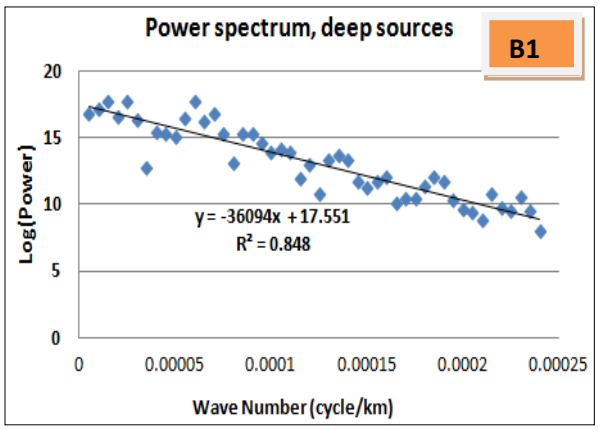
Power spectrum, deep sources
B1
y = -36094x + 17.551
R² = 0.848
Log(Power)
Wave Number (cycle/km)

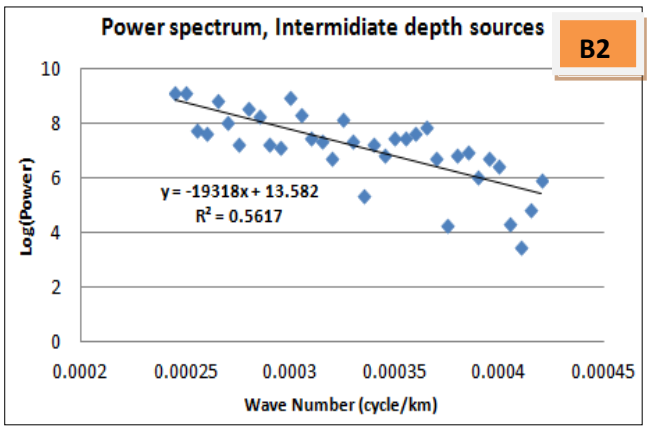
Power spectrum, Intermidiate depth sources
B2
y = -19318x + 13.582
R² = 0.5617
Log(Power)
Wave Number (cycle/km)

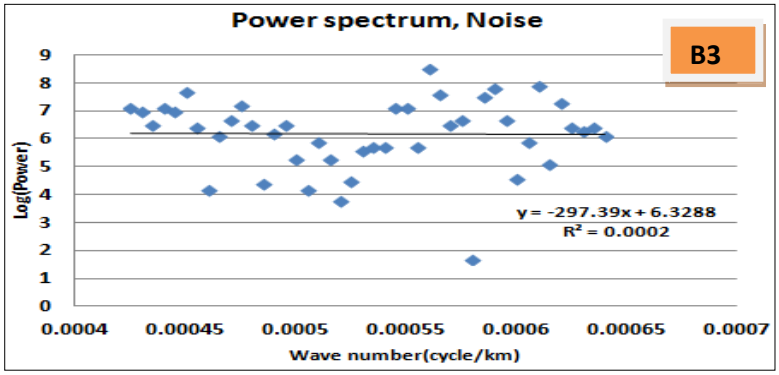
Power spectrum, Noise
B3
y = -297.39x + 6.3288
R² = 0.0002
Log(Power)
Wave number(cycle/km)

Fig.7. 9 Residual gravity profile anomaly along the rift axis that was used in the power spectral analysis (a) plot of Logarithm of the power spectral energy versus wave number decay curve (energy spectrum of the profile) (b) series of trend line segments fitted to energy decay curves to determine slopes which could help to estimates average depths to the various density interfaces (Fig. 7.9(B1), Fig.7.9 (B2) and Fig.7.9 (B3)).

The results of the power spectral analysis are summarized in Table 7.2. Source depths interfaces are categorized as shallow, intermediate and deep depending on the wave number (frequencies) and slope (gradient) variations. The depth to intermediate source along the rift axis and rift floor approximated from residual gravity anomaly is about 1.5 km while the depth to deep gravity sources is 2.87 km. The third slope estimate is nearly zero and represents the noise in the data (Fig. 7.9B3).

Profile Name	Layers gradients	Depth(m) to tops of layers	Causative source categories	Geology approximation from well-log	r^2
South-North	-36094	-2872.27	Deep	Top of crystalline basement layer	0.848
	-19318	-1537.28	Intermediate	Top of bofa basalt layer	0.5617
	-297.39	-23.6655	Noise	-	0.0002

Table 7. 2 Log spectral depth estimates and category of the anomalous source as deep, Intermediate and noise components

Three gradient values are read from the fitted trend lines (Fig. 7.9(B1), 7.9(B2) and 7.9(B3)) (Table 7.2, column 2) and depths are calculated based on Equation 7.3 and shown in column 3 of Table 7.2. As the method is used to determine mean depths to the various interfaces of density contrasts, two clearly identified interfaces are read and categorized as deep and intermediate source depths (Table 7.2, column 4). The depth estimate for the third interface is about 23 m which is estimated with r^2 value of 0.0002. Accepting 23 m as a source depth with r-square value could lead us to wrong interpretation. Thus, it would be better to consider it as noise component. Validity of the estimated top of density contrasts (Table 7.2, column 4) could be

guaranteed by comparing the gravity source depth results against the geologic stratigraphy (Fig. 7.6) produced based on well-log data. This source depth estimation method was used to estimate density horizons in northern part of Ethiopia (Mammo, 2010), which lies close to our study area.

7.3.2 Werner deconvolution

The gravity /magnetic source depth and location along the rift axis and rift floor are calculated based on an automated depth-estimation method called Werner De-convolution. The governing equation which helps to make this depth estimate is described in section 2.2.2. This method is an iterative 2D inversion technique which estimates the vertical gravity/magnetic sources depths and locations. The residual gravity anomaly along the rift axis (Fig. 7.10 (b)) is first extracted from residual gravity anomaly map (Fig.7.4(c)). This profile anomaly (Fig. 7.10 (b) is subjected to Werner algorithm to recover gravity source vertical contact depth locations. This is shown in square symbols plotted in Fig. 7.10(c). Similarly, the differentially pole reduced residual magnetic anomaly along the same profile line as the gravity profile (Fig. 7.11a) was used in Werner deconvolution analysis. The result of magnetic source depth is shown in Fig. 7.11(b).

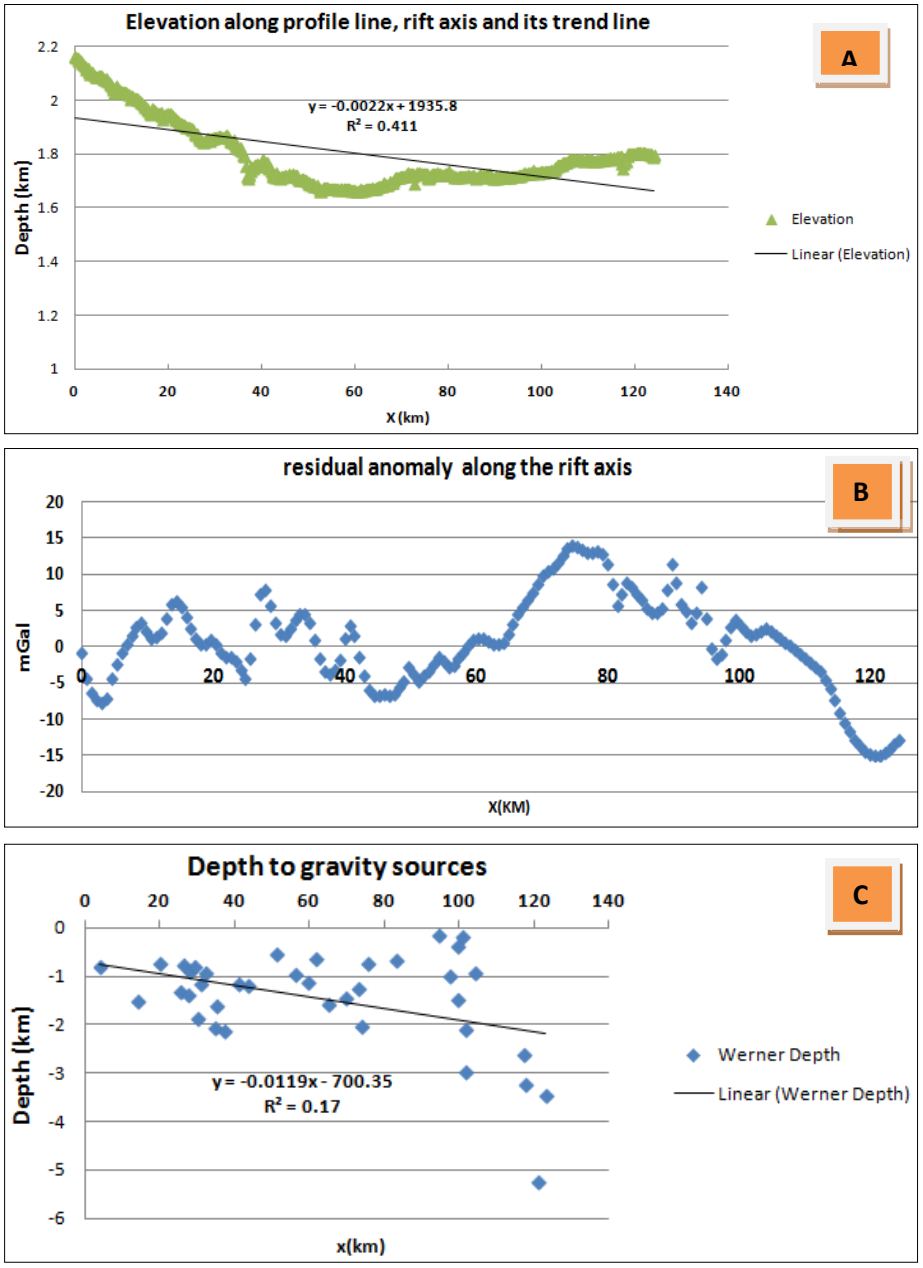

Fig.7. 10 Elevation map along the study profile and its trend line fit(a) residual gravity anomaly (b) Werner depth showing Z-contact calculated using 2D Werner de-convolution and trend line fitted to z-contact along the rift axis (c)

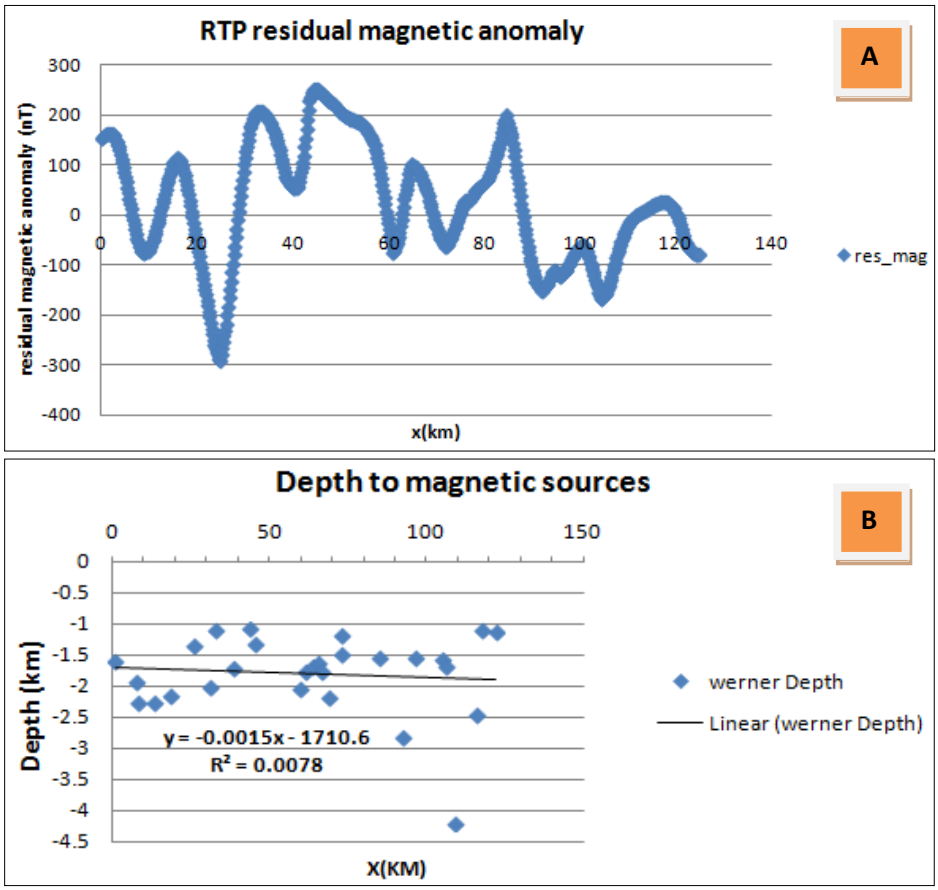

Fig.7. 11 Differentially pole reduced profile residual magnetic anomaly along the rift axis over rift floor (a) Vertical contact (square symbol plot) along the rift axis and fitted trend line (b)

The elevation profile along the rift axis was extracted from DEM (Fig. 7.10a). The trend line fitted to this elevation profile show a negative slope signifying that the elevation tends to decrease northwards. The gravity source depth estimated based on Werner automated inversion algorithm appears to deepen northwards as depicted by the fitted trend line to the gravity source depths (Fig. 7.10(c)). Similar to the trends from gravity source and elevation, the magnetic source depths also appear to deepen from south to north (Fig. 7.11(b)).

7.3.3 Source Parameter Imaging (SPI)

This is a technique used to estimate the depth to the anomalous magnetic sources which is equivalent to mapping thickness of the sedimentary-volcanic section overlying crystalline basement (magnetic basement). SPI is generally an automatic calculation of source depths from gridded magnetic data (Thurston & Smith, 1997). The method is independent of magnetic inclination, declination and pole reduction, however, the SPI operator is acted on differentially pole reduced magnetic residual anomaly. The target of the filter is to estimate depth to magnetic sources in the Ziway-Shala Lakes Basin. Oasis Montaj Geosoft software version 7.1 is used to generate a SPI value. These values are then gridded and mapped for the region under study (Fig. 7.12(a)) to show magnetic source interfaces.

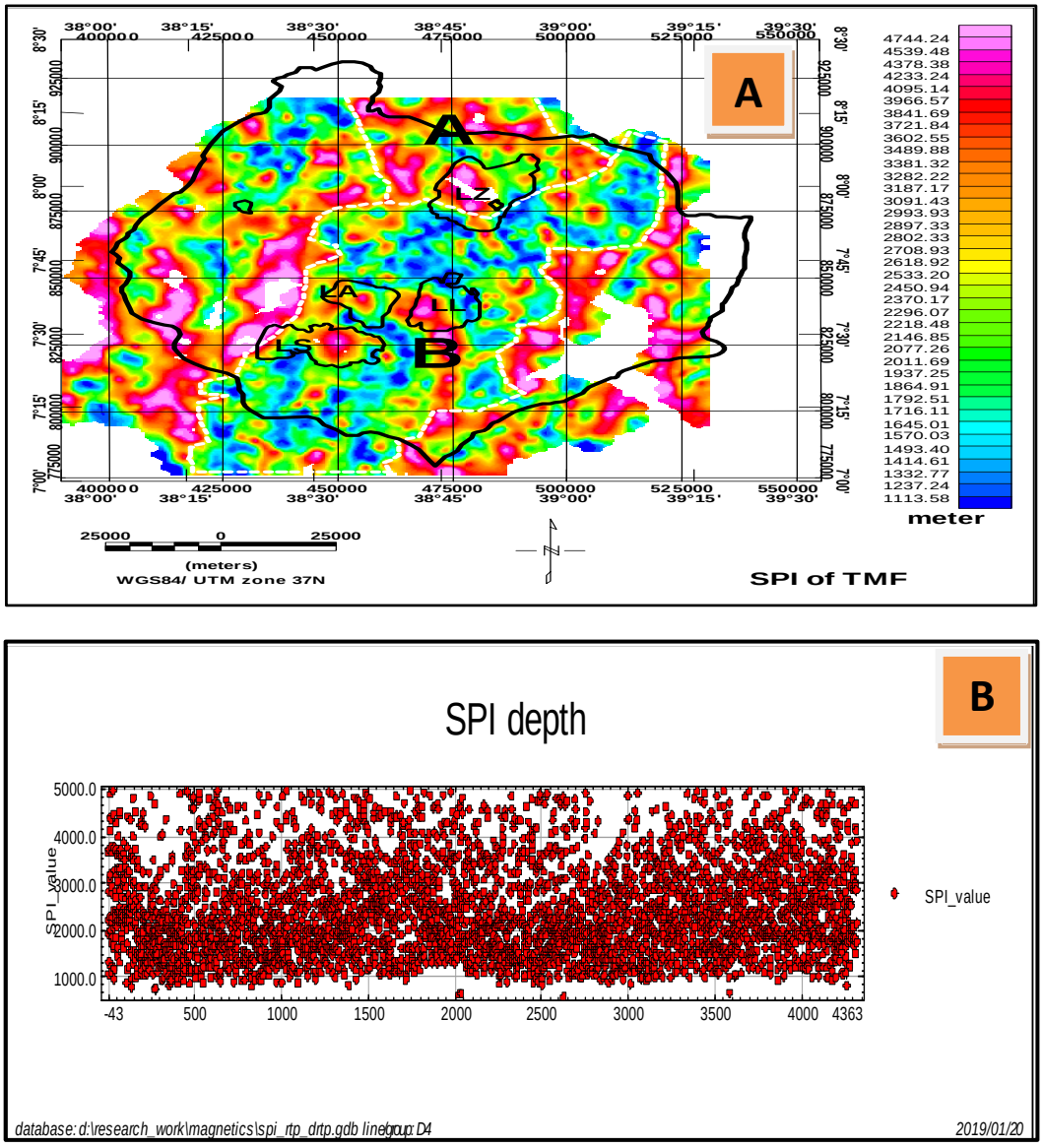

Fig.7. 12 Magnetic source locations calculated using the SPI method (a) and source depth distribution in the Ziway-Shala lakes basin (b)

Density plot of SPI depth values are made to show the depth distribution (Fig. 7.12(b)) of the magnetic sources. The depth to magnetic source body after gridding and mapping is depicted as 2D image map (Fig. 7.12 (a)). The estimated depths lie in between 1.1 km and 4.7 km. The gridded SPI value along the rift axis is categorized as “Region A” and “Region B” (Fig. 7.12 (a)) respectively showing sources of magnetic bodies from deep and shallow Earth’s. Crystalline

basement rocks are believed to be the source of magnetic anomalies. Along the rift floor, the maximum source depth of about 4.7 km is found in northern water divide, between Ziway-Shala Lakes Basin and Awash River basin. The rift floor generally shown to indicate magnetic sources situated at shallow depths (Fig. 7.12 (a)). The reason for existence of magnetic sources at shallow depth could be because of rocks thermal alteration with depths. As the study area lies in volcanically and tectonically active area, the heat sources increases with depths (Fig. 7.6) which decreases rocks magnetic susceptibilities.

7.3.4 Joint 2D Gravity/Magnetic Forward Modeling

The joint gravity/magnetic model can be considered to better reflect geology of the study area as compared to the independently generated 2D gravity and magnetic models. The 2D joint gravity and magnetic model is computed using the residual gravity/magnetic profile based on the initial constraining information listed in Table 7.1. The initial model consists of six lithologic horizons namely Pyroclastic-volcanic formation$\left(2.477\frac{\text{gm}}{\text{cc}}\right)$, followed by lacustrine sediment formation layer $\left(2.34\frac{\text{gm}}{\text{cc}}\right)$, bofa basalt, tuff and breccias layer$\left(2.81\frac{\text{gm}}{\text{cc}}\right)$, tertiary ignimbrite layer$\left(2.58\frac{\text{gm}}{\text{cc}}\right)$, Mesozoic sediment formation layer $\left(2.5\frac{\text{gm}}{\text{cc}}\right)$ and crystalline basement formation layer $\left(2.74\frac{\text{gm}}{\text{cc}}\right)$ (Fig. 7.6).

The final joint gravity and magnetic model response is taken to be acceptable with a root mean square error (RMS) of 1.61 mGal and 25.568 nT respectively (Fig. 7.13). This joint model gives a good fit between observed and calculated gravity and magnetic anomalies along the profile.

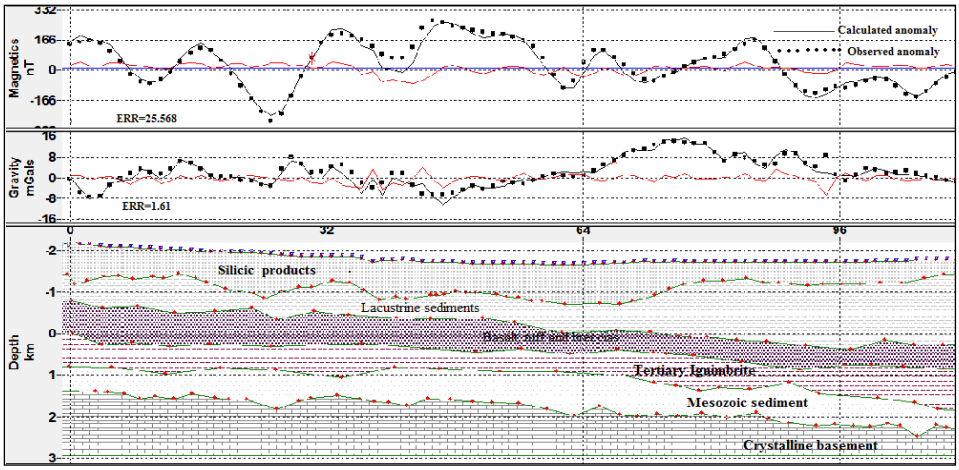

Fig.7. 13 2D joint gravity/ magnetic model of the profile running along the rift axis and rift floor, considered to show the gravity/magnetic horizons. The deeper crystalline basement sources overlying shallower sedimentary/volcanic sources.

The thickness of sediment-volcanic overlying crystalline basement increases northward as it is shown in Figure 7.13. This result agree well with the seismic velocity model result though "sediment-volcanic" layer was mapped with low-resolution (Maguire et al., 2006). These depth estimates recovered from the joint gravity/magnetic 2D modeling are consistent with the automated depth-to-source estimates made using Spectral Analysis, 2D Werner De-convolution and Source Parameter Imaging methods.

7.3.5 3D gravity structural Inversion

The 3D forward and inverse modeling approach is defined by a number of surfaces or geologic horizons inverted for mapping depth to a layer (Fig. 7.14).

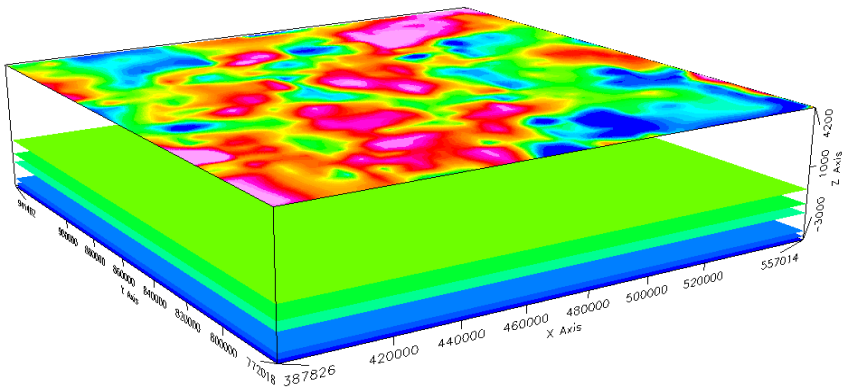

Fig.7. 14 Residual gravity anomaly (top) inverted for geometrical modification of stacked layers (bottom) particularly for crystalline basement layer.

The multi-layer, surface based, frequency domain forward and inverse modeling of Parker–Oldenburg algorithm (Oldenburg, 1974; Parker, 1972) is applied to transform the residual gravity anomaly to crystalline basement depths. An apriori information derived from existing geological and geophysical studies (Table. 7.1) are required for carrying out this inversion. It is performed for layers geometries (litho-stratigraphies) in general and crystalline basement layer in particular. Accordingly, the inversion is carried out on crystalline basement surface with the reference depth set at -3 km and layer density set to 2.74 g/cm^3. Top of this layer is considered to constitute Mesozoic sediments with a density value of 2.5 g/cm^3. The mean density contrast at the interface between crystalline basement and Mesozoic sediment is thus 0.24 g/cm^3. The smallest and greatest cut-off frequency parameters are chosen as 0.5 and 0.7 km^{-1}, respectively. The maximum iteration number is set to 10 with a convergence limit is 0.01mGal. The residual gravity anomaly is inverted for layers undulations and thicknesses. The structural inversion carried on crystalline basement layer is found to converge after four (4) iterations. For the topographic relief calculated (Fig. 7.15(d)) from the structural inversion, the corresponding calculated and misfit gravity anomaly are generated (Fig. 7.15 (b) and Fig. 7.15 (c)).

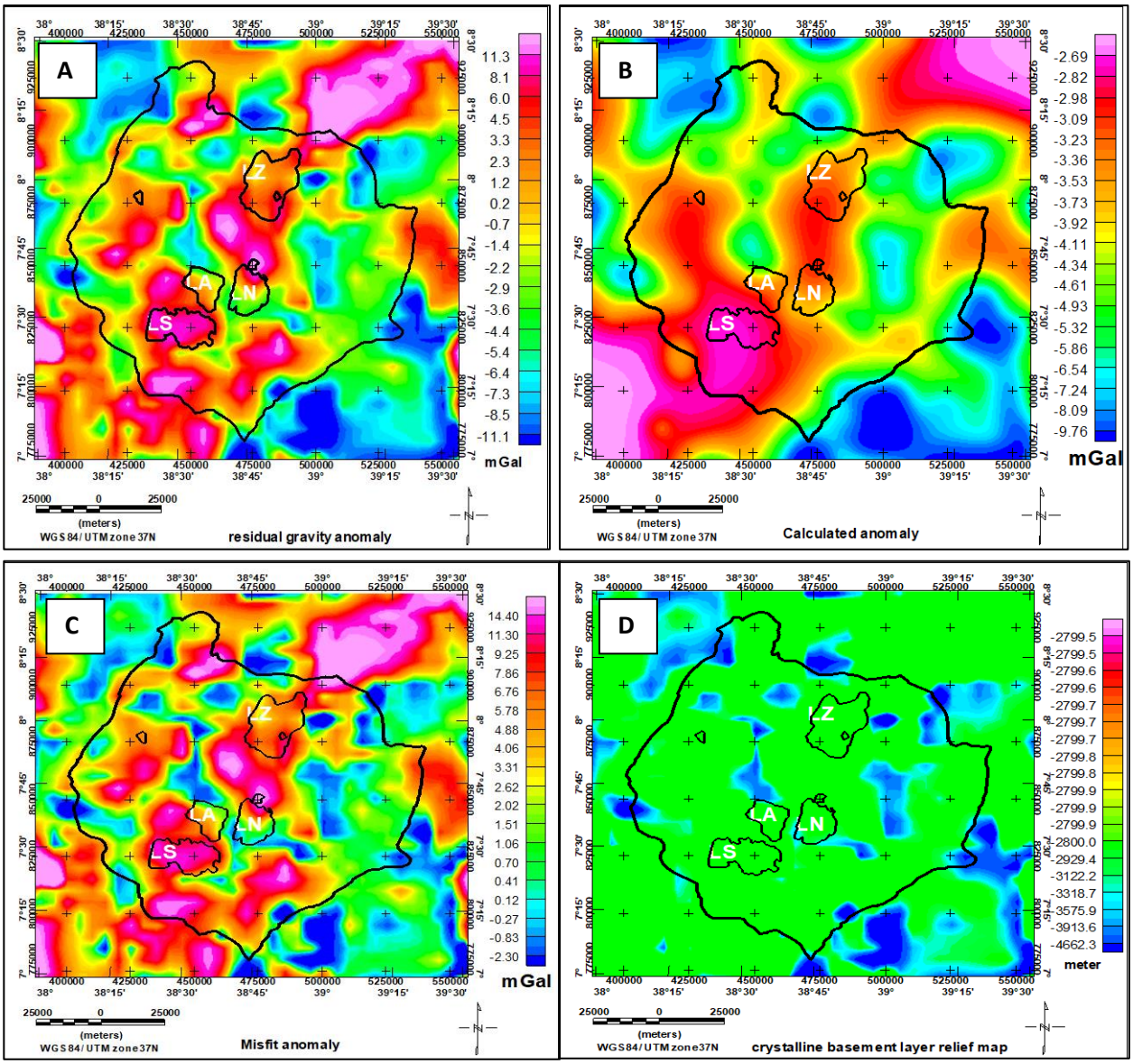

Fig.7. 15 Maps of the observed residual gravity anomaly (a) calculated gravity anomaly (b) the difference between the observed and calculated (or misfit) (c) the crystalline basement relief map (d). For all the maps, the coloring system used is based on histogram equalization.

The shallow depth to crystalline basement top layer (Fig. 7.15(d)) is 2.8 km and a deeper top depth to this layer is 4.7 km. These are 200 m up and 1.7 km down from a reference depth 3 km. Along the rift axis particularly starting north of Abiyata Lake, floor of Gademota and extending

far north to water divide area (Meki area), the gravity source depth appear to be found at deep depth. Furthermore, it is observed that gravity basement found to deepen northwards, towards Awash Basin.

The region has no previous geophysical studies at shallow/intermediate depth level for comparison of the present result. However, the result is in a fair agreement with 2D Werner De-convolution, SPI and joint 2D gravity/magnetic modeling result performed in this research work. Though mapped with low resolution, the seismic study conducted in the area showing low velocity sediment-volcanic seems to deepen northwards (Fig. 7.1(b)) (Maguire et al., 2006), in agreement to the result of 3D inversion.

7.4 Discussion

7.4.1 Subsurface Structures

The different inversion approaches employed in this research provided depth to various density and susceptibility interfaces. These density/susceptibility layers geometries are closely associated with the boundaries of geological structures (Feng et al., 2016). As documented in Section 3, the sources associated to the gravity and magnetic anomalies are determined using Power Spectral Analysis, 2D Werner De-convolution, Source Parameter Imaging (SPI), joint 2D forward Modeling and 3D gravity interface inversion methods.

In this research work, the power spectral analysis is the first inversion method used to map sources resulting in to the gravity anomalies occurring along the rift axis and over the rift floor. The analysis includes determination of slopes of the lines fitted to plots of log of power (energy) versus wave number (Fig. 7.9 (B1) and Fig. 7.9 (B2), Fig. 7.9 (B3)). These slope values which are calculated in accord with equation 7.3 and section 7.2.2.1 are employed to infer depths of the gravity source along the profile considered. The gravity sources that occur at the intermediate

depth (1.5 km) are found to possibly correspond to the top of the Bofa Basalt, tuff and breccias layer (Fig. 7.6). The gravity source having deeper origin along the profile is estimated to occur at a depth of 2.87 km and this depth is found nearby top of the crystalline basement depth (3 km) identified by Kebede et al., (2020).

Secondly, depth to top of the gravity and magnetic source interfaces along the rift axis are estimated using 2D Werner de-convolution of residual gravity anomaly and differentially pole reduced residual magnetic anomaly profile data (Fig. 7.10 (b) and Fig. 7.11 (a)). Trend lines fitted to Werner estimated gravity and magnetic source depths thought to indicate the deepening of the low velocity "sediment-volcanic" layer from south to north, along the rift axis.

The third filter used to map source depths is SPI. The result obtained from analysis of SPI of magnetic data shows, the "sediment-volcanic" layer overlaying the crystalline basement layer along the rift axis and over rift floor is thickening northwards. This means that, thickness of the low magnetic source bodies (sediments) increases northwards. In other words, the crystalline basement rock layer is far deeper in the northern region of the study area than the southern ones. Since the study area lies in rift environment where volcanic activities are active, the magnetic sources generally shown to have shallow Earth origin (Fig. 7.12 (a) and Fig. 7.12 (b)). The shallow causative magnetic sources are more easily detectable than the deep-seated targets as revealed by the SPI symbol depths density map (Fig. 7.12(b)). Most of these shallow magnetic sources are depicted in category "B" (Fig. 7.12(a)) with the depths approximately laying in between 1.1 km and 2.6 km. The deepest depth region categorized by "A" (Fig. 7.12(a)) has an approximate maximum depth of 4.7 km. From depth distribution symbols map (Fig. 7.12(b)) we

observe that, most frequent (concentrated) depth location for magnetic source bodies in the region lies in the depth range of 1 km to 3 km.

The magnetic source depth estimated from SPI along the rift axis/rift floor mostly agreed with low velocity "sediment-volcanic" layer identified by Maguire et al., (2006). The result from analysis of SPI agrees with the 2D Werner De-convolution results obtained from both gravity and magnetic data.

In the same way, the joint gravity/magnetic forward model result shows that the gravity/magnetic basement geometry tends to deepen northwards in the study area. The crystalline basement rocks appear to be the major sources of the anomalies as compared to overlying layers. For example, at the northern end of the profile, low gravity value indicates sediment accumulation (Fig. 7.4(c)) and the corresponding high magnetic value about this location (Fig. 7.5(e)) is considered to be due to the basement crystalline rocks occurring at relatively deeper depths. Results of the joint 2D model fairly agree with the results obtained from the 2D Werner de-convolution (Fig. 7.10 (c) and Fig. 7.11 (b)) and Source Parameter Imaging (Fig. 7.12(a)). Furthermore, the result of the joint 2D model is in a fair agreement with results of the seismic low velocity model layer of an EAGLE project (Fig. 7.1(b)).

Finally, 3D gravity interface inversion is conducted to map depth and geometries of crystalline basement layer. The inversion results (Fig. 7.15 (d)) have shown that the crystalline basement shallowest depth is found at -2.8 km and extends down to 4.662 km. The crystalline basement topography gets deeper towards north along the rift axis especially near water divide (north of the Meki town) between the Ziway-Shala Lakes Basin and Awash River basin (Fig. 7.15 (d)).

The overall result estimated based on automatic inversion, joint 2D modeling and 3D structural inversion shows undulating layers deepening northwards along the rift axis over rift floor. In

other words, the “Sediment-volcanic” layer resting over crystalline basement layer is thickening northwards.

7.4.2 Groundwater flow implication the mapped structures

The Ziway–Shala lakes Basin is hydrologically closed (Le Turdu et al., 1999) (Chernet et al., 2001) and there is no evidence of significant groundwater outflow (Legesse et al., 2004) from this basin. Using isotopic evidences (Darling et al., 1996) and groundwater flow modeling results the groundwater flow direction is determined to be from Lake Awassa basin (southern basin) towards the low-lying and deep Ziway-Shala lakes Basin (Ayenew, 2001). This groundwater flow direction is thought to increase both the groundwater and surface water resource in the basin.

To have a better understanding of the hydrology-hydrogeology, the water balance of the basin (Table 7.3) is determined with computations made based on the hydrological data taken from the work of Ayenew (2002).

According to Le Turdu et al.(1999) and Ayenew (2002) the mean annual rainfall ranges from about 1150 mm in the eastern and western highlands to around 600 mm in the rift floor. The annually weighted actual evapotranspiration values of the rift, the escarpments and the highlands are 656, 892 and 917 mm respectively with averaged value of 821mm/year. The annual evaporation values from Abiyata, Langano, Shala and Ziway lakes are estimated to be 2060, 2010, 2112 and 2022 mm, respectively, with an average value of 2051mm. These annual evaporation and evapotranspiration estimates are deemed to help calculation of the water balance of the basin.

In the case, the principle of conservation of mass is used to govern the flow of water in and out of a system. Precipitation (P), Evaporation (E), Evapo-transpiration (ET), Surface runoff (SRO) and groundwater flow (GF) are the various components of hydrologic cycle which are related mathematically as (Eq. 7.14)

$$\Delta S = P - E - ET \pm SRO \pm GF \qquad 7.14$$

Where, ΔS is the change in storage

On annual basis and under steady state condition where the lakes volume is stable the total inflowing water (rainfall) on the basin should equal to the total water loss (evaporation) ($\Delta S = 0$).

The estimate of water balance of the closed basin (eg. Ziway-Shala lakes basin) restated as in the following formula

$$\mathbf{Flux(GF)} = P - AET - E_L \qquad 7.15$$

Where, P is precipitation, AET is the actual evapotranspiration and E_L is evaporation from lake

Table 7. 3 below shows the computation of basin water balance made on basic hydrological data taken from (Ayenew, 2002), with all others parameters kept constant.

S. N	Lake	Surf. Area(k m^2)	Catch. Area(k m^2)	Rainfall on lake Surface(Mm^3)	Rainfall on Catch. Minus Rain on Lake Surface(Mm^3)	Total Rainfall	Evaporation from Lake surface	Evaporation from Surf. area other than lake(Mm^3)	Total Evaporation	Net outflow(Mm^3)
1	Abiyata	180	10740	117	12144	12261	369.18	8669.76	9038.94	
2	Langano	230	2000	149.5	2035.5	2185	471.73	1453.17	1924.9	
3	Shala	370	2300	240.5	2219.5	2460	758.87	1584.53	2343.4	
4	Ziway	440	7380	286	7981	8267	902.44	5697.74	6600.18	
5	Total	1220	22420	793	24380	25173	2502.22	17405.2	19907.42	5265.58

The net total flux of the basin is calculated to be 5265.58Mm^3 which is positive. The positive sign implies that the total pr**e**cipitation is greater than the total evaporation. This positive flux should be reflected on the increase of water capacity in the basin which would be manifested in rise of water level of the lakes. However, observation shows that the actual levels of the Lakes in the basin have been declining from time to time (eg. Abiyata Lake). The conclusion would be made based on the analysis of the water balance of the basin and the nature of the basin is a likely existence of geological structures acting as conduits for outflow of groundwater from the basin.

The second important parameter that characterize the relationship between geologic structures and groundwater flow is Total dissolved solute (TDS). The TDS of the lakes in the MER depends on inflow and outflow conditions (Gizaw, 1996). Table 7.4 shows the TDS estimates determined for the six Lakes that reside in the MER including Afar.

.S.N	Lakes Name	TDS(mg/l)	Source
1	Abiyata	13,480	(Ayenew, 2005)
2	Langano	3,175	(Gizaw, 1996)
3	Shala	7,262	(Gizaw, 1996)
4	Ziway	579	(Gizaw, 1996)
5	Afdera	145,129	(Ayenew, 2005)
6	Lakes in Dallol	274,467	(Gizaw, 1996)

Table 7. 4 TDS estimates of six Lakes in the MER and Afar

The salinity levels of Abiyata, Langano, Shala and Ziway Lakes in the MER remain relatively low and stable as compared to those of the closed Lakes in the Afar depression such as Lake Afdera and Lakes in Dallol (Table 7.4). It is confirmed that, salinity increases from catchment divides to the valley floors and in the direction of groundwater flow (Salama et al., 1999). The observed relatively low salinity levels of the Lakes in the Ziway-Shala Lakes basin may thus possibly be thought to indicate a regional groundwater leakage enhanced by subsurface geologic structures.

The third information that support structural control of groundwater flow could be traced from investigation of the general groundwater flow system. Alley et al., (1999) have shown that the groundwater flow in any region can be categorized as shallow (local), intermediate (sub-regional) and deep flow system. According to Alley et al., (1999), the local ground-water subsystem occurs in the upper water-table aquifer that discharge to the nearest surface-water bodies (lakes or streams) and are separated by ground-water divides beneath topographically high area. The intermediate ground-water subsystem in the water-table aquifer in which flow paths originating at the water table discharge into a more distant one. A deep (regional) ground-water-flow subsystem lies beneath the water-table subsystems and is hydraulically connected to local and sub-regional one (Fig. 7.16).

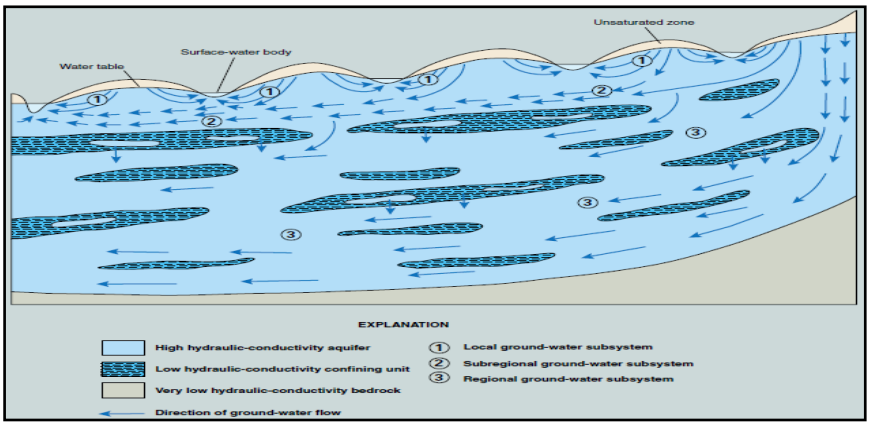

Fig.7. 16 A regional ground-water-flow system that comprises subsystems at different scales and a complex hydro-geologic framework taken from (Alley et al., 1999) and reference there in.

The gravity and magnetic data analyzed in this research work are anticipated to map the subsurface topography over rift floor all along the rift axis in the study area. The mapped subsurface interface geometries (Fig. 7.9 (c), Fig. 7.10 (b), Fig. 7.11(a), Fig. 7.12, and Fig. 7.14 (d)) resemble the conceptual model shown in Figure 7.15. The inferred subsurface structures are likely to control the sub-regional to regional groundwater flow of the area considered as they are deemed to satisfy the requirements necessary for groundwater flow on a regional scale.

Moreover, groundwater flow through aquifer types associated with rifting environments like that of the study area is likely to be governed by secondary porosity (Morgan et al., 2006) for reasons that active volcanic and tectonic activities due to rifting processes induce fracturing.

Comparison of the basin's water balance, salinity level of the lakes in the basin and the adopted conceptual groundwater flow model indicate that geologic structures control the groundwater dynamics in the study area. Generally, the groundwater dynamics among the inter-basins in the MER are likely to be governed by the subsurface geological structures, in particular layers topography mapped in this work. Therefore, it would be possible to safely conclude that groundwater outflows from the Ziway-Shala Lakes Basin to the Awash Basin (leakage between aquifers). This conclusion supports the previous findings of Abiyu Kebede (2007) who used integrated methods and approaches to map the groundwater flow in the Ziway-Koka Corridor indicating a likely groundwater migration from south to north in the corridor.

7.5 Conclusion

This study has made use of potential field data to recover depth to gravity and magnetic source bodies in the Ziway-Shala Lakes Basin. The automatic inversions, joint 2D gravity/magnetic forward modeling and 3D gravity structural inversion are employed to have a better understanding of lithological layer geometries. Horizons depicting gravity/magnetic source depths are estimated using the mentioned mathematical methods. Profile power spectral gravity depth analysis resulted in two source depths of 1.53 km and 2.87 km. 2D Werner De-convolution analysis of both gravity and magnetic data shows a source depths deepening northwards, as revealed by the fitted trend line to the geometries in vertical contact. Similarly, the depths to magnetic sources estimated using SPI method range from 1.1 km to 4.7 km and is thought to show deepening (thickening) of the low velocity overburden. Furthermore, the 2D joint gravity/magnetic forward modeling show similar results to those of the 2D Werner De-convolution and SPI results. The low velocity layer named as "sediment-volcanic" in the seismic study is categorized as six layers earth model in this study. The depth estimates resulting from

the automatic methods and gravity/magnetic joint 2D modeling are used to constrain the 3D structural gravity inversion. Accordingly, the 3D gravity interface inversion results obtained based on the Parker-Oldenburg algorithm fairly agree with the results of all the quantitative analysis methods used in this study. The combined interfaces geometries mapped with the various filtering techniques are in close agreement with each other and with the existing apriori geological and geophysical knowledge of the region. Furthermore, the shallow "sediment-volcanic" layers mapped using gravity and magnetic data appear to deepen northwards in consistent with those of the EAGLE seismic study results. The structures (layers topography) mapped in this research are believed to govern the inter-basins groundwater dynamics of the study region.

The analysis of gravity and magnetic anomalies in previous chapter directly linked to hydrogeology and geothermal resources of the area. In the next chapter the gravity data are further analyzed to map subsurface geology and geologic structures of the area and its possible link to hydrocarbon resources.

Chapter 8 Application of constrained 3D Gravity Interface Inversion techniques to map shallow Earth layer structures

8.1 Introduction

The geology of an area is characterized by varied rock types and geologic structures (Mammo, 2010) (Figs. 8.2, 8.3). Geophysical methods are the main tools used to investigate these hidden structures indirectly by characterizing physical properties of rocks (Williams, 2008) and geometries of interfaces (Feng et al., 2016). Nature of crustal structures and Moho depth undulations are some of the parameters get emphasized and studied in the Main Ethiopian rift (Mahatsente et al., 1999; Tessema & Antoine, 2004; Tiberi et al., 2005; Maguire et al., 2006; Mickus et al., 2007). The methods used to map these structures in cited references include controlled-source seismic survey, the 3D gravity forward modeling, 3D density inversion and Parker-Oldenburg structural inversion algorithms.

The Parker-Oldenburg algorithm is a multi layer 3D gravity inversion (Parker, 1972, Oldenburg, 1974) designed mainly to estimate the geometries of the interfaces which could be Moho depths or crustal structures thicknesses (Tiberi et al., 2005; Zhao et al., 2020). This method is also used in different area to estimate interface topographic variations that are responsible for the observed gravity anomaly (Salimi & Motlagh, 2012; Zhao et al., 2020; Feng et al., 2016; (Sabah & Al-rahim, 2018; Altinoglu et al., 2018). This algorithm allows us to calculate the three-dimensional geometry of the interfaces (layers) iteratively using an apriori initial model input information. This constraining information is obtained from previous geological and geophysical studies in the region under study. In addition to depths to the various gravity sources, calculated and misfit gravity anomalies are the results of the inversion. The convergence of iteration and the adjusted tolerable error limit should be guaranteed in each of the inversions run.

The seismic velocity model (Maguire et al., 2006) and 2.5 D gravity model (Mickus et al., 2007) were the two prominent surveys conducted under the Ethiopia Afar Geo-scientific Lithospheric Experiment (EAGLE) project. These studies were designed to map crustal structure thickness and Moho depths along the rift axis and over the rift floor. The maximum depth of investigation by velocity model was 50 km (Maguire et al., 2006) while the maximum depth of the gravity

model was 120 km (Mickus et al., 2007). Compared to depth of investigation, we observe that, these studies mapped the shallow subsurface structures with low resolution. We thus conclude that, the shallow/intermediate Earth layers studied in the Central Main Ethiopian Rift was least resolved.

In this study, ground based gravity data in the region are analyzed to understand layers structures/geometries (density contrast interfaces) of the shallow earth origin in the Ziway-Shala Lakes basin. To accomplish this task, 3D iterative structural inversion algorithm of Parker-Oldenburg (Oldenburg, 1974; Parker, 1972) is used. Furthermore, significance (if any) of the mapped structures for exploration of hydrocarbon resources in the region is considered.

8.1.1 Location of the study area

The Central Main Ethiopian rift (CMER) is part of Main Ethiopian rift bounded between $38^0$00'E-$39^0$30' E and $7^0$00'N - $8^0$30' N. The rift floor, the east and west fault escarpments and the NW and SE highlands characterize the physiographic features of the area (Fig. 8.1).

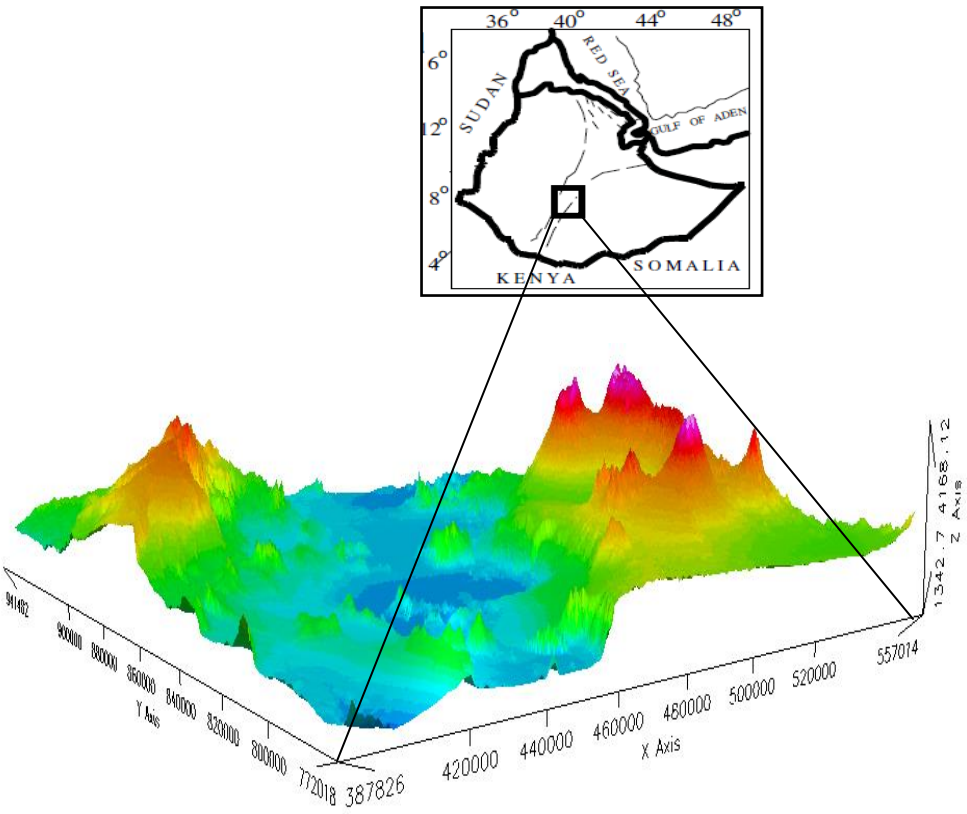

Fig. 8. 1 Location and topographic map of the Central Main Ethiopian Rift and its surroundings; the 3D view shows the geomorphologic features of the region

The Ziway-Shala Lakes Basin encompasses four main residual rift floor lakes (Le Turdu et al., 1999) respectively from north to south listed as Ziway, Abiyata, Langano and Shala lakes. This basin is hydrologically closed (Chernet et al., 2001) with its elevation varies from shallowest 1342 m a. s. l to highest 4168 m a. s. l (Fig. 8.1).

8.1.2 Geological and structural settings

The MER where the study area lies were developed over a span from the Oligocene to the Quaternary (Le Turdu et al., 1999; Woldegabriel et al., 2000). The current geologic and geomorphic features observed in the MER are as a result of geologic processes which include Cenozoic tectonism, volcanism and sedimentation activities. These process in the MER in general and CMER in particular resulted in observable geologic structures like faults (Woldegabriel et al., 2000), joints, contacts and fractures. These structures have surface expression shown in the geologic map (Fig. 8.2) and structural map (Fig. 8.3(b)). These surface structures mainly include the Wonji Fault Belt (WFB) (Mohor, 1962), Silti Debrezit Fault zone (SDFZ) and their associated boundary faults (Boccaletti et al., 1998). They generally have N-S, NNE-SSW, NE-SW, E-W and NW-SE (Korme et al., 2004) orientations. These structures are considered as young and active fault systems and are cross-cut by pre-existing NW-SE Mesozoic Ogaden rift fault (Korme et al., 2004) (Fig. 8.3(a)).

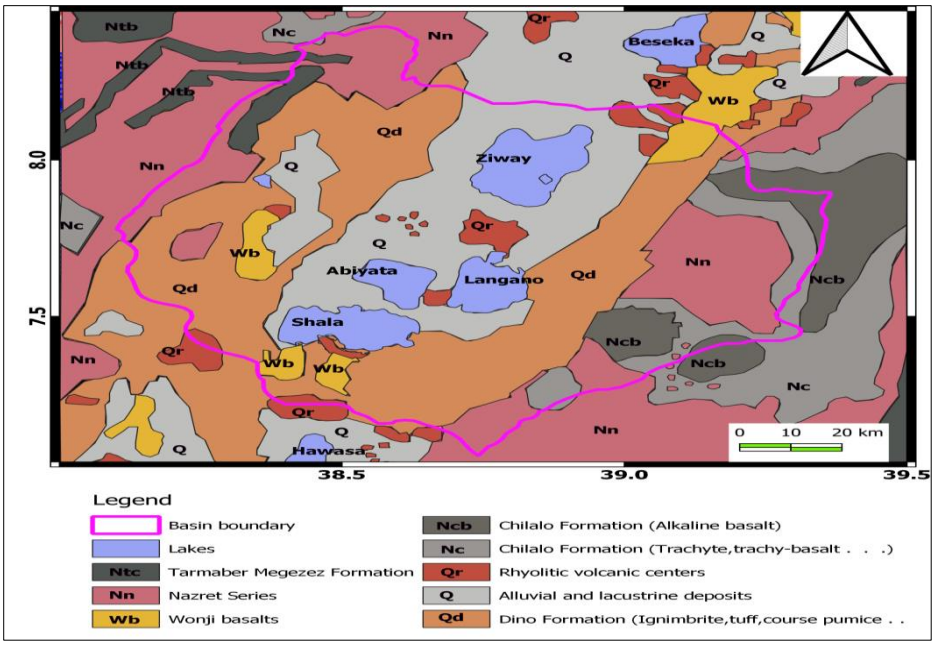

Fig. 8. 2 Geology map of the Ziway-Shala lakes Basin, Central Main Ethiopian rift modified from Tefera et al.(1996) and Molin and Corti (2015)**.**

The various lithologies within the CMER are poorly exposed (Woldegabriel et al., 2000). Woldegabriel et al (2000), however, identified localized crystalline basement, Mesozoic sedimentary rocks, and Miocene and Pliocene mafic and silicic lavas and tephra are exposed on the western rift margin of the CMER. Woldegabriel et al (2000) further identified crystalline basement, Mesozoic sandstone, limestone and mudstone on the north-eastern part of the CMER (along the southern Afar margin). The identified rocks have contributed much in the accumulation of sedimentary successions over the rift floor (Fig. 8.2).

Mesozoic succession is present in the Blue Nile Basin which formed a NW-trending rift (Gani et al., 2008), over the eastern margin of the Ethiopian Rift adjacent to the Ogaden Basin, over the southern border of the Ethiopian Rift around Dire Dawa town (Bosellini et al., 2001) and at Kella along the western margin of the CMER (Abebe et al., 2010).

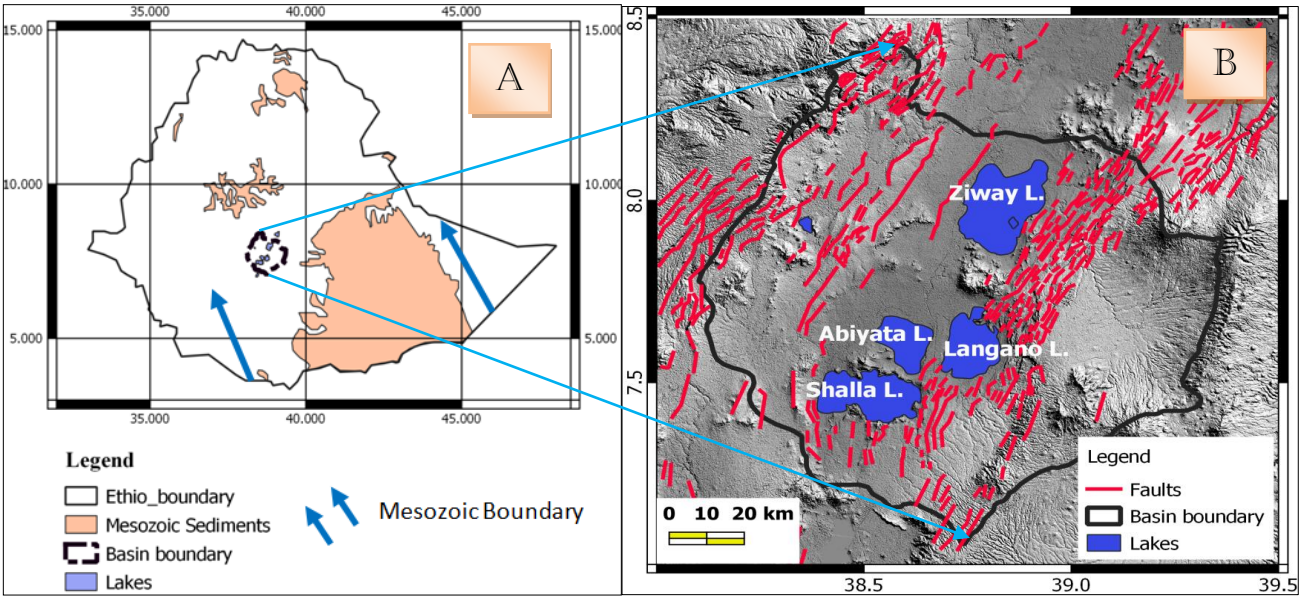

Fig. 8. 3 Mesozoic sediment surface outcrop, distribution and orientation of the outcrop surrounding the Ziway-Shala Lakes Basin (a) Fault map of the Ziway-Shala Lakes basin modified from Agostini et al., 2011 and Molin and Corti, 2015 (b)

The Mesozoic outcrop is observed to surround the study region of the Ziway-Shala Lakes Basin (Fig. 3(a)). Therefore, one could not deny the existence of Pre-Tertiary units (Mesozoic and Precambrian) at specified depth in the Central Main Ethiopian rift. Consequently, the conceptual model referring to these strata was constructed by Woldegabriel et al., (2000) and is schematically shown in Fig. 8.4.

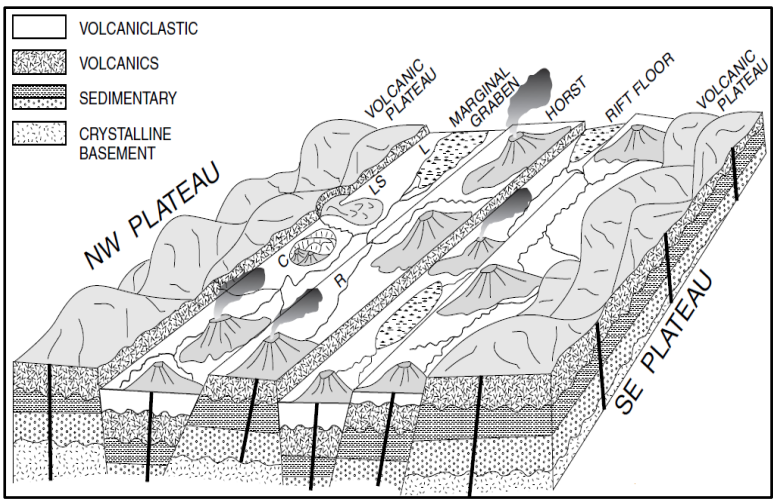

Fig. 8. 4 Schematic representation of stratified earth in the CMER adopted from (Woldegabriel et al., 2000).

Though volcanic, tectonic and sedimentation processes distort the strata and faulting characterizes the region under consideration, the strata corresponding to each fault block from top to bottom were approximated by Woldegabriel et al (2000) as volcanclastics, volcanics, sedimentary and crystalline basement formations (Fig. 8.4).

Similarly, a east-west oriented geological section was constructed over the Aluto-Langano geothermal field using well-log data (core samples) information (Cherkose & Mizunaga, 2018; Wilks et al., 2017; Hutchison et al., 2016). The resulting layers stratigraphy (Fig. 8.5) from top to bottom were identified as pyroclastic, lacustrine sediments, Bofa basalt, tuff and breccias, and Tertiary ignimbrite formation layers.

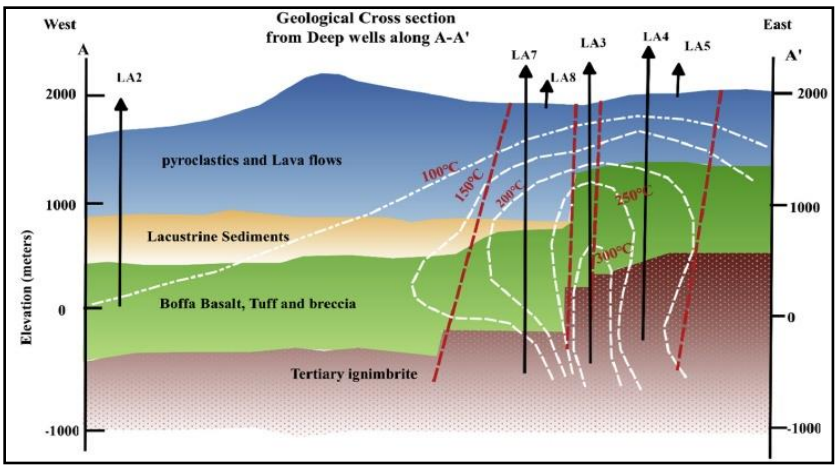

Fig. 8. 5 West-east geological cross-sections derived from core samples drilled in the Aluto-Langano geothermal field adopted from (Cherkose & Mizunaga, 2018). Depths of the eight wells range from 1300 to 2500 m below ground surface.

The stratified grids defining the layers, the type of rocks in each layer for estimating layer density, depths to interfaces are extracted from the geologic section produced using the well-log data (Fig. 8.5). These parameters are systematically put together to define an initial model information for gravity structural inversion given in section 8.2.2.

8.2. Methodology and Data

8.2.1 Governing Equation

The basis on which the gravity method depends (Telford et al., 1990) is summarized in two laws derived by Newton second law of motion

$$\vec{F} = m_o \vec{g} \tag{8.1}$$

and universal Law of gravitation

$$\vec{F} = -\frac{G \times m_o \times m}{r^2} \hat{e_r} \tag{8.2}$$

In Cartesian coordinates, F, describes the mutual force between two point masses, m and m_0 at two distinct points.

Equating equations (8.1) and (8.2), we have

$$\vec{g} = -\frac{G \times m}{r^2}\hat{e_r} \tag{8.3}$$

Extending the point masses to interfaces of constant density, the gravitational potential resulting from these layer of constant density contrast, bounded below by the horizontal plane $z = 0$ and above by the surface $z = h(r)$ at a position, r_0, is written as (Eq. 8.4) (Nagendra et al., 1996)

$$g(r) = G\rho \int_D dS \int_0^{h(r)} \frac{1}{r - r_0} dz \tag{8.4}$$

Where,

z is positive upwards,

G is universal gravitational constant, and

p is density contrast

The gravity response (anomaly) caused by an uneven and non-uniform layer of material with constant density is calculated by Fourier transform of gravity data and the sum of the interface topography's Fourier transform (Eq. 8.5) (Parker, 1972).

$$F[g\ (r)] = 2\pi G\Delta\rho e^{-|k|z_0} \sum_{n=1}^{\infty} \frac{|k|^{n-1}}{n!} F[h^n(\vec{r})] \tag{8.5}$$

Oldenburg (1974) rearranged this equation to compute the depth to the undulating interface from the gravity anomaly by means of one dimensional Fourier transform in an iterative fixed-point equation (Eq. 8.6).

$$F[h(r)] = \frac{F[g(r)]e^{|k|z_0}}{2\pi G\Delta\rho} - \sum_{n=2}^{\infty} \frac{|k|^{n-1}}{n!} F[h^n(r)] \tag{8.6}$$

Where:

$F[g(r)]$ is the Fourier transform of the gravity anomaly,

G is Newton's gravitational constant, 6.67 x $10^{-11}$$Nm^2kg^{-2}$

r is a horizontal plane

$\Delta\rho$ is the density contrast across the interface (two media),

k is the wave number,

n is an integer

$h(r)$ is the topography of the interface

z_0 is the mean (reference) depth of the horizontal interface or observation plane

$F[h^n(r)]$ is Fourier transform of the interface topography

Parker–Oldenburg iterative expression (Eq. 8.6) allows us to calculate three-dimensional geometry of the interface (layer) iteratively using interface density, $\Delta\rho$, and mean depth, z_0. The first term of equation (6) is computed by assigning *h(r)*=0. This value, *h(r),* is then used in the equation to evaluate a new estimate of *h(r+1).*This process is continued until a reasonable solution is achieved and is convergent.

The inversion operation (Eq. 8.6) is unstable at high frequencies and thus it requires a high-cut filter (low-pass) in the frequency domain for the convergence of iteration (Eq. 8.6) to be guaranteed. Oldenburg (1974) proposed a low-pass filter of the form (Eq. 8.7)

$$B(k) = \begin{cases} 1 & \left|\frac{k}{2\pi}\right| < WH \\ \frac{1}{2}\left[1 + cos\left(\frac{k-2\pi WH}{2(SH-WH)}\right)\right] & where \quad WH \le \left|\frac{k}{2\pi}\right| \le SH \\ 0 & \left|\frac{k}{2\pi}\right| \ge SH \end{cases} \tag{8.7}$$

The inversion is then governed by free parameters, density contrast, $\Delta\rho$, datum level, z_0, and the filter $B(k)$. Existences of these free parameters result in non-uniqueness of the gravity inversion. With the adjustment of the filter parameters, $WH\ and\ SH$, however, we are guaranteed the convergence of the iterative process. According to Oldenburg (1974), the error norms and convergence criterion respectively given as

$$S_n = \underset{k}{\overset{max}{Over\ all}} \left| \frac{|k|^{n-1}}{n!} F[h^n(r)] \right|$$

$$\frac{S_n}{S_2} < E \tag{8.8}$$

Where, E is some sufficiently small predefined value

The convergence criterion (Eq. 8.8) set by Oldenburg (1974) for such fixed point iterative problem (Eq. 8.6) is different from the convergence criterion that exists on any Numerical methods text book.

8.2.2 Constraints for Gravity Inversion

An apriori information about the subsurface are required for an inversion to be carried out using Parker-Oldenburg algorithm. This information includes the number of layers, mean depth to top of horizons and density of interfaces. The identified parameters are used as a starting model for determining the calculated and misfit gravity anomalies through forward modeling.

The average crystalline basement top estimated from gravity data analysis is 3.0 km deep (Kebede et al., 2020). Following the evidences documented in section 8.1.2, Mesozoic layer is identified as fifth layer below Tertiary ignimbrite and above crystalline basement layer. Here, however, a need to approximate the depth to top of Mesozoic layer.

Multi-Layer 3D Gravity forward calculation is performed by choosing different depths to top of Mesozoic layer (Table 8.1, Column 6) and sensitivity of the changes to the top depth of this layer is documented. The computation resulting in a least mean square error (5.00162 m) happened at a depth of 2.9 km which could be taken as depth to top of Mesozoic layer (Table 8.1, Column 6).

SN	Minimum	Maximum	Mean	Std. dev	Depth to top of Mesozoic layer (km)	Remark
	in m					
1	-16.4676	38.79607	6.00792	6.42845	2.6	
2	-16.8031	38.46064	5.67248	6.42845	2.7	
3	-17.1385	38.12521	5.33705	6.42845	2.8	
4	-17.4739	37.78977	5.00162	6.42845	2.9	Chosen depth

Table 8. 1 Sensitivity analysis conducted to determine the depth to top of Mesozoic layer through multi-Layer 3D gravity forward calculation. Start the invasion at shallow depth of 2.6 km then follows 2.7 km, 2.8 km and 2.9 km. The minimum error found to be at depth of 2.9 km.

Based on well-log data geological section (Cherkose & Mizunaga, 2018), geophysical studies in the study region (Kebede et al., 2020; Mammo, 2010; Maguire et al., 2006; Woldegabriel et al., 2000; Alemu, 1992) and gravity forward modeling conducted in this research, six layers with depths to top and density are approximated. The initial model is defined by a number of stacked surface horizons (Fig. 8.6) with density distributions specified for the layer (Table 8.2). These stacked grids represent, major geological boundaries where density contrasts occur.

2Layers	Layer Geology	Sub Layers Geology	Depth to top of the layer (m)	Initial Density for the interfaces (gm/cc)	The source of the information obtained from
1	Pyroclastic and Lava flows (Silicic products)	Per alkaline rhyolite lava **(47-201)_ 2.6gm/cc**	**0**	2.477	(Alemu, 1992)
		silicic breccias and weakly welded tuffs **(201-604)_ 2.43gm/cc**			
2	Lacustrine sediments		1000	2.34	
3	Bofa basalt, tuff and breccias		1500	2.81	(Alemu, 1992)

4	Tertiary Ignimbrite	2500	2.58	(Alemu, 1992)
5	Mesozoic sediments	2900	2.5	(Mammo, 2010)
6	Crystalline basement	3000	2.74	(Kebede et al., 2020)

Table 8. 2 The depth and density from top to bottom estimated from Well-log data, seismic study, gravity interpretation result and previous geological studies.

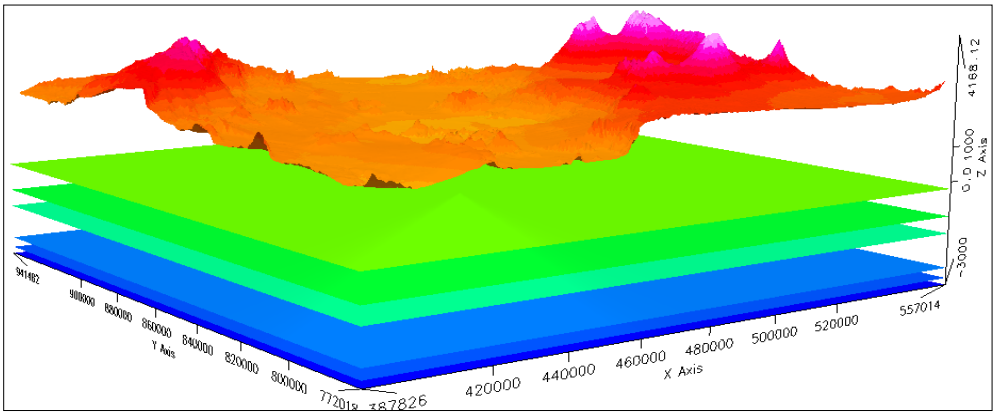

Fig. 8. 6 Initial model created from the available geological and geophysical data with different colors representing stacked horizons where density contrasts occur. The top most layers represent the elevation (DEMs) of the study area (CMER).

Setting the geological constraints help to minimize the degree of non-uniqueness of gravity data interpretation in the region considered. The overall 3D forward modeling (Parker, 1972) and 3D interface inversion (Oldenburg, 1974) procedures are summarized in the following flow chart (Fig. 8.7).

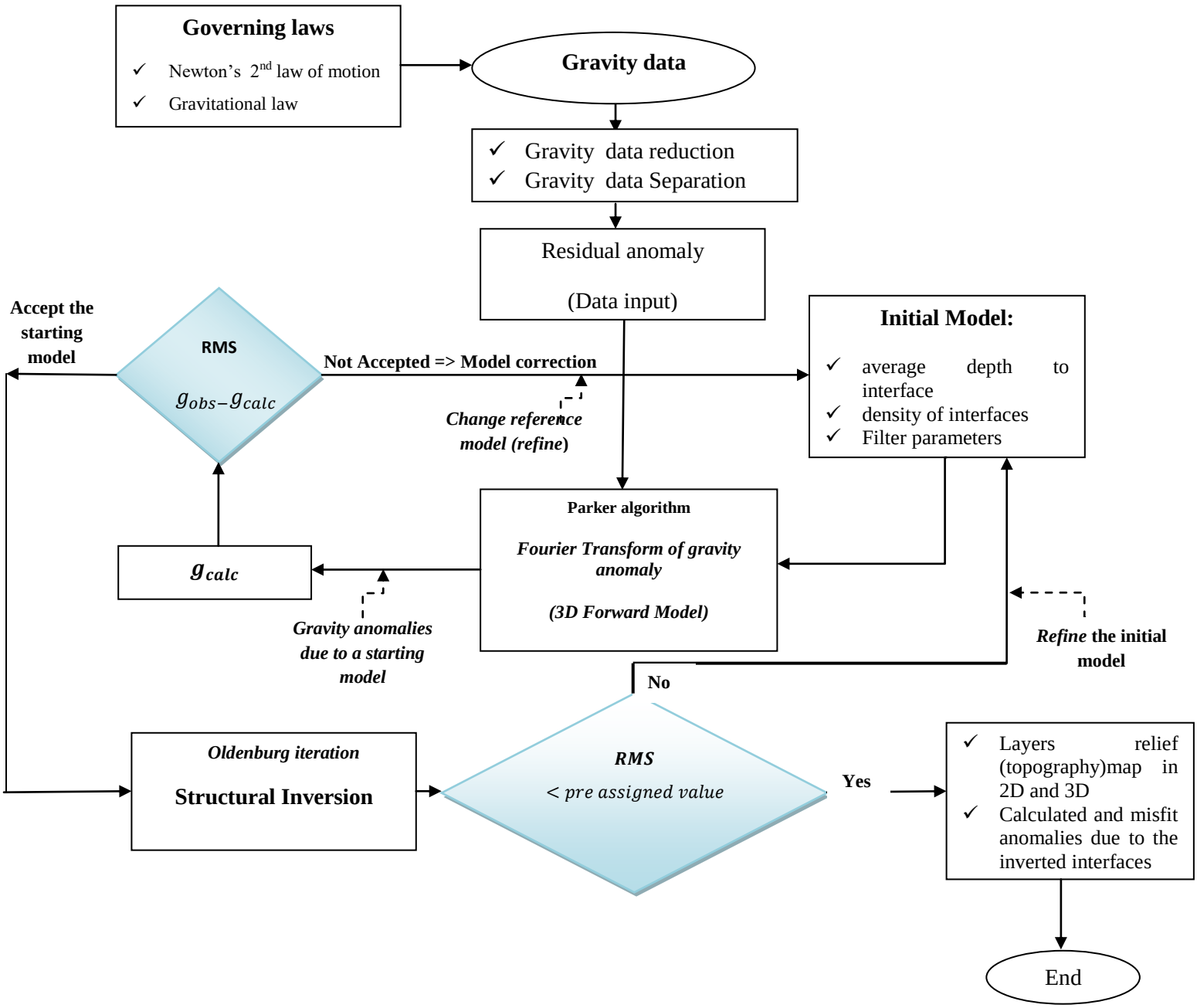

Fig. 8. 7 Summary of the 3D forward modeling and inversion process

The decision symbol on the top left of the flowchart (Fig. 8.7) help to check whether the initial model perfectly suit our predefined error tolerance (e.g. 0.01 mGal). If the initial model doesn't fulfill the criterion, we work iteratively on setting up a new initial value of the parameters. Layers geometries, density and depth (topography) of the interfaces are some of the parameters

that need to be improved through repeated refinement and forward modeling. The second decision symbol (bottom) (Fig. 8.7) helps to decide whether the 3D gravity interface structural inversion result is acceptable or not. This is based on misfit (error) anomaly map computed by taking difference of observed and calculated anomalies.

Based on the governing equation (Eq. 8.6), 3D interface inversion of residual gravity anomalies over the Ziway-Shala lakes basin are performed to estimate layers undulations of crystalline basement, Mesozoic sediment and Tertiary Ignimbrite formation layers.

In addition to structural inversion, single density interface inversions are performed to estimate the density of layers after structural inversion run. This inversion calculates the error grid cell by cell and does an estimate of the density for all cells, then averages them to get an overall density change.

8.2.3 Gravity Data

About 3013 ground based secondary gravity data were reprocessed, homogenized to the International Gravity Standardization Network 1971 (IGSN71) and corrected (reduced) to produce the Bouguer gravity anomaly (Fig. 8.8b). The upward continuation height of 6.0 km (Kebede et al., 2020) is used to estimate the regional anomaly (Fig. 8.8c) and this anomaly is subtracted from Bouguer gravity anomaly to have the residual anomalies of the region under study (Fig. 8.8d).

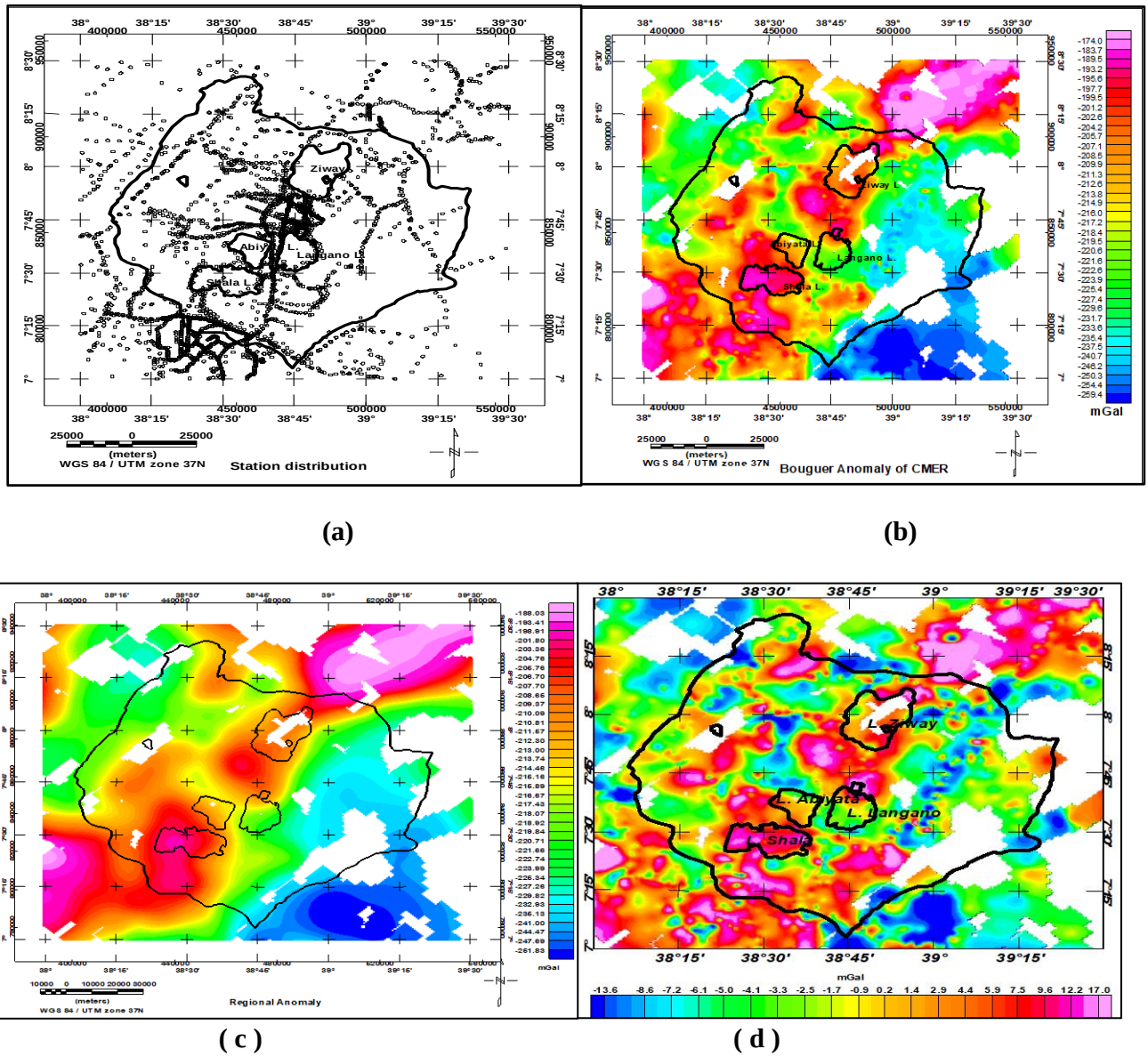

Fig. 8. 8 Gravity stations distribution map (a) Bouguer gravity anomaly map (b) regional gravity anomaly map (c) and residual gravity anomaly map (d)

Jacobsen (1987) stated that when the potential field data are upward continued to a height $'2\boldsymbol{Z}'$; it maps the sources found at and below the depth $'\boldsymbol{Z}'$. The residual gravity anomalies depicted in Fig. 8.1d) has revealed gravity source bodies located to depth of 3 km. It is these anomalies that are subjected to structural inversion for layers geometries in the region under study.

8.3. Results

Once the initial model is complied as documented in section 8.2.2, the multi layer, surface based frequency domain forward and inverse modeling are carried out using Parker-Oldenburg algorithm. A top most layer in Fig. 8.9 is the residual gravity anomalies inverted for interfaces geometries.

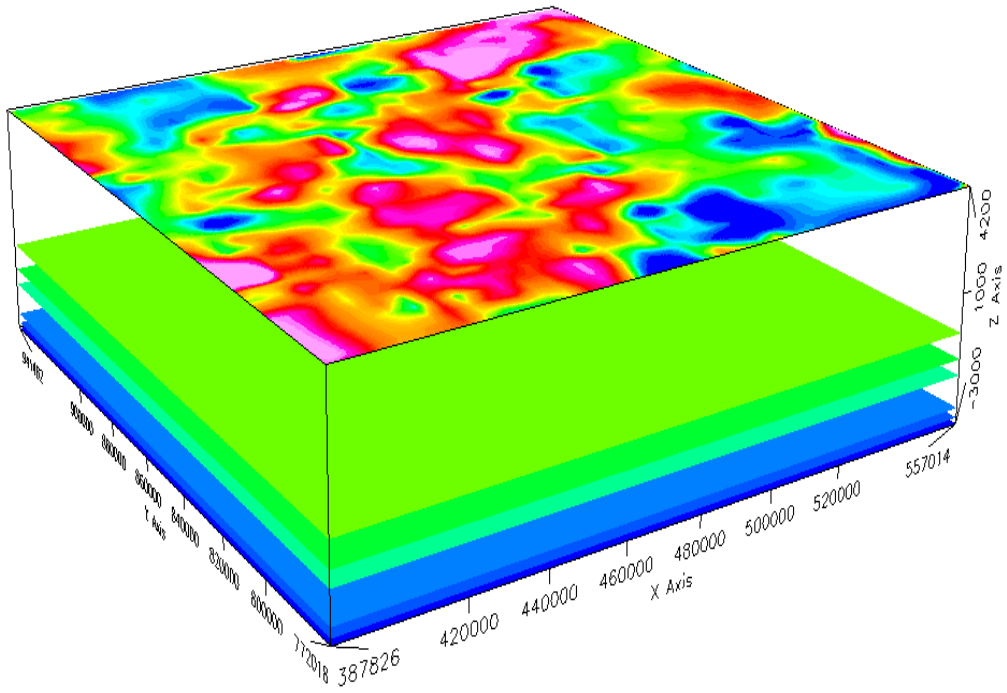

Fig. 8. 9 Six geological horizons stacked and configured at depths to top of 0 m, 1000 m, 1500 m, 2500 m, 2900 m and 3000 m depth and corresponding layers densities $\mathbf{2.477g/cm^2}$, $\mathbf{2.34\ g/cm^2}$, $\mathbf{2.81\ g/cm^2}$, $\mathbf{2.58\ g/cm^2}$, $\mathbf{2.5\ g/cm^2}$ **and** $\mathbf{2.74\ g/cm^2}$ are identified from well-log data, previous geological and geophysical analysis in central Main Ethiopian rift.

8.3.1 Inversion on for the basement

We start the inversion with the deepest interface (crystalline basement) formation layer with the aim of fitting the calculated and the observed residual anomalies. Correspondingly, after an inversion the original layer geometry is altered.

The gravity data analysis in the study area shows that the crystalline basement horizon is found at an estimated mean depth of 3.0 km (Kebede et al., 2020). The reference (initial) depth of the horizon is then set at -3 km and layer density set to 2.74 g/cm^3. Top of this layer is Mesozoic sediment with a density of 2.5 g/cm^3. The average density contrast is thus 0.24 g/cm^3. The smallest and greatest cut-off frequency parameters are chosen as 0.5 and 0.7 km^{-1}, respectively. The maximum inversion iteration number is set to 20 and convergence limit is set as 0.01mGal. Since the objective of the study focus on shallow earth, the residual gravity anomaly is inverted for layers undulation and thickness. The result of which given in (Fig. 8.10 (a)-(d))

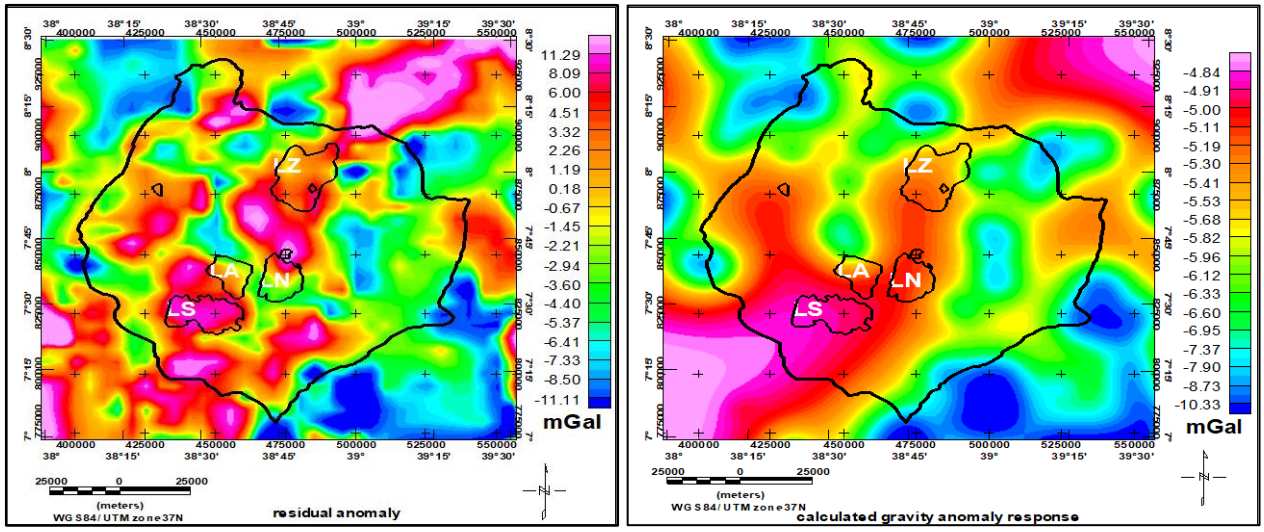

(a) (b)

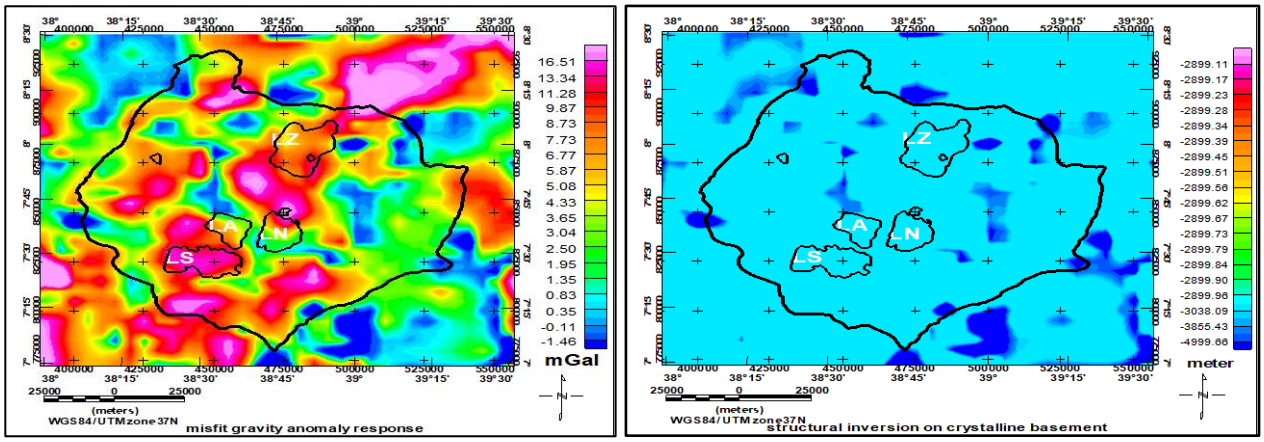

(c) (d)

Fig. 8. 10 Maps of the residual gravity anomaly (a) calculated gravity anomaly due to topography of crystalline basement (b) and the difference between observed and calculated gravity anomaly (c). The basement undulation map (crystalline basement-Mesozoic layer interface) obtained through application of structural inversion on crystalline basement layer and using residual gravity anomaly (d).

The structural inversion on this layer modified the initial constant layer and generates crystalline basement topography of the area (Fig. 8.10d). The inversion converges after 12 maximum iterations run. In this modeling, the minimum error is -12.0 m, maximum error is 37.1m, and means error is 5.7m and standard deviation 5.5 m.

The calculated crystalline basement topography (Fig. 8.9d) shows that the layer shallowest depth starts at a depth of 2899 m and extends down from this depth. The basement topography gets deeper at some specific area near northern water divide (Meki area and its surroundings), floor of Gademota caldera and N to NNW of Abiyata Lake. Here only the anomalies within the rift floor get interpreted to avoid edge effects caused by the calculation process.

8.3.2 Structural inversion for the Mesozoic surface

Initially before structural inversion on Mesozoic surface, the depth of this horizon is set at -2.9 km and the layer density set to 2.5 g/cm^3. Top of this layer is Tertiary ignimbrite layer with a density of 2.58 g/cm^3. The average density contrast is thus 0.08 g/cm^3. The smallest and greatest cut-off frequency parameters are chosen as 0.5 and 0.7 km^{-1}, respectively. These high-cut filter parameters should guarantee the convergence of the iterative scheme. The convergence limit is set at 0.01 mGal. The maximum inversion iteration number set to 20. The iteration converges after an iteration run of 2 with root mean square error of 5.8m and standard deviation of 5.4 m. The inversion result shows that the shallowest of Mesozoic sediment found at around 2499m which is -401m from the reference depth 2900m and extends down to -3060m. The maximum thickness of this layer is thus 561m. The sediments is found at the rift floor nearby Meki area extending south-west to the Gademota caldera and to north of Abiyata lake.

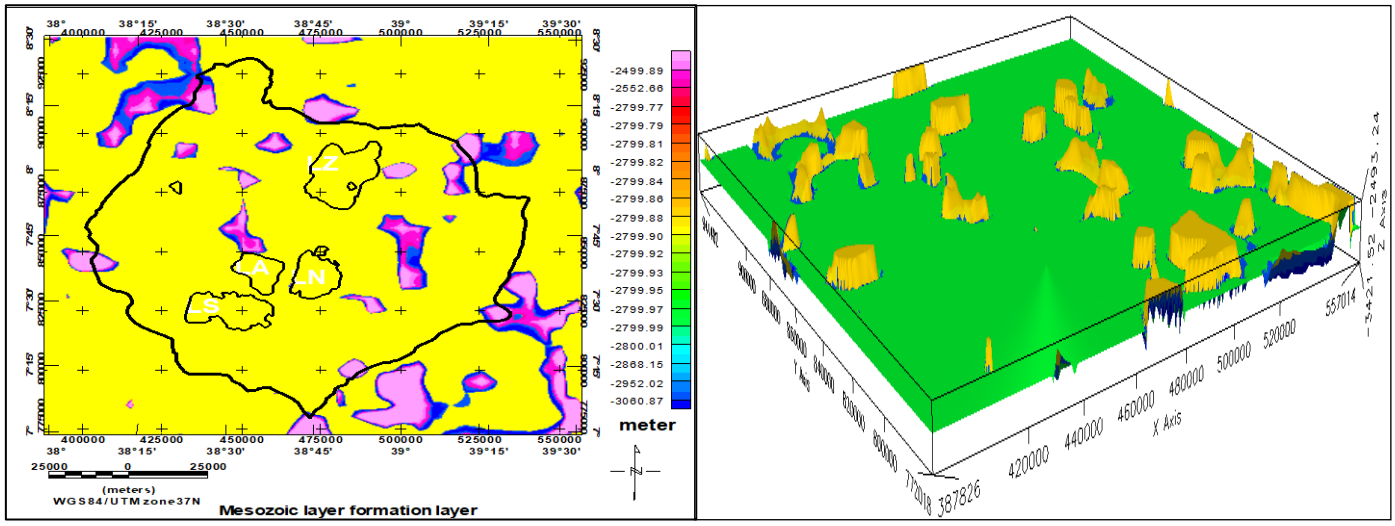

(a) **(b)**

Fig. 8. 11 Mesozoic layer topography in 2D view (a) and 3D view (b)

8.3.3 Structural inversion for tertiary ignimbrite layer

To run the structural inversion on Tertiary ignimbrite layer, the depth of the horizon was set at -2.5 km and the layer density set to 2.58 g/cm^3. Top of this layer is Bofa basalt layer with a density of 2.81 g/cm^3. The average density difference put into calculations is considered to be 0.23 g/cm3. The cut-off frequency, the maximum iteration number and convergence limit is similar to the previous inversion setup. After structural inversion, the layer extends up -1608 m from the reference depth -2500 m and moves down -2900 m from this depth. The iteration converges at an iteration number 9. The RMS error is 3.8 m and standard deviation of 4.6 m. The maximum thickness of this layer is 1292 m. The shallowest depth is found at the rift floor, nearby Meki extending south-west to Gademota caldera and to north of Abiyata lake. Thick Tertiary ignimbrite is correspondingly found at the mentioned locations.

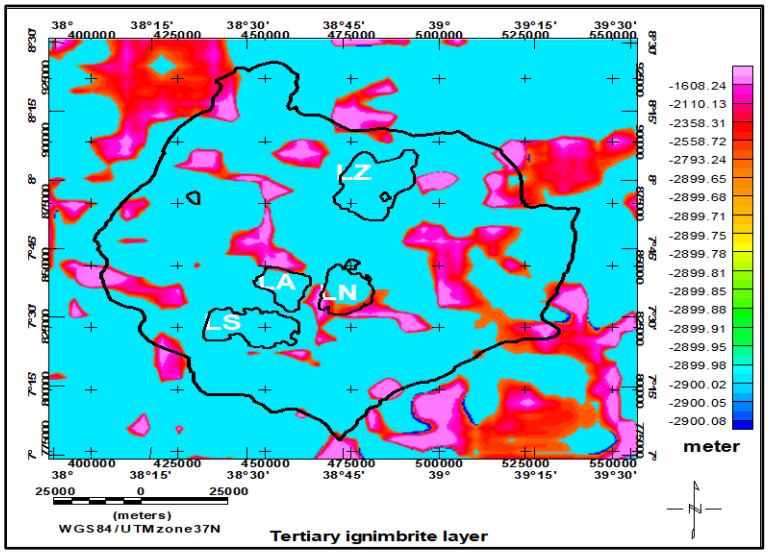

Fig. 8. 12 Relief map of tertiary ignimbrite formation layer

8.4. Discussions

8.4.1 Layers geometry through structural inversion

The constraining parameters used in gravity interface inversion are compiled from previous geological and geophysical studies carried out in and around CMER. These information help to generate a better inversion result within the set tolerable error limit. A priori information defined in section 8.2.2 help us only to define constant density for each layers with corresponding single density values. Though the cases, the layers geometries are changed as an inversion iteration progresses. Inversion are carried out first on crystalline basement layer, secondly on Mesozoic layer and finally on Tertiary ignimbrite layer. The summery of the inversion result are described in Table 8.3.

Inv. N	Minimum	Maximum	RMS error	Std. dev	Inversion surface/layer	Total _ iteration for Convergence	Minimum value (m)	depth to top of the layer (m)	Shallowest depth (m)	Estimated max. layer thickness (m)
	in meter									
1	-12.05	37.12	5.75	5.47	Crystalline basement	12	-	-3000	-2899	
2	-11.87	37.14	5.81	5.44	Mesozoic layer	2	-3060	-2900	-2499	-561
3	-12.61	33.76	3.83	4.65	Tertiary Ignimbrite	9	-2900	-2500	-1608	-1292

Table 8. 3 Successive structural inversions statistics on stated layers

In all inversion run the iteration converges and mean square error ranges from 3.83 to 5.75 meter. The estimated layers thickness (Table 8.3) for each of the three inversion layers and their undulations give a good first approximation to topographic map of the layers.

The inversion on crystalline basement layer modifies the geometry of the layer (grid) and produces the undulation of the surface with estimated shallow depth of 2899 m. This depth is

measured from surface and extends down from this depth. The inversion on Mesozoic layer produces the shallow topographic depth of 2499 m and the deepest depth of 3060 m. The estimated maximum layer thickness for Mesozoic sedimentary formation is 561 m. The inversion carried on Ignimbrite formation layer result in a shallow top of 1608 m and deepest depth of 2900 m. The thickness of the Ignimbrite formation layer is then estimated 1292 m. Comparison of this layer thickness with Tertiary ignimbrite layer geologic section thickness (Fig. 8.5) are made and compared. The comparison is found to be in a good agreement.

The inversion on the remaining top three layers such as Pyroclastic and Lava flows (Silicic products), Lacustrine sediments and Bofa basalt, tuff and breccias formation layers gives noised result and should be excluded from interpretation.

8.4.2 Implications for hydrocarbon potential

Characterizing the geology of an area is an important task to understand the role that geology play in the growth of petroleum reserves. Gravity method is one of the geophysical methods used to delineate oil and gas-bearing sedimentary basins and locating main trap structures (Zhang et al., 2019). These generally include locating source rocks, reservoir rocks; trap (seal) and the wider basin structures that are responsible for accumulation of hydrocarbon resources.

The hydrocarbon source rocks potential investigations are the main parameter need to be studied for oil and gas resources. These type of rocks are composed of very small mineral fragments in between them are remains of organic material. This study identified a Mesozoic layer which lies in between crystalline basement layer and Tertiary ignimbrite (sedimentary) layer which could help the accumulation of these remains. The identified Mesozoic interface was believed to be formed as a result of transgressive-regressive processes in Mesozoic era.

The estimated thickness of volcanic overburden including Tertiary sedimentary is 2.5 km (Fig. 8.5). Growth of petroleum reserves needs such kind of geology where the sedimentary basin overlain by volcanic rocks (Mammo, 2010). For example, in Yerer Tulu Welel Volcanic Lineament (YTVL) zone the presence of volcanic activity and low enthalpy geothermal systems

lead to the heating of the underlying Mesozoic sediments which then liberate a considerable carbon dioxide gas and other gases (nitrogen, sulphur and argon) (S. Kebede, 2013).

The identified Mesozoic and Tertiary sedimentary formation thickness is estimated to -1853 m. These formations possibly help the growth of hydrocarbon resources in the region considered. In this region, the observed temperature increases with depth (Cherkose & Mizunaga, 2018) (Fig. 8.5) , when this temperature exceed 120^{o} C the organic remains within the rocks begin to be "cooked" and as a result of which oil and natural gas are formed. These suggest the presences of organically rich sedimentary rocks (source rocks).

In the study region, the volcanic overburden claimed to turn the sediments into hard rock strata with further burial guarantee temperature increase. Furthermore, the region is dominated by active volcanism and tectonics which is manifested by hydrothermal fluids and fumaroles. These fluids are important in mobilizing and moving hydrocarbons (Schutter, 2003) to reservoirs (Fig. 8.13). The hydrocarbons matured in Mesozoic sedimentary rocks and can migrate vertically or laterally into structurally higher igneous rocks (tertiary ignimbrite). These rocks are considered to be porous and permeable and might act as good hydrocarbon reservoirs.

Lacustrine sediment layer exists above Tertiary ignimbrite layer at top depth of 1000 m (Fig. 8.13) which might act as a seal or trapping structures.

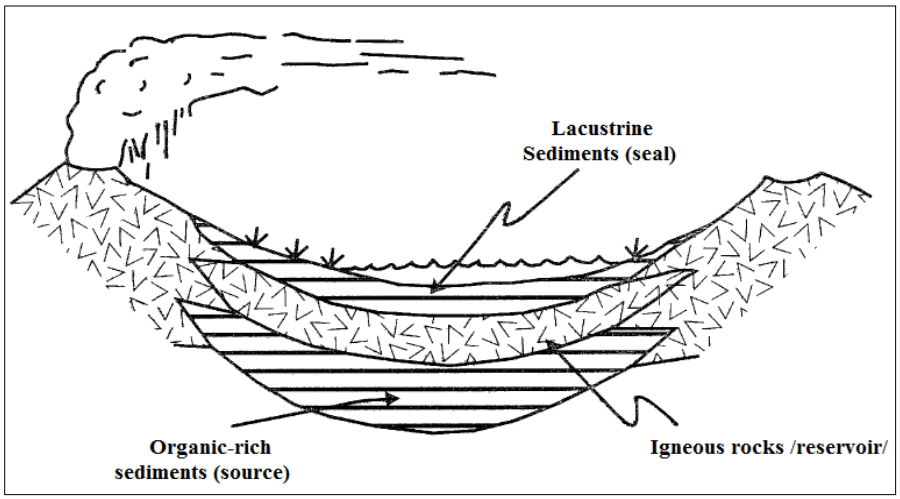

Fig. 8. 13 Theoretical hydrocarbon system model based on elements commonly found in rift basins taken from (Schutter, 2003)

Hutchison et al., (2015) estimated total carbon dioxide (co_2) emitted from Aluto volcanic center to be in between 250–500 $t\,d^{-1}$. Seismicity study in the same area was conducted to map magmatism, faulting and hydrothermal circulation (Wilks et al., 2017). Both studies have shown existence of magma storage at about 5 km depth. In contrary, Magneto-telluric (MT) study conducted at Aluto volcano (Samrock et al., 2015) showed that there is no magmatic sources directly under Aluto. The other study that confirm Samrock et al., (2015) result was conducted by Hübert et al., (2018), which evidenced the non-existence of conductive region at 5 km depth.
The previous two studies (Wilks et al., 2017) (Hutchison et al., 2015) are against the later two studies (Samrock et al., 2015) (Hübert et al., 2018) on the location of magma storage. Magnetic data analysis (Chapter 6) conducted in the region found to support the results of the latter two findings. Therefore, we conclude that Aluto volcano deprive of heat source (magma) sources beneath. However, one should ask the source of co_2 degassing.
The possible source of this gas is claimed to be as a result of combustion of fossil fuels (coal, oil, and natural gas) or magma storage. In North and North-West of the Central Main Ethiopian Rift for example the CO2 gas emanates from the Mesozoic sediment de-carbonation (S. Kebede, 2013). This has led to the formation of numerous naturally sparkling springs, notably around Ambo, Woliso, Diddessa Valley, South of Lake Tana, and Filwuha thermal springs around Addis Ababa (S. Kebede, 2013).
This study for the first time identifies Mesozoic formation in the region considered which could possibly be the source of carbon dioxide gas.

The Mesozoic layer structure/geometries mapped in this study are based only on the input constraining information (Table 8.2) and does not reflect the Mesozoic source at any other layers and outcrop at the surface. The resource exploration however needs detail investigations on how the geology of the area significantly controls the growth of hydrocarbon (petroleum) reserves with more refined data sources. The existence of the Mesozoic layer within the basin leads the researcher to suspect hydrocarbon resources though detail investigation is required.

8.4.3 Constant density inversion

Constant density inversion calculates the error grid cell by cell and does an estimate of the density for all cells, then averages them to get an overall density change. The procedure is based on Parker's algorithm and with an initial layer density for the interfaces (Table 8.2) and layers

configuration (Fig. 8.9). To compute a single density for an interface we first estimate the layers horizons relief (topography) as shown in Figure 8.10d, Figure 8.11a and Figure 8.12 using structural inversion. The computed and optimized constant density of each selected model layer is given in Table 8.4.

Layers	Layer Geology	Sub Layers Geology	Depth to top of the layer (m)	Initial Density for the interfaces (gm/cc)	single density inversion after structural inversion (gm/cc)
1	Pyroclastic and Lava flows (Silicic products)	Per alkaline rhyolite lava (47-201)_2.6gm/cc silicic breccias and weakly welded tuffs (201-604)_ 2.43gm/cc	0	2.477	2.4983898748
2	Lacustrine sediments		1000	2.34	2.3861097941
3	Basalt, tuff and breccias		1500	2.81	2.8280985006
4	Tertiary Ignimbrite		2500	2.58	2.5816582477
5	Mesozoic sediments		2900	2.5	2.4892385754
6	Crystalline basement		3000	2.74	2.7538995576

Table 8. 4 Interface geology, depth to top, Initial density and optimized density columns. Single density inversion is run after structural inversion geometric modifications.

The recalculated gravity anomalies and the misfit (error) gravity anomalies after constant density inversion are shown respectively in Fig. 8.14a,b.

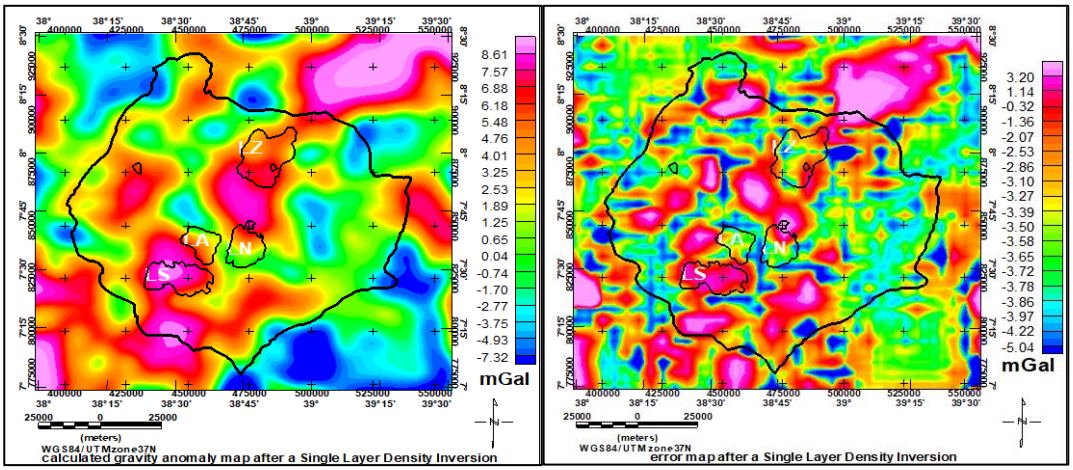

(a) (b)

Fig. 8. 14 Multi-Layer 3D Gravity Forward Calculation of calculated gravity anomaly (a) and the misfit gravity anomaly (b) using optimized constant density of each stacked layers (Table 8.4).

Before geometric and constant density inversion the ranges of observed residual gravity anomalies lies between -11.11mGal to 11.29 mGal. The density and geometric change optimizes the calculated gravity anomalies to lie in between -7.32 mGal and 8.61mGal and the misfit anomaly lies in between -5.04 mGal and 3.2 mGal.

8.5. Conclusion and Recommendation

Shallow crust structures of the Ziway-Shala Lakes Basin are investigated using 3D structural inversion of Parker-Oldenburg iterative program. The algorithm calculates the subsurface topography resulting from density contrasts between interfaces. In each step the errors between the observed and calculated anomalies are computed at all points by iteratively improving the misfit. The study initially approximated the layers as stratified strata though tectonic, volcanic and sedimentation processes distorts the strata and faulting are the main characteristics properties of the region under consideration. 3D structural inversion of residual gravity anomaly is performed with parameters of layers information obtained from previous geological and geophysical studies. Six layers are identified which are listed from top to bottom include Pyroclastic and volcanic rocks formation, Lacustrine sediment formation; Bofa baslt, tuff and breccias formation; Tertiary ignimbrite formation; Mesozoic sediment formation and crystalline basement formation layers. The density contrast is defined by defining the density to each six

horizons. The geometries of the last three layers (relief maps) are produced in each inversion run (Fig. 9d, Fig. 10 and Fig. 11). The layers thicknesses are validated using well-log data drilled for the purpose of geothermal study. This study reveals the presence of a Mesozoic layer starting at a shallow depth of -2499 m extending to a deeper depth of –3060 m and having a maximum thickness of -561 m. Beneath the Mesozoic formations, a crystalline basement layer of shallowest depth start at an approximate depth of –2899 m and extends downwards. The inversion results give fair first approximations to the topographic map (lithostratigraphy) of the layers in the region considered. The fact that the basin is a closed sedimentation processes characterizes the region under consideration. The research has also identified the presence of Mesozoic sediments underlying a thick volcanic cover of thickness 2.5 km. This mapped stratified geology underlying the sedimentary basin and overlain by volcanic rocks might be favorable for the growth of hydrocarbon deposits in the area. The researchers thus claim the possible existence of hydrocarbon resources in the area. From previous observations made in area the source of CO2 gas could not be related to a magma chamber as there is no magma under the Aluto area. Therefore, the source of CO2 could probably be due to metamorphic de-carbonation of carbonate rocks of Mesozoic origin.

Parker–Oldenburg algorithms used in this study assumed either a constant or a laterally varying density for layers involved. In reality, densities vary both vertically and laterally for a given strata. The results obtained are approximation and crude generalization of interfaces/layers topography. Thus, it is much required to work on gridded potential field data either air borne or ground based for a better geologic and structural mapping. Furthermore, it is required to update the results obtained by incorporating more refined initial models whenever information about the subsurface is obtained.

To supplement subsurface structures mapped in previous chapters from gravity and magnetic data, the shallowest subsurface structures (bed rock geometries) of the particular area are mapped from analysis of ambient noise seismic data, in the next chapter.

Chapter 9 Passive Seismic Survey carried to map the shallow subsurface topography

9.1 Introduction

To supplement the above potential field geophysical study results (Chapter 4 to Chapter 8), passive seismic technique consists in recording seismic noise (seismic tremor) survey are conducted. The noise sources are wind, ocean waves and anthropogenic activity which are considered as surface Rayleigh and Love waves. These sources produce the ambient seismic energy which propagates in continuous excitation creating seismic resonance within the nearby subsurface geologic materials. The resonance is a function of shear-wave velocity of the subsurface layers and thickness which its magnitudes either amplified or diminished depending on acoustic impedance contrast. TROMINO seismometer is an ultra-compact and ultra-lightweight instrument used to record the three component ambient seismic noise data (*TROMINO User's Manual*, 2017). In recent years the analysis of this data become widely used for seismic site effects (Panzera et al., 2013) and seismic microzonation (Gosar, 2017), passive seismic stratigraphy (Johnson & Lane, 2016), Vs30 estimation from constrained H/V curve fitting studies (Roser & Gosar, 2010) and Archaeological Prospection (Zeid et al., 2017). The method is based on the spectral ratio of Horizontal to Vertical component (HVSR) of microtremors (Nakamura, 1989) which help to extract the fundamental frequency of soft sediments overlying bedrock.

This study targeted to determine the very shallow impedance contrast layer geometry (bed rock topography) of the northern end of the Ziway-Shala Lakes Basin, near water divide (Fig. 9.1). To accomplish this task the horizontal and vertical components of passive seismic data are analyzed to define depths to impedance contrast.

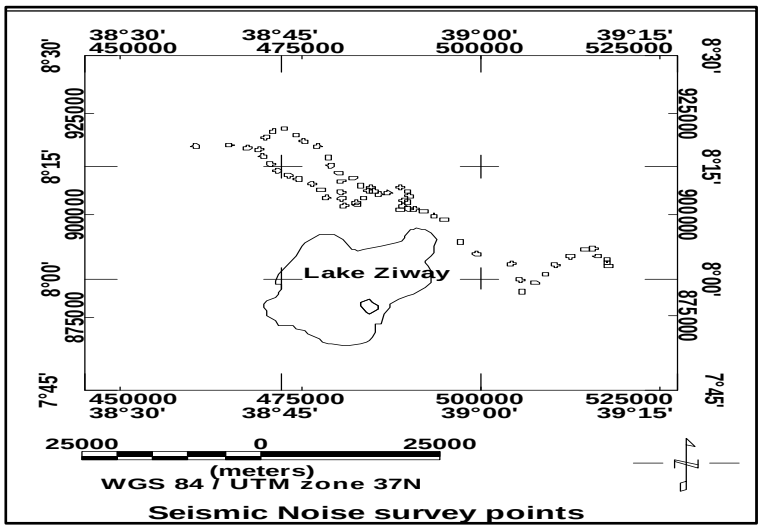

Fig. 9. 1 Location of the ambient seismic survey, circles shows the station locations.

9.2. Data and Methodology

9.2.1 Seismic noise data

The recorded data are a time series data having three components, (X, Y and Z) (Fig. 9.2 (b)) recorded with a Tromino seismometer that is designed to record the background seismic noise within frequency ranges of 0 to 128 Hz and set at a time-period from 1 min to 60 min. The seismometer records three components and the data are analyzed by the software (Grilla) (Tromino®Grilla, 2009). The survey was conducted in support of a potential field investigation conducted in the area and the procedures of the data measurements are as follows

- ✓ select a suitable site
- ✓ adjust the seismometer to magnetic north and tightly couple the seismometer spikes into the ground
- ✓ Level the seismometer
- ✓ Three perpendicular components of the seismic noise are recorded for about 10 minutes per site each. The recording times of the survey are chosen so as to have more spatial coverage in the area
- ✓ The records is downloaded and processed using Grilla software

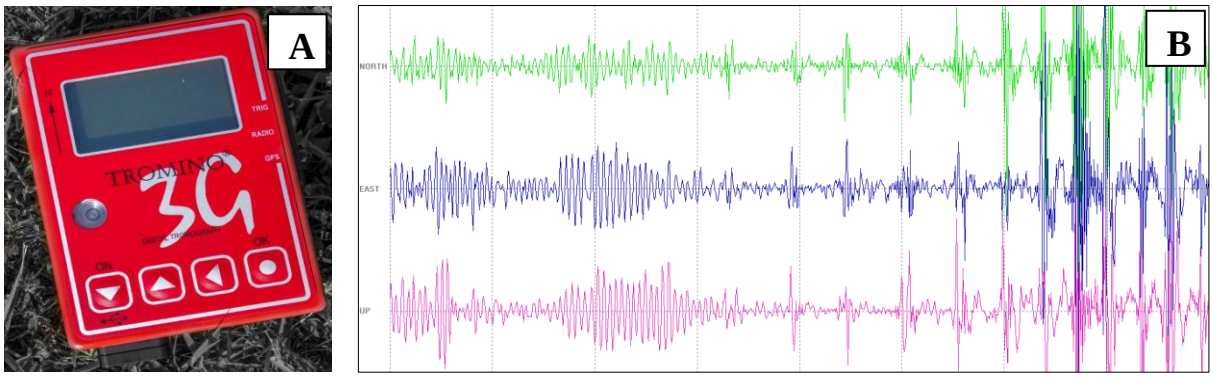

Fig. 9. 2 Tromino Seismometer (a) and the raw time series data of three components are recorded with Tromino and viewed with Grilla software (b)

The two horizontal components (East-West and south-north) and the one vertical component (up-down) (Fig. 9.2 (b)) are the main seismic data that were collected. About 62 single station measurements are collected at the boundaries between the Ziway-Shala Lakes basin and Awash basin near water divide. All measurements (Fig. 9.3) are made for recording times of 10 minutes at 128 hz.

Fig. 9. 3 Single station noise measurement using TROMINO seismometer

9.2.2 Methodology

The raw single station data (Fig. 9.2b) were analyzed by a FFT to the horizontal and vertical time series data to create a power spectrum where by the Horizontal to vertical (H/V) power spectral ratio graph is generated. The ratio value at each frequency (Roser & Gosar, 2010) is defined as in Eq. 9.1

$$HVSR\ (f) = \frac{\sqrt{H_{NS}(f).H_{EW}(f)}}{V(f)} \tag{9.1}$$

where,

$H_{NS}(f)$ is north-south, $H_{EW}(f)$ east-west are horizontal spectra components and its resultants is simply called horizontal component (H)

$V(f)$ is vertical spectra component

The shear wave resonance frequency manifests itself within this ratio value registering peak value and is read from the graph. The analysis of HVSR allows to quickly estimating depth to impedance contrast of the layers. It generally help estimate the thickness of softer sediment cover over hard basement rocks ranging from 0 to 500m. In this study, the different depth estimation approaches are discussed before employing one

9.2.2.1 Unknown Layer thickness

The resonant frequency of the unconsolidated deposits was read from HVSR graph and the shear wave velocity is approximated either from 1D modeling or through characterization of soft layer geology of the area with respect to shear velocity (Tromino®Grilla, 2009). Having the resonant frequency and shear wave velocity, the depth to sediment- bedrock boundary can be determined using an equation (Eq. 9.2) derived by Nakamura (2000)

$$Z = \frac{V_S}{4f_0} \tag{9.2}$$

Where,

Z is the thickness of the unconsolidated sediments in m,

f_0 is the resonance (peak)frequency (Hz) determined from HVSR and

V_S is the S-wave velocity of the location in m/s.

Equation 9.2 is used for the sites where sediment thickness was unknown with an approximation of shear-wave velocity of the location under study. The shear wave velocities at shallow depth (high frequency) in the soft layer typically have the following values (Tromino®Grilla, 2009)

Vs = 100 m/s ➔ typical of low quality clays, turfs…

Vs = 200 m/s ➔ typical of medium-good quality clays and sandy silts

Vs = 300 m/s ➔ typical of sand and gravel

Vs = 400 m/s ➔typical of gravel and alterated/soft rocks

Vs = 500 m/s ➔typical of soft /layered sedimentary rocks

For cross-checking the depth estimate made using Eq.9.2, frequencies estimated based on H/V spectral curve and shear wave velocities given above, the 3 depth classes of the bedrock-like layer is categorized based on frequencies (5-50 Hz, 1-10 Hz, 0.1-1 Hz) and is shown in Fig. 9.4 (a, b and c) (Tromino®Grilla, 2009).

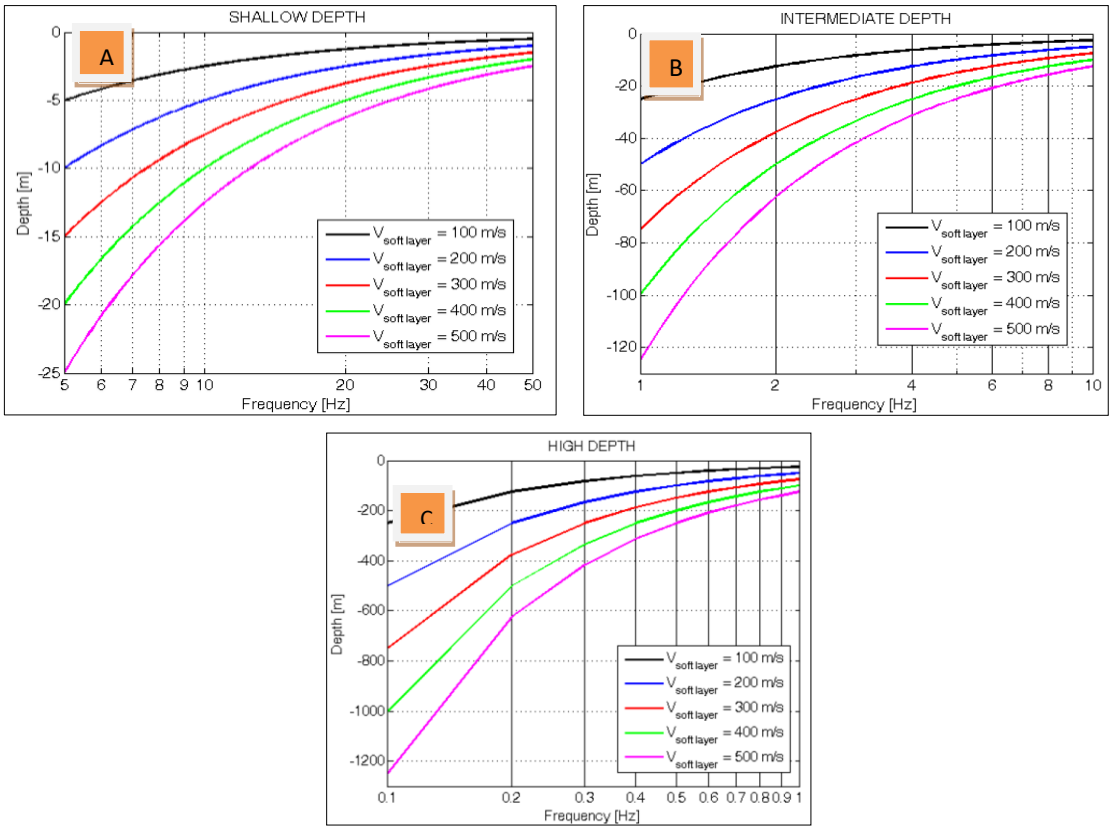

Fig. 9. 4 An example of the typical frequency – shear wave velocity – bedrock depth relation for a 1D, 2-layer basic system, high frequency detail (a) mid frequency detail (b) and low frequency detail (c)

Impendence contrast depth is estimated from reading graph of the frequency, shear wave velocity, bedrock depth relation for a 1D, 2-layer basic system for high frequency detail given in Fig. 9.4.

With known depths obtained from nearby drilling an estimate of average local sediment shear-wave velocity given by equation

$$V_s = \sum_{i=1}^{n} \frac{(4z_i f_{0i})}{n} \tag{9.3}$$

Where,

- ✓ z_i is the thickness of the unconsolidated sediments (m) at location i,
- ✓ f_{0i} is the resonance frequency (Hz) determined from HVSR
- ✓ v_s is the shear-wave velocity of the location.
- ✓ n is the number of locations where the depth to rock is known

The shear wave velocity estimated using equation 9.3 can be used in equation 9.2 to estimate the depth to bedrock.

9.2.2.2 Known thickness and H/V peak frequencies

The sediment thickness can also be determined by application of a power-law regression equation model given by (Ibs-von & Wohlenberg, 1999)

$$z_i = c{f_{0i}}^a \tag{9.4}$$

Where, f_{0i} are resonance frequency observations at each site

z_i are a range of known depths to bedrock that constrain the model

The constants c and a are to be determined from regression through linearization of equation 9.4.Thus, taking the logarithm of both sides of the equality gives

$$lnz_i = lnc + alnf_{0i} \tag{9.5}$$

This (Eq. 9.5) can re-expressed as a linear function of the parameters as

$$z_i{}^* = c^* + af_{0i}{}^* \tag{9.6}$$

Solving for the constants c^* and a using least square minimization we have a matrix solution of the form

$$\begin{bmatrix} c^* \\ \boldsymbol{a} \end{bmatrix} = \begin{pmatrix} \mathbf{2} & \sum f_{0i}{}^* \\ \sum f_{0i}{}^* & \sum f_{0i}{}^{*2} \end{pmatrix}^{-1} * \begin{pmatrix} \sum z_i{}^* \\ \sum z_i{}^* f_{0i} \end{pmatrix} \tag{9.7}$$

The constant parameters in equation 9.4 are determined by solving equation 9.7. These equations help to compute the thickness of the cover layer at any Tromino readings away from drillholes based on the measured H/V peak frequency alone. However, regression equation varies from one survey area to another survey area depending on the acoustic properties of the rocks. Therefore the regression equation from one area cannot generally be used for other areas. This method is more reliable when there are sufficient drillholes available for such calibration.

Figure 9.5 shows the conceptual model of stratified Earth, impedance contrast layers, depth of over lying covers, shear velocities of over lying cover and resonant frequencies

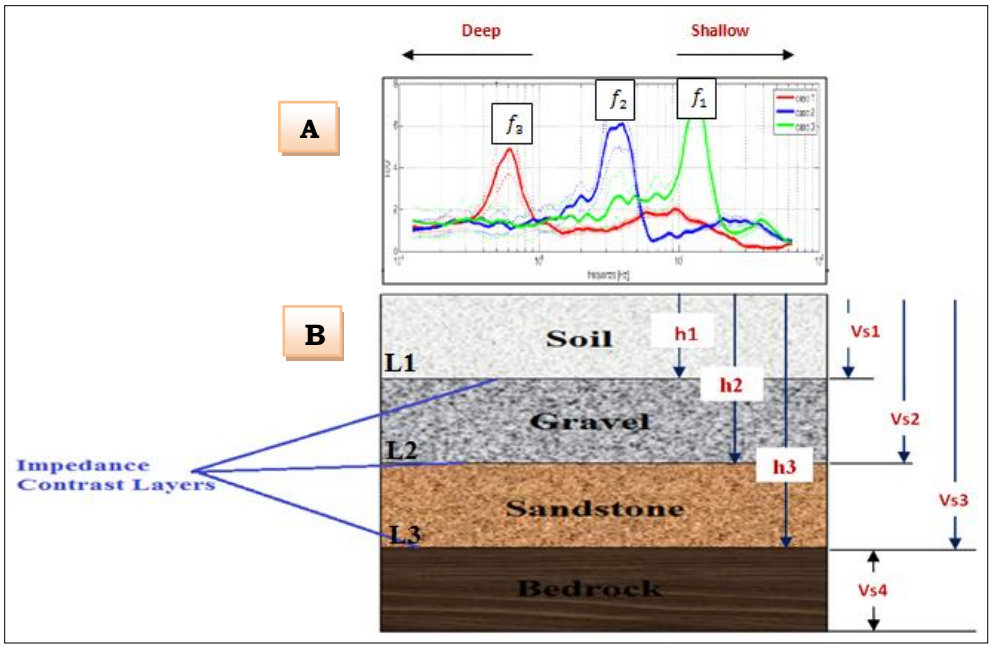

Fig. 9. 5 Multiple frequencies peaks (f_1, f_2 and f_3) is read from H/V spectral ratio curve and occurs at each respective impedance contrast layers (L1, L2 and L3). The h's are the thickness of the cover of each layer and Vs's are the shear velocities of the over laying formation

The estimate of depth to bed-rock like layer in study region considered follows the procedures documented in section 9.1. In depth estimation equation (Eq. 9.2) , the peak resonant frequencies is read from H/V spectral map and shear wave velocity in the soft layer geology is obtained from (Tromino®Grilla, 2009).

9.3 Results and Discussion

The horizontal to vertical spectral ratio (HVSR) is a seismic technique which helps to measure the thickness of unconsolidated deposits resting on bedrock and depth to bedrock. The depth of the bedrock changes from place to place on earth (subsurface topography). In some regions, the bedrock is nearby the surface, exposed to air. In the other places, it might be hundreds of meters deep, beneath loose sediments and broken rocks. The Earth's bedrock consists of many types of

rock, such as sandstone, limestone and granite. It has varying amount of void spaces in them where groundwater accumulates and circulates. The analysis of this survey data which covers north of the Ziway-Shala Lakes Basin (Fig. 9.1) assists the shallow groundwater resource mapping and dynamics. According to SESAME 2005 guidelines, two criteria such as the standards for reliable H/V curve and six criteria for a clear H/V peak (Appendix 2) should be fulfilled for a single station analysis. Out of 62 data collected only 17 data fulfilled SESAME criterion. Those data satisfying SESAME are subjected to single station analysis which helps in mapping depth to sediments-bed-rock like layer (Fig.9.6).

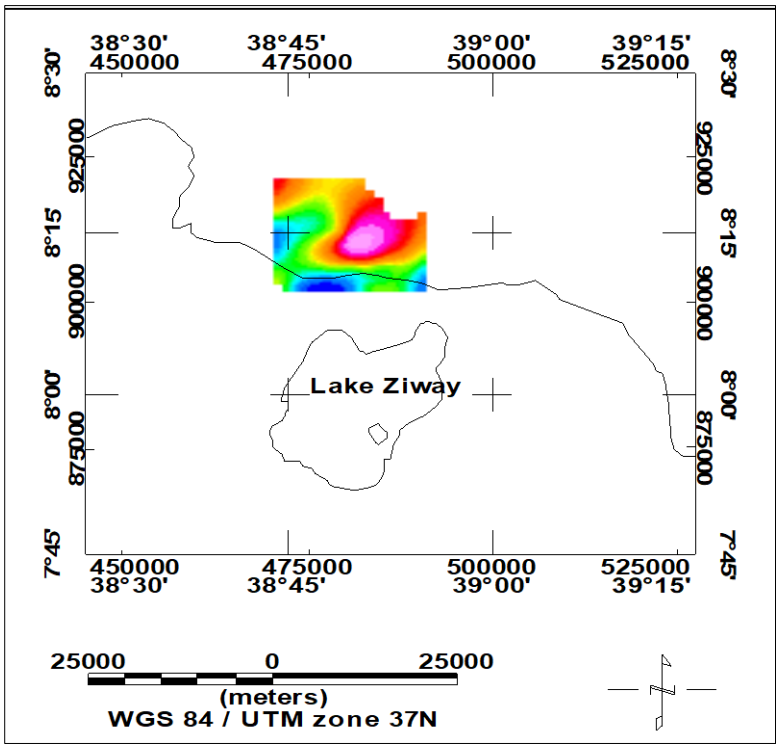

Fig. 9. 6 The seismic data passing SESAME criterion are displayed

Horizontal-to-Vertical spectral ratio (H/V) is a fast and quick way to get properties of a site for groundwater availability and dynamics indirectly through mapping the sediment thickness, depth to bedrock and bedrock topography.

The sample report that automatically generated for a single station, WOKOLE site (West of Meki Town) and AM7 (East of Meki Town) are shown respectively in Figure 9.7 and 9.8. The processing generates H/V ratio maps from which resonant frequencies are read.

WOKOLE, WOKALE

Instrument: TE3-0312/01-17

Data format: 16 byte

Full scale [mV]: 51

Start recording: 25/11/18 07:54:08 End recording: 25/11/18 08:04:08

Channel labels: NORTH SOUTH; EAST WEST ; UP DOWN

GPS location: 038°47.2571 E, 08°12.7199 N (1696.9 m)

(UTC time synchronized to the first recording sample): not available in this acquisition mode + 0 + 0 samples

Satellite no.: 6

Trace length: 0h10'00''. Analysis performed on the entire trace.

Sampling rate: 128 Hz

Window size: 20 s

Smoothing type: Triangular window

Smoothing: 10%

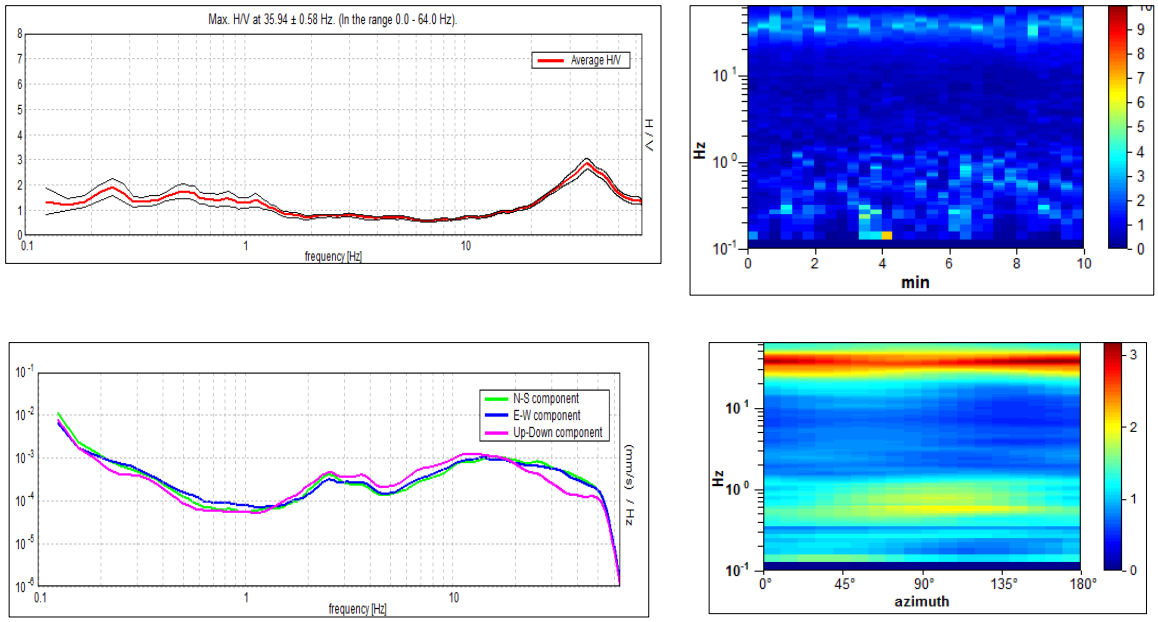

Fig. 9. 7 Horizontal to vertical spectral ratio map (a) H/V time history map (b) Directional H/V (c) and single component spectra (d)

AM7

Instrument: TE3-0312/01-17

Data format: 16 byte

Full scale [mV]: 51

Start recording: 24/11/18 08:45:52 End recording: 24/11/18 08:55:52

Channel labels: NORTH SOUTH; EAST, WEST; UP DOWN

GPS location: 039°06.8890 E, 08°03.0067 N (not available)

(UTC time synchronized to the first recording sample): not available in this acquisition mode + 0 + 0 samples

Satellite no.: 3

Trace length: 0h10'00''. Analysis performed on the entire trace.

Sampling rate: 128 Hz

Window size: 20 s

Smoothing type: Triangular window

Smoothing: 10%

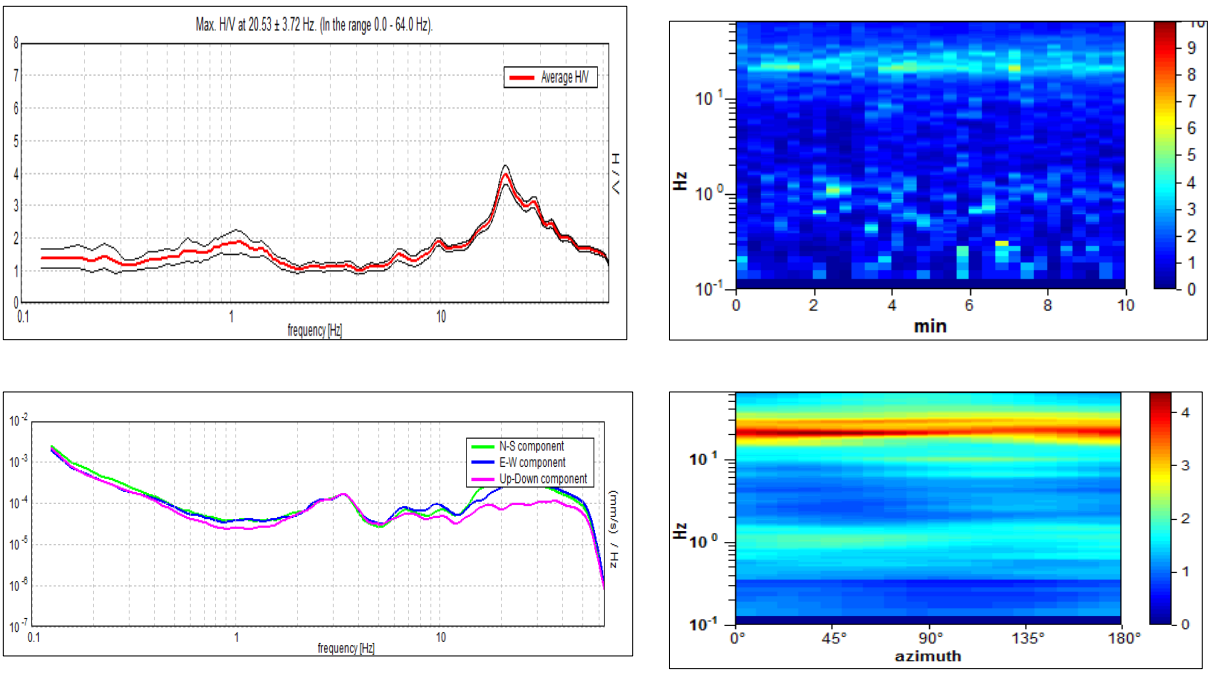

Fig. 9. 8 Horizontal to vertical spectral ratio map (a) H/V time history map (b) Directional H/V (c) and single component spectra (d)

Corresponding to the four maps generated for each site the European project Site EffectS assessment using AMbient Excitations criterion (SESAME) guidelines are generated automatically which are used to check the reliability and clarity of H/V. According to SESAME, 2005 guidelines two criteria such as the standards for reliable H/V curve and six criteria for a clear H/V peak should be fulfilled for a single station analysis. Accordingly, the Arbale site (Fig. 9.7) with UTM coordinate (512659, 889844) for example fulfilled the three basic criteria for reliability and the six-criterion mentioned for clear amplitude value. However, the second example (Fig. 9.8) fulfilled the three basic criteria and deficit of fulfilling two out of six

(Appendix 3). This should not be considered as H/V curve is not working, in fact, a perfect recording on rock would give "no" to all these criteria.

The fundamental frequency which can be read from Fig. 9.7 is 35.94 hz which could help to estimate the depth to be around 3.5 m **(**read from **Fig. 9.4)** with shear wave velocity of Vs=400m/s as the geology of the area taken as alterated/soft rocks. It is also possible to estimate the depth using equation (9.2) as

$$h = \frac{400m/s}{4x35.94\ /s} = 3.478m$$

In the second example (Fig. 9.8), the depth value is calculated using equation 9.2

$$h = \frac{400m/s}{4x20.53\ /s} = 4.87m$$

The results do not agree with the shallow and BH depth of the sites. This might be the problem of the existence of strong acoustic impedance contrast within the sediments above the bedrock surface. These are observed not only in the two sites but it is observed also in almost all of the observation points as the estimation of depths from HVSR graphs (Fig. 9.9) confirms.

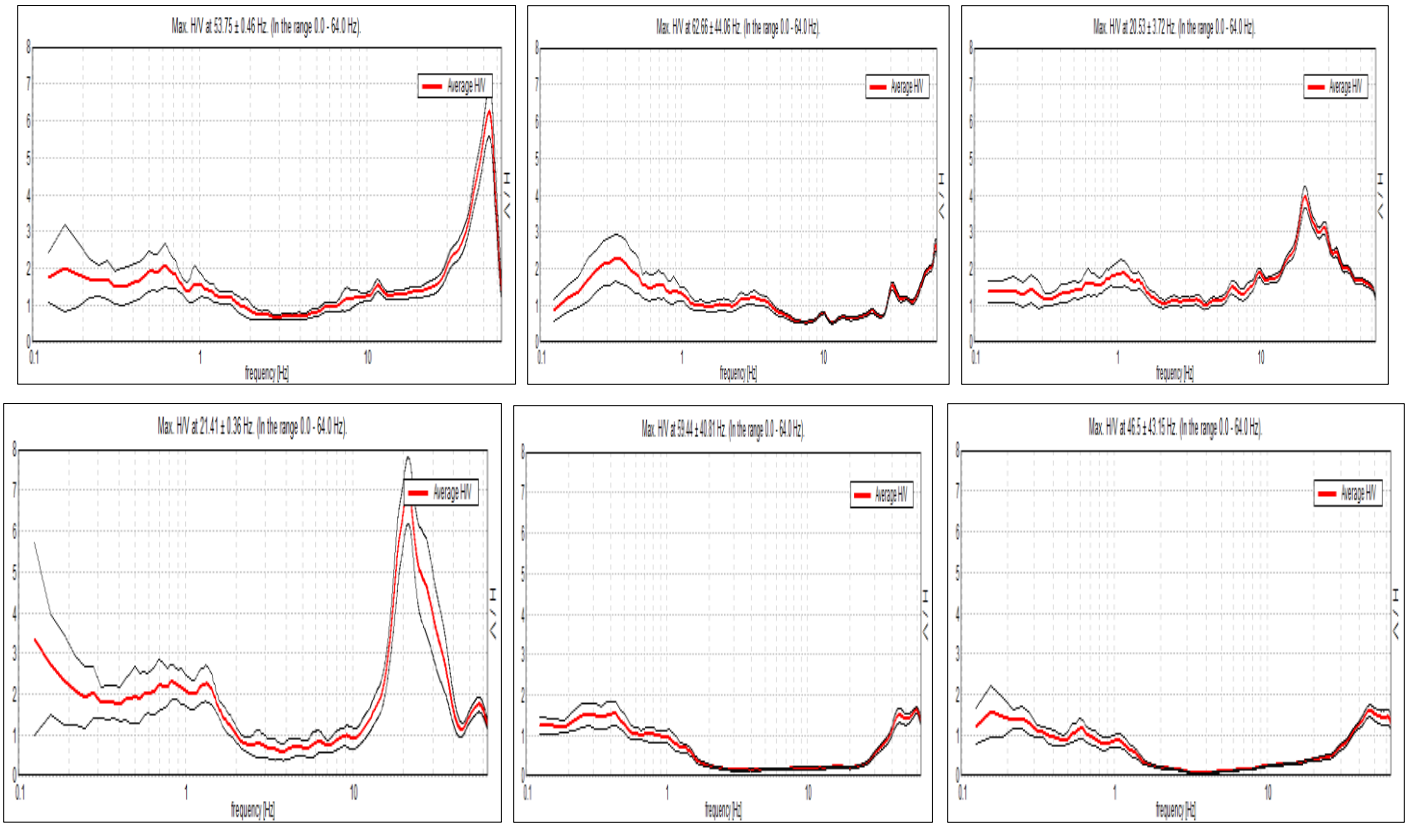

Fig. 9. 9 Sample H/V spectral plots displaying the peak H/V amplitude and high frequencies peaks (f_0) due to shallow soil cover above lithified sediments in the cover sequence.

The overall depth estimates that passes SESAME criterion are gridded and the shallowest density contrast depth is plotted (Fig.9.10)

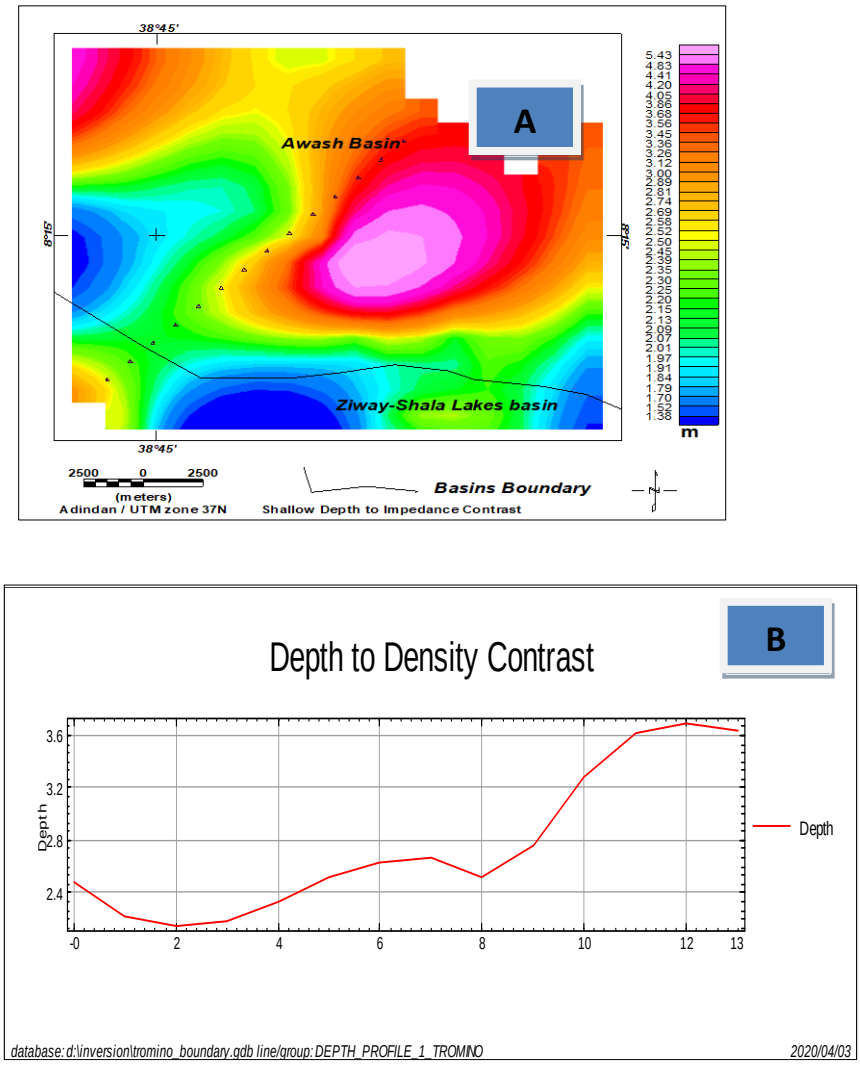

Fig. 9. 10 Depth estimates of the shallowest impedance contrast gridded and mapped to show the shallowest subsurface topography (a) and depth profile extracted from gridded bedrock topography map along the dotted line (b) the elevation of the bedrock surface along the cross-section

From gridded impedance contrast (Fig. 9.10(a)), we observe that the thickness of overlying soils thickened northwards, towards Awash basin (Fig. 9.10(b)).

The other problem for using the HVSR method to map bedrock depth in the study area could be lack of a strong acoustic impedance contrast at the sediment-bedrock interface. These might indicate that the bedrock is found at a depth beyond the depth of investigation using TROMINO

seismometer at the surveyed time period. Thus H/V peak can't be recognized from the graph. One proposed method is the use of increasing recoding time from 10 minutes to 20 or 30 minutes.

9.4 Conclusion

Horizontal to Vertical spectral ratio (HVSR) method is used to analyze the passive seismic data in northern part of the Ziway-Shala Lakes Basin, near water divide, to map the layer of highest frequency in the region considered. The method first generate H/V spectral ratio curve and those maps which passes SESAME criterion are get interpreted. The fundamental frequency **(f_0)** is read from the **H/V** spectral ratio map and the impedance contrast depth is then approximated based on equation 9.1. The depth estimates of each site are then gridded and mapped which could show the undulation of the shallowest bedrock layer. The recording time of 10 minutes in each station limits the method from mapping the lowest frequency (deeper) impedance contrast layer. The shallowest topography in the region considered is mapped and are shown to deepen northwards towards Awash basin.

In previous chapters' gravity, magnetic and seismic data are analyzed for mapping subsurface geology and geologic structures of the area. Furthermore, their possible links to resource of the area are made. In the next chapter syntheses of all the work done are summarized and future directions are set.

Chapter 10: General Conclusions and Future Directions

10.1 Summery of the Research

Geological structures mapped earlier in the region under consideration focused on surface structures, crustal structures and Moho depth undulations. However, little attention is given to the shallow to intermediate depth geological structures occurring at specified depths and their significance for assessment of their associated resources. Therefore, this study aims at improving knowledge of the shallow to intermediate depth geological structures of the Ziway-Shala Lakes Basin.

Ground based secondary gravity data of 3013 were reprocessed, homogenized to the IGSN71, reduced using the Geodetic Reference System 1967 (GRS67), corrected and gridded to generate the complete Bouguer gravity anomalymap of the study area. This anomaly is the sum of the effect of high and low frequency causative sources and needs to be separated into its respective components. The low frequency (regional) component is approximated by 6 km upward continuation of the Bouguer anomalies and the corresponding residual component is calculated by subtracting the estimated regional from the gridded Bouguer anomalies map.

Similarly, the magnetic data of about 855 are analyzed in the region to map magnetic anomaly patterns and volcano-tectonic features associated with geothermal prospect area. To extract such information, the low latitude problems of magnetic data interpretation get resolved using Differential Reduction to Pole Filter. The reduction resulted in observed magnetic anomaly to lay above the anomalous sources beneath. This observed anomaly is separated into regional and residual components which could respectively reflect the deep and shallow geology of the area.

The analysis of these low/high frequency signals of gravity and magnetic anomaly could help to map the geology and geologic structures of the study area.

Gridded gravity, magnetic and DEM data are used to map gravity, magnetic and topographic lineaments of the area respectively. Accordingly, the subsurface lineaments identified using the gravity and magnetic data appear to be generally oriented NW-SE while most of the surface

lineaments identified using the DEM data tend to be oriented SW- NE. A few of these surface lineaments appear to extend depth wise so as to have both surface and subsurface signatures.

The layers relief maps which show the undulations and thickness of each horizon (Lithologies) are mapped using gravity and magnetic data. The analyses of subsurface structures (interface topographies) are made along the rift axis and over rift floor. In this investigation, Power spectral analysis, 2D Werner De-convolution, 2D forward modeling, Source parameter Imaging (SPI) and 3D gravity Interface Inversion are used in mapping the undulation along the rift axis. The overall results show that, the crystalline basement is deepening northwards, which implies the thickening of overlaying fluvio-lacustrine sediments and the rift floor volcanic units. The 3D inversion further identified a new Mesozoic layer sandwiched between a Tertiary ignimbrite layer and the crystalline basement. The thickness of Mesozoic sediment is estimated about 561 m and that of Tertiary sediments are 1292 m.

A horizontal to Vertical Spectral ratio (HVSR) computations (estimations) of the seismic noise data around the water divide between the Ziway-Shala Lakes Basin and the Awash basin are performed. The ratio is used to generate the resonant frequencies which help to estimate the depth to bed rock of each measured site. These depth values are gridded and mapped to determine the subsurface topography of the shallowest layer in the region considered. Both the gridded map and profile data show that the shallowest depth undulation is deepening northwards.

The water balance calculation of the Ziway-Shala Lakes Bain, salinity analysis and adopted conceptual groundwater flow model indicate how geologic structure mapped in an area has governing role on groundwater dynamics among the inter-basins.

The geothermal significance of the thesis work can be drawn from mapping magnetic anomaly patterns and volcano-tectonic features related to this energy sources. The anomaly patterns observed over the area fairly indicate the anomalous sources occurring beneath that area. A prominent structures mapped using magnetic data indicated the existence of a heat conducting (conduction) structural path between the SDFZ and the Aluto volcanic complex. This path is

thought to conduct heat between a heat source claimed to be located nearby the SDFZ and a heat reservoir occurring at the Aluto-Langano geothermal field.

Furthermore, the magnetic lineaments mapped using magnetic data are oriented NNW-SSE to NW-SE and most of them trend in the direction of pre-existing Mesozoic structures and in the direction of thermally altered structures.

The fact that the basin is closed implies that sedimentation processes characterize the region under consideration. The research also investigated Mesozoic sediments under thick volcanic cover of 2.5 km. Growth of petroleum reserves need such kind of geology where the sedimentary basins are overlain by volcanic rocks (Mammo, 2010). The existences of a Mesozoic layer in the basin lead the researcher to claim the availability of hydrocarbon resources in the region under consideration.

The non-existence of heat sources (magma chamber) under Aluto volcano (Samrock et al., 2015) (Hübert et al., 2018) and the existence of co_2 degassing in the same region suggest that the plausible co_2 source is not related to magma chamber. Thus, the possible source of this gas is claimed to be as a result of combustion of fossil fuels (coal, oil, and natural gas).

10.2 Contribution of the research work

Though the contribution of the thesis work is more or less indicated in the respective chapters of this thesis, the input made to geological and geophysical knowledge of the area is shortly be summarized as follows:

- ✓ The thesis work showed the procedures' on how to select appropriate low frequency signals (regional anomalies) for potential field gravity/magnetic data
- ✓ Identification of gravity lineaments showing subsurface structures at different depth levels are made and validations are performed against topographic lineaments extracted from DEM in the same region
- ✓ Work on different mathematical filters and choose the appropriate filter that rectify the low latitude problems hindering magnetic data interpretation

- ✓ Magnetic anomaly patterns of the study area resulting from the underlying causative sources are mapped
- ✓ Heat conducting structural path laying between the Aluto volcanic center and the Silti Debre Zeyet Fault Zone is identified
- ✓ Lithological (interface) geometries of layers particularly Mesozoic layer with thickness of 561 m identified in between Crystalline basement and Tertiary ignimbrite layer
- ✓ The shallowest bedrock topography is mapped using HVSR of seismic noise data in region between Ziway-Shala Lakes Basin and Awash Basin
- ✓ The possible interconnection of the mapped structures with respect to hydro-geological, geothermal and hydrocarbon resources are clearly documented

10.3 Limitation of the thesis work

The research work targeted to map geological structures from gravity, magnetic and seismic noise data. In doing these, the following constraints are encountered

- ✓ The measurements of the data are randomly performed and subjected to uneven distribution.
- ✓ Mathematical and computer algorithms used are all non-unique and no single chosen approaches.
- ✓ Not sufficient constraining geological and geophysical information exists in the study region

10.4 Future Direction and Recommendation

In this thesis work the integrated gravity, magnetic and seismic noise datasets are used with numerous filtering and modeling (inversion) methods. With the mentioned data sets and methodologies the targeted objective of mapping subsurface structures and their resource implications are identified. However, there are still many gaps that need further work and therefore the following recommendations are forwarded

- ✓ refining the existing data to better understand the shallow to intermediate subsurface

structures of the study region

- ✓ Work on new gridded dataset collected either ground based or air borne for best estimate of subsurface geology in the region considered
- ✓ a need to exhaust all the existing mathematics and computer algorithms to better extract information about the subsurface from potential field data
- ✓ Need to invert gravity/magnetic data to recover three-dimensional (3D) density/magnetic susceptibility model
- ✓ Need to perform 2D joint gravity and magnetic modeling across the rift axis
- ✓ Magneto-telluric (MT) method is recommended overall the CMER for best estimation of subsurface geology
- ✓ The hydrocarbon resource exploration studies needs detail investigations of on how the geology of the area significantly controls the growth of hydrocarbon reserves with more refined data sources.
- ✓ increasing recoding time of the TROMINO seismometer from 10 minutes to 20 or 30 minutes for deeper bedrock mapping

References

Abdullah, A., Akhir, J. M., & Abdullah, I. (2010). The extraction of lineaments using slope image derived from digital elevation model : case study of Sungai Lembing – Maran area , Malaysia . *Journal of Applied Sciences Research*, *6*(11), 1745–1751.

Abebe, T., Balestrieri, M. L., & Bigazzi, G. (2010). The Central Main Ethiopian Rift is younger than 8 Ma : confirmation through apatite fission-track thermochronology. *Terra Nova*. https://doi.org/10.1111/j.1365-3121.2010.00968.x

Adiri, Z., El Harti, A., Jellouli, A., Maacha, L., & Bachaoui, E. M. (2016). Lithological mapping using Landsat 8 OLI and Terra ASTER multispectral data in the Bas Drâa inlier, Moroccan Anti Atlas. *Journal of Applied Remote Sensing*, *10*(2), 025013. https://doi.org/https://doi.org/10.1117/1.JRS.10

Agostini, A., Bonini, M., Corti, G., Sani, F., & Manetti, P. (2011). Distribution of Quaternary deformation in the central Main Ethiopian Rift, East Africa. *Tectonics*, *30*(4), 1–21. https://doi.org/10.1029/2010TC002833

Alemu, A. (1992). The gravity field and crustal structure of the Main Ethiopian Rift. Ph.D. thesis, Royal institute of technology, department of Geodesy, report No. 26 (TRITA GEOD 1026), Stockholm, Sweden.

Alimoradi, A., Angorani, S., Ebrahimzadeh, M., & Panahi, M. S. (2011). Magnetic inverse modelling of a dike using the artificial neural network approach. *Near Surface Geophysics*, *9*, 339–347. https://doi.org/10.3997/1873-0604.2011008

Alley, W. M., Reilly, T. E., & Franke, O. L. (1999). *Sustainability of Ground-Water Resources: U.S. Geological Survey Circular 1186 Report*.

Arkani-hamed, J. (2007). Differential reduction to the pole : Revisited. *Geophysics*, *72*(1), 13–20.

Aydogan, D. (2011). Extraction of lineaments from gravity anomaly maps using the gradient calculation : Application to central Anatolia. *Earth Planets Space*, *63*, 903–913. https://doi.org/10.5047/eps.2011.04.003

Ayenew, T. (2001). Numerical groundwater flow modeling of the central main Ethiopian rift

Lakes basin. *SINET: Ethiopian Journal of Science*, *24(2)*(ISSN:0379-2897), 167–184.

Ayenew, T. (2002). Recent changes in the level of Lake Abiyata, central main Ethiopian Rift. *Hydrological Sciences Journal*, *47*(3), 493–503. https://doi.org/10.1080/02626660209492949

Ayenew, T. (2005). Major ions composition of the groundwater and surface water systems and their geological and geochemical controls in the Ethiopian volcanic terrain. *SINET: Ethiopian Journal of Science*, *28*(2), 171–188. https://doi.org/10.4314/sinet.v28i2.18253

Blaikie, T. N., Ailleres, L., Betts, P. G., & Cas, R. A. F. (2014). Interpreting subsurface volcanic structures using geologically constrained 3-D gravity inversions: Examples of maar-diatremes, Newer Volcanics Province, southeastern Australia. *Journal of Geophysical Research: Solid Earth*, *119*(April 2014). https://doi.org/10.1002/2013JB010751

Boccaletti, M., Bonini, M., Mazzuoli, R., Abebe, B., Piccardi, L., & Tortorici, L. (1998). Quaternary oblique extensional tectonics in the Ethiopian Rift (Horn of Africa). *Tectonophysics*, *287*, 97–116.

Bonini, M., Corti, G., Innocenti, F., Manetti, P., Mazzarini, F., Abebe, T., & Pecskay, Z. (2005). Evolution of the Main Ethiopian Rift in the frame of Afar and Kenya rifts propagation. *Tectonics*, *24*. https://doi.org/10.1029/2004TC001680

Bosellini, A., Russo, A., & Assefa, G. (2001). The Mesozoic succession of Dire Dawa, Harar Province, Ethiopia. *Journal of African Earth Sciences*, *32*(3), 403–417. https://doi.org/10.1016/S0899-5362(01)90105-8

Chen, Z., Mou, L., & Meng, X. (2016). The horizontal boundary and top depth estimates of buried source using gravity data and their applications. *Journal of Applied Geophysics*, *124*, 62–72. https://doi.org/10.1016/j.jappgeo.2015.11.003

Cherkose, B. A., & Mizunaga, H. (2018). Resistivity imaging of Aluto-Langano geothermal field using 3-D magnetotelluric inversion. *Journal of African Earth Sciences*, *139*, 307–318. https://doi.org/10.1016/j.jafrearsci.2017.12.017

Chernet, T., Travi, Y., & Valles, V. (2001). Mechanism of degradation of the quality of natural water in the lakes region of the Ethiopian Rift Valley. *Water Research*, *35*(12), 2819–2832. https://doi.org/10.1016/S0043-1354(01)00002-1

Cooper, G. R. J., & Cowan, D. R. (2005). Differential reduction to the pole. *Computers and Geosciences*, *31*(8), 989–999. https://doi.org/10.1016/j.cageo.2005.02.005

Corti, G., Sani, F., Philippon, M., Sokoutis, D., Willingshofer, E., & Molin, P. (2013).

Quaternary volcano-tectonic activity in the Soddo region , western margin of the Southern Main Ethiopian Rift. *Tectonics*, *32*, 861–879. https://doi.org/10.1002/tect.20052

Darling, W. G., Gizaw, B., & Arusei, M. K. (1996). Lake-groundwater relationships and fluid-rock interaction in the East African Rift Valley: Isotopic evidence. *Journal of African Earth Sciences*, *22*(4), 423–431. https://doi.org/10.1016/0899-5362(96)00026-7

Dugda, M. T., Nyblade, A. A., Julia, J., Langston, C. A., Ammon, C. J., & Simiyu, S. (2005). Crustal structure in Ethiopia and Kenya from receiver function analysis : Implications for rift development in eastern Africa. *Journal of Geophysical Research*, *110*, B01303. https://doi.org/10.1029/2004JB003065

Ellis, R. G., Wet, B. de, & Macleod, I. N. (2012). Inversion of Magnetic Data from Remanent and Induced Sources. In *22 nd International geophysical conference and exhibition, 26-29 February 2012 - Brisbane, Australia* (pp. 1–4).

Feng, J., Zhang, S., & Meng, X. (2016). Constraint 3D density interface inversion from gravity anomalies. *Arab J Geosci*, (9), 1–8. https://doi.org/10.1007/s12517-015-2213-9

Gabriel, G., Vogel, D., Scheibe, R., Lindner, H., Pucher, R., Wonik, T., & Krawczyk, C. M. (2011). Anomalies of the Earth's total magnetic field in Germany – the first complete homogenous data set reveals new opportunities for multiscale geoscientific studies. *Geophysical Journal International*, *184*, 1113–1118. https://doi.org/10.1111/j.1365-246X.2010.04924.x

Gani, N. D., Abdelsalam, M. G., Gera, S., & Gani, M. R. (2008). Stratigraphic and structural evolution of the Blue Nile Basin, northwestern Ethiopian plateau. *Geological Journal*, *43*, 487–510. https://doi.org/10.1002/gj

Gizaw, B. (1996). The origin of high bicarbonate and fluoride concentrations in waters of the Main Ethiopian Rift Valley, East African Rift system. *Journal of African Earth Sciences*, *22*(4), 391–402. https://doi.org/10.1016/0899-5362(96)00029-2

Gosar, A. (2017). Study on the applicability of the microtremor HVSR method to support seismic microzonation in the town of Idrija (W Slovenia). *Natural Hazards and Earth System Sciences*, 925–937. https://doi.org/https://doi.org/10.5194/nhess-17-925-2017

Guo, L., Meng, X., Chen, Z., Li, S., & Zheng, Y. (2013). Preferential filtering for gravity anomaly separation. *Computers and Geosciences*, *51*, 247–254. https://doi.org/10.1016/j.cageo.2012.09.012

Gupta, H., & Roy, S. (2007). *Geothermal Energy: An alternative resource for the 21st century* (First edit). Elsevier B.V.

Gupta, V. K., & Ramani, N. (1980). Some aspects of regional- residual separation of gravity anomalies in a Precambrian terrain. *Geophysics*, *45*(9), 1412–1426. https://doi.org/10.1190/1.1441130

Hansen, R., & Pawlowski, R. S. (1989). Reduction to the pole at low latitudes by Wiener filtering. *Geophysics*, *54*(12), 1607–1614.

Hartman, R., Friedberg, L., & Corporation, A. S. (1971). A system for rapid digital Areomagnetic interpretation. *Geophysics*, *36*(5), 891–918.

Hübert, J., Whaler, K., & Fisseha, S. (2018). The electrical structure of the central Main Ethiopian Rift as imaged by Magnetotellurics : Implications for magma storage and pathways. *Journal of Geophysical Research: Solid Earth*, *123*, 6019–6032. https://doi.org/10.1029/2017JB015160

Hutchison, W., Mather, T. A., Pyle, D. M., Biggs, J., Yirgu, G., Sciences, E., et al. (2015). Structural controls on fluid pathways in an active rift system : A case study of the Aluto volcanic complex. *Geosphere;*, (3), 542–562. https://doi.org/10.1130/GES01119.1

Hutchison, W., Pyle, D. M., Mather, T. A., Yirgu, G., Biggs, J., Cohen, B. E., et al. (2016). The eruptive history and magmatic evolution of Aluto volcano: new insights into silicic peralkaline volcanism in the Ethiopian rift. *Journal of Volcanology and Geothermal Research*, *328*, 9–33. https://doi.org/10.1016/j.jvolgeores.2016.09.010

Ibs-von, S., & Wohlenberg, J. (1999). Microtremor measurements used to map thickness of soft sediments. *Bulletin of the Seismological Society of America*, *89*(1), 250–259.

Jacobsen, B. H. (1987). A case for upward continuation as a standard separation filter for Potential-field maps. *Geophysics*, *52*(8), 1138–1148. https://doi.org/10.1190/1.1442378

Johnson, C. D., & Lane, J. W. (2016). Statistical comparison of methods for estimating sediment thickness from Horizontal-to-Vertical Spectral Ratio (HVSR) seismic methods: An example from Tylerville, Connecticut, USA. In *Symposium on the Application of Geophysics to Engineering and Environmental Problems*. Denver, Colorado: Proceedings: Denver, Colorado, Environmental and Engineering Geophysical Society, 7 p.

Jordan, G., Meijninger, B. M. L., & Hinsbergen, D. J. J. Van. (2005). Extraction of morphotectonic features from DEMs : Development and applications for study areas in Hungary and NW Greece. *International Journal of Applied Earth Observation and Geoinformation 7*, *7*, 163–182. https://doi.org/10.1016/j.jag.2005.03.003

Kearey, P., Michael, B., & Ian, H. (2002). *An Introduction to Geophysical Exploration*. Blackwell Science Ltd Editorial Offices.

Keating, P., Pinet, N., & Pilkington, M. (2011). Comparison of some commonly used regional residual separation techniques. *The Society of Exploration Geophysicists and the Chinese Geophysical Society*, (April 2016), 14–14. https://doi.org/10.1190/1.3659055

Kebede, A. (2007). Groundwater Flow System and Hydrochemistry of Ziway-Koka Corridor in the Main Ethiopian Rift . *Msc Thesis Submitted to School of Graduate Studies of Addis Ababa University*, (February).

Kebede, B. (2014). Application of gravity, magnetic and electrical resistivity methods for geothermal investigation at the Corbetii Caldera, Main Ethiopian Rift, Ethiopia. *MSC Thesis Work, Addis Ababa University*.

Kebede, H., Alemu, A., & Fisseha, S. (2020). Upward continuation and polynomial trend analysis as a gravity data decomposition , case study at Ziway-Shala basin , central Main Ethiopian rift. *Heliyon*, *6*, e03292. https://doi.org/10.1016/j.heliyon.2020.e03292

Kebede, S. (2013). *Groundwater in Ethiopia: Features, Numbers and Opportunities*. Springer Hydrogeology. https://doi.org/DOI 10.1007/978-3-642-30391-3

Kelemework, Y. (2016). *Integrated geophysical investigations of the central main Ethiopian Rift and adjacent plateaus: An implication to crustal structure and Moho depth determinations. MSC thesis work, Addis Ababa University.*

Korme, T., Acocella, V., & Abebe, B. (2004). The role of pre-existing structures in the origin, propagation and architecture of faults in the Main Ethiopian Rift. *Gondwana Research*, *7*(2), 467–479.

Legesse, D., Vallet-coulomb, C., & Gasse, F. (2004). Analysis of the hydrological response of a tropical terminal lake , Lake Abiyata (Main Ethiopian Rift Valley) to changes in climate and human activities Abstract : *Hydrological Processes*, *18*, 487–504. https://doi.org/10.1002/hyp.1334

Li, Y., & Oldenburg, D. W. (1998). 3-D inversion of gravity data. *Geophysics*, *63*(1), 109–119.

Li, Y., & Oldenburg, D. W. (2001). Stable reduction to the pole at the magnetic equator. *Geophysics*, *66*(2), 571–578.

Maguire, P. K. H., Keller, G. R., Klemperer, S. L., Mackenzie, G. D., Keranen, K., Harder, S., et al. (2006). Crustal structure of the northern Main Ethiopian Rift from the EAGLE controlled-source survey ; a snapshot of incipient lithospheric break-up. *The Geological Society of London*, 269–291.

Mahatsente, R., Jentzsch, G., & Jahr, T. (1999). Crustal structure of the Main Ethiopian Rift

from gravity data : 3-dimensional modeling. *Tectonophysics*, *313*, 363–382.

Mammo, T. (2010). Delineation of sub-basalt sedimentary basins in hydrocarbon exploration in North Ethiopia. *Marine and Petroleum Geology*, *27*(4), 895–908. https://doi.org/10.1016/j.marpetgeo.2009.12.009

Mammo, T. (2012). Analysis of gravity field to reconstruct the structure of Omo basin in SW Ethiopia and implications for hydrocarbon potential. *Marine and Petroleum Geology*, *29*(1), 104–114. https://doi.org/10.1016/j.marpetgeo.2011.08.013

Mariita, N. O. (2007). The magnetic method. In *Presented at Short Course II Surface Exploration for Geothermal Resources, organized by UNU-GTP and KenGen, at Lake Naivasha, Kenya* (pp. 2–17).

Menke, W. (1989). *Geophysical data analysis : Discrete inverse theory* (Vol. 45). A series of monographs and textbooks: Academic press, INC.

Mickus, K., Tadesse, K., Keller, G. R., & Oluma, B. (2007). Gravity analysis of the main Ethiopian rift. *Journal of African Earth Sciences*, *48*, 59–69. https://doi.org/10.1016/j.jafrearsci.2007.02.008

Mohor, P. (1962). *The Ethiopian Rift System*. Bull. Geophys. Observ., Addis Ababa, 5, 33–62.

Molin, P., & Corti, G. (2015). Topography, river network and recent fault activity at the margins of the Central Main Ethiopian Rift (East Africa). *Tectonophysics*, *664*, 67–82. https://doi.org/10.1016/j.tecto.2015.08.045

Montesinos, F. G., Blanco-montenegro, I., & Arnoso, J. (2016). Three-dimensional inverse modelling of magnetic anomaly sources based on a genetic algorithm. *Physics of the Earth and Planetary Interiors*, *253*, 74–87. https://doi.org/10.1016/j.pepi.2016.02.004

Morgan, K., Jankowski, J., & Taylor, G. (2006). Structural controls on groundwater flow and groundwater salinity in the Spicers Creek catchment , Central West region , New South Wales. *Hydrological Processes*, *20*, 2857–2871. https://doi.org/10.1002/hyp.6079

Nabighian, M. N. (1972). The analytic signal of two dimensional magnetic bodies with polygonal cross-section: Its propertices and use for automated anomaly interpretation. *Geophysics*, *37*(3), 507–517.

Nagendra, R., Prasad, P. V. ., & Bhimasankaram, V. L. . (1996). Forward and inverse computer modeling of a gravity field resulting from a density interface using Parker-Oldenberg method. *Computers & Geosciences*, *22*(3), 227–231.

Nakamura, Y. (1989). A method for dynamic characteristics estimation of subsurface using microtremor on the ground surface. *Geotechnical Engineering & Disaster Prevention Laboratory*, *30*(1), 25–33.

Nakamura, Y. (2000). Clear identification of fundamental idea of Nakamura's technique and its applications. *Proc. 12WCEE, No.*, (2656), 177–402.

Okiwelu, A., Osazuwa, I., & Lawal, K. (2010). Isolation of residuals determined from polynomial fitting to gravity data of Calabar Flank, southeastern Nigeria. *The Pacific Journal of Science and Technology*, *11*(1), 576–585.

Oldenburg, D. . (1974). The inversion and interpretation of Gravity anomalies. *Geophysics*, *39*(4), 526–536.

Panzera, F., Lombardo, G., Amico, S. D., & Galea, P. (2013). Speedy techniques to evaluate seismic site effects in particular geomorphologic conditions : faults , cavities , landslides and topographic irregularities. *Intech*. https://doi.org/http://dx.doi.org/10.5772/55439 105

Paola, G. M. D. I. (1972). The Ethiopian Rift Valley (Between 7° 00' and 8 ° 40' lat . North).

Parker, R. L. (1972). The rapid calculation of potential anomalies. *Geoplhys J. R. Astr. Soc*, *31*, 447–455.

Rajagopalan, S. (2003). Analytic signal vs . reduction to pole : Solutions for low magnetic latitudes. *Exploration Geophysics*, *34*(4), 257–262.

Reynolds, J. M. (1997). *An Introduction to Applied and Environmental Geophysics. John Wiley and Sons Ltd*.

Roser, J., & Gosar, A. (2010). Determination of Vs30 for seismic ground classification in the Ljubljana area, Slovenia. *Acta Geotechnica Slovenica*, *1*(2007).

Saibi, H., Nishijima, J., Hirano, T., Fujimitsu, Y., & Ehara, S. (2008). Relation between structure and low-temperature geothermal systems in Fukuoka city , southwestern Japan. *Earth Planets Space*, *60*, 821–826.

Saibi, H., Aboud, E., & Ehara, S. (2012). Analysis and interpretation of gravity data from the Aluto-Langano geothermal field of Ethiopia. *Acta Geophysica*, *60*(2), 318–336. https://doi.org/10.2478/s11600-011-0061-x

Salama, R. B., Otto, C. J., & Fitzpatrick, R. W. (1999). Contributions of groundwater conditions to soil and water salinization. *Hydrogeology Journal*, (7), 46–64. https://doi.org/10.1007/s100400050179

Salimi, P., & Motlagh, A. T. (2012). Mapping of the bedrock topography using gravity data : A case study in the south of hormozgan province, Iran. *Journal of Remote Sensing & GIS*, *1*(2), 1–6. https://doi.org/10.4172/2169-0049.1000105

Samrock, F., Kuvshinov, A., Bakker, J., Jackson, A., & Fisseha, S. (2015). 3-D analysis and interpretation of magnetotelluric data from the Aluto-Langano geothermal field, Ethiopia. *Geophysical Journal International*, *202*, 1923–1948. https://doi.org/10.1093/gji/ggv270

Schutter, S. R. (2003). Hydrocarbon occurrence and exploration in and around igneous rocks. *Geological Society, London, Special Publications*, (214), 7–33.

Searle, R., & Gouin, P. (1972). A gravity survey of the central part of the Ethiopian Rift Valley. *Tectonophysics*, *15*(1/2), 41–52.

Siler, D. L., Faulds, J. E., Hinz, N. H., Dering, G. M., Edwards, J. H., & Mayhew, B. (2019). Three - dimensional geologic mapping to assess geothermal potential : examples from Nevada and Oregon. *Geothermal Energy*. https://doi.org/10.1186/s40517-018-0117-0

Silva, J. B. C. (1986). Reduction to the pole as an inverse problem and its application to low-latitude anomalies. *Geophysics*, *51*(2), 369–382.

Skilbrei, J. R. (1991). Interpretation of depth to the magnetic basement in the northern Barents Sea (south of Svalbard). *Tectonophysics*, *200*, 127–141.

Spector, A., & Grant, S. (1970). Statistical models for interpreting areomagnetic data. *Geophysics*, *35*(2), 293–302.

Talwani, M., Worzel, L., & Landism, M. (1959). Rapid gravity computations for two-dimensional bodies with application to the Mendocino submarine fracture zone. *Journal of Geophysical Research*, *64*(1).

Tapia, J., Townley, B., Córdova, L., Poblete, F., & Arriagada, C. (2016). Hydrothermal alteration and its effects on the magnetic properties of Los Pelambres , a large multistage porphyry copper deposit. *Journal of Applied Geophysics*, *132*, 125–136. https://doi.org/10.1016/j.jappgeo.2016.07.005

Tefera, M., Chernet, T., & Haro, W. (1996). Geology of Ethiopia. *Geological Survey of Ethiopia*. Retrieved from www.gse.gov.et/index.php/geology-of-ethiopia

Teklemariam, M., & Kebede, S. (2010). Strategy for geothermal resource exploration and development in Ethiopia. In *Proceedings World Geothermal Congress* (pp. 25–29).

Telford, W. M., Geldart, L. ., & Sheriff, R. . (1990). *Applied geophysics (2nd ed.) Cambridge*.

Cambridge University Press.

Tessema, A., & Antoine, L. A. G. (2004). Processing and interpretation of the gravity field of the east african rift: Implication for crustal extension. *Tectonophysics*, *394*(1–2), 87–110. https://doi.org/10.1016/j.tecto.2004.07.057

Thakur, N. K., Rao, T. G., Khanna, R., & Subrahmanyam, C. (2000). Magnetic basement in the Bay of Bengal through Werner deconvolution. *Marine Geology*, *162*, 599–605.

Thurston, J. B., & Smith, R. S. (1997). Automatic conversion of magnetic data to depth , dip , and susceptibility contrast using the SPI (TM) method. *Geophysics*, *62*(3), 807–813.

Tiberi, C., Ebinger, C., & Stuart, G. (2005). Inverse models of gravity data from the Red Sea – Aden – East African rifts triple junction zone. *Geophys. J. Int*, 775–787. https://doi.org/10.1111/j.1365-246X.2005.02736.x

Tromino®Grilla. (2009). The short tromino ® how to (pp. 1–26). Retrieved from www.tromino.eu

TROMINO User's Manual. (2017). MOHO, Science & Technology. Retrieved from www.moho.world

Tsepav, M. T. (2018). Comparative analysis of the source parameter imaging and spectral depth techniques of determining depth to magnetic sources in a sedimentary environment, using aeromagnetic sata. *International Journal of Scientific & Engineering Research*, *9*(3), 1535–1543.

Le Turdu, C., Tiercelin, J. jacques, Gibert, E., Travi, Y., Lezzar, K. E., Richert, J. P., et al. (1999). The Ziway – Shala lake basin system , Main Ethiopian Rift : Influence of volcanism , tectonics , and climatic forcing on basin formation and sedimentation. *Palaeogeography, Palaeoclimatology, Palaeoecology*, *150*, 135–177.

Verduzco, B., Fairhead, J. D., Green, C. M., & Mackenzie, C. (2004). New insights into magnetic derivatives for structural mapping. *Leading Edge*, (13), 116–119.

Weiler, P. D. (2007). Cross-references magnetic anomalies for geology. *Encyclopedia of Geomagnetism and Paleomagnetism*, 477–482. https://doi.org/http://www.springer.com/978-1-4020-3992-8

Werner, S. (1953). Interpretation of Magnetic Anomalies of Sheet-like Bodies. *Sveriges Geologiska Arsbok, Stockholm, 43*.

Wilks, M., Kendall, J. M., Nowacki, A., Biggs, J., Wookey, J., Birhanu, Y., et al. (2017).

Seismicity associated with magmatism, faulting and hydrothermal circulation at Aluto Volcano, Main Ethiopian Rift. *Journal of Volcanology and Geothermal Research*, *340*(November), 52–67. https://doi.org/10.1016/j.jvolgeores.2017.04.003

Williams, N. C. (2008). Geologically constrained UBC-GIF gravity and magnetic inversions with examples from the Agnew-Wiluna Greenstone Belt, western Australia. PhD thesis. *The University of British Columbia*, (October).

Wladis, D. (1999). Automatic lineament detection using Digital Elevation Models with second derivative filters. *Photogrammetric Engineering & Remote Sensing*, *65*(4), 453–458.

Woldegabriel, G., Aronson, J., & Walter, R. C. (1990). Geology , geochronology , and rift basin development in the central sector of the Main Ethiopian Rift. *Geological Society of America Bulletin*, *102*, 439–458. https://doi.org/10.1130/0016-7606(1990)102<0439

Woldegabriel, G., Heiken, G., White, T. D., Hart, W. K., & Renne, P. R. (2000). Volcanism, tectonism, sedimentation, and the paleoanthropological record in the Ethiopian Rift System. *Geological Society of America*, *345*(January). https://doi.org/10.1130/0-8137-2345-0.83

Xu, Y., Hao, T., Li, Z., Duan, Q., & Zhang, L. (2009). Regional gravity anomaly separation using wavelet transform and spectrum analysis. *Journal of Geophysics and Engineering*, *6*(3), 279–287. https://doi.org/10.1088/1742-2132/6/3/007

Yao, L., Dian-Jun, X., & Ming, W. (2010). *Reduction to the pole at the geomagnetic equator*. *Chinese Journal of geophysics* (Vol. 53). https://doi.org/10.1002/cjg2.1578

Zeid, N. A. B. U., Corradini, E., Bignardi, S., Nizzo, V., & Santarato, G. (2017). The Passive Seismic Technique ‘ HVSR ’ as a Reconnaissance Tool for Mapping Paleo-soils : The Case of the Pilastri Archaeological Site , Northern Italy. *Archaeological Prospection*, *24*, 245–258. https://doi.org/10.1002/arp.1568

Zhang, M., Qiao, J., Zhao, G., & Lan, X. (2019). Geology Regional gravity survey and application in oil and gas exploration in China. *China Geology*, *2*(3), 382–390. https://doi.org/10.1016/S2096-5192(19)30188-0

Appendix/Appendices:

Appendices 1: Title and Abstract of published and submitted manuscripts to different journals

Appendix 1.1 Upward continuation and polynomial trend analysis as gravity data decomposition, case study at Ziway-Shala Basin, Central Main Ethiopian rift. Heliyon, published by Elsevier Ltd.

Abstract

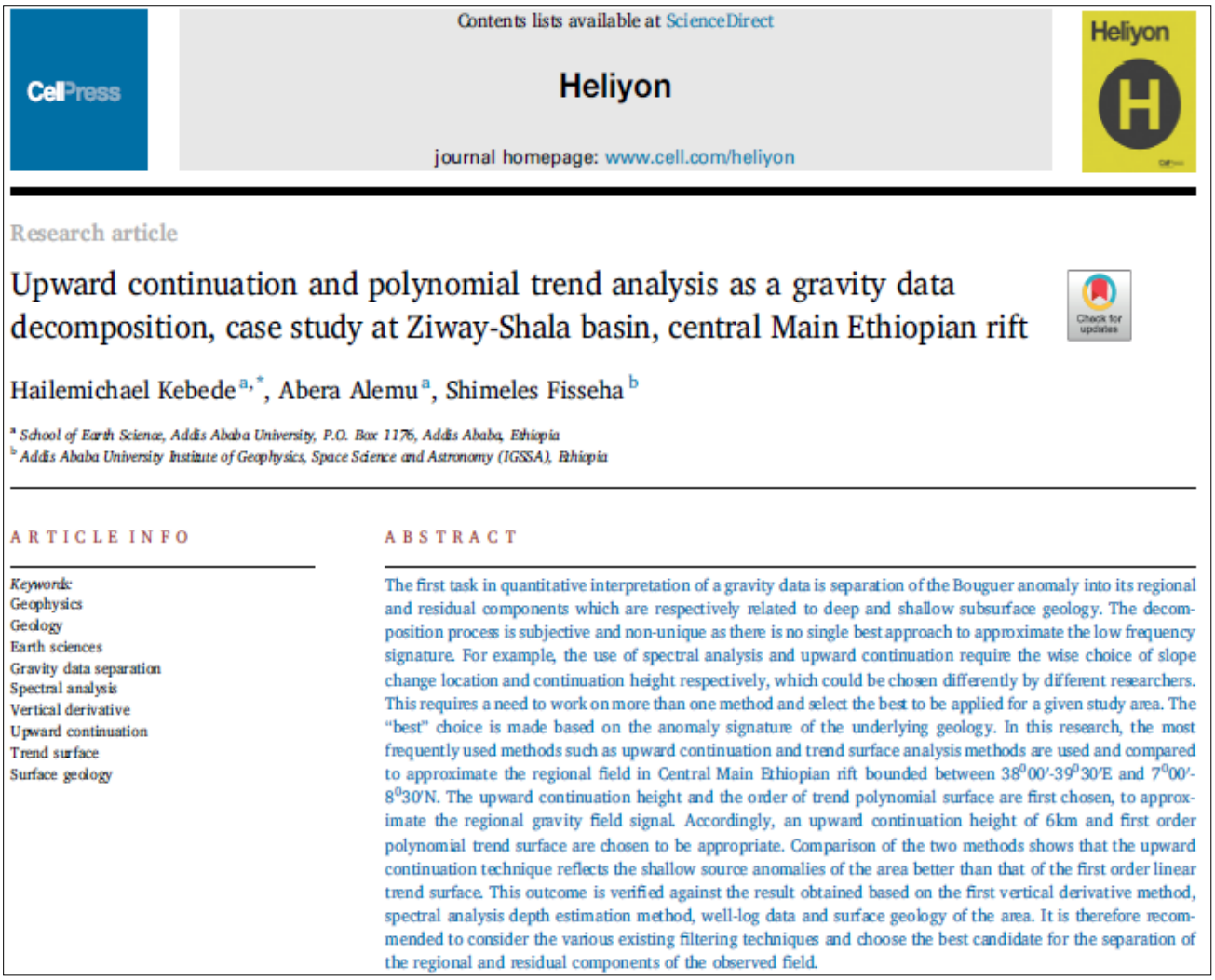

Contents lists available at ScienceDirect

Heliyon

journal homepage: www.cell.com/heliyon

Research article

Upward continuation and polynomial trend analysis as a gravity data decomposition, case study at Ziway-Shala basin, central Main Ethiopian rift

Hailemichael Kebede[a,*], Abera Alemu[a], Shimeles Fisseha[b]

[a] School of Earth Science, Addis Ababa University, P.O. Box 1176, Addis Ababa, Ethiopia
[b] Addis Ababa University Institute of Geophysics, Space Science and Astronomy (IGSSA), Ethiopia

ARTICLE INFO

Keywords:
Geophysics
Geology
Earth sciences
Gravity data separation
Spectral analysis
Vertical derivative
Upward continuation
Trend surface
Surface geology

ABSTRACT

The first task in quantitative interpretation of a gravity data is separation of the Bouguer anomaly into its regional and residual components which are respectively related to deep and shallow subsurface geology. The decomposition process is subjective and non-unique as there is no single best approach to approximate the low frequency signature. For example, the use of spectral analysis and upward continuation require the wise choice of slope change location and continuation height respectively, which could be chosen differently by different researchers. This requires a need to work on more than one method and select the best to be applied for a given study area. The "best" choice is made based on the anomaly signature of the underlying geology. In this research, the most frequently used methods such as upward continuation and trend surface analysis methods are used and compared to approximate the regional field in Central Main Ethiopian rift bounded between $38^0$00′-$39^0$30′E and $7^0$00′-$8^0$30′N. The upward continuation height and the order of trend polynomial surface are first chosen, to approximate the regional gravity field signal. Accordingly, an upward continuation height of 6km and first order polynomial trend surface are chosen to be appropriate. Comparison of the two methods shows that the upward continuation technique reflects the shallow source anomalies of the area better than that of the first order linear trend surface. This outcome is verified against the result obtained based on the first vertical derivative method, spectral analysis depth estimation method, well-log data and surface geology of the area. It is therefore recommended to consider the various existing filtering techniques and choose the best candidate for the separation of the regional and residual components of the observed field.

Appendix 1.2 Mapping Geologic Structures from Gravity and Digital Elevation Model, Submitted to Journal of Scientific Reports, Springer Nature

Abstract

This study attempts to delineate subsurface lineaments for the tectonically and volcanically active region of the Ziway-Shala Lakes basin, Central Main Ethiopian rift. Most of the previously mapped subsurface structures in the region under consideration focus on delineating crustal structures thicknesses and Moho depths undulations. Moreover, near-surface structures in the same region were mapped using analysis of Digital Elevation Model image data. On the other hand, there are few studies that have targeted in mapping geologic structures laying at intermediate depth levels between the shallower and deeper Earth. The objective of this research is thus to map the subsurface geologic structures/lineaments to an average depth of 3 km (crystalline basement layer depth) from surface using gravity data. These investigation results are validated by Digital Elevation Model extracted lineaments. Filtering techniques including derivative filters, upward-continuation and line module algorithm of PCI Geomatica are used to extract the gravity and topographic lineaments of the region. Orientation analyses of these subsurface and surface lineaments are made using line direction histogram of the QGIS software. Accordingly, the gravity subsurface lineaments mapped in this study are found to be dominantly oriented in the NNW-SSE to NW-SE and E-W direction on average. These results appear to be contrary to the NNE-SSW to NE-SW trending surface geologic structure mapped on the bases of actual field observation carried out by previous researchers and automatically extracted lineaments based on Digital Elevation Models data considered in this research. The subsurface lineaments mapped using gravity data coincide with the orientation of pre-existing subsurface structures crossing the rift orthogonally. These structural lineaments which are considered to be masked in the subsurface coincide with the orientation of the Mesozoic Ogaden rift as compared to the overlaying surface structures which appear to coincide with the orientation of the Cenozoic Main Ethiopian rift.

Appendix 1.3 Magnetic anomaly patterns and volcano-tectonic features associated to geothermal activities, submitted to Earth and Space Science Journal, ESS-AGU, Wiley publisher

Abstract

The Ziway-Shala Lakes Basin is a structural depression found in the Main Ethiopian rift being associated with Cenozoic volcanism, faulting and sedimentation activities. The Aluto-Langano volcanic complex is one of the geothermal prospect sites found in this basin and is currently being exploited for geothermal power production. Although it contradicts with the previous research results, recent observations using magneto-telluric method reveal nonexistence of a heat source beneath the Aluto volcano. Instead existence of a strong conductor possibly a magmatic heat sources claimed to occur beneath the Silti Debre Zeyet Fault Zone that lays far NW of the Aluto volcanic complex. In this study, ground based magnetic survey is carried out to map magnetic anomaly patterns and structural features associated with the Aluto-Langano. The volcano-tectonic features are extracted from the differentially pole reduced total magnetic field anomaly map and its derivative maps compiled by applying upward continuation, first vertical derivative and tilt derivative filters. Interpretation of the complied anomaly maps reveal existence of a heat conduction structural path along a traverse running from the Aluto-Langano geothermal to the Silti Debre Zeyte Fault zone and laying between 1.5 km and 3 km depths. This result could be taken to prove the most likely heat source feeding the Aluto-Langano geothermal field is found at about the locality of the Silti Debre Zeyte Fault Zone. The research work also identified magnetic lineaments most of which oriented in the direction of pre-existing Mesozoic structures and in the direction of thermally altered structures.

Appendix 1.4 Potential field source depth estimates using 2D/3D inversions and Source Parameter imaging techniques, Submitted to Heliyon, Elsevier Publisher.

Abstract

Quantitative analysis of potential field data are made in the Ziway-Shala lakes basin over an area bounded by $38^0$00' E - $39^0$30' E and $7^0$00' N - $8^0$30' N. Most previous geophysical studies in the region under consideration focus on mapping the crustal structures and undulation of the Moho depth. Only few studies are targeted at mapping the shallow subsurface structures. The main focus of this paper is mapping geometries of the major lithological and structural units of the shallow subsurface using gravity and magnetic data. The ultimate objective of the research is to understand the hydrogeological dynamics of the region through mapping interfaces geometries. Automatic Inversions, 2D joint forward modeling and 3D inversion are the major techniques employed. The 2D Werner de-convolution based on both gravity and magnetic data along the rift axis showed source depths tending to deepen northwards. Source depths estimates determined by Source Parameter Imaging also showed similar tendency. This is further strengthened by the joint 2D forward modeling of gravity and magnetic data which showed the top of the basement is sloping northwards. The result of the 3D gravity interface inversion agrees with results of the above mentioned depth estimation techniques. Finally, the gravity power spectral analysis resulted in two depth estimates, 1.53 km and 2.87 km which approximate the positions of two density interfaces. The shallow depth interface is thought to presumably delineate the low density Fluvio-lacustrine sediments including the rift floor volcanic units and crystalline basement. Our investigation results agree with the results of previous seismic studies which identified low velocity ("sediment-volcanic") horizon in the rift floor with low resolution. The information obtained with regard to water balance of the basin, salinity level of the lakes and the conceptual hydrological flow model appears to reveal that the groundwater flow in the study region is controlled by subsurface structures, particularly, the mapped interface topographies.

Appendix 1.5 Application of constrained 3D Gravity Interface Inversion techniques to map shallow Earth layer structures

Abstract

Multi layer 3D gravity inversion for layered structures and density interfaces are performed in the Central Main Ethiopian rift bounded between 38000'-39030' E and 7000'- 8030' N. The inversion is carried out in wave number domain using Parker-Oldenburg algorithm and is constrained with initial model information. The previous studies in the region focused on mapping crustal structures and Moho depths and least is known about the shallow earth. This study thus targets on mapping layers relief of shallow earth origin. Stacked horizons with depth to tops of density contrast are obtained from well log data, previous geophysical studies and gravity data analysis in this study. These stacked grids represent major geological boundaries where density contrast occurs. The model utilizes observed residual gravity anomaly and generates the structural relief maps of the respective layers with their corresponding calculated gravity anomaly responses and the associated errors. Successive structural inversions are performed on three layers with their corresponding acceptable mean misfits. The iteration converges successively for each layer in each structural inversion and the result is validated against a priori information. In addition to the topography/thickness of each layers, this study for the first time identified a new Mesozoic horizon laying between a Tertiary ignimbrite layer and the crystalline basement at depths between -2499 m and -3060 m and a having maximum thickness of 561 m. The identified Mesozoic sediment formation underlies a thick volcanic cover of 2.5 km which might be a suitable geologic setting for the growth of hydrocarbon reserves in the area and could probably be the source of CO2 degassing.

Appendix 1.6 Passive Seismic Survey carried to map the shallowest subsurface topography in Northern water divided between the Ziway-Shala lakes basin and Awash basin, Central Main Ethiopian Rift, to be submitted to peer-reviewed journals

Abstract

The passive seismic survey is carried in Northern water divided of the Ziway-Shala Lakes Basin, Central Main Ethiopian Rift. The method is a rapid and non-invasive technique which records a three component measurements of ambient seismic noise data. This data are processed and analyzed using average Horizontal to Vertical Spectral Ratio to determine resonance frequencies of the region. These will help to estimate layers cover thickness of near-subsurface. The potential field study carried in the region relatively focused on mapping the intermediate to deeper earth and least is given due emphasis of the shallowest layers. This study is therefore help to map the bedrock topography of shallowest earth origin. The depth to shallowest layer is determined for each sites and this depth value is gridded and mapped to show subsurface topography of the highest frequencies. The result shows that the shallowest bedrock layer is deepening northwards towards Awash basin.

Appendix 2 The SESAME, 2005 guidelines

Max. H/V at 35.94 ± 0.58 Hz (in the range 0.0 - 64.0 Hz).		
Criteria for a reliable H/V curve [All 3 should be fulfilled]		
$f_0 > 10 / L_w$	35.94 > 0.50	**OK**
$n_c(f_0) > 200$	21562.5 > 200	**OK**
$\sigma_A(f) < 2$ for $0.5f_0 < f < 2f_0$ if $f_0 > 0.5$Hz **$\sigma_A(f) < 3$ for $0.5f_0 < f < 2f_0$ if $f_0 < 0.5$Hz**	Exceeded 0 out of 1474 times	**OK**
Criteria for a clear H/V peak [At least 5 out of 6 should be fulfilled]		
Exists f^- in $[f_0/4, f_0]$ | $A_{H/V}(f^-) < A_0 / 2$	22.094 Hz	**OK**
Exists f^+ in $[f_0, 4f_0]$ | $A_{H/V}(f^+) < A_0 / 2$	56.469 Hz	**OK**
$A_0 > 2$	2.83 > 2	**OK**
$f_{peak}[A_{H/V}(f) \pm \sigma_A(f)] = f_0 \pm 5\%$	|0.01617| < 0.05	**OK**
$\sigma_f < \varepsilon(f_0)$	0.58123 < 1.79688	**OK**
$\sigma_A(f_0) < \theta(f_0)$	0.2144 < 1.58	**OK**

Threshold values for σ_f and $\sigma_A(f_0)$					
Freq. range [Hz]	< 0.2	0.2 – 0.5	0.5 – 1.0	1.0 – 2.0	> 2.0
$\varepsilon(f_0)$ [Hz]	0.25 f_0	0.2 f_0	0.15 f_0	0.10 f_0	0.05 f_0
$\theta(f_0)$ for $\sigma_A(f_0)$	3.0	2.5	2.0	1.78	1.58
log $\theta(f_0)$ for $\sigma_{logH/V}(f_0)$	0.48	0.40	0.30	0.25	0.20

Appendix 3 The SESAME, 2005 guidelines

Max. H/V at 20.53 ± 3.72 Hz (in the range 0.0 - 64.0 Hz).					
Criteria for a reliable H/V curve [All 3 should be fulfilled]					
$f_0 > 10 / L_w$			20.53 > 0.50	OK	
$n_c(f_0) > 200$			12318.8 > 200	OK	
$\sigma_A(f) < 2$ for $0.5f_0 < f < 2f_0$ if $f_0 > 0.5$Hz **$\sigma_A(f) < 3$ for $0.5f_0 < f < 2f_0$ if $f_0 < 0.5$Hz**			Exceeded 0 out of 986 times	OK	
Criteria for a clear H/V peak [At least 5 out of 6 should be fulfilled]					
Exists f^- in $[f_0/4, f_0]$ | $A_{H/V}(f^-) < A_0 / 2$			14.219 Hz	OK	
Exists f^+ in $[f_0, 4f_0]$ | $A_{H/V}(f^+) < A_0 / 2$			41.438 Hz	OK	
$A_0 > 2$			3.95 > 2	OK	
$f_{peak}[A_{H/V}(f) \pm \sigma_A(f)] = f_0 \pm 5\%$			|0.18122| < 0.05		NO
$\sigma_f < \varepsilon(f_0)$			3.72075 < 1.02656		NO
$\sigma_A(f_0) < \theta(f_0)$			0.2864 < 1.58	OK	
Threshold values for σ_f and $\sigma_A(f_0)$					
Freq. range [Hz]	< 0.2	0.2 – 0.5	0.5 – 1.0	1.0 – 2.0	> 2.0
$\varepsilon(f_0)$ [Hz]	0.25 f_0	0.2 f_0	0.15 f_0	0.10 f_0	0.05 f_0
$\theta(f_0)$ for $\sigma_A(f_0)$	3.0	2.5	2.0	1.78	1.58
log $\theta(f_0)$ for $\sigma_{logH/V}(f_0)$	0.48	0.40	0.30	0.25	0.20